



**Bergische Universität Wuppertal  
Fachbereich Mathematik und Naturwissenschaften  
Fachgruppe Physik**

**Optimization of nanostructures  
for field emission cathodes**

**Dissertation zur Erlangung des Doktorgrades  
der Fachgruppe Physik der Bergischen Universität Wuppertal**

**Dmitry Lysenkov**

Wuppertal  
2006  
**WUB-DIS 2006-02**

Die Dissertation kann wie folgt zitiert werden:

urn:nbn:de:hbz:468-20060113

[<http://nbn-resolving.de/urn/resolver.pl?urn=urn%3Anbn%3Ade%3Ahbz%3A468-20060113>]

## Abstract

Nanostructures with high aspect ratio, e.g. carbon nanotubes (CNT) and metallic nanowires (NW), have opened attractive possibilities for development of high performance cold field emission (FE) cathodes for vacuum electronics. CNT on porous alumina were synthesized using ferrocene as a single source precursor in a chemical vapor deposition (CVD) process. In order to influence the number density of CNT emitters and their anchoring, the pore diameter of the alumina templates was varied between 20 and 200 nm. The field emission performance of such CNT cathodes of some ten mm<sup>2</sup> size was integrally measured in a spacer-free diode configuration with luminescent screen, and the current distribution has been derived by means of developed image analysis software, which utilizes a calibration of the light intensity as function of the current. A strong increase of the integral dc current density has been found for pore diameters below 60 nm. The current distribution and conversion results in maximum local values of 108 mA/cm<sup>2</sup> at 7 V/μm (dc). In pulsed mode, peak values of up to 0.2 A/cm<sup>2</sup> at 11.5 V/μm averaged over several mm<sup>2</sup> size have been achieved with much improved luminescence and homogeneity of the emission which is, as demonstrated, suitable for light source applications.

The high current carrying capability of the CNT emitters on porous alumina was confirmed by local measurements with a field emission scanning microscope (FESM), which provided Fowler-Nordheim-like (FN) currents of up to 19 μA from single emitters. FESM voltage scans show high emitter number densities of up to 60000/cm<sup>2</sup> at  $E < 20$  V/μm. It was found that both field enhancement factors ( $\beta$ ) and emitter number densities are strongly dependent on the CVD growth conditions. Moreover, sparse emitters with comparably low average  $\beta \sim 300$  are preferable for high current densities, rather than those which are densely grown with  $\beta \sim 1100$ . Single CNT emitters on porous alumina have shown fluctuations, long-term instabilities, and strong ( $\sim 50\%$ ) current drift over some hours. Resolved in a ms time scale the emission current reveal a switching between several electronic states, which is caused by the adsorbates. Cathode processing at different pressures and currents results in much improved current stability of  $\pm 10\%$  as measured over 18 hours.

First experiments on copper NW with different geometrical properties, electrochemically grown in the etched ion-tracked pores of polymers, resulted in an emission site density of up to  $1.4 \times 10^5$  cm<sup>-2</sup> at 6 V/μm. Only 6% of the free-standing and vertically aligned NW were strong emitters. Nearly all NW showed unstable FN behavior with a mean  $\beta$  value of  $\sim 250$ , which corresponds to a cylindrical emitters with sharp edges.

# Contents

## Abbreviations

<b>Introduction .....</b>	<b>1</b>
<b>1. Electron field emission from conductive nanostructures .....</b>	<b>3</b>
1.1 Fowler-Nordheim emission from metallic surfaces .....	3
1.2 Local field enhancement by nanostructures .....	5
1.2.1 Carbon nanotubes (CNT) .....	6
1.2.2 Metallic nanowires .....	9
1.3 Mutual shielding effect.....	10
1.4 Adsorbate effects.....	11
1.5 Electron transport properties and stability limitations .....	13
<b>2. Fabrication of nanostructures on planar cathodes .....</b>	<b>17</b>
2.1 Bottom-up growth of CNT .....	17
2.1.1 Growth models .....	18
2.1.2 Random CNT on porous alumina by MOCVD.....	21
2.1.3 CNT patches on Si by MWCVD.....	24
2.2 Metallic nanowires in polymer ion-track templates.....	25
<b>3. Experimental techniques for field emission and surface analysis.....</b>	<b>28</b>
3.1 Integral measurement system with luminescent screen (IMLS) .....	28
3.1.1 Layout of the system .....	28
3.1.2 Processing of samples and electrode spacing calibration.....	30
3.1.3 Pulsed operation .....	31
3.1.4 Imaging of the emitter distribution and software analysis .....	32
3.1.5 Conversion of the IMLS images into current maps .....	34
3.2 Field emission scanning microscope (FESM).....	40
3.3 Surface analysis.....	43
<b>4. Results of field emission from nanostructures.....</b>	<b>44</b>
4.1 CNT on Si.....	44
4.2 CNT on porous alumina .....	46
4.2.1 Variation of the precursor type and amount.....	48
4.2.2 Influence of the alumina particles .....	53
4.2.3 Influence of the sample curvature .....	56

4.2.4	FESM studies of CNT on Anodisc®.....	60
4.2.5	Influence of the pore diameter on the current density.....	65
4.2.6	FESM studies of CNT on EPAM.....	70
4.2.7	Current stability of single CNT emitters.....	78
4.2.8	Current conditioning and pressure dependence of CNT cathodes.....	80
4.2.9	Maximum current densities in dc and pulsed modes.....	84
4.3	Metallic nanowires.....	87
4.4	Status of FE from nanostructure cathodes.....	90
<b>5.</b>	<b>Field emission applications of nanostructures.....</b>	<b>93</b>
5.1	Requirements for cold FE cathodes.....	93
5.2	Light source demonstrators.....	94
5.3	RF-gun with high brightness.....	96
5.4	Compact x-ray tubes.....	98
5.5	Field emission displays (FED).....	99
5.6	Multiple e-beam lithography.....	100
5.7	Outlook.....	101
	<b>Summary.....</b>	<b>103</b>
	<b>Acknowledgements.....</b>	<b>107</b>
	<b>References.....</b>	<b>108</b>

## Abbreviations

ADC	Analog-to-Digital Converter
AES	Auger Electron Spectroscopy
AFM	Atomic Force Microscope
B	Brightness
CCD	Charge Coupled Device
CCVD	Catalytic Chemical Vapor Deposition
CNT	Carbon Nanotube(s)
CRT	Cathode Ray Tube
CVD	Chemical Vapor Deposition
DC	Direct current
E	Electric field
EDX	Energy Dispersive X-ray Analysis
$E_{\max}$ , $E_{\max\text{eff}}$	Maximum field, maximum effective field
$E_{\text{on}}$	Onset field
EPAM	Electrochemically Etched Porous Alumina Membrane
FE	Field Emission
FED	Field Emission Display
FEM	Field Emission Microscope
FESM	Field Emission Scanning Microscope
Fig.	Figure
FN	Fowler-Nordheim
GPIO	General Purpose Interface Bus
h	Height
I, $I_{\text{peak}}$	Current, peak current
IEEE-488	= GPIO
IMLS	Integral Measurement System with Luminescent Screen
j	Current density
LCD	Liquid Crystal Display
MAFIA	Solution of the Maxwell equations by the Finite Integration Algorithm
MOCVD	Metal-Organic Chemical Vapor Deposition
MWCVD	Microwave Chemical Vapor Deposition
MWNT	Multi-Wall Carbon Nanotubes
N	Emitter number density
n.m.	Not measured
OLED	Organic Light-Emitting Diode
p	Pressure
P	Power
PC	Personal Computer
PDP	Plasma Display Panel
PID	Proportional-Integral-Derivative
r	Radius
RF	Radio Frequency
RGB	Red Green Blue
S, $S_{\text{FN}}$	Effective emitting surface
SEM	Scanning Electron Microscope
SWNT	Single-Wall Carbon Nanotubes
t	Time
T	Temperature

Tab.	Table
TEM	Transmission Electron Microscope
$T_{\text{period}}$	Pulse period
$T_{\text{pulse}}$	Pulse length
TED	Total Energy Distribution
U	Voltage
UHV	Ultra High Vacuum
VLS	Vapor Liquid Solid
XRD	X-ray Diffraction
Y	Pixel intensity
$\alpha$	Field correction factor
$\varnothing$	Diameter
$\Phi$	Work function
$\beta, \beta_{\text{FN}}$	Field enhancement factor
$\Delta z$	Electrode spacing
$\Delta Z_{\text{max}}$	Maximum height difference
1D, 2D, 3D	One, Two, Three Dimensional

---

## Introduction

The first evidence of cold electron field emission (FE) from metal surfaces at high electric fields was obtained at the beginning of the last century [1]. At first, in 1928 R.H. Fowler and L.W. Nordheim (FN) [2] succeeded in its correct interpretation. They describe FE as a quantum-mechanical tunnelling effect through a potential barrier at the metal – vacuum boundary under the influence of an applied electric field. As calculated from the FN theory electric fields of 2000 – 4000 V/ $\mu\text{m}$  are required for FE from flat clean metal surfaces. Experimentally FE occurred at much lower fields in the several V/ $\mu\text{m}$  range [3,4,5]. This enhanced field emission appeared locally in a certain spots of the metal surface, where particles, defects or scratches were identified by means of the microscopic measurements [6,7,8]. The classic FN theory was accordingly modified with the concept of local field enhancement ( $\beta$ ) [9]. Its applicability was proved in a number of experiments on metallic tips [10,11]. The FE is seen as alternative to thermionic electron emission, with advantages such as higher efficiency (cold) and brightness, faster turn-on times and compactness.

The discovery of the carbon nanotubes (CNT) in the year of 1991 [12] opened a new epoch in the development of FE materials and caused the entry of many scientists into this field. They were stimulated at first by the remarkable 1D effects predicted for their electronic properties [13,14] and the subsequent unique applications [15,16,17]. The major breakthrough, occurred in 1996 when Smalley et al. [18] synthesized bundles of aligned single-wall CNT with a small diameter distribution, thereby making it possible to carry out many sensitive experiments relevant to 1D quantum physics [19,20]. The versatile multi-wall CNT (MWNT) were investigated as reinforcements in high performance composites [21] and robust cold field emitter arrays [22]. They have been recognized as a very promising FE structures due to their relatively simple production, chemical inertness and low operation fields [23]. This initial success has triggered a worldwide effort to grow nanotubes with a specified geometry and distribution over flat substrates. The great progress in this direction was achieved by employing of Chemical Vapour Deposition (CVD) [24,25,26]. The simple and cheap growth methods, such as one-stage metal-organic CVD with template (e.g. porous alumina) controlled MWNT growth, could be commercially preferred [27]. In the past several years there has been a rapidly growing interest in investigating other novel nanomaterials for cold cathodes [28]. These include wide and narrow band-gap semiconductor and metallic nanowires, which have best values close that reported for CNT [29].

The utilization of the advantages of CNT [30] for the FE applications is currently an intensively developing field. Such cold cathodes should be implemented in light [31] and x-ray sources [32], which are already developed as commercial prototypes [33,34], field emission displays (FED) [35,36], multiple electron beam lithography [37], etc. Depending on the application different requirements are demanded from the cathode materials. While cathodes for x-ray tubes should provide high, stable currents up to  $\sim 1$  A from  $\text{cm}^2$  areas, the FEDs require high densities of the emitters ( $n \sim 10^6/\text{cm}^2$ ), low operation fields ( $< 10$  V/ $\mu\text{m}$ )



---

and uniform emission from up to  $10^3 \text{ cm}^2$  areas over at least 10.000 hours at high vacuum (HV) conditions ( $p \sim 10^{-6}$  mbar). Therefore, an integral measurement system with the luminescent screen (IMLS) was built at the University of Wuppertal for the tests of the above mentioned parameters for up to  $30 \times 30 \text{ mm}^2$  size samples [38]. In this apparatus the integral emission current, overview of the relative strength of emitters, their uniformity and stability can be measured. For the investigation of the local FE parameters of cathode materials the field emission scanning microscope (FESM) has been built within a conventional surface analysis system (Escalab II) [7]. This device provides high ( $\sim \mu\text{m}$ ) spacial resolution for the investigation of the FE properties and their direct correlation to the surface morphology and chemical composition of emitters. The investigation of the samples both in IMLS and FESM allows comprehensive study of the cold cathode materials.

The main goal of this work is the investigation of the usefulness of CNT and metallic nanowires as cold cathodes, and their optimization for various applications. For this purpose, the existing IMLS has been extended and improved. A power supply with PID regulated voltage output has been employed for the hardware extension, which allows safe conditioning of the cathodes at a constant current. In order to decrease the typical heat loads of some  $\text{W}/\text{cm}^2$  on the luminescent screen, thus reducing the discharge risk, a pulsed power regime has been enabled for the same power supply. This makes higher peak current densities achievable, than for dc operation. The image AnalySIS<sup>TM</sup> software automatizes the data processing and helps in investigation of short- and long-term fluctuations of emitters, which are undesirable in the devices. It is quite challenging to obtain information about the current distribution from the IMLS images by attribution of light clusters to the localized emitters. The developing of an algorithm for the conversion of the IMLS images into current maps, which utilizes a calibration of the light intensity as function of the current has enabled a fast analysis of the emitter strength. By means of these techniques for optimised MWNT on porous alumina, record high current densities, excellent stability and homogeneity were achieved. This material has been employed as a FE cathode in a light source demonstrator. The work was carried out in close cooperation with the Technical University of Darmstadt, where the investigated materials were fabricated.

## 1. Electron field emission from conductive nanostructures

The Fowler-Nordheim (FN) theory describes electron field emission (FE) from an ideal metallic surface. For real conditions the FN theory should be modified by the local field enhancement factor, which is applied for the investigation of the emission from novel nanostructures. For densely packed emitters, a mutual shielding effect strongly decrease the emission current from the sample surface. Gas atoms adsorbed on the samples lead to the current fluctuations, which are not considered by the FN theory. The current carrying capability and stability of nanostructure emitters are further influenced by the electron transport properties, which might be ballistic in case of nanotubes.

### 1.1 Fowler-Nordheim emission from metallic surfaces

FE was first discovered by R. W. Wood in 1897 [1]. The theoretical study was started by W. Schottky (1923), who tried to describe the FE by means of electrons thermally excited over a potential barrier at a surface, the width of which is reduced by an applied electric field [39]. Required fields of  $10^4$  V/ $\mu\text{m}$  at room temperature for the emission initiation were up to 50 times higher than experimentally obtained values. The expected dependencies of the emission current on the electric field ( $I \sim \sqrt{E}$ ) and on temperature were, however, not observed experimentally [40,41,42]. R. A. Millikan and C.C. Lauritsen [43] found that the emission current depends exponentially on the applied potential, and in 1928 R. H. Fowler and L. W. Nordheim developed a first correct theory of field emission based on quantum mechanical tunneling of electrons through a surface barrier [2]. There the electrons in the metal are described by the Sommerfeld free electron model with Fermi-Dirac statistics [44] at temperature  $T = 0$  K. The metal surface is taken to be planar, thus the surface electric field is uniform. The potential barrier and schematic model of the FN emission are presented in Fig. 1.1.

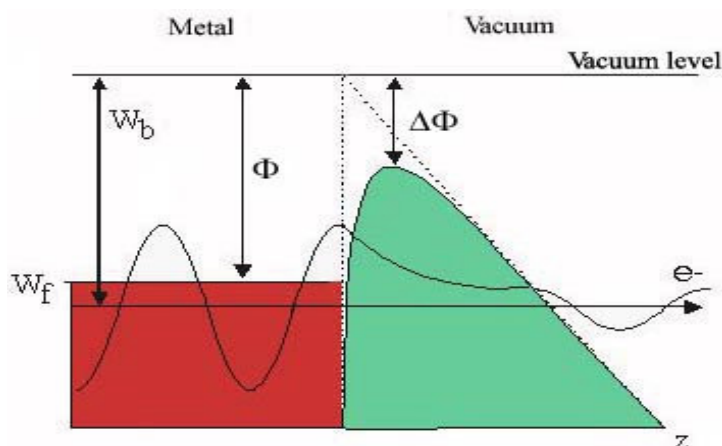


Fig. 1.1. Schematic illustration of the potential barrier at the metal-vacuum boundary and of the wave function of the tunneling electron with binding energy  $W_b$  below the fermi level  $W_f$  in the conduction band.  $\Delta\Phi$  is the reduction of the work function  $\Phi$  due to image charge correction [38].

The current density through the barrier is calculated by

$$j = e \int_0^{\infty} n(W) D(W, E) dW \quad (1.1)$$

where  $n$  is the incident flux of electrons with energy  $W$ ,  $D$  is the tunneling probability for the electric field  $E$  and  $e$  is the electron charge. The barrier is described by a function, which takes into account the image forces, resulting in the rounding of the triangle barrier;

$$V(z) = -\frac{e^2}{16\pi\epsilon_0 z} - eEz, \text{ with } \Delta\Phi(E) = \sqrt{\frac{e^3 E}{4\pi\epsilon_0}} = 3.79 \cdot 10^{-2} \sqrt{E} \quad (1.2)$$

where  $z$  is the coordinate perpendicular to the metal surface and  $\epsilon_0$  is the dielectric constant of the vacuum. Then the classic FN formula is

$$j(E) = \frac{AE^2}{\Phi t^2(y)} \exp\left(-\frac{B\Phi^{\frac{3}{2}} v(y)}{E}\right) \quad (1.3)$$

with  $j(E)$  in  $A/cm^2$ ,  $E$  in  $MV/m$ , work function  $\Phi$  in  $eV$ , constants  $A = 154$ ,  $B = 6830$  and  $t(y)$  and  $v(y)$  are the Nordheim functions, which depends on the relative reduction of the barrier through the image charge

$$y = \frac{\Delta\Phi}{\Phi} = \frac{(e^3 E / 4\pi\epsilon_0)^{1/2}}{\Phi}. \quad (1.4)$$

They are tabulated and can be found in [45]. Often used estimations are  $t^2(y) = 1.1$  and  $v(y) = 0.95 - y^2$ , which are without image charge correction both are set equal to 1. The FN current density behavior of materials with work functions in a range of 4 – 5 eV and the influence of the image charge effects at high fields are presented in Fig. 1.2.

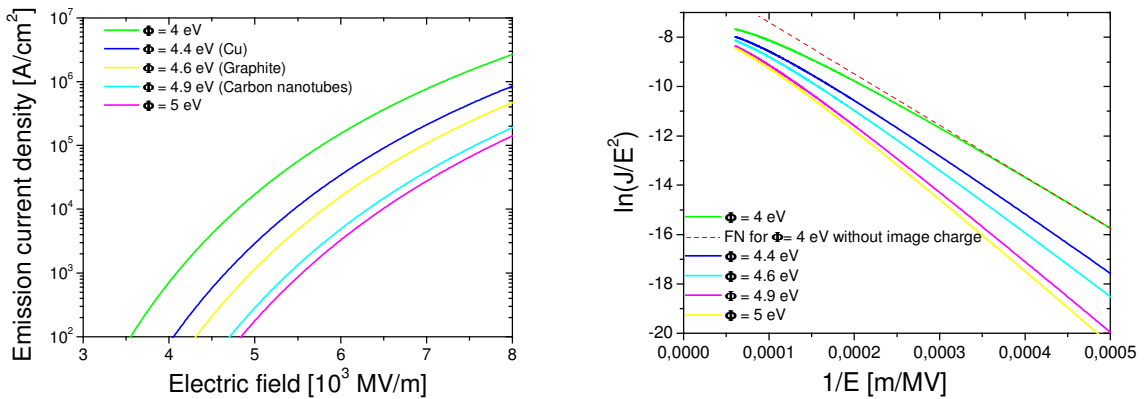


Fig. 1.2. FN curves  $j(E)$  calculated for the work functions of important FE materials in a range of 4 – 5 eV (left) and calculation of  $\ln(j/E^2)$  on  $1/E$  dependence with (solid lines) and without (dashed line) image charge correction at high fields (right).

The exponential decrease of the tunneling probability with increased binding energy of electrons and small probability of occupied states above the fermi level at temperatures below  $500^\circ C$  reveal the sharp energy distribution of tunneling electrons. Though the FN theory was

confirmed by a number of experiments, in general, it is very simplified. The Fermi-gas model of free electrons, assumed atomic scale surface smoothness and the one particle approximation, an inconsistency in combining of classic particles flow with quantum-mechanical tunneling and 1D problem with a potential profile, which accounts only to image forces are the major problems of the FN theory. In 1950s was predicted the deviation from FN behavior at high fields and high current densities [46]. Ehrlich and Plummer in 1978 finally shows the non-correspondence of the experimental current densities from microscopic tips to that of predicted by FN-theory [47]. Later investigations reveal the presence of high- and low-energy tails in the emitted electron spectrum [48].

## 1.2 Local field enhancement by nanostructures

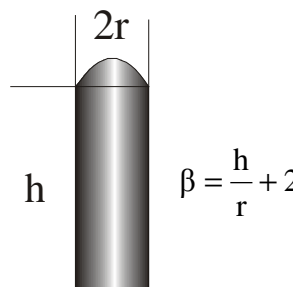
The theory presented above is suitable for the description of clean and flat metal surfaces. In experiments with real metal cathodes, however, the emission current appeared already at fields  $< 100 \text{ V}/\mu\text{m}$  [3, 4]. Schottky suggested the local field enhancement caused by surface roughnesses as an explanation [39]. Then it was established, that this enhanced field emission appeared in certain spots on the metal surface and reveal FN behavior i.e.  $\ln(I/E^2)$  is proportional to  $1/E$ . Therefore, the macroscopic field  $E$  in the FN equation (1.3) should be modified with geometrically enhanced by a factor  $\beta$  microscopic value  $\beta \cdot E$ . The modified FN equation is

$$I(E) = \frac{AS\beta^2 E^2}{\Phi} \exp\left(-\frac{B\Phi^{\frac{3}{2}}}{\beta E}\right) \quad (1.5)$$

where  $S$  is the fit parameter, which might be interpreted as effective emitting surface through which the emission current  $I$  flows. The  $\beta$  and  $S$  can be found by means of the slope of FN plot,  $K = d(\ln(I/E^2))/d(1/E)$ , and ordinate crossing  $C$  (or its linear fit)

$$\beta = \frac{B\Phi^{\frac{3}{2}}}{K}, \quad S = \frac{\Phi}{A\beta^2 \exp(C)}. \quad (1.6)$$

The slope is a function of both  $\beta$  and  $\Phi$ , two inseparable parameters in classical field emission. The model of the field enhancement was analytically and numerically applied to different emitter geometries. It has been shown, that if the  $\beta$  factors are computed as a



$$\beta = \frac{h}{r} + 2 \quad (1.7)$$

Fig. 1.3. Field enhancement factor  $\beta$  of the conducting cylinder with half-sphere on the top.

function of  $h/r$ , the ratio of their height  $h$  to a tip radius of curvature  $r$ , they can all be characterized to a good approximation by the unifying expression (Fig. 1.3) [50], provided  $h/r \geq 5$ .

This simple model is often used for estimations of the field enhancement on structures with a defined geometry and high aspect ratio. According to the above equations, the emission current is strongly dependent on the following three factors: the work function of the emitting surface, the radius of curvature of the emitter apex, and the effective emission area. Microscopic tips of different geometries have been used in investigations of electron FE since the 1950s [10,11]. However, the real breakthrough occurred after the discovery of nanoscale objects, such as carbon nanotubes and metallic nanowires, which reveal remarkable field emission properties. Due to the wide field of potential applications they are currently of great interest [12,28,51,52,53].

### 1.2.1 Carbon nanotubes (CNT)

Carbon nanotubes were discovered in 1991 by Iijima [12]. They represent one of the examples of novel nanostructures which have a simple chemical composition, but reveal the great diversity of structure-property relations among all nanomaterials. The CNT has cylindrical configuration and consists of one (single-wall nanotube (SWNT)) [18] or several (multi-wall nanotube (MWNT)) [24] atom-thick graphite layers (also called graphene) and in general has length up to few  $\mu\text{m}$  and diameter up to 20 nm (Fig. 1.4) [54]. It is possible,

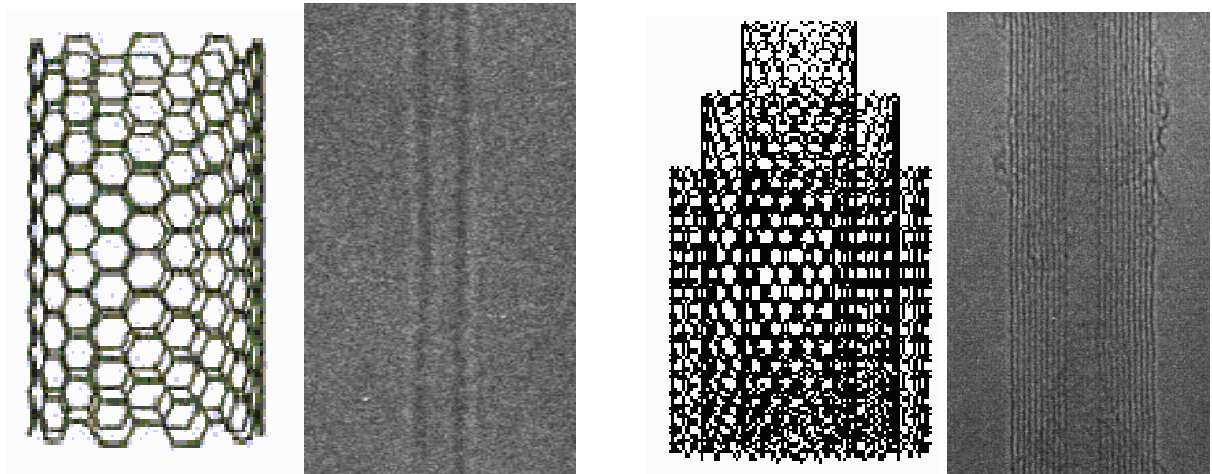


Fig. 1.4. Models of SWNT(left) and MWNT(right) with corresponding TEM images, which resolve graphene layers of nanotubes. Carbon-carbon distance is  $1.421\text{\AA}$ . For a MWNT the different walls are obvious, they are separated by  $3.4\text{\AA}$ .

however, to grow ultra-long CNT with lengths of up to 4 mm [55] or thicknesses up to 100 nm [56]. The structure of the CNT can be described by the chiral vector  $C_h$  which connects two crystallographically equivalent sites on the 2D graphene sheets (Fig. 1.5(left)) [13].

$$C_h = na_1 + ma_2 \quad (1.8)$$

The construction of single walled nanotube (SWNT) depends on  $(n, m)$  which describes the chiral vector  $C_h$ . In Fig. 1.5 the  $\theta$  - chiral angle between  $C_h$  and “zig-zag” direction ( $\theta = 0$ ) is shown. By the orientation of the carbon hexagons to the axis of the nanotube, in other words, the method of rolling of graphite to a tube, they can be either a zig-zag ( $\theta = 0$ ), armchair ( $\theta = 30^\circ$ ), or helical type ( $0 < \theta < 30^\circ$ ) (Fig. 1.5 (right)) [52].

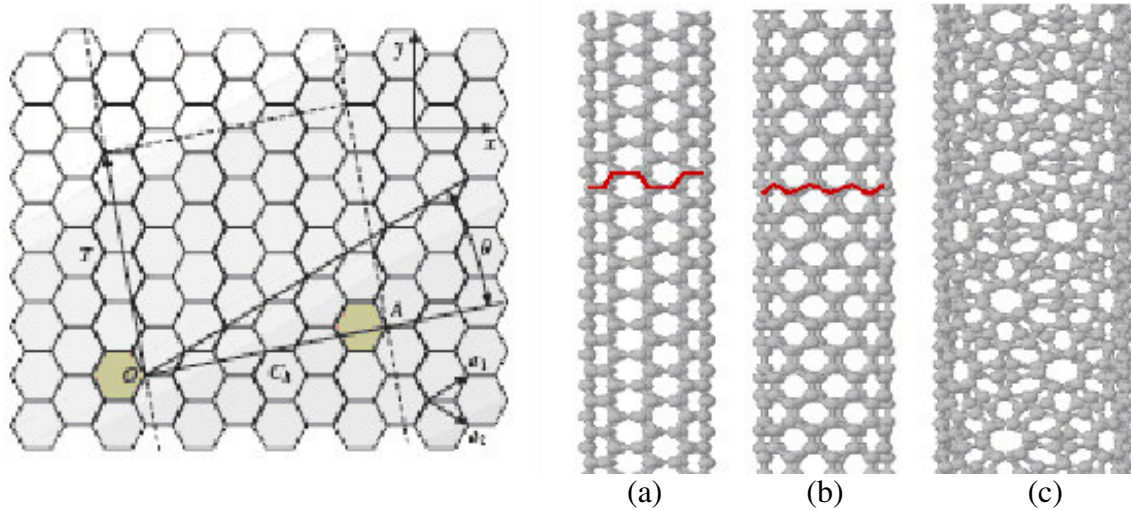


Fig. 1.5. Definition of the chiral vector  $C_h$  (OA) by unit vectors  $a_1$  and  $a_2$  and the chiral angle  $\theta$  (left) [52]. Three different nanotube structures are shown as examples for (a) an armchair type ( $\theta = 30^\circ$ ), (b) a zig-zag type ( $\theta = 0$ ), and (c) a “chiral” type ( $0 < \theta < 30^\circ$ ) nanotube.

Due to a symmetry and unique electronic structure of graphene, the structure of a nanotube strongly affects its electrical properties. For a given  $(n, m)$  nanotube, if  $2n + m = 3q$  (where  $n$ ,  $m$  and  $q$  are integers), then the nanotube is metallic; otherwise it is a semiconductor (Fig. 1.6). The metallic nanotubes became models for single electron charging, weak localization, ballistic transport and quantum interference. The semiconducting nanotubes are used to be a part of nanoelectronics as transistors, logic and memory devices [57-60].

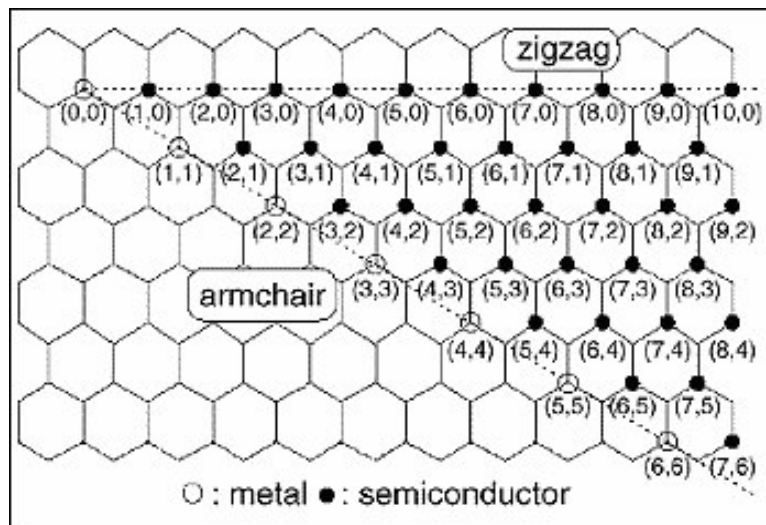


Fig. 1.6. Possible vectors specified by the pairs of integers  $(n, m)$  for general carbon nanotubes including zig-zag, armchair and chiral nanotubes [52].

It has been established that nanotube ends are often closed with half-sphere fullerenes (e.g.  $C_{60}$ ) [54]. Under normal conditions carbon tube ends close rapidly [52], which allows for an estimation of the field enhancement on nanotubes using a conducting cylinder model. Due to their high aspect ratio [61] the emission current appeared already at fields of some  $V/\mu\text{m}$  [13]. The linear FN behavior has been observed for both SWNT and MWNT [62,63]. The work function for MWNT is typically  $4.9 \pm 0.1$  eV [64], which is slightly higher than that of graphite (4.6 eV). However, the significantly reduced work function of 3.7 eV was observed for SWNT [65].

Despite of the simplicity of formula (1.7) it correctly reflects the field enhancement on CNT. In case of protrusions on the nanotube end or its opening, the behavior is more complex (Fig. 1.4.). Some protrusions on the CNT end leads to an increased field enhancement [66], which further decreases the onset field. Calculations of the field enhancement factors

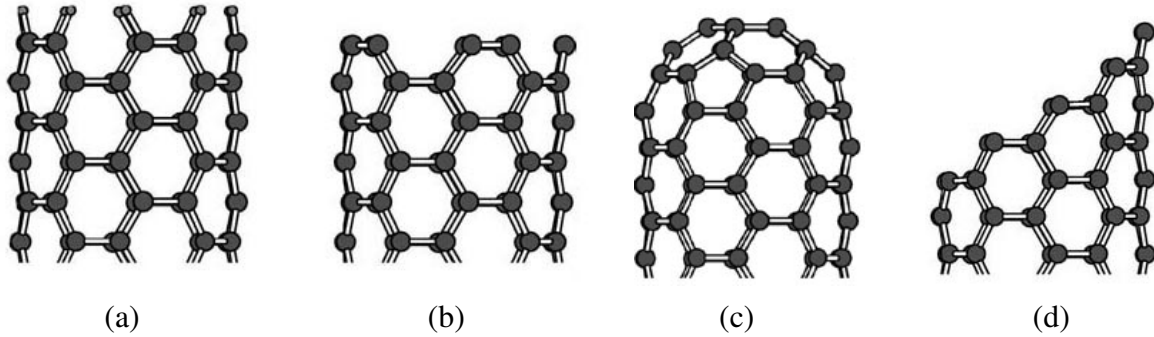


Fig. 1.7. Edge structures of the CNT (a) H attached (stabilized), (b) flat cut, (c) closed and (d) slant cut CNT.

for hydrogen attached, flat, closed and slant cut SWNT (Fig. 1.4.) reveal the highest field enhancement for (d) the slant cut configuration [67]. The extrapolations for the realistic  $2 \mu\text{m}$  long tube leads to the field enhancement factors of 1700, 1900, 2100, and 3300 for (a)-(d) geometries in Fig. 1.7, respectively. Thus, for opened CNT the field enhancement should be calculated using different relations as in formula (1.7) (Fig. 1.8).

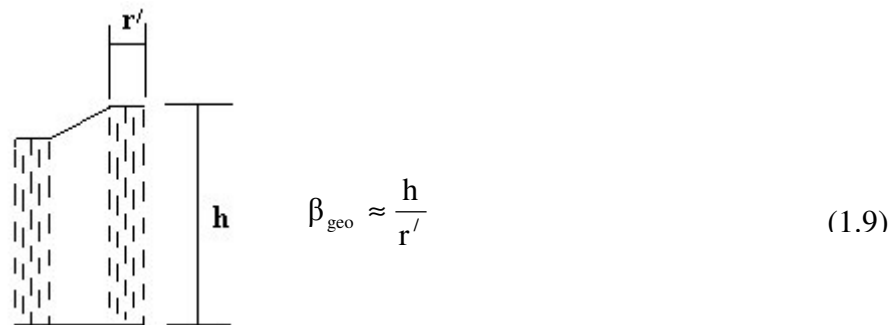


Fig. 1.8. Field enhancement for the open MWNT (schematic cross section) with the slant cut tip configuration. Dashed lines show the graphene layers.

The thickness of the tube walls should be taken as  $r'$ , instead of the radius of the MWNT. The spacing between the graphene layers is essentially the same as the interplanar spacing in

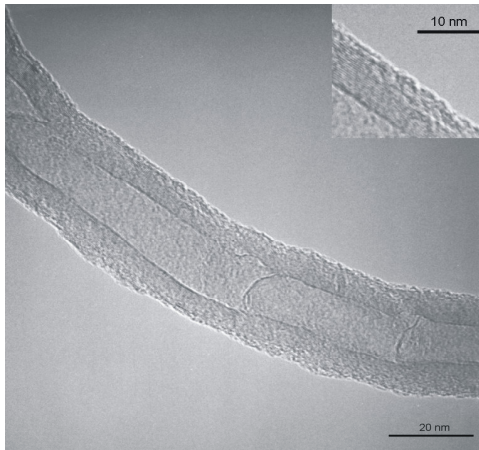


Fig. 1.9. HRTEM image of the MWNT [68]. The nanotube walls consist of 20 graphene layers.

graphite ( $\sim 3.4 \text{ \AA}$ ), resulting for the e.g. twenty wall CNT ( $\varnothing \sim 20 \text{ nm}$ ) the  $r' \sim 6.8 \text{ nm}$ . The internal spacing in the MWNT can be significantly higher than  $r'$  (Fig. 1.9)[68]. Thus, the field enhancement for the opened MWNT is about a factor of 1.5 higher than for closed. An electron holography measurement of the electric field distribution along a field-emitting multiwall CNT [69] reveals that the FE current concentrates precisely at the tip and not at the tube defects such as sidewall imperfections. The measurement is consistent with the scenario that there is no potential drop along the micrometer-long tube. Zheng et al. [70] made simulations of

emission from  $1 \mu\text{m}$  long SWNT on tungsten calculating about 8000 atoms in the tip. The electric field was well shielded for the bulk of the CNT, while penetrating the tip. The single layer of carbon atoms shield the field for up to  $10 \text{ V}/\mu\text{m}$ . The field which penetrates the tip lowers the potential barrier and results in the deep potential well in the tip region where a large amount of excess electrons reside. The lowering of barrier height leads to a significant increase of emitting current, which might reveal a non-classic nature of the CNT FE mechanism. Thus, the low threshold field for electron emission from the nanotubes can be the result of both large field enhancement factor and a reduction of the work function.

## 1.2.2 Metallic nanowires

Metallic nanowires are another potential candidate for field emission applications [71, 72]. Typical examples of nanowires include metals such as Mo, W, Cu, Bi, Au, and their oxides  $\text{MoO}_2$ ,  $\text{WO}_2$  etc. which have high melting points, relatively low work function, high electrical conductivity and robustness [71-75]. In addition, it is not trivial to produce metallic CNT in a controlled way; therefore, the nanowires are considered to be important cold cathode materials. They are straight, with diameters in the range from 30 to 330 nm and lengths of up to  $20 \mu\text{m}$ . Since the conductive wires can enhance the external electric field due to their geometry by several orders of magnitude as well as CNT,  $\beta$  modified FN theory can be also applied to the metallic nanowires [73]. However the FE properties of nanowires were investigated much less systematically in comparison to CNT. The measurements are concentrated mainly on the I-V characteristics, threshold fields and current densities.

The  $h/r$  ratio does not show the field enhancement correctly, because in the majority of cases the profiles of nanowires show non-spherical ends (Fig. 1.10). The field enhancement of nanowires seems to be higher than in formula in Fig. 1.3 at least in factor 3, due to field enhancement on the fine edge radius of the wires (Fig. 1.10) [73], similar to what is seen for slant cut nanotubes.



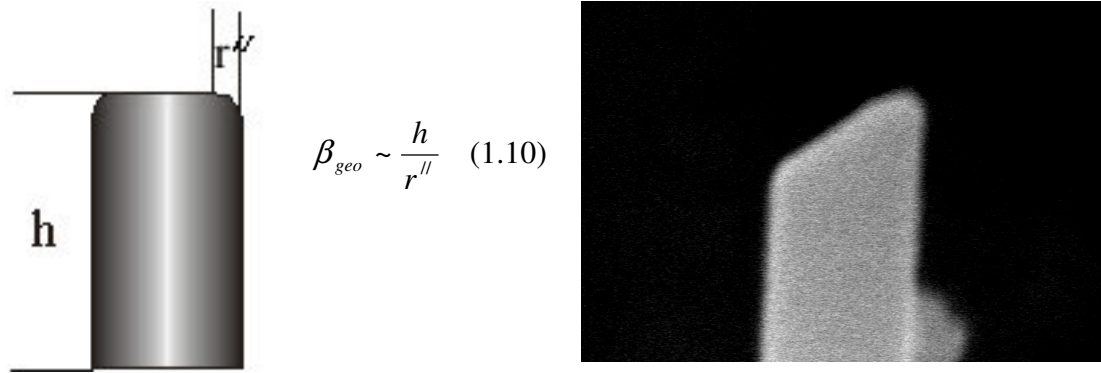


Fig. 1.10. Field enhancement factor  $\beta$  of a conducting nanowire with fine etched edges (schematic draw left) and the SEM image of 100 nm thick slant cut Cu nanowire.

### 1.3 Mutual shielding effect

Groening [65], Nillson [76] and Bonard [77] found that closely packed emitter arrays are not suitable configuration for the FE, due to mutual shielding (also screening) effect. Electrostatic calculations of the field penetration between parallel standing tubes for different intertube distances are shown in Fig. 1.11. The equipotential lines and thus the field enhancement factor  $\beta$  are seen to be strongly affected as the inter-tube distance is decreased. The optimum distance between neighbor 1  $\mu\text{m}$  tubes in accordance with the experiment was 2  $\mu\text{m}$ , where the emission was the strongest. It is worth nothing, that this effect is dominated by the field penetration, which is determined by the relative height of the CNT compared to the intertube distance. A variation in the tube tip apex changes the magnitude of the field amplification, but does not significantly influence the optimum distance.

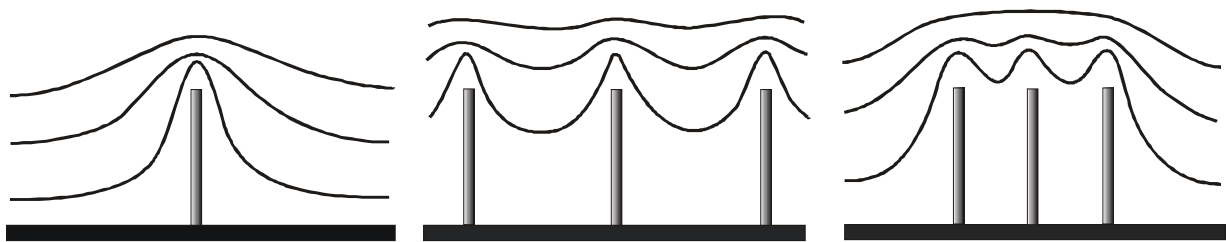


Fig. 1.11. Simulation of the equipotential lines of the electrostatic field for carbon nanotube emitters (adapted from [36]).

The measurements show that the emission from densely packed CNT films is poor because of reduction of the field enhancement factor due to the screening effect [78] when the distance between CNT is sufficient to reach substantial local fields. The available emitter number density, however, is sufficient for adequate emission currents. Depending on the approach and requirements emission is always affected by the height of emitters and distance between them. The experiments proved, that for the power applications field enhancement the distance between neighbor emitters should be similar to their height (Fig. 1.12) [77, 79].

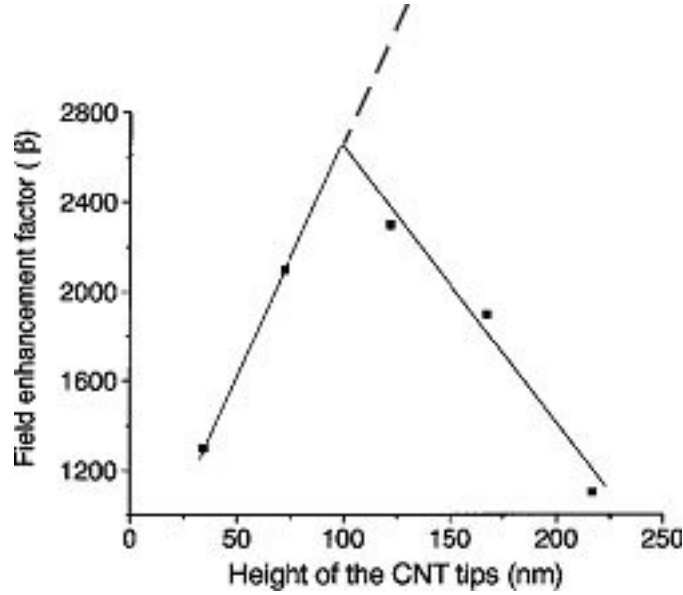


Fig. 1.12. Experimentally measured dependence of the field enhancement on the CNT height (solid line), where the inter-tube distance is 104 nm [79]. The dashed line shows the expected result without screening.

#### 1.4 Adsorbate effects

Field emission is very sensitive to changes of the surface barrier due to the influence of external atoms or molecules, which can be adsorbed onto the surface. Under real conditions even at ultra high vacuum (UHV) pressures ( $10^{-9}$ - $10^{-10}$  mbar) after about one hour the atomic monolayer should be taken into account [80]. At room temperature the ad- or desorption of the atoms produce instabilities and reversible switching between electronic states [81,82]. At first, such effects were explained by means of the changing of the work function through the adsorbates [83, 84], which, however show some inconsistencies. The FN analysis is consist in the determination of the parameters  $\beta_{\text{FN}}$  and  $S_{\text{FN}}$  at a given work function, which principally can not be considered as real geometric parameters. For the tungsten with given work function  $\Phi_0 = 4.5$  eV,  $\beta_{\text{FN}}$  and  $S_{\text{FN}}$  for the real work function  $\Phi$  show the following dependencies [85]:

$$\beta_{\text{FN}} = \beta_{\text{geo}} \left( \frac{\Phi_0}{\Phi} \right)^{3/2}, \quad S_{\text{FN}} = S_{\text{geo}} \exp(\Delta x p \left( \frac{\Phi}{\Phi_0} \right)^3), \quad (1.10)$$

where  $\beta_{\text{geo}}$  and  $S_{\text{geo}}$  are the parameters of the clean W emitter and  $\Delta C$  is the change of the FN axis crossing. Thus, the adsorption phenomena can greatly change the FN parameters.

Investigations of adsorbates on metal surfaces were first made by Duke and Alferieff in 1967 [86], and then revised by Gadzuk [87], who investigated the influence of virtual impurity to the total energy distribution of electrons (TED) in FEM. Resonance effects should be observable as a structure in the TED of field-emitted electrons, reflecting the perturbed energy levels of the adsorbed atom. The authors characterize the resonance tunneling by an enhancement factor

$$R(W) = \frac{dj/dW}{dj_0/dW}, \quad (1.11)$$

where  $dj_0/dW$  is the TED of emitted electrons,  $dj/dW$  is the TED in the presence of an atom. The maximum of the enhancement factor for emission through the impurity can be very large, falling within the range  $1 < R(W) < 10^4$  [86].

The accepted theory is as follows: when an atom (molecule or cluster) is adsorbed onto a metal surface the field emission barrier (Fig. 1.1) is augmented by a potential well with a diameter about of adsorbed atom as displayed in Fig. 1.13. The electronic state of this atom is characterized by a discrete level, which is broadened into a band and referred to as a local density of states. If the energy of the tunneling electron lies within an energy level of the atom, the electron can tunnel through the atom, get across the spatial domain of the atom without decrease of the probability amplitude, and then tunnel through the narrower barrier as schematically shown in Fig. 1.13.

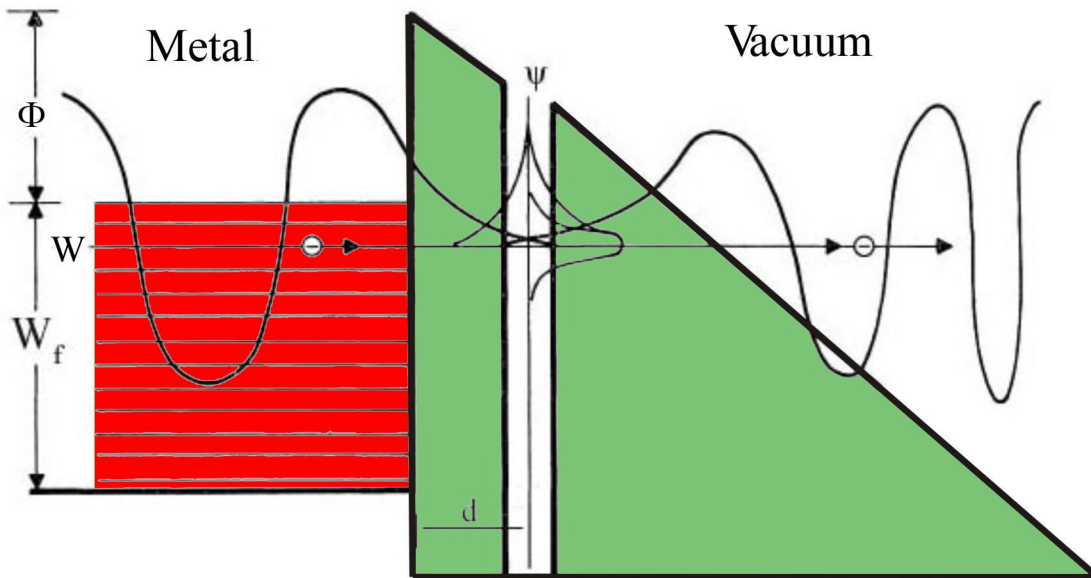


Fig. 1.13. Schematic model of resonance tunneling presented by Gadzuk [86], which describes the wave function of the tunneling electron from band below  $W_f$  under the influence of the adsorbate atom potential at the distance  $d$ .  $\psi$  is the localized virtual impurity function.

The increase or decrease of the tunneling probability through adsorbates can be found by the solution of the Schrödinger equation [88]. An increase of the FN emission is expected, when the adsorbate states lay in the region near Fermi energy. If the adsorbates have no constrained states or it is not in the conducting band of the metal the emission current will be decreased [85].

Every surface under the normal atmospheric conditions is covered with adsorbates. In FE e.g. from CNT the adsorbed atoms can lead to the high current instabilities or saturation of the emission current [89], due to field and current-induced decrease in the tunneling enhancement of the adsorbate states. External atoms (molecules) can be easily desorbed by heating in high vacuum conditions, which, however, does not suppress the building up of the

---

adsorbate layers afterwards even at UHV, resulting in a reversible current–voltage characteristics [89].

Adsorbing molecules have important consequences for the physical properties of nanostructures. They might effectively lower the ionization potential (IP) and facilitate the extraction of electrons. Such an experimental work was done at Motorola [90], where changes in field-emission behavior of CNT in the presence of various gases were studied, i.e., O<sub>2</sub>, H<sub>2</sub>, and water vapor. While H<sub>2</sub> did not affect the field-emission behavior appreciably, adsorbed water was found to significantly enhance the emission current. A high sensitivity of CNT to O<sub>2</sub> adsorption was found, which allows one to use them as small chemical sensors with high sensitivity at room temperature [91]. At high voltages, O<sub>2</sub> increase the onset field of the FE and decrease the emission current permanently. This effect is related more to the etching of the emitters. Modern material science concentrates primarily on the investigation of the sensitivity of CNT [51] and metal oxide nanowires [92] to certain gases for detection of toxic, pollution and combustion vapors.

A calculation made by Stan et al. allows one to predict the adsorption of arbitrary gases within CNT or nanotube bundles [93]. Logically, small atoms and molecules (He, Ne, H<sub>2</sub>) can be adsorbed within both interstitial channels and the tubes while large atoms and molecules (Kr, Xe, CH<sub>4</sub>, CF<sub>4</sub>) almost exclusively adsorbed within the tubes.

## 1.5 Electron transport properties and stability limitations

The study of the electrical transport properties of nanostructures is important for their characterization, especially applying to electronic devices, and the investigation of unusual transport phenomena in one-dimensional quantum effects. Important factors that determine the transport properties of nanostructures are their diameter, material composition, surface conditions, crystal quality, and crystallographic orientation along the tube/wire axis. Electronic transport phenomena in low-dimensional systems can be roughly divided into two categories: ballistic and diffusive transport. Ballistic transport phenomena occur when electrons travel across the nanostructure without any scattering, then the nanotubes/wires have lengths smaller than the carrier mean free path. In this case, the conduction is mainly determined by the contacts between the nanowire and the external circuit, and the conductance is quantized into an integral number of universal units  $G_0 = 2e^2/h$  [94]. For nanotubes/wires with lengths much larger than the carrier mean free path, the electrons (or holes) undergo numerous scattering events when they travel along the tube/wire. In this case, the transport is in the diffusive regime, and the conduction is dominated by carrier scattering within the nanostructures due to phonons, boundary scattering, structural defects and impurities.

For the ideal metallic SWNT conductance is  $2G_0$ , due to two bands crossing the Fermi level, which corresponds to a resistance of 6.5 k $\Omega$ . The  $2G_0$  may not be applicable for each shell of the MWNT, moreover the interactions between nanotube walls can reduce the

conductance [95]. The main problem is to contact all walls of a MWNT and not only the outermost. The technique combining electrode formation and MWNT growth allows to form a perfect electrical contact [96]. At a room temperature such pure MWNT have resistance of some tens of ohm, and current carrying capability up to 7 mA at a bias voltage 0.25 V, which corresponds to a current density of  $10^8$  A/cm<sup>2</sup> and a dissipated power of 1.82 mW (Fig. 1.14).

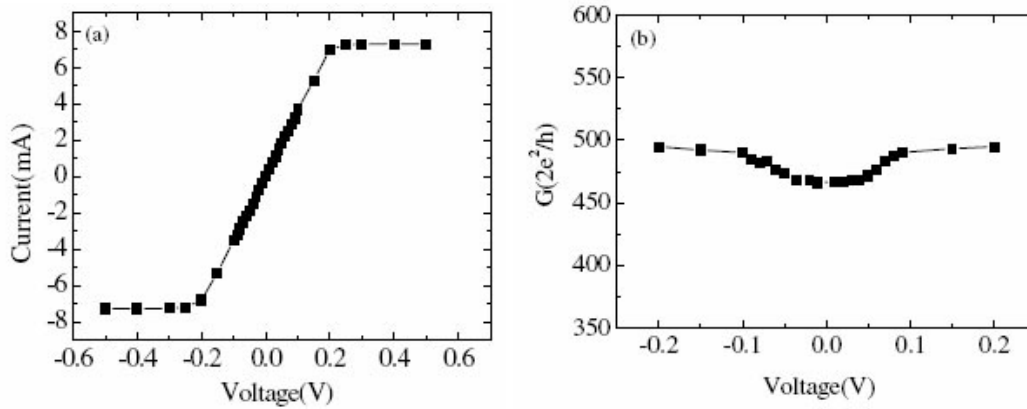


Fig. 1.14. (a) I-V characteristic curves of an as-grown single MWNT at room temperature and (b) its conduction trace.

According to a simple heat transfer analysis, the temperature in the MWNT would be at least several ten thousands K at such high current density if the thermal conductivity is assumed as 25 W/mK [97]. Such enormous power handling capability can be explained only by quasiballistic conductive phenomena. The measured conductance is a factor of 3 higher for each wall of MWNT, than maximum expected by SWNT (for 74 walls MWNT the conductance was found  $460G_0$ ) [96]. Large current capabilities explained by the large diameters of nanotubes and participation of inner walls. This multichannel conductance increases with temperature growth. The impurities and high fields lead to high energy consumption and destroy the ballistic transport, which results in current saturation [98].

Ballistic properties appeared also for ultra-short ( $< 0.5$  nm) wires, whose length is comparable to the Fermi wavelength (so called “quantum wires”) [99]. For long metallic nanowires this effect has not been detected. For single-crystalline copper nanowires at room temperature the resistivity is 10 times higher than for the bulk material [100]. This can be due to contact resistance, scattering of electrons within the nanowire, which is also natural for nanotubes, or oxidation. Since the metallic nanowires have a high surface to volume ratio, they are vulnerable to oxidation especially when carrying high currents. The resistance increases by 6 orders of magnitude for copper nanowires by exposure to aerial oxygen. A similar effect was observed for molybdenum [101].

There are several effects in vacuum technique which reduce the stability and lifetime of the emission or leads to the destruction of emitters. Vacuum breakdown is a catastrophic phenomenon, where the insulating properties of the vacuum gap are spontaneously lost as the result of an electrical discharge between the electrodes. It can be observed at fields  $< 10$  V/ $\mu$ m and results complete change of the emission properties of the electrodes, sometimes building

new structures on their surfaces [102]. The breakdown has several causes. In 1960s it had been recognized that spot on the anode can be heated up by the bombardment of the electrons. After reaching critical value of the e-beam the anode material evaporates, causing what is known as “anode-initiated” breakdown between electrodes. In the case of cathode spot thermal instability, the breakdown called “cathode initiated” [103]. More recent analysis reveal that in interelectrode gap generate plasma and in analysis should be included effects related to ion bombardment, ion desorption and surface diffusion of contaminants [103].

The major technical challenge is to achieve high emission current density (up to ampere per  $\text{cm}^2$ ) from nanostructures. CNT operating at such a current level are often unstable and may experience a vacuum breakdown, which is often catastrophic and can lead to the malfunction of devices. So far, there is not a clear understanding of the physical mechanism responsible for initiating such a breakdown. Bonard *et al.* [104] attributed the evaporation of a MWNT to a resistive heating at the contact to substrate. The failure occurred at applied fields and currents below 4 V/nm and  $< 10 \mu\text{A}$ . It was found that MWNT are heated up to 2000 K during FE for currents  $2 \mu\text{A}$  [105] and the emitting CNT will involve a self-heating process [106-108]. This may result in subliming and melting of emitting structures and ultimately causes a cathode-initiated vacuum breakdown process. Pressure effects such as bombardment of emitters by ions of gas at high pressures  $\sim 10^{-3}$  mbar can reduce the quality of emitters, thus causing reduction of the emission current. Breakdown can occur at these pressures also by ionization of desorbed atoms from the emitter surface. SWNT ends of nanotubes can be field evaporated in a highly controllable manner during field emission without catastrophic arcing [106]. Experiments have demonstrated a substantial thermal contribution to the field-

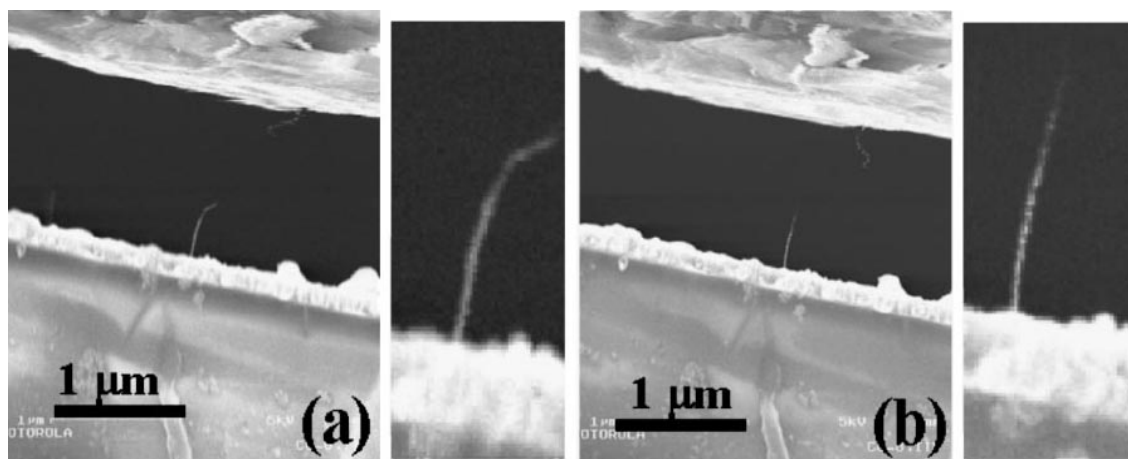


Fig. 1.15. Permanent deformation of the CNT after field emission [56]. The CNT is shown (a) before field emission, (b) after field emission. This SEM image was taken after the electric field was removed. The nanotube stayed in the straight shape. The inset to the right-hand side of each image is an enlarged look at the nanotube.

evaporation process resulting from current-induced heating of the nanotube end. Their tip temperature during field evaporation is approximately 1600 K, resulting in a current limit for an individual SWNT. CNT protruding from a substrate can be flexed, bent, and reoriented by an electric field (Fig. 1.15) [109]. For moderate electric fields, the flexing and re-orienting is reversible, but under high-field conditions sufficient to extract large field emission currents, the nanotube remains irreversibly deformed even after the electric field is removed.

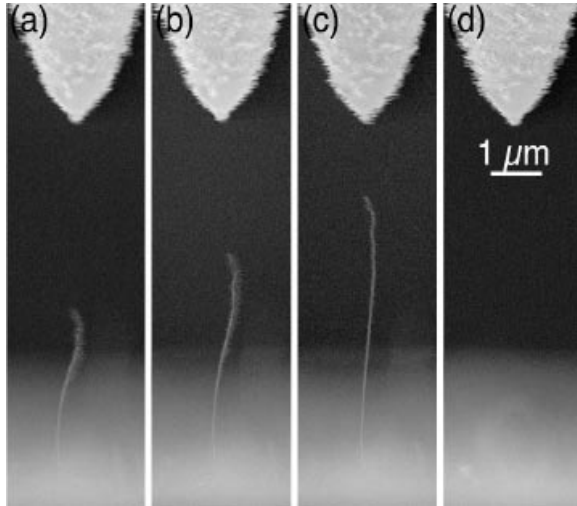


Fig. 1.16. Pull out of the CNT. The SEM micrographs of a CNT at (a) 0-, (b) 2-, (c) 4-V applied voltage before and (d) after destruction of the tube [104].

High electrostatic forces can pull out CNT, if they are not well fixed to the surface (Fig. 1.16) [104]. Nanotubes that field emitted at a high current for long times were shortened (Fig. 1.17(left)), indicating a lifetime-limiting mechanism for vacuum microelectronic devices [109]. Wang *et al.* [110] suggested the instability in emission current can be caused by structural damage during emission (Fig. 1.17(right)).

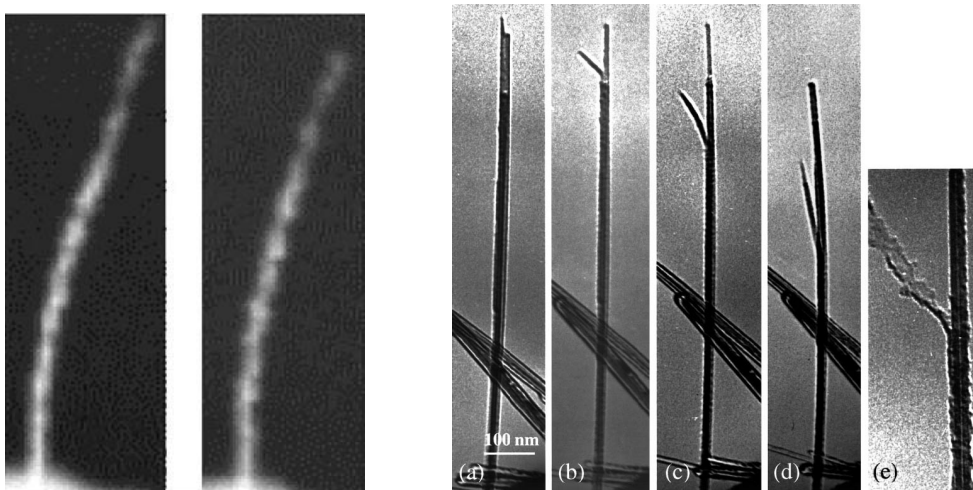


Fig. 1.17. (Left) shortening of the CNT after field emission [56]. The CNT length was decreased by 10% over 30 min. (Right) the “splitting” process in structural damage of CNT. Series of TEM images (a) - (d) show the damage of CNT during FE, (e) CNT which is experiencing a splitting of its outer layers [110].

They observed splitting of the nanotubes segment-by-segment, due to electrostatic forces acting on the tip. The second process in [110] involves the burning of nanotubes layer-by-layer (thus sharpening) due to local temperature created by the emission current.

---

## 2. Fabrication of nanostructures on planar cathodes

The unique field enhancement properties of nanostructures makes them very attractive for cold cathode applications. However, their controlled fabrication requires a clear understanding of growth models. For the mass fabrication of CNT the catalytic chemical vapour deposition (CCVD) process is preferable. Theoretical modelling of CNT formation shows its dependence on the properties of the catalyst precursors and the growth temperature. For applications the simple structuring of wafers is required. This chapter focuses on the metal-organic CVD (MOCVD) method for CNT growth on porous alumina resulting in a MWNT spread over the surface. Additionally, the compact CNT grown with microwave CVD (MWCVD) on Si with preformed catalyst patches were investigated. Since the production of CNT with given dimensions is hard, the polymer etching method for the fabrication of metallic nanowires will be also presented.

### 2.1 Bottom-up growth of CNT

There are two general ways available for the production of nanomaterials. The first way is to start with a bulk material and then break it into smaller pieces using mechanical, chemical or other form of energy (top-down strategy). An opposite approach is to synthesize the material from atomic or molecular species via chemical reactions, allowing for the precursor particles to grow in size (bottom-up strategy). Among various methods of CNT growth, such as arc discharge [111], laser ablation [18] and solar heating [112], the CCVD currently plays the key role [113]. Its main advantage is the reproducibility of grown CNT. Moreover, it allows to effectively produce CNT (especially MWNT) in large scales and with different morphologies [114,115]. CCVD consists in activating a catalysed chemical reaction between the substrate surface and a gaseous precursor, which can be achieved either by heating (Thermal CVD) [25], ionisation (Plasma Enhanced CVD) [26] or irradiation (Microwave CVD) [63]. As a carbon source hydrocarbon gases (methane, propylene etc.) are often used, and as a catalysts, typically, transition-metals (iron, cobalt, nickel, chromium, or alloys). At high temperatures, carbon has finite solubility in these metals, thus resulting in the formation of carbon-metal solutions. Both catalyst and carbon source can be combined in one compound e.g. metallocene precursor for MOCVD [68]. The general CNT growth mechanism can be described by the vapor-liquid-solid model (VLS) [116] and involves the dissociation of hydrocarbon molecules or carbon rich gases catalyzed by the transition metal clusters (typically 1-100 nm in diameter) and dissolution and saturation of carbon atoms in the metal particle (Fig. 2.1). When the metal-carbide clusters are supersaturated in carbon, carbon islands precipitate on the cluster surface and nucleate CNT. Two general nanotube growth



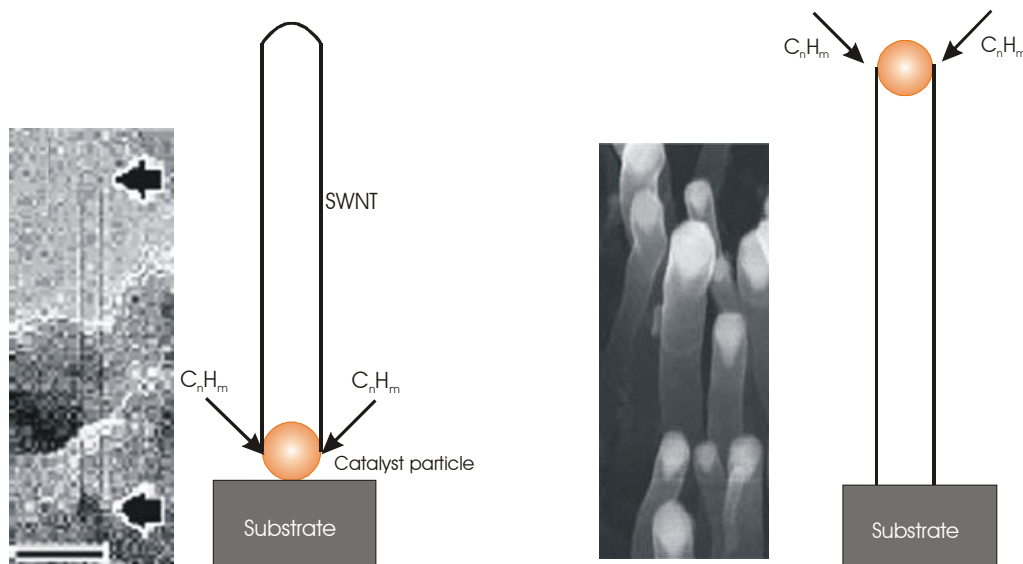


Fig. 2.1 Two general growth modes of nanotubes in CCVD. Left diagram: base growth mode and HRTEM image of the SWNT grown from discrete  $\sim 2$  nm  $\text{Fe}_2\text{O}_3$  nanoparticle (scale bars: 10 nm) [51]. Right diagram: tip growth mode and SEM image of CNT with catalytic (Ni) particles on the tip [117].

modes are presented in Fig. 2.1. With large catalyst particles (or in the absence of any substrate) the CNT generally follows a “tip growth” scheme, i. e. the catalyst will move forward while the rejected carbon form the nanotube behind, whether there is a substrate or not. In this case, chances are high that one end is open [99]. Alternatively, when catalyst particles deposited onto a substrate are small enough (nanoparticles) to be refrained to move by the interaction forces from the substrate, the growth mechanism will follow a “base growth” scheme, i. e. the carbon nanotube grows away from the surface leaving the catalyst nanoparticle attached to the substrate. The precipitation of carbon leads to the formation of the tubular  $sp^2$  structure. Tubule formation is favored over other forms of carbon such as graphitic sheets with open edges. This is due to the fact that a tube contains no dangling bonds and therefore is in a low energy form [118].

### 2.1.1 Growth models

Under vacuum conditions the size of the catalyst clusters and the growth temperature are the parameters which determine the diameter and quality of nanotubes. During the thermal process the metal catalysts form clusters on the surface, providing future seeds for CNT growth. These metal clusters have two main functions in the VLS model. They act as a catalyst to form reactive carbon species from the gas phase and as a solvent for these species [119, 120]. Thus, the partial melting of catalyst nanosize particles is very important for CNT growth. Although the VLS model provides a simple explanation of the essence of the CNT growth, it does not include atomistic details, such as the mechanism of graphitic cap nucleation on the cluster surface, how the open end of the nanotube is maintained during the

growth, how the defects, that may occur in the CNT structure are healed, and what determines the diameter and chirality of the CNT.

Molecular dynamic studies have provided deeper understanding of catalyzed CNT growth. At temperatures significantly below the melting point surface atoms can already move from their lattice positions resulting in cluster asymmetry and surface melting [121]. All developed models for the description of metal nanoparticles predict that their melting point depends inversely on their diameter, thus a linear decrease with  $N^{-1/3}$  [122], where  $N$  is the number of metal atoms in a cluster. This has been validated experimentally [123-125]. The reduction of the melting point of 5 (10) nm clusters is  $\sim 10$  (5) %, as compared to bulk material. Moreover the introduction of carbon into the metal clusters lowers their melting points further by 9 (4) % for the 5 (10) nm clusters [122]. This suggest that up to 1200 K (typical for CCVD) iron-carbide clusters should not be completely molten and CNT growth occurs when the surface layer becomes supersaturated in carbon.

Simulations made by F. Ding et al. [126] by means of the potential energy surface model show that SWNT growth on iron particles originate in several steps (Fig. 2.2):

- Carbon atoms dissolve in the catalyst particle until supersaturation, and then precipitate on the cluster surface. Small carbon strings and polygons nucleate on the particle surface,
- The strings and polygons grow into small carbon islands, typically one of the islands lifts off the surface to form a carbon cap while the other, smaller islands remain on the surface,
- The smaller islands dissolve back into the cluster and the cap increases in the diameter and length to form SWNT.

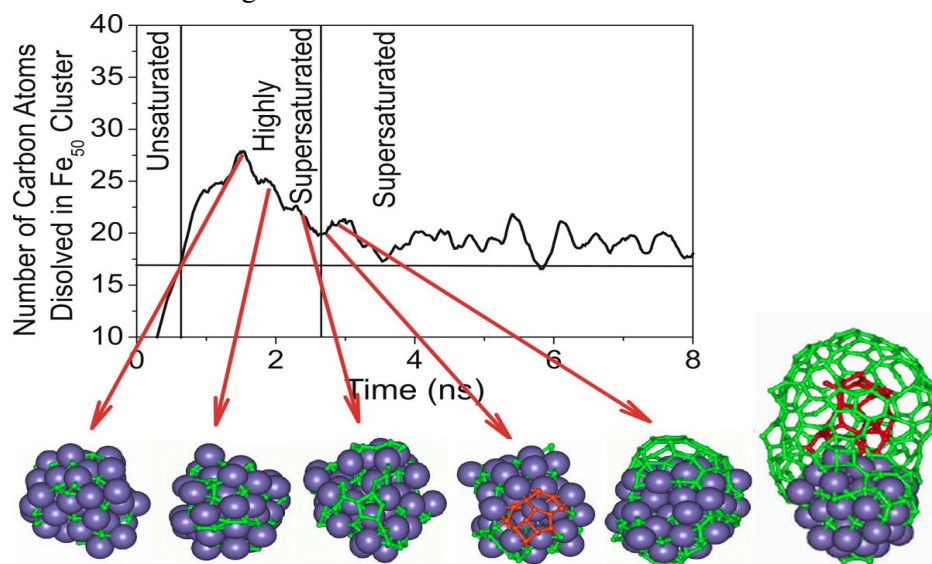


Fig. 2.2. Simulation of the nucleation and growth process of SWNT on the surface of an Fe-C cluster at 1000 K. The Fe atoms are shown as big spheres and carbon atoms as green compound. The red atoms build up a carbon island, grey atoms joined inside the nanotube due to defects. The top graph shows the carbon quantity in the cluster during growth [126].

CNT nucleation sites grow on the surface only when the cluster is supersaturated in carbon (Fig. 2.2). As soon as they are formed, large islands reduce the C concentration. After the formation of the cap the carbon in the cluster remains constant at the saturation level. This means only one SWNT can grow from a cluster, since the formation of new islands is not possible. Moreover no temperature gradient is required for CNT growth. Edges of growing SWNT attract further carbon, which results in the nanotube growth. One should notice that CNT formation and growth is incredibly fast i.e. it can reach a speed of  $11 \mu\text{m/s}$ . The growth mechanism does not depend on the cluster size. The CNT size, on the other hand, does.

Experimental works proves that the diameters of both SWNT and MWNT are equal to the metal cluster sizes. It has been shown that the smallest diameter of catalytically grown SWNT is  $\sim 0.6 \text{ nm}$  [127], which corresponds to a cluster size of  $\sim 20$  atoms. The relationship between the SWNT and cluster diameter is shown in Fig. 2.3 (right). Except for  $\text{Fe}_{10}$  and  $\text{Fe}_{15}$ , the diameters of the cluster and SWNT are similar [126].

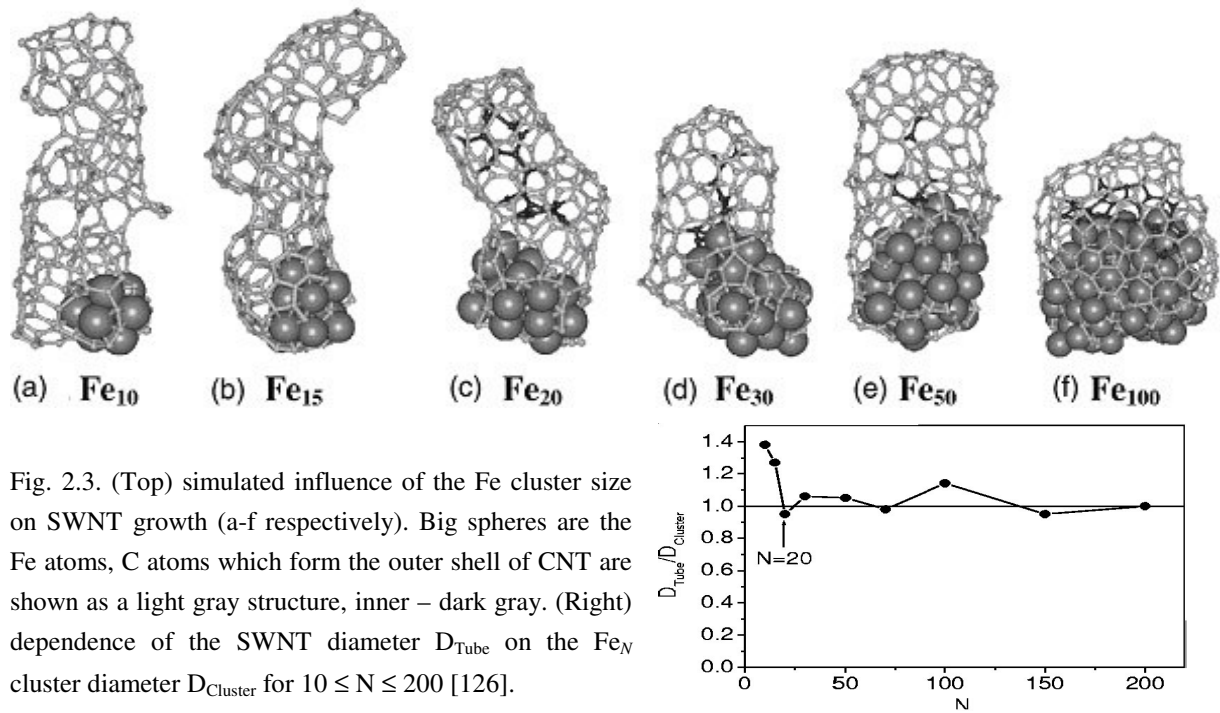


Fig. 2.3. (Top) simulated influence of the Fe cluster size on SWNT growth (a-f respectively). Big spheres are the Fe atoms, C atoms which form the outer shell of CNT are shown as a light gray structure, inner – dark gray. (Right) dependence of the SWNT diameter  $D_{\text{Tube}}$  on the  $\text{Fe}_N$  cluster diameter  $D_{\text{Cluster}}$  for  $10 \leq N \leq 200$  [126].

As shown in Fig. 2.3 (top) the CNT grown from 10 and 15 atom clusters have many defects, while those from clusters larger than 20 atoms, have a tubular structure and few edge bonds. The non-ideal structure of the simulated CNT in comparison to experimental ones can be explained by the following:

- The longer experimental times allow CNT annealing during growth,
- The lower carbon source gas pressure leads to slower C precipitation, thus healing of defects,
- Healing of defects itself was not correctly included to the simulation.

However, this does not affect the growth mechanism and dependence of SWNT structure on the cluster sizes, which are described correctly.

Klinke et al. [128] have developed a thermodynamic model of MWNT growth, which allows one to predict their growth rate on basis of a finite element method. The calculations of the heat distribution and carbon concentration in the catalyst show highly temperature dependent MWNT growth due to an increase of the diffusion coefficient with temperature. The lower limit for the MWNT formation is 500°C, when carbon starts to diffuse into the bulk iron. Well-defined MWNT growth occurred at 500 – 850°C. At higher temperatures carbon atoms adsorb on the CNT walls and reduce or stop the CNT growth rate. Oversupply of carbon or increase of pressure can also stop the process, due to the formation of iron carbide, which has a very low diffusion coefficient. The reduction of pressure or etching in H<sub>2</sub> can extend the CNT growth. The model also reflects the finding, that the growth rate ( $v_{\text{growth}}$ ), diameter ( $d_{\text{CNT}}$ ), density and crystallinity of CNT can be controlled with the growth temperature [129]. According to experimental data the growth time of CNT is  $t_{\text{growth}} \propto l_{\text{CNT}}$  (length) and the  $v_{\text{growth}} \propto 1/d_{\text{CNT}}$ , which can be adjusted for larger  $d_{\text{CNT}}$  by a higher temperature (Fig. 2.4) [128].

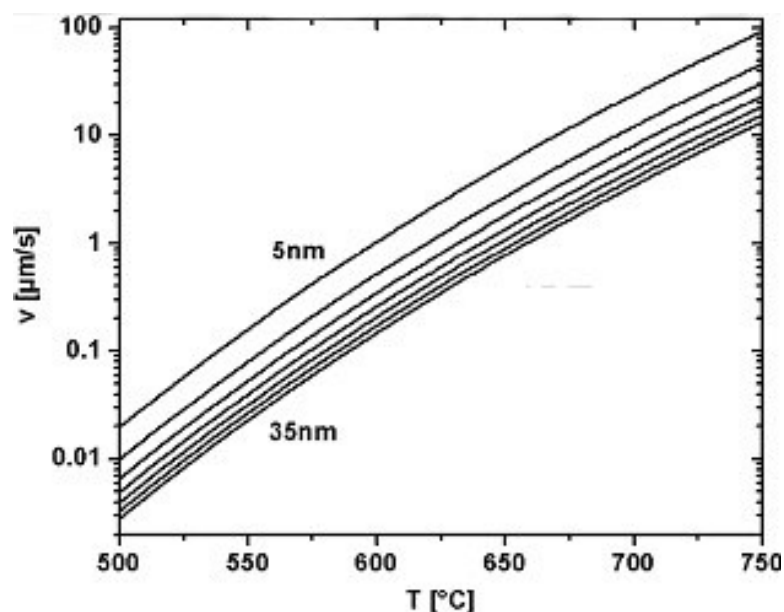


Fig. 2.4. Calculated growth rate as a function of deposition temperature (500-700°C) and nanotube diameter (5-35 in 5 nm increments) [128].

### 2.1.2 Random CNT on porous alumina by MOCVD

Among the various methods of CNT growth MOCVD deserves the most attention. Its main advantages are simplicity and low expense. In this work, robust MWNT emitters for devices have been directly grown on porous alumina by one-step catalytic CVD from metallocene precursors, which results in well-anchored CNT randomly distributed over the sample surface [68]. The samples were obtained from the group of Prof. Dr. J.-J. Schneider at the Technical University of Darmstadt. The three zone CVD furnace in the MOCVD reactor for the CNT growth with gas supplies is illustrated in Fig. 2.5, and is described in the thesis work of Dr. J. Engstler [68].

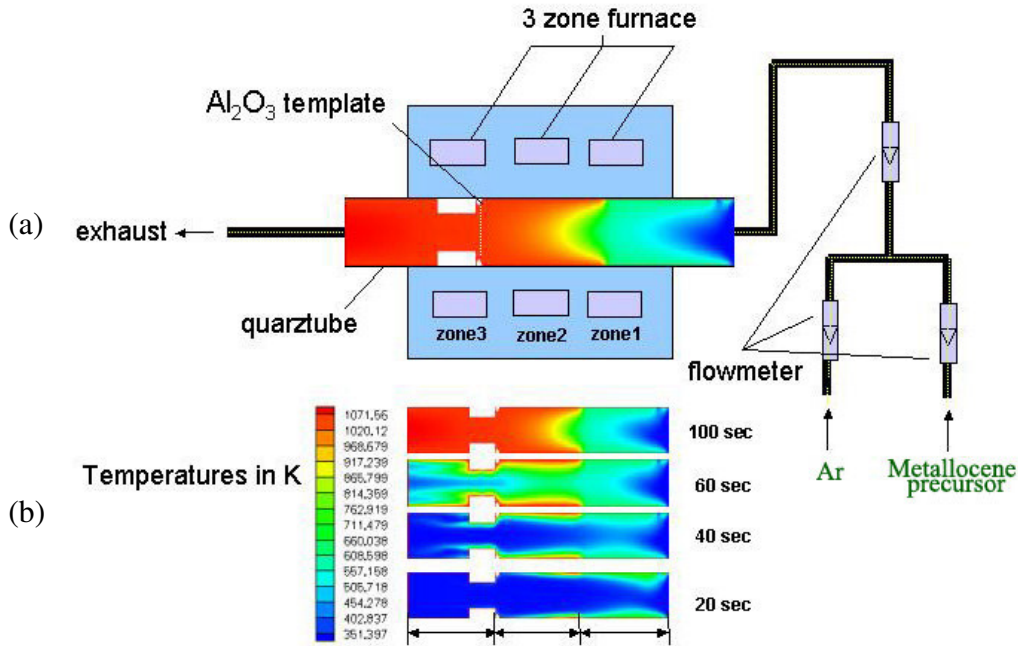


Fig. 2.5. Schematic illustration of the (a) CVD-furnace used for the synthesis of CNT on alumina membranes and (b) simulation of the temperature profile within the reaction tube during CNT synthesis.

Mesoporous Al<sub>2</sub>O<sub>3</sub> (alumina) was used as a template for CNT growth. Its porous structure increases the mechanical stability of the nanotubes by fixing them on the pore walls. The templates for the present work were obtained from Whatman (Anodisc® 25) [130] or made by anodic oxidation of aluminum at constant voltage [68], resulting in electrochemically etched porous alumina membranes (EPAM). They consist of hexagonal cells with the cylindrical pore in the center, normal to the template surface. The pore diameter and thickness of the membrane was constant for commercial Anodisc® membranes (200 nm diameter and 60 μm thickness). For the self-developed EPAM process these parameters varied in the range of 16 - 200 nm (pore diameter), 60 - 200 μm (thickness). The main disadvantage of these material is its brittleness. At the slightest mechanical stress the membranes easily broke into several pieces, which made it impossible to cut the samples with specified configurations.

In order to achieve sparse CNT growth with less screening effect the membrane surface was partially closed with additional Al<sub>2</sub>O<sub>3</sub> as suggested by results of B. Günther [38] (Fig. 2.6(middle)). In this way prepared membranes were introduced into the CVD reactor where the final CNT growth occurred (Fig. 2.6(bottom)). The one step process of CNT growth requires a special precursor which contains both catalyst and carbon source. As precursors metallocenes (ferrocene, nickelocene, cobaltocene, chromocene and Fe-Co-S complex) were used, which combine the above mentioned advantage. In the first zone

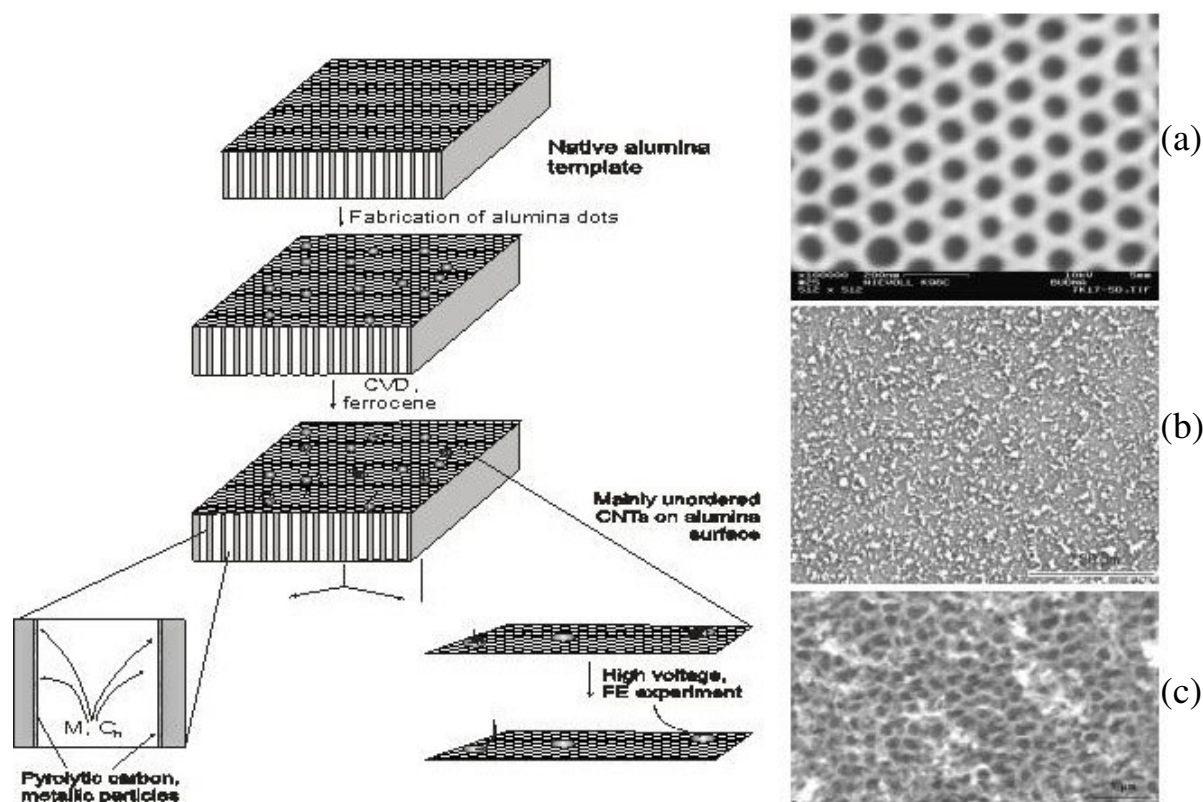


Fig. 2.6. Schematic model of the CNT growth and SEM images of the porous alumina which corresponds to each step of CNT growth. On the stage (a) the native membrane is shown, (b) represents the membrane surface covered with alumina particles, (c) shows the membrane after the MOCVD process with grown nanotube layer.

of the CVD furnace the metalorganic precursor sublimates at about 300 – 350°C and in flow of the inert gas (Ar) transferred to the template in zone 3. There the growth of CNT occurred at about 750 – 850°C. The mass flow conditions of precursor and carrier gases and the temperature distributions in geometrically varied CVD reactors were systematically simulated by the commercial CFD code FLUENT, solving the transport equations with temperature dependent transport coefficients from Prof. Dr. O. Deutschmann at the University of Karlsruhe. Uniform temperature distributions were established at the substrates, but stagnation flow was not achievable. Moreover, asymmetric flow was obtained in the case of the usual gas outlets which was confirmed by the CNT distribution found on samples (Fig. 2.5). One should note, that the porous alumina shrink due to heating in the CVD reactor, thus the substrates were always non-flat. In general they have a wavy surface with up to a few mm height difference, which in combination with extreme brittleness creates difficulties for their investigation.

The resulting membranes were visually black after the CVD process. Investigation of the samples show that the surface is covered with a layer of MWNT and alumina particles. The SEM images of the Anodisc® (Fig. 2.7 (left)) reveal, that CNT originate from the pores and have a visual length of much less than  $\mu\text{m}$ . Probably some of them grow perpendicular to the membrane and have a greater length. However, no such long nanotubes were found in the

layer. The CNT grown on the EPAM have up to some  $\mu\text{m}$  length and grow apart the surface often fixed to the alumina clusters (Fig. 2.7 (right)).

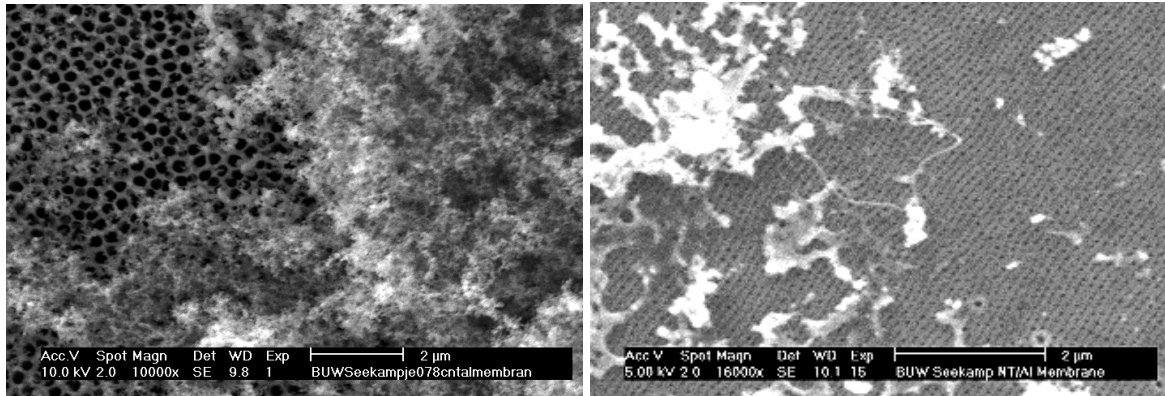


Fig. 2.7. SEM images of the porous alumina surface after the MOCVD process with the equal resolution. Left image shows the Anodisc® surface (pore diameter 200 nm), carbon nanotubes are about 100 nm long. In the right image EPAM surface is presented (pore diameter  $\sim 55$  nm) with  $\sim 2$   $\mu\text{m}$  long CNT growing on the surface.

Energy dispersive x-ray spectroscopy (EDX), with iron as the scanned element, was made for ferrocene grown nanotube samples. For both Anodisc® and EPAM no correlation between the catalyst and grown nanotubes, in both fast and slow scans, was observed (Fig. 2.8). However, obviously iron forms the ring structures of  $\sim 200$  nm size on the Anodisc® surface which represents the catalyst particles in the pore walls (Fig. 2.8 (left)).

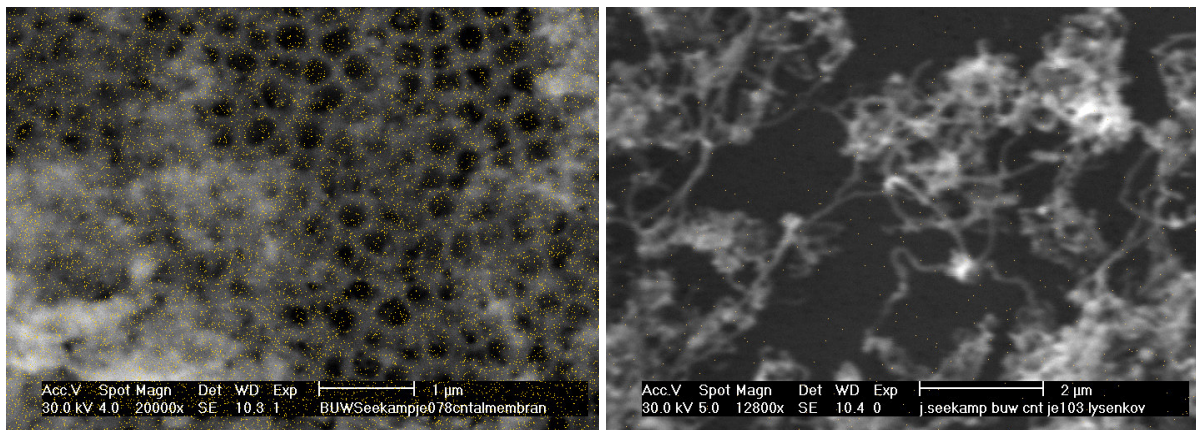


Fig. 2.8. SEM images of Anodisc® (left) and EPAM (right) surface with imposed corresponding EDX maps. White points mark the Fe particles.

### 2.1.3 CNT patches on Si by MWCVD

Another approach of cold cathode manufacturing is the selective growth of CNT by means of lithographic patterning of catalyst on substrates. For this purpose, especially for the growth of aligned CNT, a modification of the method of gas-phase deposition of carbon films—activation by a pulsed microwave discharge (MWCVD) has been developed [131,

132]. In the regime of pulsed plasma excitation, during the time intervals between the pulses, the radicals and ions recombine with a characteristic time on the order of a few milliseconds. The difference between the recombination rates for different plasma components responsible for the growth or etching of different carbon phases allows one to shift the deposition process toward the production of films with the desired characteristics.

The CNT samples for the FE measurements were obtained from the group of Dr. N. V. Suetin at Moscow State University (Russia). The Si (100) substrates were covered first with a 100 nm Ti barrier diffusion layer by means of magnetron sputtering and then with 10 nm thick Ni catalyst patches 3.3  $\mu\text{m}$  in diameter. They form squares with the dimensions of 500 x 500  $\mu\text{m}^2$ . A 6-kW microwave power, generated at a frequency of 2.45 GHz, was supplied through matching elements and a waveguide to the CVD reactor. The discharge was ignited in the center of the vacuum chamber in the antinode of the microwave electric field. The chamber design ensured that the microwave energy was focused in the region above the substrate holder so that the discharge plasma was in the immediate vicinity of the substrate [133].

As result the surface with the catalyst was covered with a some  $\mu\text{m}$  thick nanotube layer (Fig. 2.9). Non-aligned CNT of a few  $\mu\text{m}$  length and less than 100 nm in diameter could be identified on the surface.

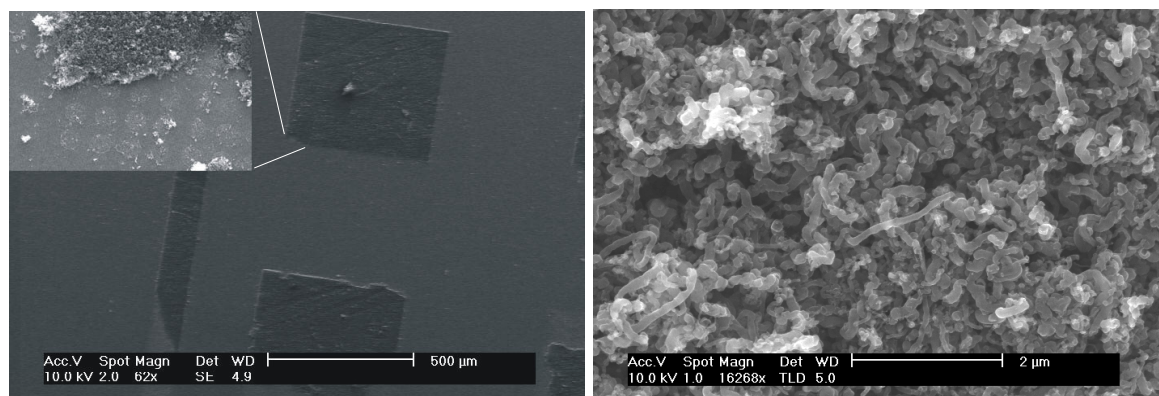


Fig. 2.9. SEM images of the 500 x 500  $\mu\text{m}^2$  squares covered with the CNT layer (left). The scratched area shows the form of the Ni patches (top left). The resulting CNT on the sample surface can be seen in the enlarged SEM image (right).

## 2.2 Metallic nanowires in polymer ion-track templates

For the fabrication of metallic nanowires various methods have been developed: CVD, physical vapour deposition (PVD), direct heating and electrochemical deposition [71,73,134,135]. In this work polymeric ion track membranes were used for nanowire fabrication with diameters between 30 - 500 nm and aspect ratios of up to 500 [73]. Copper was chosen as a material for deposition due to well-known properties and high conductivity [136]. The formation of Cu nanowires was made in the group of Dr. H. Fueß at the Technical University of Darmstadt. The full procedure consists of several steps (Fig. 2.10) [137].



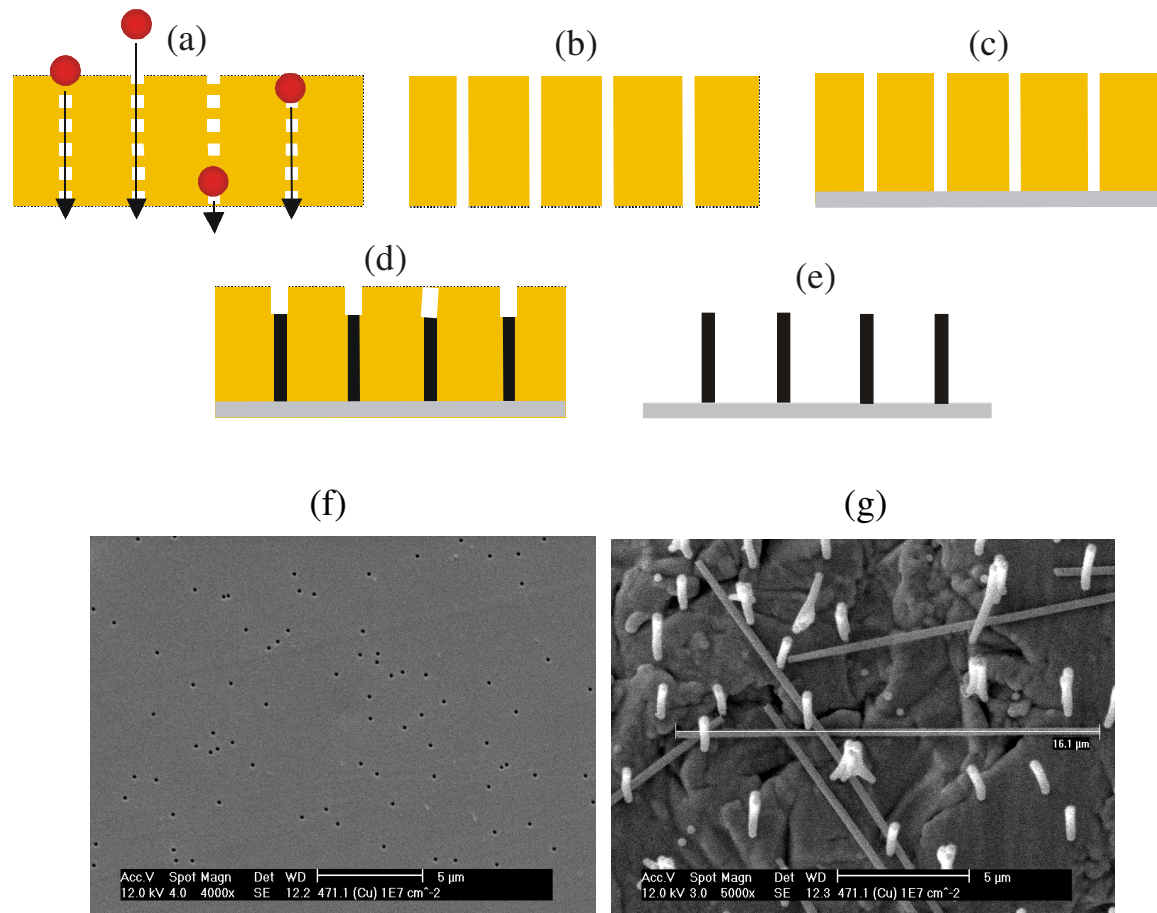


Fig. 2.10. Scheme of the Cu nanowires cathode fabrication: (a) irradiation of the polymer foil by swift heavy ions, (b) chemical etching of ion tracks, (c) deposition of the metallic layer, (d) filling of the pores with Cu, (e) dissolution of the membrane and SEM images of (f) the irradiated foil and (g) resulting nanowires.

Polycarbonate foils (MAKROFOL, Bayer Leverkusen; thickness: 30  $\mu\text{m}$ ) were irradiated at the UNILAC facility of the “Gesellschaft für Schwerionenforschung” with highly charged ions ( $^{238}\text{U}$ ) with energies of some tens MeV/nucleon (Fig. 2.10(a, f)) with fluences  $10^6 - 10^9$  ions/ $\text{cm}^2$  resulting in randomly distributed ion tracks of some nm in diameter over the membrane. The by ions damaged material was removed by the chemical etching (Fig. 2.10(b)). To enhance etching along the irradiation tracks instead of an undesired etching of the bulk material each side of the foils was exposed to UV light prior etching. Preferred etching along the irradiation tracks results in cylindrical-shaped pores which depends linearly on the etching time. Electrochemical deposition was accomplished in a two-compartment cell, in which each side of the template could be etched and deposited without removing the foil. After that a thin Au film was sputtered to one side of the template to provide an electric conductive cathode layer and establish mechanical stabilisation (Fig. 2.10(c)). The electrolyte was filled into the compartment two to three hours before deposition and held at 50°C, thus diffusing into the pores and reaching an energetic equilibrium. The further filling of produced pores were performed at 50°C. The height of the grown wires (Fig. 2.10(d)) can also be determined by Faraday’s law

$$h = \frac{4M}{Fz\rho\pi} \frac{q}{d^2 A_{\text{eff}} f}. \quad (2.1)$$

$A_{\text{eff}}$  is the effective area of deposition ( $A_{\text{eff}} = 0.5 \text{ cm}^2$ ) and  $f$  is the fluence of the irradiation,  $d$  is the diameter of the nanowires,  $M$  is the molar mass of the deposited element ( $M_{\text{Cu}} = 63.55 \text{ g}\cdot\text{mol}^{-1}$ ),  $F$  is the Faraday constant ( $F = 96485 \text{ C/mol}$ ),  $z$  is the valence of the deposited element ( $z_{\text{Cu}} = 2$ ),  $\rho$  is the density of the deposited element ( $\rho_{\text{Cu}} = 8.92 \text{ g/cm}^3$ ),  $q$  the transferred charge and  $d$  the diameter of the deposition area ( $d = 0.8 \text{ cm}$ ). Internal control of the height of the grown wires stops the deposition, when a certain predetermined height

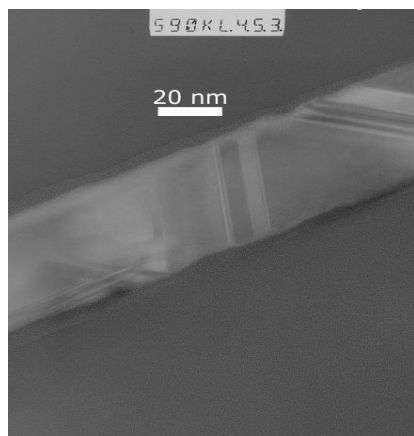


Fig. 2.11. TEM image of the single crystal Cu nanowire with a thickness of ~ 40 nm.

reached. The last step (Fig. 2.10(e)) is the releasing of the grown nanowires to a self-standing vertically aligned array. The polycarbonate template was dissolved in polar organic solvents, resulting in free standing Cu nanowires on the mechanically stable cathode layer (Fig. 2.10(g)) with aspect height determined by formula (2.1). Thus,  $d$  and  $f$  have to be determined prior to the deposition. Both single and poly crystalline properties were observed for the resulting nanowires, depending on their size. For the thinnest 30 nm x-ray diffraction (XRD) measurements shows that most of the observed structures were single crystals (Fig. 2.11).

One of the advantages of nanowires over CNT is that they may be grown into different morphological structures, which can be useful for low-field emission. This may be seen in Fig. 2.12, where Cu nanowires of different shape are shown. In particular, the tower shaped Cu nanowires and bundles can be favourable for FE current carrying capability and stability.

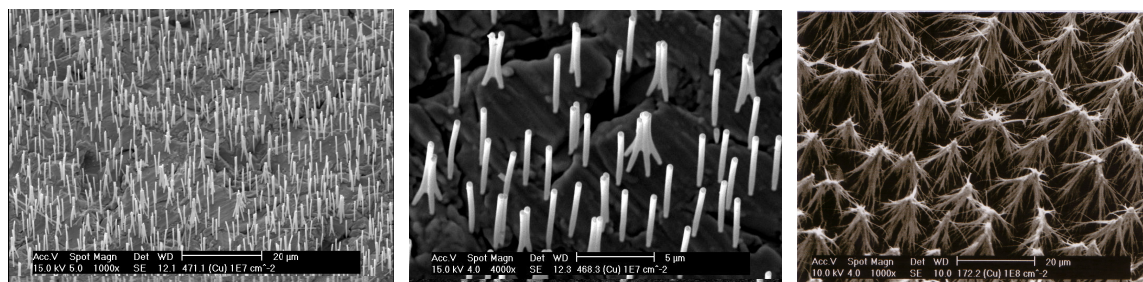


Fig. 2.12. SEM images of the aligned (left), bundles (center) and tower like conglomerates (right) of Cu nanowires.

### 3. Experimental techniques for field emission and surface analysis

The integral measurement system with luminescent screen (IMLS) was built at the University of Wuppertal for the investigation of FE parameters of centimeter scale cold cathodes [38]. For an improvement of the emission current stability and an increase of the current carrying capability, which are required for optimization of these cathodes, the IMLS was extended with a power supply with proportional-integral-derivative (PID) regulation and pulsed operation modus. The uniformity of the emitter distribution was obtained and investigated with the software package AnalySIS®, which facilitates online data acquisition and processing. On the basis of the IMLS images, an algorithm for their conversion into current maps was developed. In order to pursue spatially resolved FE measurements, a field emission scanning microscope (FESM) was used, which had been constructed and extended in the context of several thesis works [7, 8, 85]. In the present work it was mainly used for local investigations of the emitter stability. The correlation between FE results and surface morphology was made by means of SEM and profilometer investigations.

#### 3.1 Integral measurement system with luminescent screen (IMLS)

##### 3.1.1 Layout of the system

The IMLS (Fig. 3.1) provides the integral current/voltage curves of cold FE cathodes, as well as information about the number density, uniformity and stability of the emitters up to high field levels [10]. By means of a fore- and turbomolecular pump (Hastings PM043), a base pressure of about  $10^{-7}$  mbar is usually reached in the 15 cm diameter chamber after some hours. The IMLS avoids a central spacer, allowing an in-situ variation of the electrode spacing, and provides best pressure control at the sample, thus reducing the discharge problem, which is caused by gas desorption. The whole assembly allows for direct access and sample installation into the chamber. Ten isolated electrodes inside the chamber serve for the connection of additional extraction electrodes and/or a heating station with built-in temperature sensors. The stepper motor (Newport UI31PP) is mounted on a rotatable feedthrough and enables a controlled in-situ variation of the electrode spacing of up to 25 mm. It allows the movement of the sample holder in steps of 0.1  $\mu\text{m}$ . The minimum distance is given either by the unflatness of the sample or by the parallax error, which can be reduced during the assembly to about 10  $\mu\text{m}$  over the maximum cathode size of 30 mm square by means of a tilting system. The luminescent screen [139], which consists of a glass plate with a special phosphor (doped ZnS) layer, can be removed for the electrode parallelism control. For the usual electrode spacing of between 100 and 400  $\mu\text{m}$  and high voltages of up to 5 kV, electric fields up to 50 V/ $\mu\text{m}$  can be obtained with a maximum error of  $\pm 10\%$ . Images of the emitter distribution are made through the window and a lens, required for the compensation of the small focusing distance, by means of a coupled-charge device (CCD) camera, resulting in

a maximum lateral resolution of 20  $\mu\text{m}$ . A needle valve allows to vary the vacuum pressure and gas species. For the fast pressure decrease after the long-time opening of the chamber the heating wires and the thermoregulation system (Horst GmbH) is installed, which allows to heat up the chamber up to about 100 $^{\circ}\text{C}$  (limited by the rubber seals).

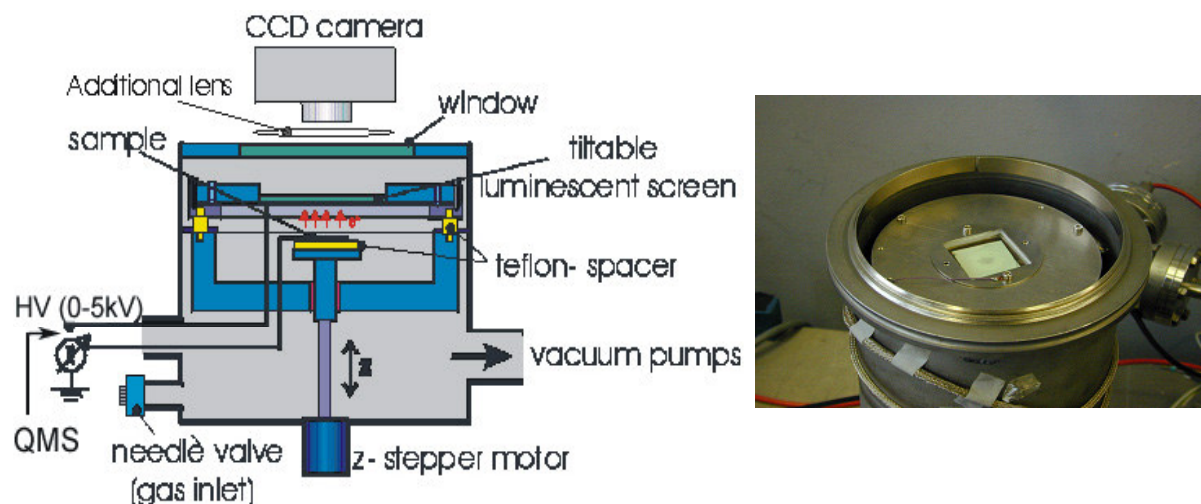


Fig. 3.1. Schematic of the integral measurement system with luminescent screen (IMLS) and a the top view into the vacuum chamber of the IMLS, showing the luminescent screen.

Electronically the IMLS is a diode configuration where positive voltage is usually applied to the luminescent screen and the emission current is measured between the sample holder and ground potential (Fig. 3.2). The reversed implementation of the negative voltage to the sample and measurement of the current of different polarity between the luminescent screen and ground is also possible.

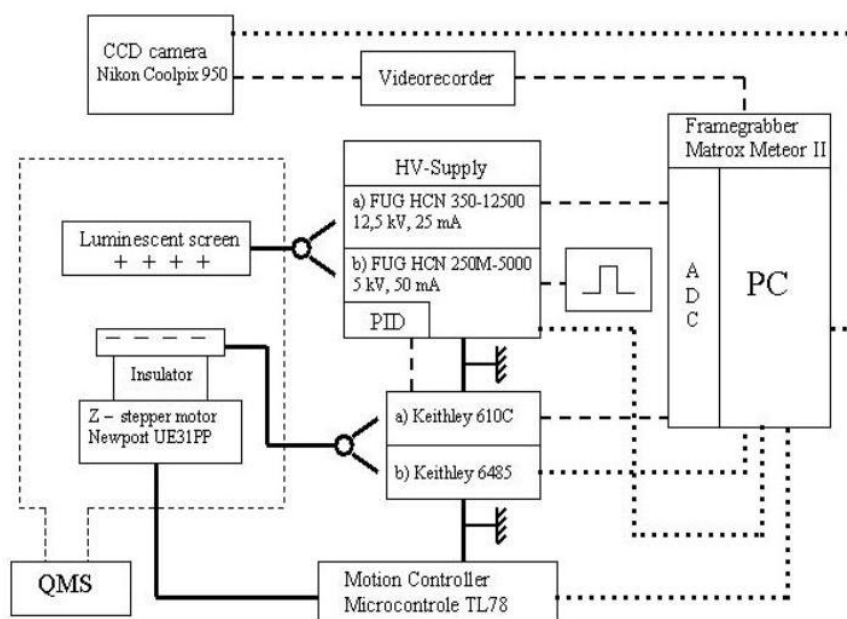


Fig. 3.2. Block diagram of the electric circuits of the IMLS with supply connections (full), analog (dashed) and digital control lines (dotted).

Two power supplies can be chosen: a) a manually or analog controlled source for up to 12.5 kV and 25 mA dc output, or b), a remote controlled source for up to 5 kV and 50 mA, which have positive dc or pulsed output with 2 ms full height rise time and can be triggered by a pulse generator or through a digital IEEE – 488 (GPIB) interface. The current is measured a) either by a solid-state electrometer (Keithley 610C) which provides pA/mA resolution within s/ms, or b) a Keithley 6485E for up to a rate of 1 kHz. The distance between the electrodes can be adjusted with 0.1  $\mu\text{m}$  precision by the stepper motor and the motion controller (Microcontrol TL78), which is also digitally addressable. The emitter distribution, as imaged by the cathodoluminescent screen and CCD camera (Nikon Coolpix 950) can be either taken as single shot with high resolution (1600 x 1200 pixel), or online observed and recorded by a videorecorder and framegrabber (Matrox meteor II) with medium resolution (768 x 576 pixel composite video). Real-time data processing and saving with a frequency of 10 Hz is possible by means of the AnalySIS<sup>®</sup> software package. All signals are displayed as real-time curves (e.g.  $I(t)$ ,  $I(U)$  etc.) on a PC and stored for further data analysis either through an analog-to-digital converter (ADC) for the Keithley 610C, or through GPIB for the Keithley 6485/E. A quadrupole mass spectrometer (QMG 112) serves for additional control of luminescent layer evaporation with a sensitivity limit of  $5 \times 10^{-11}$  mbar (e.g. for S and C).

### 3.1.2 Processing of samples and electrode spacing calibration

The IMLS is very attractive for the initial conditioning of  $\text{cm}^2$  size samples. The processing at constant voltage (Fig. 3.3 (left)) usually results in the decrease of the emission current. However, sometimes a self-activation of the emission current was observed during conditioning, due to onset of the emitters (see Chapter 4), which often resulted in discharge problems. Therefore the power supply (FUG HCN 250M-5000) with positive output of 5 kV, 50 mA was installed into the system, enabling voltage PID regulation by the emission current as measured with the solid-state electrometers Keithley 610C or Keithley 6485 [5].

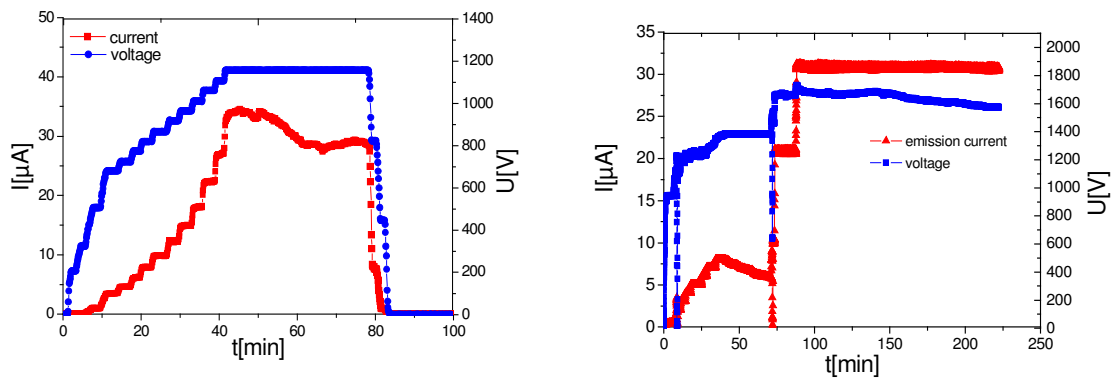


Fig. 3.3.  $U(t)$  and  $I(t)$  processing curves of a CNT sample for the non- (left) and PID regulated (right) current.

Comparison of the potentiometer set point to the analog Keithley output results in a regulation of the output voltage towards constant current with ms response time. The initial dc processing of the cathodes at constant PID regulated currents (Fig. 3.3 (right)) increases the homogeneity of the emission and activates the emitters more safely than in non-regulated mode. Through the destruction/degradation of the strongest emitters, the total emitter number density is usually increased at slightly higher field levels.

The typical nonplanarity of the samples (see Chapter 2) hinders a precise definition of the electrode spacing during the installation phase. By means of  $U(z)$  plots (at PID regulated current) the effective distance between electrodes for both concave and convex curved substrates can be calibrated with maximal error of  $10\ \mu\text{m}$  (Fig. 3.4), resulting in a determination of the average electric field typically within  $\pm 5\%$ .

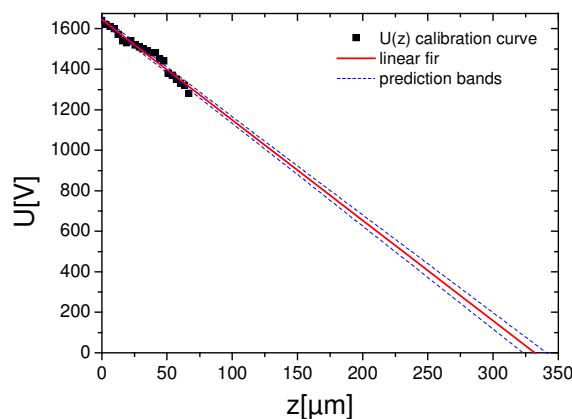


Fig. 3.4. Field calibration by means of  $U(z)$  plot at constant current of  $1\ \mu\text{A}$ , resulting in  $E = 5\text{V}/\mu\text{m}$  (slope) and electrode spacing  $330\ \mu\text{m}$  (X-axis crossing).

### 3.1.3 Pulsed operation

DC operation of carbon nanotubes at high voltages, however, has often shown discharges especially in the event of strong current switches (see Chapter 4). In order to reduce current fluctuations and prevent discharges, an externally controllable power supply (FUG HCN 250M-5000) (Fig. 3.2) was used. One of the main parameters in pulsed operation is the duty cycle, which is equal to the ratio of pulse length ( $T_{pulse}$ ) to pulse period ( $T_{period}$ ) (sometimes written in percents) and increases the peak emission current

$$I_{peak} = \frac{T_{period}}{T_{pulse}} \bar{I}, \quad (3.1)$$

where  $\bar{I}$  is the average emission current. The power load on the luminescent screen is reduced in pulsed regime accordingly

$$\bar{P} = \bar{I}U \quad (3.2)$$

thus making it possible to achieve higher fields and current densities.

The pulse parameters are controlled by an external signal generator (HP 8013A) and enable the increase of the output voltage from 0 to 5 kV within 2 ms (Fig. 3.5), which is limited by the delay of the emission current with respect to pulse generator signal. Therefore,

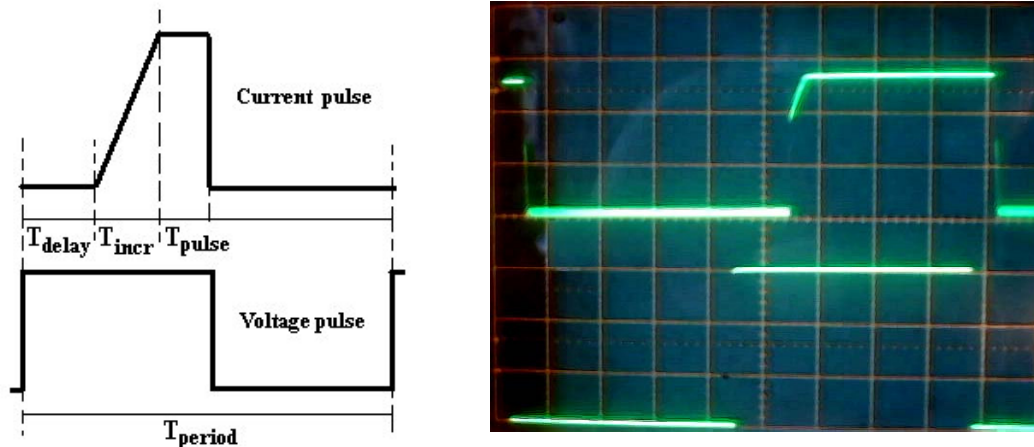


Fig. 3.5. Scheme of the current with respect to the generator pulse and the oscilloscope image of the emission current (upper curve  $1\mu\text{A}/\text{div.}$ ) for square input voltage pulses ( $2\text{V}/\text{div.}$ ) at  $1\text{ms}/\text{div}$  time scale.

the resulting minimum pulse length is about  $500\ \mu\text{s}$ . The power supply can also be triggered through the IEEE-488 interface. The average emission current in pulsed operation is measured with a solid-state electrometer Keithley 610C, which provides s/ms resolution in the pA/mA range. The actual current can be measured with a Keithley 6485/E at rates of up to 1000 Hz in the mA range. Alternatively, pulsed output voltage and emission current can be estimated by the oscilloscope.

### 3.1.4 Imaging of the emitter distribution and software analysis

Every emitter creates on the luminescent screen a light spot, which is bigger than the emitters itself due to divergence of the electron beam and the spreading of light in the phosphor layer. The light spots are imaged by the CCD camera and then recorded by the videorecorder. Its output produce the composite video signal (0.5 megapixel), which can be processed by the framegrabber of the PC. High resolution 2 megapixel (24 bit, RGB) images (Fig. 3.6) can be transferred to the computer from the camera; however, can not be processed online. Data acquisition and processing have been performed by the AnalySIS® [141] software. This package provides the automatic image acquisition, measurements and saving as well as online analysis and data reduction for applications in microscopy. The main advantages of the program are:

- simultaneous presentation of multiple images, including live image,
- video option (10 Hz),
- large number of measurement functions for the multiphase analysis and intensity, measurements, as well as 3D-presentation with image scaling,

- artifact-free particle detection/analysis/classification,
- fully automatic measurements and analysis incl. data reduction for chain-measurements,
- automatic data archiving and documentation.

These options are used in the IMLS for:

- Automatic size calibration and processing of the images,
- Emitter classification and fast calculation/analysis for a large series of images,
- Fluctuation analysis and long-term stability investigations,
- Long-term online cathode functionality control.



Fig. 3.6. Example of the IMLS luminescent screen image (left) (horizontal size 5 mm) and example of the image analysis with identification of emitters with size above 20 pixels, resulting in 16 clusters and their classification by area.

Measurement of the I-V curves reveal information about the average current fluctuations. There are two main effects seen in the IMLS images: repeated switching of light spots in a second range and a permanent activation/deactivation of emitters. Fluctuations can be processed by means of the comparison of the several images taken with short  $\sim 0.1$  s time interval. For the long-term stability, the scheme of the analysis is shown in (Fig. 3.7(left)):

- obtain the image series over a defined period of time,
- average of the image series with intensity scaling,
- compare of two or more averaged images to distinguish the stable, activated, and deactivated emitters in the resulting image (Fig. 3.7(right)).

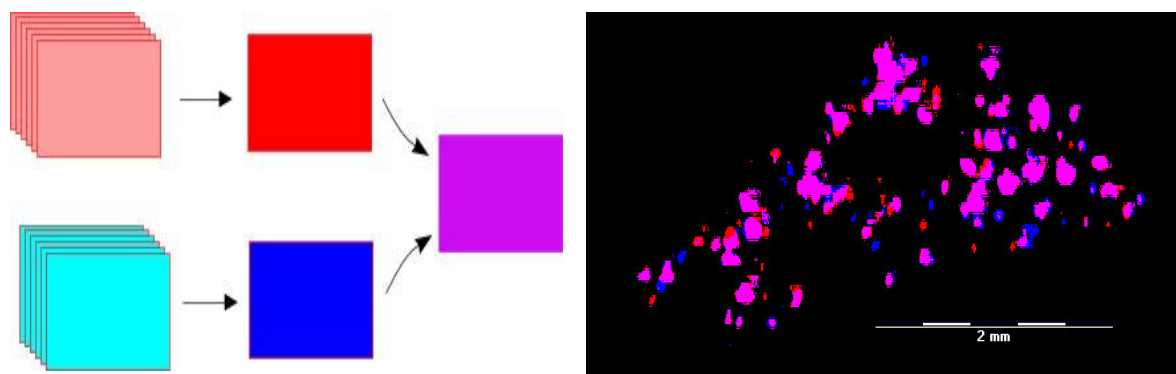


Fig. 3.7. Scheme (left) and an example (right) of the image analysis of the CNT sample resulting in 71% stable (violet), 14% activated (red), and 15% deactivated emitters (blue).



### 3.1.5 Conversion of the IMLS images into current maps

The IMLS images provide qualitative information about the number and distribution of emitters. The current distribution over the sample surface is usually measured in scanning probe configurations [52,78], which requires, however, a lot of time. Therefore, a method of conversion of the IMLS images to current maps was developed, which expands the possibilities of the integral system for fast investigation of current distributions over the emitting surface. Moreover, it gives additional opportunities for emitter counting and classification.

Each emitter creates a light cluster on the luminescent screen, which is recorded by the CCD camera as accumulation of illuminated pixels. The IMLS image consist of black background and light clusters, containing some bright pixels in their centers, which corresponds either to central areas directly hit by the electrons and some halo around, i.e. additional pixels due to spreading of light in the luminescent screen. In such a way the number of pixels in  $m$ -ths cluster is

$$n^m = n_{Cij}^m + n_{Hij}^m, \quad i = 1 \dots \Delta x_m, \quad j = 1 \dots \Delta y_m, \quad m = 1 \dots K \quad (3.3)$$

where  $n_{Cij}$  is the number of central pixels ( $C_{ij}$ ),  $n_{Hij}$  the number of pixels in the related halo ( $H_{ij}$ ),  $K$  is the number of clusters,  $i$  and  $j$  are the coordinates of the pixels belonging the cluster with dimensions  $\Delta x_m$ ,  $\Delta y_m$ . There are 3 possibilities for  $n_{Cij}$  positioning with respect to the CCD matrix (Fig. 3.8).

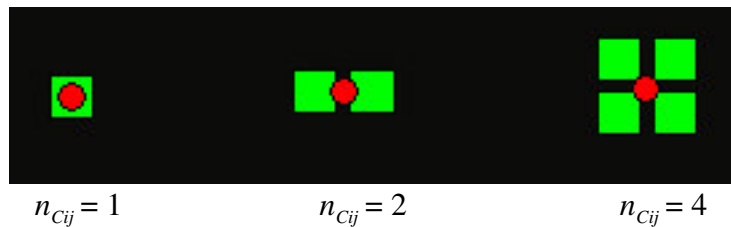


Fig. 3.8. Three possibilities for positioning of the brightest pixels  $n_{Cij}$  (green) with respect to one emitter below the luminescent screen (red).

In contrast,  $n_{Hij}$  might vary strongly as a function of the emitter strength and becomes difficult to be defined in case of high emitter densities. The total number of the illuminated pixels of the screen is

$$N = \sum_{m=1}^K n^m, \quad (3.4)$$

In the stored IMLS images (24-bit, RGB) each spot has 3 independent brightnesses, which corresponds to red, green, and blue color components. For an extraction of the brightness from the RGB-image, it should be converted by means of the YUV model, which defines a color space in terms of one Y - luminance (the brightness), and two U,V - chrominance (color) components. The weighted values of R, G, and B are added together to produce a single Y signal, representing the overall light intensity in that pixel

$$Y = 0.299R + 0.587G + 0.114B. \quad (3.5)$$

In the Y-image each pixel has the intensity  $0$  (black)  $\leq Y_{ij} \leq 255$  (white). The resulting brightness of individual  $m$ -th cluster is

$$B^m = \sum_{i,j=1}^{A,B} Y_{ij}^m, \quad (3.6)$$

where  $Y_{ij}^m$  - reflects the intensity of the pixel with coordinates  $i, j$  as a part of the  $m$ -th cluster representing the emitter. The sum of brightnesses of all clusters yields the total brightness of the whole image

$$B = \sum_{m=1}^K B^m, \quad (3.7)$$

is equal to a sum of all pixel intensities

$$B = \sum_{i,j=1}^{a,b} Y_{ij} \quad (3.8)$$

and can be used for calculation of the total brightness without cluster identification, e.g. for image calibration by means of AnalySIS®, where  $a$  and  $b$  are given by the sample dimensions. The light from the luminescent screen is registered by all pixels of the CCD matrix, having  $Y_{ij} > 0$ . The black color, which we see on the IMLS images contains pixels with  $Y_{ij}$  between 0 and 20. They were truncated as background noise and not used in the calculations.

For cluster identification and further brightness calculation an algorithm was developed. For each pixel  $(i,j)$  of the image with intensity  $Y_{ij}$  above 20 it searches in the nearest neighborhood (8 spots) pixels with intensity higher than the previous one, until the maximum of the intensity will be found, which define the cluster center  $n_{Cij}$ . All pixels  $B_{ij}$ , which define the  $n_{Cij}$  or in the other words comes by means of the algorithm to the same  $C_{ij}$ , are marked as belonging to one cluster with the central pixel  $C_{ij}$ . The sum of their  $Y_{ij}$  is the cluster brightness (formula (3.6)).

In most cases, however, cluster centers consist of a number of points  $n_{Cij} > 1$ . All neighbor  $n_{Cij}$  ( $i, j = \pm 1$ ) with equal intensities are fused together with corresponding  $B_{ij}$  in one resulting cluster. The geometrical center of all fused  $C_{ij}$  gives the new center of the cluster. The brightness of each cluster and the total brightness of the image are calculated with formula (3.6) and (3.7), respectively. For the correct algorithm calculation in rare cases of  $C_{ij}$  with equal intensities, separated with odd number of pixels splitting operation is foreseen. In this case the  $Y_{ij}$  of the middle pixel, which has the minimum in that region, can be correctly divided between neighbor clusters.

To correlate the cluster brightness information with the emitter current, the voltage and the power dependence of the luminescent screen image was calibrated. Each IMLS image was converted with the YUV-model. The brightness of the images was calculated by means of AnalySIS® software (see 3.1.4) and formula (3.8). The cathodoluminescence is an optical and electrical phenomenon whereby a beam of electrons is generated by an electron gun (e.g.

cathode ray tube) and then impacts on a luminescent material such as a phosphor, causing the material to emit visible light. Cathodoluminescence occurs because the impingement of a high energy electron beam onto a semiconductor will result in the promotion of electrons from the valence into the conduction band, leaving behind a hole. When an electron and a hole recombine, it is possible for a photon to be emitted. The energy (color) of the photon, and the probability that a photon and not a phonon will be emitted, depends on the material, its purity, and its defect state.

Screens that were used for the measurements have different threshold levels of luminescence (Fig. 3.9 (a, b)); therefore, they were calibrated separately. This calibration procedure is demonstrated for a sensitive screen in the Fig. 3.9(b), where the electrons should be accelerated with at least 0.3 kV to produce light. The observed dependence of  $B$  on the voltage  $U$  show the coincidence of the curves at the same field levels (Fig. 3.9(b)), thus show the current dominance. Moreover, in Fig. 3.9(c)  $B \propto f(E^2)$  and reveals a threshold of the luminescence at  $E \sim 1.1 \text{ V}/\mu\text{m}$ .

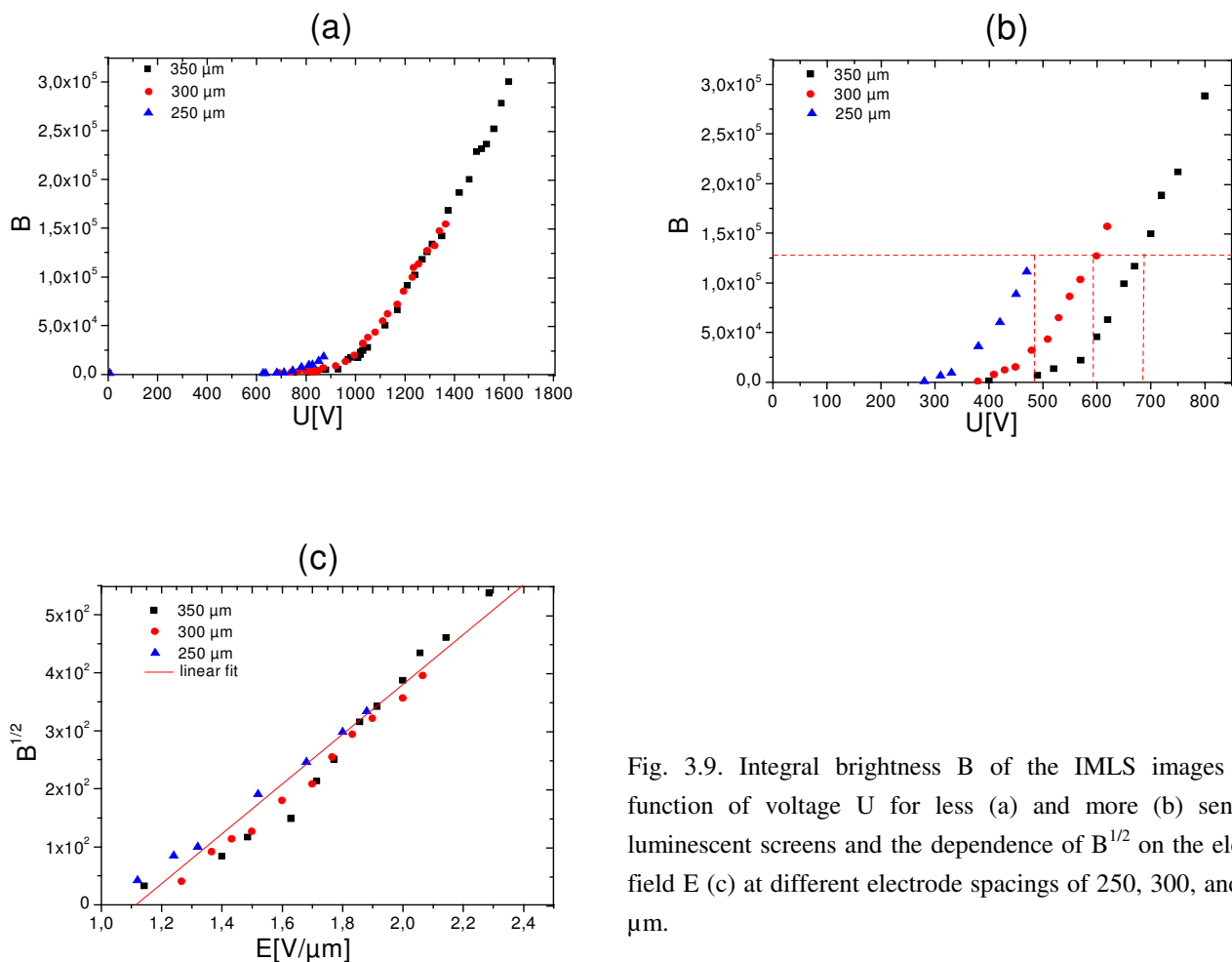


Fig. 3.9. Integral brightness  $B$  of the IMLS images as a function of voltage  $U$  for less (a) and more (b) sensitive luminescent screens and the dependence of  $B^{1/2}$  on the electric field  $E$  (c) at different electrode spacings of 250, 300, and 350  $\mu\text{m}$ .

The  $B(I)$  curve (Fig. 3.10(a)) shows saturation at  $B > 10^5$  as seen by the occurrence of pixels with a brightness of 255. Pixels which are directly hit by electrons could not exceed this brightness limitations even at high currents therefore the energy deposited in that spot

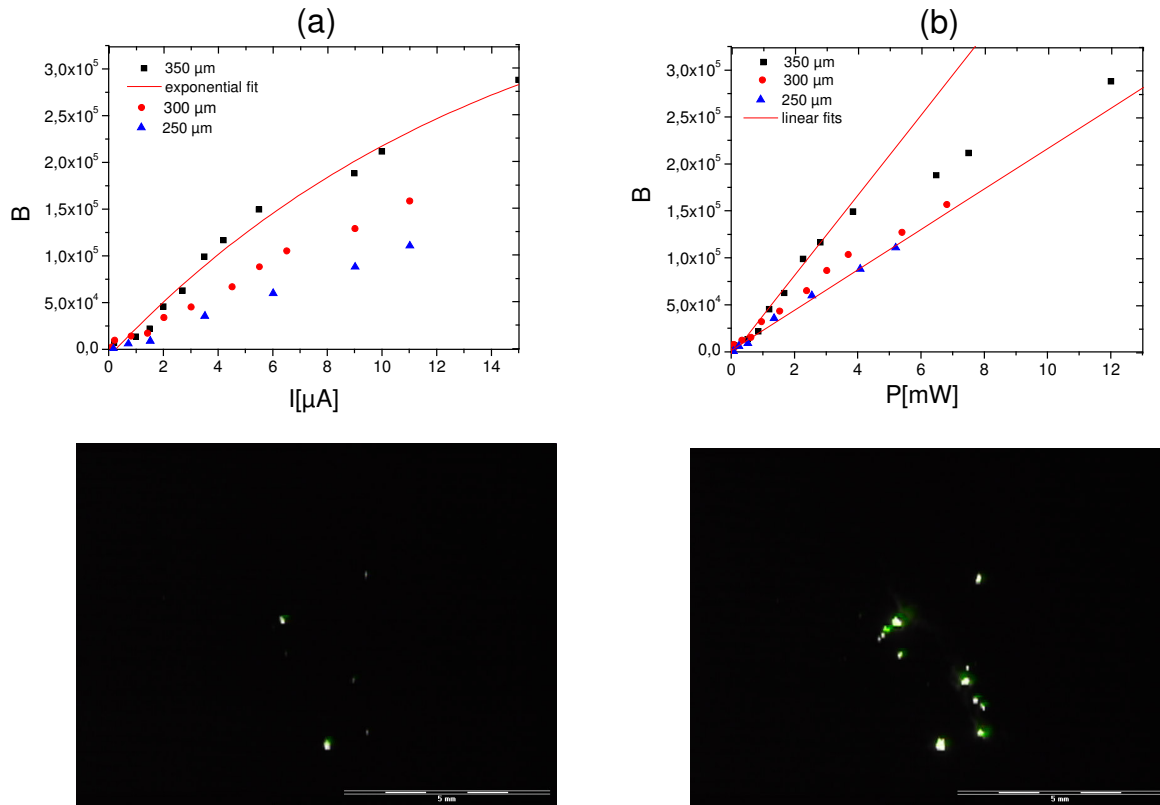


Fig. 3.10. Integral brightness  $B$  of the IMLS images as a function of the emission current  $I$  (a) and power  $P$  (b) at different electrode spacings ( $250$ ,  $300$  and  $350 \mu\text{m}$ ) in dc mode. Corresponding IMLS images (resolution  $768 \times 576$  pixel) were taken at  $U = 600 \text{ V}$ ,  $I = 2 \mu\text{A}$  (bottom left) and  $U = 800 \text{ V}$ ,  $I = 15 \mu\text{A}$  (bottom right). The resulting number of emitters are  $6$  and  $13$ , respectively.

converted into light with decreased effectiveness. One can also notice that the brightness below  $10^5$  (Fig. 3.10(b)) is nearly a straight line and can be described by a linear function, which is also valid for the current. The exemplary difference of brightness and number of emitters between the images at taken at different voltages and currents is shown in Fig. 3.10 (bottom).

Calibration of brightness in pulsed operation was made in the same voltage interval as in dc operation for pulse length  $T_{\text{pulse}} = 0.5 \text{ ms}$  and duty cycle  $1:12$  (Fig. 3.11). It reveals nearly the same dependencies for the voltage and electric field. However, brightness in pulsed operation was two times less than in dc mode under the same conditions.

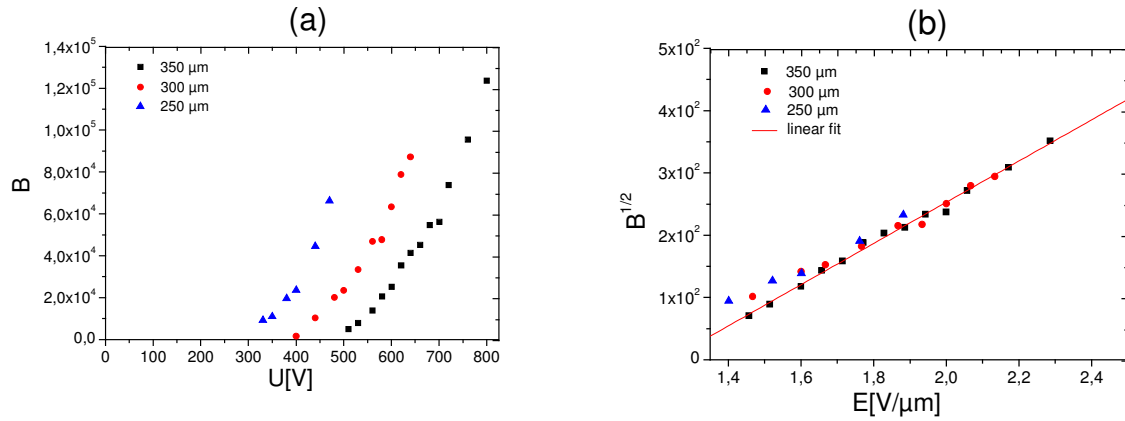


Fig. 3.11. Integral brightness  $B$  of the IMLS image as a function of voltage  $U$ (a) and dependence of  $B^{1/2}$  on  $E$  in pulsed mode for  $T_{\text{pulse}} = 0.5$  ms and duty cycle 1:12 (b) at different electrode spacings of 250, 300 and 350  $\mu\text{m}$ .

On the other hand, no saturation occurred in pulsed operation up to a peak current  $I_{\text{peak}} = 30 \mu\text{A}$  (Fig. 3.12(a)), and the power up to 1.5 mW (Fig. 3.12(b)), which was calculated in this case as in formula (3.2). This means the pulsed operation increase the non-saturated interval of brightness by a factor of 4 (duty cycle 1:12), which allows to use linear functions in current and power calculations. Moreover, this afterglow effect is well known for the luminescent layers and favors the operation of CNT based light sources in pulsed mode.

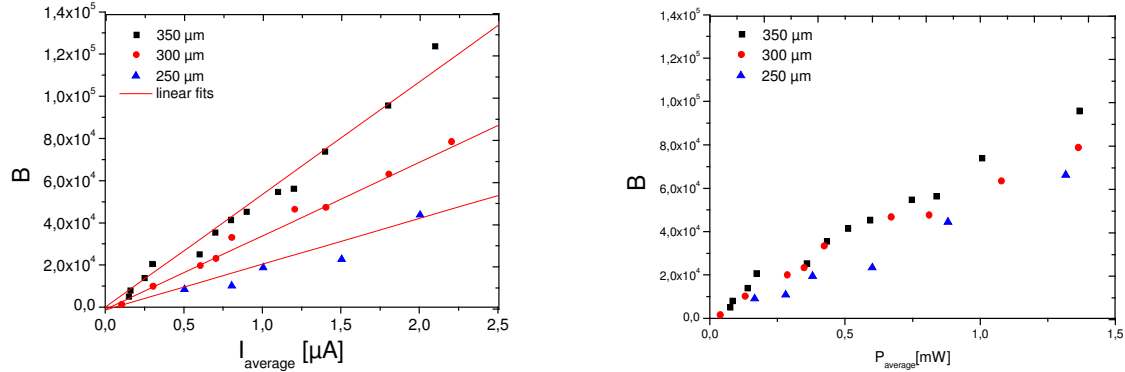


Fig. 3.12. Integral brightness  $B$  of the IMLS image as a function of  $I_{\text{average}}$ (a) and  $P_{\text{average}}$ (b) at different electrode spacings.

The  $B(z)$  dependence is hyperbola like and can be described by a function of  $B \propto f(1/z)$  (Fig. 3.13) both in dc and pulsed modes. The brightness increases fast with the electrode spacing reduction. The brightness of the image reduced in pulse mode in comparison to dc by factor 1.5 for 3.3 ms and by 2.7 for 1.2 ms pulses. Pulse length variation (Fig. 3.14) at constant pulse period corresponds to duty cycle change from 1:12 to dc and reveal the saturation limit for the

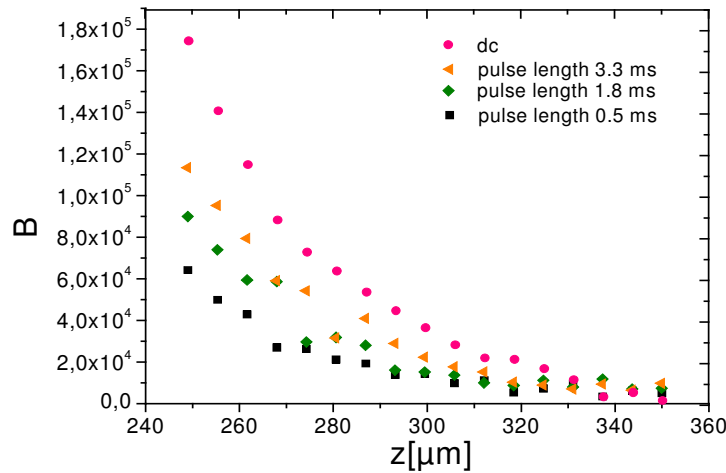


Fig. 3.13. Integral brightness  $B$  of the IMLS image as a function of electrode spacing in dc and in pulsed mode for different  $T_{\text{pulse}}$  at a constant pulse period of 6 ms and constant voltage  $U = 570$  V.

voltage of 800 V for  $T_{\text{pulse}} \sim 1.5$  ms at constant pulse period of 6 ms and electrode spacing of 350  $\mu\text{m}$ . The slight saturation occurred above  $B \sim 10^5$  also by 690 V. In the lower region the dependence is nearly linear.

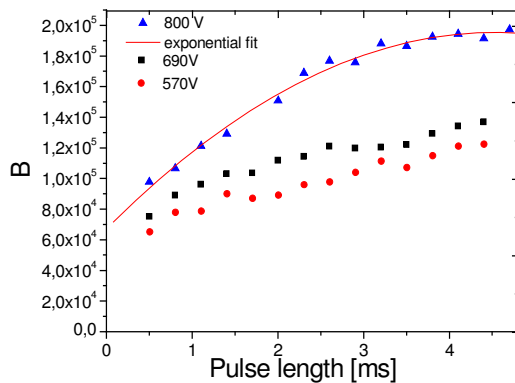


Fig. 3.14. Integral brightness  $B$  of the IMLS image as a function of  $T_{\text{pulse}}$  at different voltages at constant  $z = 350$   $\mu\text{m}$  and pulse period of 6 ms.

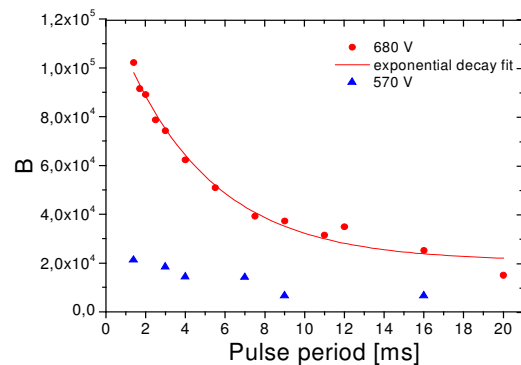


Fig. 3.15. Integral brightness  $B$  of the IMLS image as a function of pulse period at different voltages at constant  $\Delta z = 300$   $\mu\text{m}$  and  $T_{\text{pulse}} = 0.5$  ms.

At the constant voltage and  $T_{\text{pulse}}$  the brightness decreases with an increase of pulse period (Fig. 3.15). An exponential fit shows that the brightness of the screen decreased by a factor of 4 from dc to pulses with 1:40 duty cycle for  $U = 680$  V, due to a reduction of power. Since we can register continuous stream of images even for pulse periods up to 20 ms, phosphorescence seems to play a specific role in afterglow processes.

The program code for the conversion of the images was written using Visual C++ 6.0 and Microsoft Foundation Classes [142].

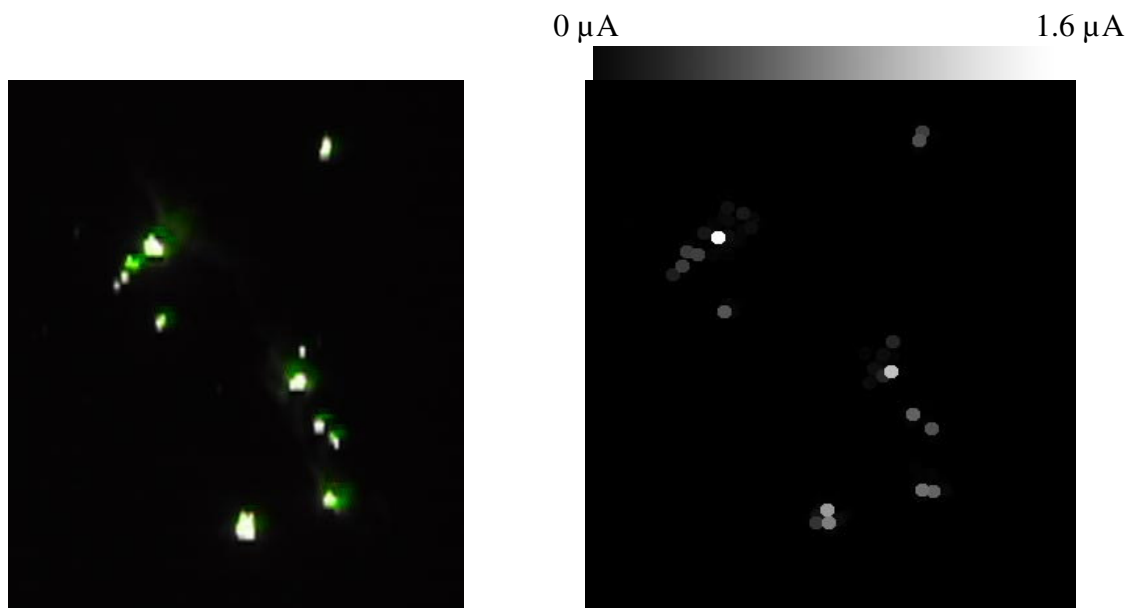


Fig. 3.16. Conversion of the IMLS image in Fig. 3.10 (left) into a current map (right). Number of emitters on the IMLS image is 26. Number of identified clusters 22. The total current is 15  $\mu\text{A}$ .

A manual calculation of emitters in the same IMLS image as in Fig. 3.10 (cut to resolution 253 x 295 pixel) (Fig. 3.16(left)) reveals 26 light spots. The corresponding I-map (Fig. 3.16(right)) reveals 22 clusters with currents from 1.6  $\mu\text{A}$  to 0.1  $\mu\text{A}$ . Strong halos limit the precision of cluster identification. For this purpose the manual operation of the fusion of clusters in program is foreseen.

In conclusion, this method can be used for counting and classification of emitters, and calculation of current distribution. In dc mode (saturated brightness) non-linear dependencies provide the precise brightness calculation. In pulse mode, on the other hand, simpler linear functions of brightness can be used. The presented method was applied for the IMLS images both in dc and pulsed modes (see Chapter 4) for the investigations of current distribution over the surface and calculation of the maximum achievable current densities from investigated CNT samples.

### 3.2. Field emission scanning microscope (FESM)

The FESM is an advanced microscope for the localization of field emitters on flat cathodes of up to 30  $\text{mm}^2$  by zooming FE scans down to nanoscale resolution and measuring the FE properties of single emitters (Fig. 4). It is located in the focus of an UHV surface analysis system (ESCALAB) with a base pressure of  $10^{-10}$  mbar. In-situ SEM and AES [7,8,85] can be used to identify the emitters with about 1  $\mu\text{m}$  resolution which is limited by the finite electron gun distance of about 3 cm. Moreover the ion gun permits in-situ processing of emitters [85]. The samples are installed via a linear transport system into the xyz-scanning stage of the FESM or a rotatable holder for up to seven reserve samples through

a preparation chamber with a base pressure of  $10^{-7}$  mbar, which contains a resistive heating stage up to  $1200^{\circ}\text{C}$  (Kammrath&Weiss). By means of a separate turbomolecular pump and two gate valves, the preparation chamber also serves as a load lock with about 1 hour cycling time for sample exchange. The whole system is isolated against vibrations and ground motion.

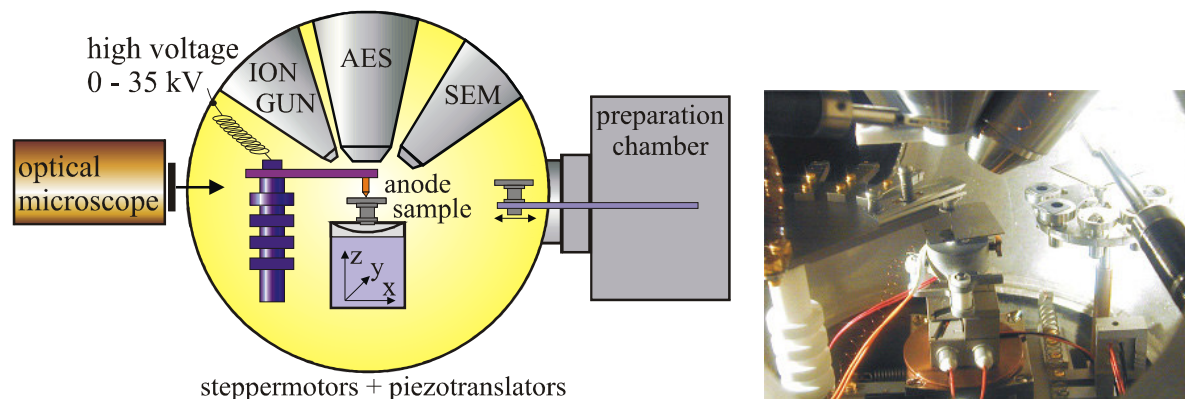


Fig. 3.17. Schematic of the field emission scanning microscope (FESM) (left) and a view into the UHV analysis chamber of the FESM (right). The sample (center) is assembled in the focus of the SEM, AES, and ion gun (top) on the 3D piezo translator which can be tilted on sliding XYZ stages (bottom). High voltage is supplied to selectable needle anodes (left), one of which can be exchanged by the manipulator (right).

In order to change the resolution of the FE scans and local measurements, up to eight anodes can be chosen which are fixed on the rotatable anode holder (Fig. 3.17 (right)). The anodes are self-made from tungsten wires either conical with  $50\text{-}1000\ \mu\text{m}$  diameter or needle-like with  $50\ \text{nm}\text{-}50\ \mu\text{m}$  tip diameter. Since the finest anodes are occasionally destroyed (e.g. by discharges) a special tip holder has been constructed which can be exchanged, as with samples. The sample under investigation is fixed by a screw into the xyz-stage which consists of a piezotranslator block and sliding tables inside UHV. The spacing between the anode and the sample can be monitored with  $\mu\text{m}$  precision by means of a long distance optical microscope (Questar) with CCD camera and the SEM. Special care is required to guarantee a constant distance between anode and scanned area. For this purpose a tilting system has been integrated within the xyz-stage which enables a tilt accuracy of  $\pm 1\ \mu\text{m}$  over  $1\ \text{cm}^2$  and is thus sufficient even for piezo scans. Nevertheless electric field homogeneity remains difficult to achieve especially in the case of rough or curved surfaces.

Calculations with MAFIA show that by the plane tip electrode configurations the electric field should be modified with correction factor  $\alpha$ , resulting decreased electric field  $E = U/\alpha d$ . The correction factor depends on the electrode spacing and the anode tip radius [85]. The real electric field can be decreased by up to factor 4 and will be taken into account for all presented results.

The electronic scheme of the FESM is shown in Fig. 3.18. Positive voltages of up to 35 kV can be applied to the insulated anode holder, and the emission current is measured



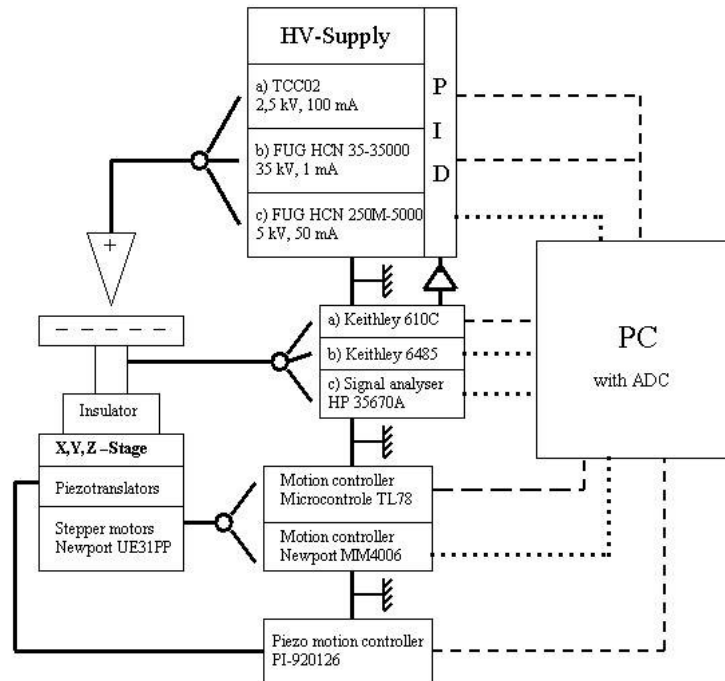


Fig. 3.18. Block diagram of the electric circuits of the FESM with supply connections (full), analog (dashed) and digital control lines (dotted). Please note the analog PID loop for fast voltage regulation.

between the cathode and ground potential. Three power supplies can be chosen: a) a dc 2.5 kV source for currents of up to 10 mA, b) a dc 35 kV source for currents of up to 1 mA, and c) the remote controlled dc or pulsed source which provides up to 5 kV and 50 mA mentioned already for the IMLS. The current can be measured with a) the same electrometer as for the IMLS in case of dc operation, or b) with a Keithley 6485/E up to a rate of 1 kHz, or c) with a signal analyser (HP 35670A) for transient effects and noise investigations. The maximum bandwidth is limited by the capacitance of the FESM which is mainly given by the length of the coaxial cable to about kHz, so current slopes faster than a ms cannot be detected correctly. This delay also contributes to the maximum speed of the direct voltage regulation loop which is driven by the analog Keithley output and the integrated PID regulators of the power supplies. Depending on the voltage level and PID settings, most emitters can be protected from destruction by high currents as long as the scanning speed is not too high.

The range and resolution of the xyz-stage depends on the choice of stepper motors (full range, step width 63.5 nm) or piezotranslators (40  $\mu\text{m}$ , 40 nm/V) and the stability of the motion controllers. By means of a personal computer with a 12 bit four channel ADC, the FESM can be operated in three scanning modes. Voltage scans  $U(x,y)$  are preferred for non-destructive initial testing of samples. For a given maximum voltage and electrode distance the location and strength of emitters are detected by the voltage drop which results from the PID regulation loop which is used to keep a chosen onset current (e.g. 1 nA). Current scans  $I(x,y)$  for a constant voltage and given electrode distance provide maps comparable to IMLS images but are more dangerous with respect to microdischarges if the current limit is set above a  $\mu\text{A}$ . Most sophisticated are relative distance scans  $\Delta z(x,y)$ , where the z-piezo is regulated to keep

the emission current constant for a given voltage [8]. Obviously such scans require very smooth surfaces with a roughness less than 10% of the average electrode distance. Keeping a minimum distance of 500 nm because of safety reasons and using the finest needles of 40 nm diameter an ultimate scanning resolution of 100 nm was achieved. This would allow to easily detect  $10^8$  emitters/cm<sup>2</sup>, a density which would be sufficient for most cold cathode applications.

### 3.3 Surface analysis

#### a) SEM

The in-situ SEM of the FESM is mainly used for the control of the installation, tilting and roughness of the surface and for large ( $> 1 \mu\text{m}$ ) particle identification. For nanoscale resolution of emitters, however, the external measurements are required. Most of such measurements were made by means of the HRSEM Philips XL-30 with W cathode [143]. The acceleration voltage of the electron beam of 0.2 kV – 30 kV and a 1 - 2 nm beam diameter results in  $\sim 1$  nm resolution. This microscope is additionally equipped with the EDX system for the determination the energy spectrum of x-ray radiation for  $Z \geq 11$  with lateral resolution of  $\leq 10$  nm. The BSE (back scattered electrons) detector visualizes material contrasts while using the different densities of the elements, and presents corresponding intensity levels in the images. A pre-characterization of some samples direct after the MOCVD process was made at the University of Darmstadt also with the same modified HRSEM Philips XL-30 FEG.

#### b) Profilometer

A MicroProf® profilometer (Fig. 3.19) from FRT GmbH [144] serves for the measurement of the sample curvatures, which greatly influences the FE. Using the CHR 150 optical sensor, the sample is illuminated by a focused white light. Internal, passive optics, using chromatic aberration splits the white light into different colors (corresponding to different wavelengths). A miniaturized spectrometer detects the color of the light reflected by the sample and determines the position of the focus point, and by means of an internal calibration table, the vertical position measured on the sample surface. The profilometer provides a resolution in the z direction of 3 nm, and in the lateral direction of  $\sim 2 \mu\text{m}$ . The maximum range of the measurements in z direction is  $\sim 300 \mu\text{m}$ . The tests are fast due to lack of movement in z direction, and non-destructive. It is also equipped with thin film sensor and an atomic-force microscope (AFM), which were not employed in this work.



Fig. 3.19. Profilometer with 2 optical sensors and AFM. The granite plate provides stability for the investigations at the nm scale.

## 4. Results of field emission from nanostructures

The following chapter is dedicated to the investigation and optimization of the FE properties of nanostructures. The comparative tests of CNT on Si and porous alumina reveal the difference in the properties of compact and distributed emitters, thus the influence of the shielding effect. The influence of the precursor type, amount and membrane morphology on the FE will be shown by the SEM and IMLS images. The corresponding FE measurements are focusing on emitter number density, stability and homogeneity towards high current densities. The local FESM studies of CNT on Anodisc® reveal the onset and operation fields, field enhancement and current limits of single emitters. For CNT on EPAM, as a major result of this work, it was found that the current densities are strongly influenced by the pore diameter. The current fluctuations of single emitters and stability of CNT cathodes has been improved by means of current conditioning, measured as a function of pressure and visualised by AnalySIS® software. The maximum current densities were achieved in pulsed operation of the IMLS. First results on novel copper nanowires will be given, too. Finally, the status of FE from the tested nanostructure cathodes will be compared to other published results.

### 4.1 CNT on Si

In order to investigate the influence of the densely packed emitters to the FE the CNT sample on Si was fabricated by means of MWCVD as described in the Chapter 2.1.3. The SEM images in Fig. 4.1 show that the CNT build a compact layer on the substrate surface with diameters of 20 - 75 nm and lengths up to 5  $\mu\text{m}$  (as seen at the edges). The longest CNT have diameters of about 50 - 75 nm. Such a structure is common for CNT growth by MWCVD, where the thickest CNT are the longest [78]. Both opened and closed nanotubes were observed on the surface. Thus, the resulting field enhancement factors  $\beta$  of single emitters should be widely spread. Following the conducting cylinder model considering that opened CNT have about factor 1.5 higher  $\beta$  values than closed, the maximum field enhancement values up to about 300 should be expected at least at the edges.

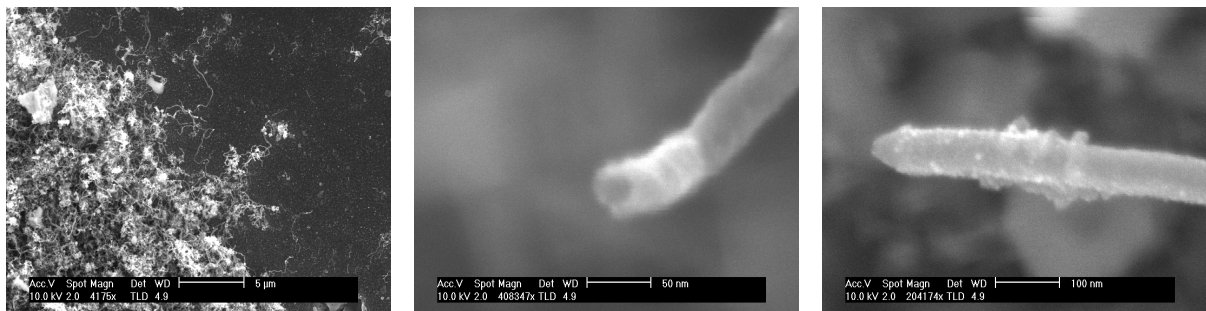


Fig. 4.1. SEM images of the MWCVD grown CNT layer on the Si surface (left), single CNT with opened (center) and closed (right) tips.

The IMLS tests reveal only few dominating emitters at the edges of the square patches ( $0.5 \times 0.5 \text{ mm}^2$ ) up to electric field of  $6 \text{ V}/\mu\text{m}$ . Converted IMLS images showed for the total current of  $300 \text{ nA}$  the maximum  $I$  of  $50 \text{ nA}/\text{emitter}$ . The U-maps obtained in FESM showed inhomogeneous emitter distribution on the surface as shown in Fig. 4.2 up to electric fields of  $15$  and  $17.5 \text{ V}/\mu\text{m}$ , respectively. Only weak emitters were found in the central part of the square patch, while the strongest were observed at the edges. The emitter number density

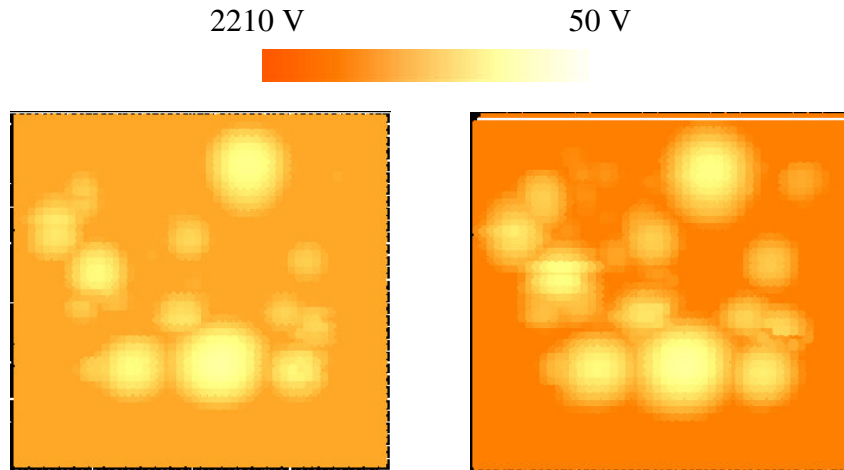


Fig. 4.2. U-maps (scan area  $0.75 \times 0.75 \text{ mm}^2$ ) of a MWCVD grown CNT sample made with  $30 \mu\text{m}$  W anode at  $60 \mu\text{m}$  electrode spacing for current limit of  $1 \text{ nA}$  at  $E < 15 \text{ V}/\mu\text{m}$  (left) and  $E < 17.5 \text{ V}/\mu\text{m}$  (right). The resulting emitter number densities are  $5600/\text{cm}^2$  and  $9600/\text{cm}^2$  respectively.

was about  $5600$  ( $9600$ )/ $\text{cm}^2$  at  $E = 15$  ( $17.5$ )  $\text{V}/\mu\text{m}$ , respectively. The local measurements of the 12 random CNT emitters were made in the FESM with  $\varnothing = 30 \mu\text{m}$  W anode at  $30 \mu\text{m}$  electrode spacing. Two exemplary FN curves of CNT emitters measured up to  $I = 50 \text{ nA}$  are shown in Fig. 4.3. While the emitter 1 show slight degradation (the field enhancement decreased from  $140$  to  $126$ ), the emitter 2 reveal more evident activation ( $\beta$  increased from  $131$  to  $160$ ). Obviously, in this current range the emitters do not show strong current fluctuations.

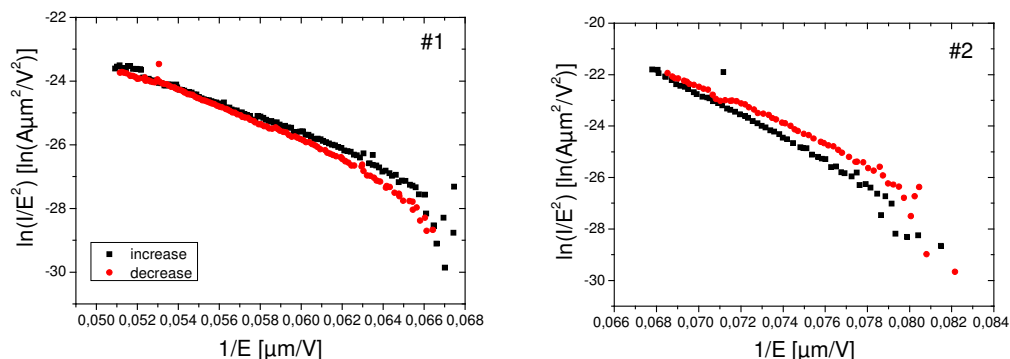


Fig. 4.3.  $I(U)$  curves of 2 random emitters of the MWCVD grown CNT sample in FN illustration.

The emitters showed the  $\beta$  values between  $140$  and  $360$  (as calculated for  $\Phi = 4.9 \text{ eV}$ ) and onset fields of the emission for  $1 \text{ nA}$  current in the range between  $12.9$  and  $20 \text{ V}/\mu\text{m}$  (Fig.

4.4). The emitters can be splitted into two groups. First include the emitters with low field enhancement from the central area of the patch of  $\beta = 140 - 170$  and  $E_{on} = 12 - 16 \text{ V}/\mu\text{m}$ . Another group are the emitters at the edges of the patch, which have  $\beta = 230 - 370$  and  $E_{on} = 13 - 21 \text{ V}/\mu\text{m}$ . Since no significant difference in the structure of CNT was observed at the

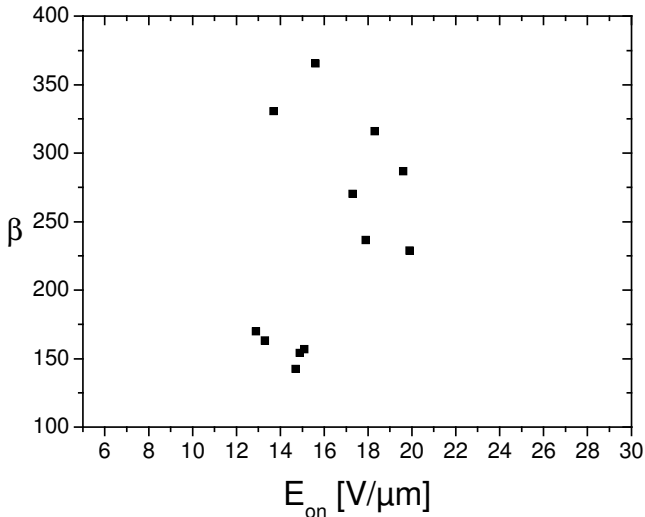


Fig. 4.4. Field enhancement factors  $\beta$  of random single MWCVD grown CNT emitters as a function of onset field  $E_{on}$  for a current of 1 nA.

edges and in the central part, such a distinction of nearly factor 2 in field enhancement is due to mutual shielding of the emitters. The distance between CNT at the patch edges is about of their length, thus they reveal higher  $\beta$  (Fig. 4.1(left)). The emitters show the deviation of field enhancement from the inverse dependence on the onset field. Calculation of the effective emitting area  $S$  for the first group of emitters with low field enhancement show the mean values  $\sim 6 \times 10^{-11} \text{ cm}^2$ . Consequently, the  $30 \mu\text{m}$  W anode extracted in the central part of the patches the emission current of 1 nA from several shielded CNT. This explain low onset fields  $E_{on} = 12 - 16 \text{ V}/\mu\text{m}$  of weak emitters with corresponding  $\beta < 170$ . For another group  $S$  values were up to one order of magnitude lower, which represents the single closed MWNT. Despite of some strong emitters at the edges, the central area of the patches show only a few shielded emitters. Thus, densely packed CNT are useless for FE applications.

## 4.2 CNT on porous alumina

In order to control the density of CNT, the porous alumina was used as a template for their growth as described in Chapter 2.1.2. Therefore, the fabrication parameters of CNT have to be optimised for the FE, thus to achieve best homogeneity, stability and high current densities. In Tab. 4.1 an overview of the investigated samples as fabricated with varying parameters is shown. In order to test the reproducibility of the results the series of the CNT samples on porous alumina with equal parameters were fabricated.

Sample name	Precursor type	Precursor amount [mg]	PoreØ [nm]	Sample thickness [µm]	Growth T°C in MOCVD
JE19	Nickelocene	70	200	60	791
JE20	Chromocene	70	200	60	810
JE40	Cobaltocene	100	200	60	644
JE42-1,2 <sup>*</sup>	Fe-Co-S	70	200	60	800
JE78-1,2,3;N1	Ferrocene	70	200	60	800
JE105,109	Ferrocene	100	200	60	834
JE110 <sup>**</sup>	Ferrocene	100	200	60	834
JE98	Ferrocene	70	200 / n.m.	60	800
JE102	Ferrocene	50	40 / 60	80	815
JE103	Ferrocene	70	100 / 42	200	835
JE112 <sup>*</sup>	Ferrocene	70	52 / 36	50	839
JE116-1,2 <sup>*</sup>	Ferrocene	100	52 / 16	80	810
JE120	Ferrocene	70	52 / 65	90	830
JE122,123	Ferrocene	70	65 / 28	100	835
JE124,125	Ferrocene	70	105 / 62	190	835

Tab. 4.1. Overview of the fabrication parameters for all tested CNT samples on porous alumina. For each sample the type and amount of the precursor, which was used in the MOCVD process, the average nominal/real (measured with SEM) pore diameters and thickness of the porous alumina are shown. Rosa marks the rows, which describe the CNT samples on Anodisc® prepared without ferrocene, yellow – with ferrocene. Blue marks the CNT samples on EPAM. (\*) For the fabrication of the JE42-2, JE112 and JE116 no additional alumina particles were used. (\*\*) The JE110 surface was covered with large amount of alumina particles.

For the fabrication of CNT on porous alumina, five metalorganic precursors were used – nickelocene, chromocene, cobaltocene, Fe-Co-S complex and ferrocene. The amount of the precursor vary in a range of 50 - 100 mg, which influence the quantity of CNT on the porous alumina surface. The amount of alumina particles, which were used for pore closing was for most of the samples ~ 100 mg (except (\*) and (\*\*)). The temperature of the CNT growth by MOCVD process was about 800°C (except Cobaltocene), resulting in constant diameter of MWNT ~ 20 nm [122]. The template pore diameters vary between 16 and 200 nm, the thickness between 50 and 200 µm. The SEM investigations of the EPAM show strong deviation of the real pore diameters from the expected (nominal) values, predicted by the known from the literature etching voltage (Tab. 4.1) [68].

While the influence of the precursor type and amount on the FE, and the reproducibility of the results were measured by CNT samples on Anodisc®, the investigation of the influence of the membrane morphology to the FE was mainly concentrated on the CNT samples grown on EPAM. For both types of the porous alumina the local measurements were provided to distinguish the FE parameters and stability of single CNT emitters.

### 4.2.1 Variation of the precursor type and amount

At first, the influence of the catalyst type and amount was investigated for CNT samples on Anodisc®, commercial porous alumina with the pores of 200 nm in diameter (see Chapter 2.1.2). For the measurements, the membranes were broken into pieces of 7 - 25 mm<sup>2</sup> size. The flexibility of the 60 μm thick template allows slight bending, thus glue the samples flat to the holders. The overview of the FE results obtained in the IMLS in dc mode is presented in Tab. 4.2. The maximum electric fields  $E_{\max}$  were limited by the discharges, which occurred due to evaporation of the phosphor layer of the luminescent screen [146]. The employment of the QMS allows in some cases to predict such an effects and shift the critical field of the discharge to the higher level by means of e.g. slow conditioning of the samples. Since maximum achieved fields are different, the emitter number and current densities were compared at the intermediate field level of  $E = 3 \text{ V}/\mu\text{m}$ , which was reached by all samples.

Sample Name	Metallocene precursor	Sample area (mm <sup>2</sup> )	$E_{\text{on}}$ (1nA) [V/μm]	$N/\text{cm}^2$ at $E=3\text{V}/\mu\text{m}$	$J[\mu\text{A}/\text{cm}^2]$ at $E=3\text{V}/\mu\text{m}$	$N_{\max}/\text{cm}^2$	$j_{\max} [\mu\text{A}/\text{cm}^2]$	$E_{\max}$ [V/μm]
JE19	Nickelocene	9.5	1	500	16	4000	82	5
JE20	Chromocene	8	2.2	380	19	1000	2500	6.3
JE40	Cobaltocene	10	3.8	0	0	200	12	4.3
JE42-1	Fe-Co-S-Complex	7	2.6	370	31	1000	560	5.6
JE78-2	Ferrocene	15	0.6	3500	700	5000	1100	3.5

Tab. 4.2. Integral FE properties obtained in dc mode for the CNT samples fabricated on Anodisc® with different precursors. For each sample the area, the onset field for the current of 1 nA, emitter number and current density at  $E = 3\text{V}/\mu\text{m}$ , achieved emitter number ( $N_{\max}$ ) and current density ( $j_{\max}$ ) at maximum reached field level ( $E_{\max}$ ) are shown.

It is well known, that some metals as Fe [147], Ni [148], Cr [149], Co [150] greatly increase the growth rate of CNT. Nevertheless, there are some preferences of the CNT growth with definite catalysts and templates conditioned by e.g. adhesion, temperature resistance of the substrate etc. The first measurements of B. Günther by the investigation of the CNT samples on porous alumina prepared with pyrolysis of propene and ferrocene [38] showed, that the CNT grown with catalyst reveal good uniformity of FE and sufficient emission currents. However, only a few tests with such a membranes were provided. In order to define the preferred catalyst the comparative FE measurements of the CNT samples on Anodisc® grown with five different precursors: nickelocene (JE19), chromocene (JE20), cobaltocene (JE40), Fe-Co-S complex (JE42-1) and ferrocene (JE78-2) were provided in the IMLS. The examples of the emission homogeneity from these samples are presented in Fig. 4.5. The fabrication of the CNT samples with different precursors, investigation of their morphology and partially the corresponding FE measurements, which have been made in Wuppertal, were described by J. Engstler in his thesis work [68].

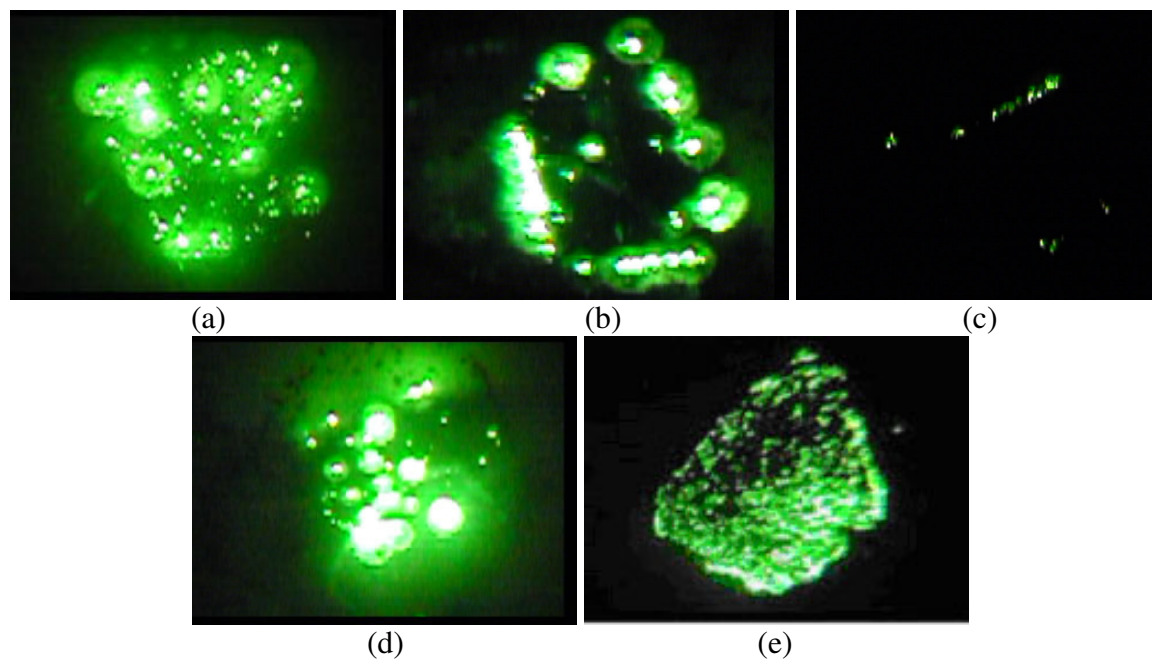


Fig. 4.5. IMLS images of the emission from the CNT samples prepared with (a) nickelocene (JE19), (b) chromocene (JE20), (c) cobaltocene (JE40), (d) Fe-Co-S complex (JE42-1) and (e) ferrocene (JE78-3) at corresponding  $E_{\max}$  listed in the Tab. 4.2.

For the nickelocene grown CNT samples moderate number of emitters  $\sim 4000/\text{cm}^2$  was obtained at  $E = 5 \text{ V}/\mu\text{m}$ . The cluster like emission leads to the relatively poor homogeneity. The emission, however, was observed over the whole sample surface (Fig. 4.5(a)). Alternatively, the CNT samples grown with chromocene reveal strong emission at the edges and a few emitters in the central part at  $E = 6.3 \text{ V}/\mu\text{m}$  (Fig. 4.5(b)). Cobaltocene sample reveal the lowest emitter number density (Fig. 4.5(c)) and homogeneity. Only few emitters were observed at the edges at  $E = 4.3 \text{ V}/\mu\text{m}$ . Fe-Co-S complex based samples showed cluster-like inhomogeneous emission. About 20 strong light spots, probably the emission from large bundles of CNT, were seen in the IMLS images. Their entry, however, can not be resolved on the luminescent screen due to high brightness (Fig. 4.5(d)). Finally the ferrocene based CNT samples reveal the best homogeneity of the emission over the most of the sample surface and highest number of emitters of  $\sim 7000/\text{cm}^2$  (Fig. 4.5(e)) at an electric field of  $3.5 \text{ V}/\mu\text{m}$ . The homogeneity of the emission was, however, disturbed by the non-flatness of the substrate, while the top left area of the sample reveal low  $\sim 2000/\text{cm}^2$  and the bottom right – highest number of emitters.

The total emission current, measured in the IMLS, is produced by the emitters distributed over the sample surface. Their strength and current carrying capability, however, are different. The maximum obtained current density by the nickelocene sample (JE19) was  $j = 82 \mu\text{A}/\text{cm}^2$  at  $5 \text{ V}/\mu\text{m}$ . Alternatively, despite of the poor homogeneity and emitter number density the chromocene sample (JE20) reproducibly shows the emission current up to  $200 \mu\text{A}$ , resulting in the  $j = 2.5 \text{ mA}/\text{cm}^2$  at the electric field  $E = 6.3 \text{ V}/\mu\text{m}$ . In general, the non-ferrocene samples are characterised by onset fields  $> 1 \text{ V}/\mu\text{m}$  for the current of  $1 \text{ nA}$  and



current densities 16 – 31  $\mu\text{A}/\text{cm}^2$  at  $E = 3 \text{ V}/\mu\text{m}$ . In contrast, for the ferrocene sample JE78-2 about 20 times higher current density of 700  $\mu\text{A}/\text{cm}^2$  was achieved at the same field level. Since the good homogeneity of the emission from the CNT on porous alumina and highest current density were obtained even without the additional structuring of the substrates, ferrocene was chosen as a potentially best catalyst for the cold cathode manufacturing.

The variation of the precursor amount in the MOCVD process influence the quantity of CNT grown on the porous alumina.

Sample Name	Sample area ( $\text{mm}^2$ )	$E_{\text{on}}$ (1nA) [ $\text{V}/\mu\text{m}$ ]	$N/\text{cm}^2$ at $E=3\text{V}/\mu\text{m}$	$J$ [ $\mu\text{A}/\text{cm}^2$ ] at $E=3\text{V}/\mu\text{m}$	$N_{\text{max}}/\text{cm}^2$	$j_{\text{max}}$ [ $\mu\text{A}/\text{cm}^2$ ]	$E_{\text{max}}$ [ $\text{V}/\mu\text{m}$ ]
JE78-2	15	0.6	3500	700	5000	1100	3.5
JE78-3	24.7	0.5	7000	1300	7000	1200	3
JE105	10	0.5	2500	400	6000	1400	3.7
JE109	8	0.86	2400	250	7000	1700	4.3

Tab. 4.3. Integral FE properties of the CNT samples on Anodisc® grown with 70 mg ferrocene (green) and 100 mg (rose). For each sample the area, the onset field for the current of 1 nA, emitter number and current densities of the sample at  $3\text{V}/\mu\text{m}$ , achieved emitter number ( $N_{\text{max}}$ ) and current densities ( $j_{\text{max}}$ ) at maximum reached field levels ( $E_{\text{max}}$ ) are shown.

The investigation of this dependence was provided for two ferrocene grown CNT sample series on Anodisc® JE78 (samples JE78-2, 78-3) and JE105 (samples JE105, 109), prepared with 70 and 100 mg ferrocene, respectively (Tab. 4.3).

The SEM image of the sample JE78-3 (Fig. 4.6) show that the surface is covered with the layer consists of the CNT and alumina particles. The CNT grown from the pores are 35 - 500 nm long. The number of CNT observed in the central part of the membrane can differ from the value observed in edge region. The process modelling shows, that the heating in the

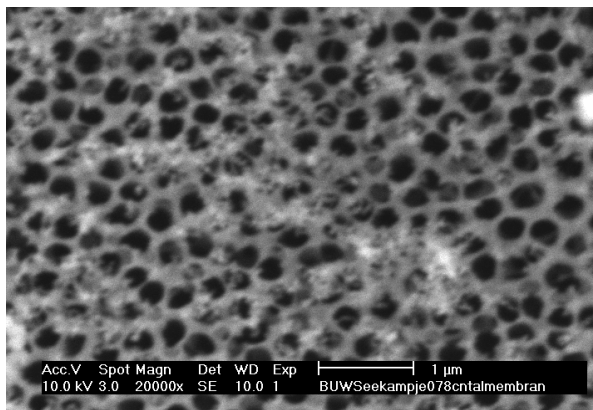


Fig. 4.6. SEM images of the sample of JE78 serie, which shows the short CNT grown from the pores and alumina particles.

MOCVD process starts at the edge of the membrane and continue to the center. The temperature stabilises only after 100 s (Chapter 2.1.2), while the CNT growth rate can achieve some tens of  $\mu\text{m}/\text{s}$ . The IMLS tests show, that the samples taken from the central and the edge regions of the membrane reveal slightly different FE properties. The EDX scans show, however, that in the central part Fe quantity does not change at least in the 0.2 mm scale (Fig. 4.7). The influence of the catalyst distribution, which is hard to

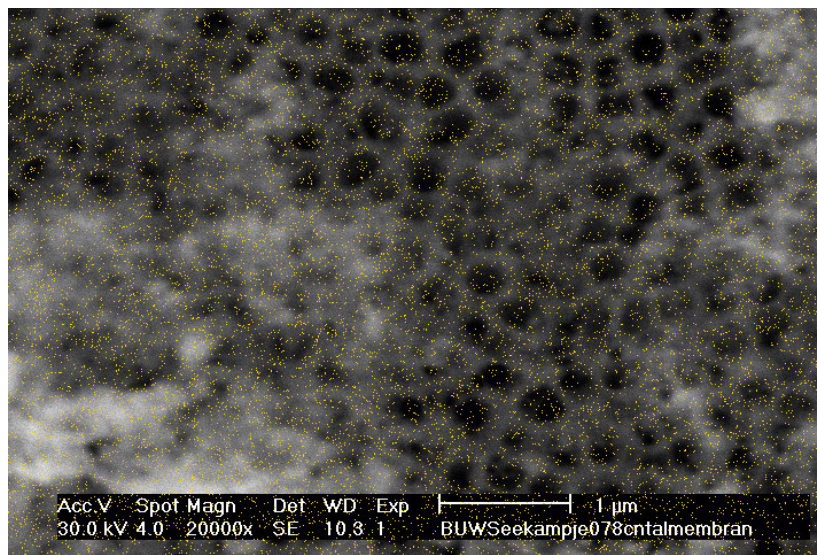


Fig. 4.7. SEM image of the surface of sample JE78-3 with corresponding EDX scan, which represents the iron on the surface and inside the pores (yellow spots), where the catalyst build the ring structures.

take into account, can be minimized e.g. by means of the testing of the samples taken from the central part of the membranes. The difference of the CNT number density between JE78 and JE105 sample series was not observed in the SEM images due to solid layer of CNT on both templates. It can be, however, detected in the IMLS tests. The emitter number densities for the samples of the serie JE78 were  $3500/\text{cm}^2$  and  $7000/\text{cm}^2$  at the field level of  $E = 3 \text{ V}/\mu\text{m}$ . For the JE105 and JE109, the emitter number densities of  $2500/\text{cm}^2$  and  $2400/\text{cm}^2$ , respectively, which are, however, up to by factor 3 lower than for JE78 serie, were observed at the same field level (Fig. 4.8). The higher quantity of nanotubes for JE105 and JE109 increase the influence of the shielding effect, thus increase the extraction field of emitters.

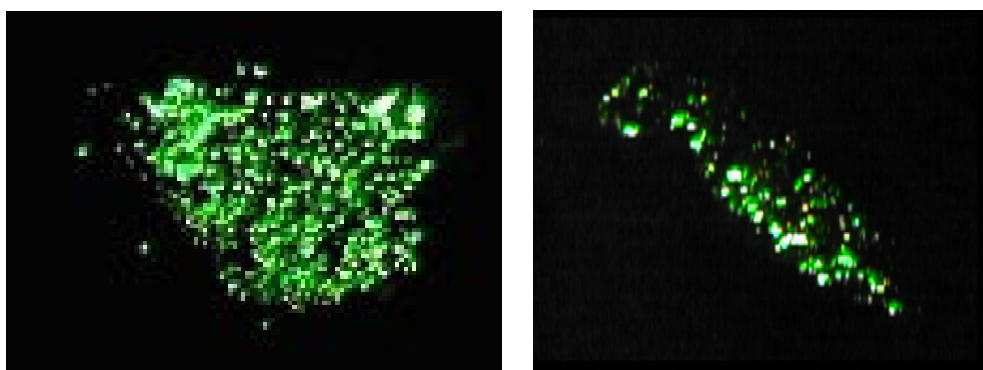


Fig. 4.8. IMLS images of the Anodisc® samples (a) JE78-2 (size  $18.2 \text{ mm}^2$ ) and (b) JE109 (size  $8 \text{ mm}^2$ ) taken at  $E = 3 \text{ V}/\mu\text{m}$ . The emitter number densities are  $3500/\text{cm}^2$  and  $2370/\text{cm}^2$ , respectively.

At the maximum field levels of up to  $4.3 \text{ V}/\mu\text{m}$  the emitter number densities are nearly the same. Moreover, one can expect the higher emitter number density for JE105 and JE109 at higher fields due to increased number of CNT on the surface. The long CNT, which are responsible for the onset of the integral emission for  $I = 1 \text{ nA}$  at  $\sim 0.5 \text{ V}/\mu\text{m}$  present on both samples typically at the edges, where the macroscopic field enhancement is the highest. Thus, the onset fields for 1 nA current of these samples are nearly equal.

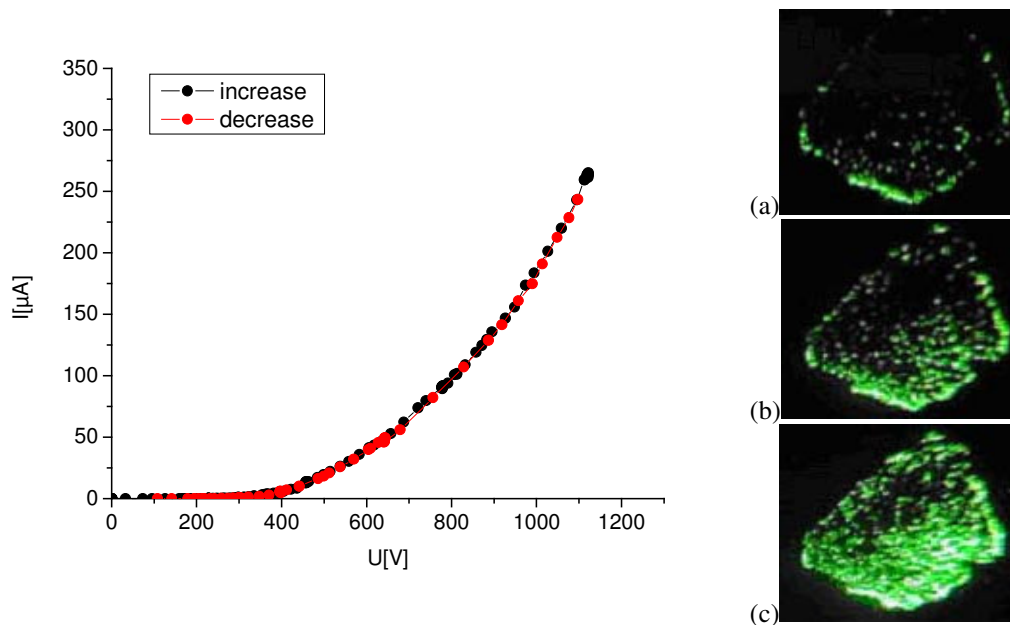


Fig. 4.9.  $I(U)$  curve of the sample JE78-3 in linear illustration (left) and corresponding IMLS images (right) taken at (a)  $I = 70 \mu\text{A}$  ( $U = 650 \text{ V}$ ), (b)  $I = 150 \mu\text{A}$  ( $U = 870 \text{ V}$ ) and (c)  $I = 260 \mu\text{A}$  ( $U = 1100\text{V}$ ). Electrode spacing  $\Delta z = 400 \mu\text{m}$ .

The reproducible  $I$ - $V$  curves of the sample JE78-3 are shown in Fig. 4.9 up to emission current of  $I = 300 \mu\text{A}$ . Such a plots are usually obtainable after several hours of the sample conditioning. The virgin samples typically show the current fluctuations up to 50%, due to processing effects (see Chapter 4.2.8). The sample JE78-2 shows by factor 2 reduced number of emitters and correspondingly lower FE current at  $E = 3 \text{ V}/\mu\text{m}$ . This effect is caused by using of the piece from the edge region of the template. The  $I$ - $V$  curves of the sample JE109 are shown in Fig. 4.10.

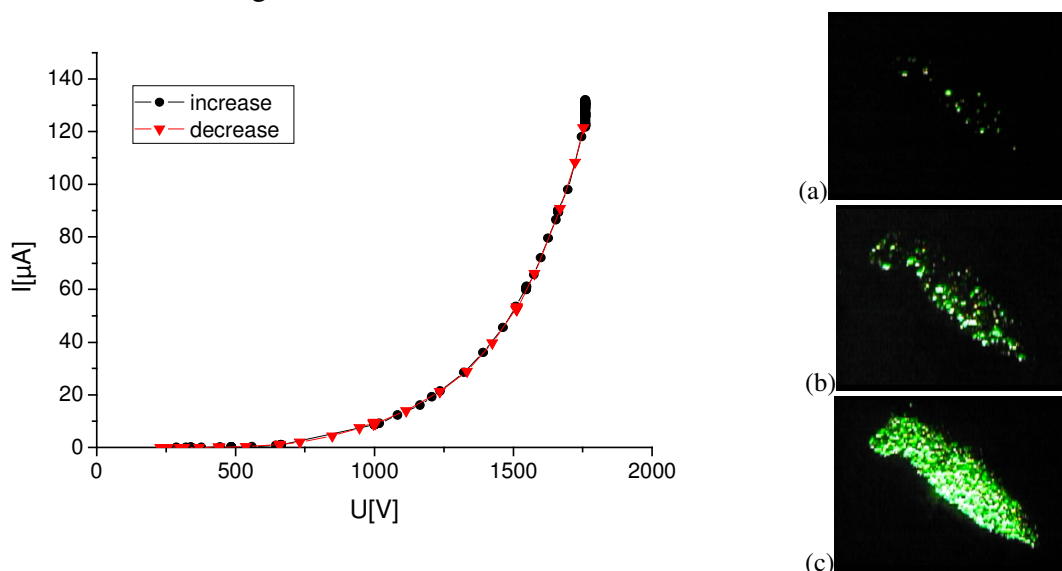


Fig. 4.10.  $I(U)$  curve of the sample JE109 in linear illustration (left) and corresponding IMLS images (right) taken at (a)  $I = 3 \mu\text{A}$  ( $U = 997 \text{ V}$ ), (b)  $I = 8 \mu\text{A}$  ( $U = 1235 \text{ V}$ ) and (c)  $I = 135 \mu\text{A}$  ( $U = 1725\text{V}$ ). Electrode spacing  $\Delta z = 400 \mu\text{m}$ .

The reproducibly achieved emission current was  $I = 135 \mu\text{A}$  at  $E = 4.3 \text{ V}/\mu\text{m}$ . The Fig. 4.11 shows the comparison of the  $j(E)$  dependence for the samples JE78-2,3 and JE105,109. The current densities of  $0.4$  and  $0.25 \text{ mA}/\text{cm}^2$  were achieved for the samples JE105 and JE109 at field level  $3 \text{ V}/\mu\text{m}$ , which are up to factor 5 lower than for the samples JE78-2 and JE78-3. For the nanostructure cathodes it is always a compromise between the number of emitters, thus total current, and onset field. Low amount of CNT on the surface leads to the high field enhancement of emitters, thus low onset/operation fields. Alternatively, the excess of CNT results in high current densities, but also the shielding effect, which increase the extraction voltage of emitters. Thus, the amount of ferrocene allows to vary the output parameters of the CNT samples in order to achieve high currents or low operation fields.

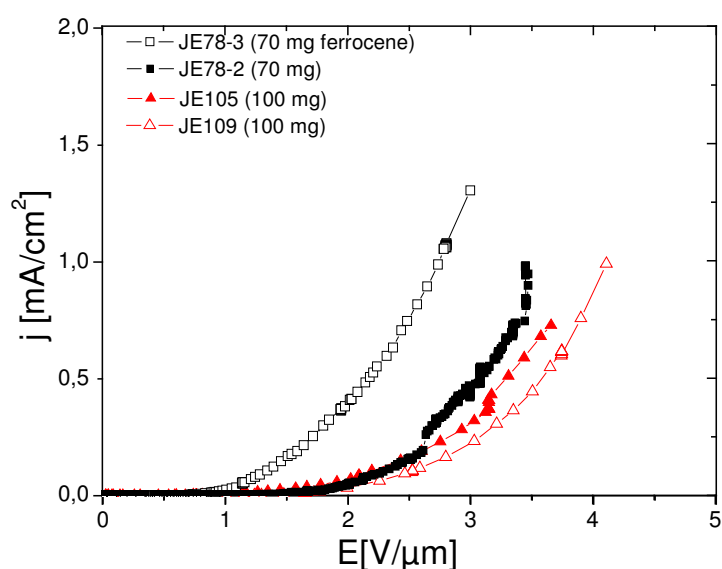


Fig. 4.11. Comparison of the achieved current densities for the CNT samples fabricated with 70 and 100 mg ferrocene at the electric fields up to  $4.3 \text{ V}/\mu\text{m}$ .

#### 4.2.2 Influence of the alumina particles

The alumina particles on the porous template surface play two important roles: they close the pores reducing the growth of the nanotubes and serve as an anchor for them, increasing the mechanical stability of emitters. In comparison to the samples on Anodisc® (JE42-2, JE110), the morphology of EPAM (JE112 and JE116) is different on its opposite sides. One side have the fully opened pores (f-side), another – partially (p-side). Only part of the pores is opened on the p-side and their diameters are less than on the f-side. Moreover, it can not be predicted by membrane producers (Tab. 4.4). It was established in previous works, that the amount of  $\sim 100 \text{ mg}$  of alumina particles reduce the shielding effect [38,68]. The influence of the lack or excess of alumina particles on the surface to the FE was not investigated.

The CNT on Anodisc® JE42-2 were fabricated at the same conditions as JE42-1, but without alumina particles. Two pieces of the sample were investigated and reproducibly low emission current as obtained. Only a few emitters were observed in the IMLS on the sample surface up to  $E = 6.7 \text{ V}/\mu\text{m}$ , which for the CNT is a rather high value.

Sample name	Sample area [mm <sup>2</sup> ]	Config. of pores	Pore diameter [nm]		$E_{\text{on}}$ (1nA)	$N_{\text{max}}/\text{cm}^2$	$j_{\text{max}}$ [ $\mu\text{A}/\text{cm}^2$ ]	$E_{\text{max}}$ [ $\text{V}/\mu\text{m}$ ]
			Nom.	Real				
JE42-2	8	I	200		3.8	50	<1	6.7
JE110	12	I	200		3	100	4	8.8
JE112	10	p,I	52	33-40	n.m.	10	<1	5
JE116	11	p,I	52	12-20	0.9	250	180	2.8
	12	f,O	-	44-62	2.1	270	33	4.6

Tab. 4.4. Influence of the alumina particles on the integral FE properties of the CNT samples on porous alumina. The 3<sup>rd</sup> column shows that the sample have fully (f) or partially (p) (only for EPAM) opened pores and served as gas-inlet (I) or –outlet (O) in the MOCVD process. The nominal (estimated by the etching voltage) and the real (measured with the SEM) pore diameters are presented in the 4<sup>th</sup> column. The last three columns from the left shows the achieved emitter number ( $N_{\text{max}}$ ) and current densities ( $j_{\text{max}}$ ) at maximum reached field level ( $E_{\text{max}}$ ) respectively.

The SEM image (Fig. 4.12) show that the sample surface is covered with the large number of short shielded CNT with cluster-like graphite structures, which are not suitable for enhanced FE. On the other hand, the excess of the alumina on the surface suppress the field emission too. The CNT sample on Anodisc® JE110 was produced with three times higher amount of alumina particles (350 mg) than for the sample JE78-3. The emission current density of  $4 \mu\text{A}/\text{cm}^2$  was reached at  $E = 8.8 \text{ V}/\mu\text{m}$ . In the case of the increased layer of alumina particles the FESM contact measurements reveal the decrease of the conductivity and isolation of some parts of the membrane. The contact between the emitting surface and the cathode through the

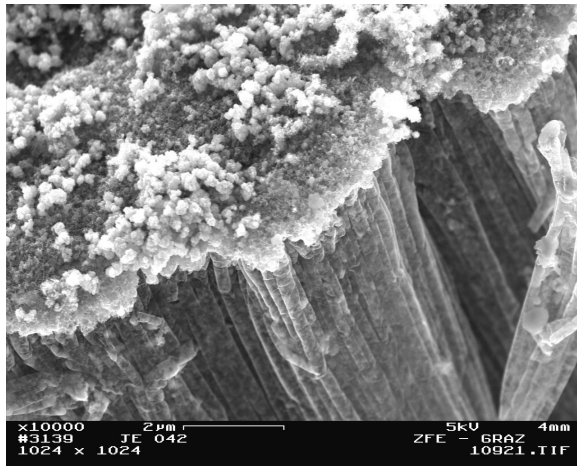


Fig. 4.12. SEM image of the sample JE42-2. The surface is covered with the solid layer of short CNT.

conducting carbon which fill up the template pores for most of the sample surface is disturbed.

The sample JE112 was fabricated with the opened pores on the p-side. However, no additional deposition of alumina particles was made. The pores were so treated, that they build isles and their diameters (Fig. 4.13) are nearly equal to the pores on the f-side (Tab. 4.4). Than the p-side was used as inlet side for the CNT growth. The idea was to grow non-shielded CNT by means of spread pores and reach good homogeneity of the emission without

additional alumina particles, thus simplify the process. During the MOCVD process carbon build the cluster-like structures on the sample surface with few CNT (Fig. 4.13). The current density of  $< 1 \mu\text{A}/\text{cm}^2$  was achieved at  $E = 5 \text{ V}/\mu\text{m}$ . The role of alumina particles seems to be more important for the CNT growth, than simply mechanical stabilisation and structuring. Probably, the porous structure together with alumina particles also simplify the seeding of the CNT. However, no experimental modelling which can prove this idea, was found in the

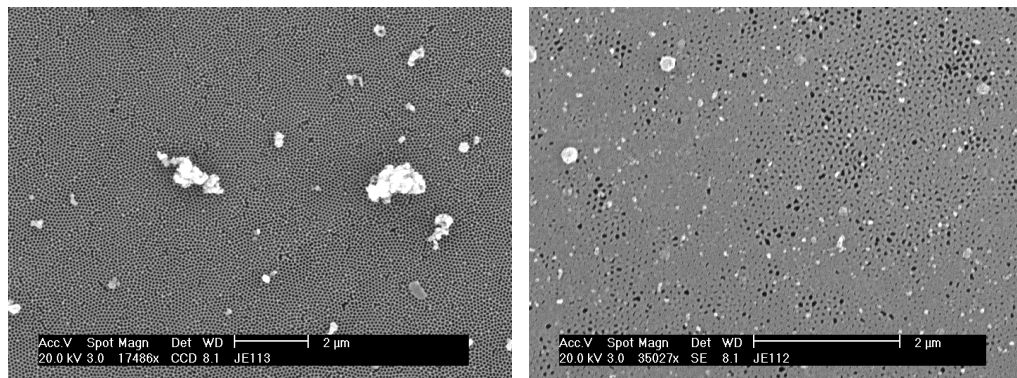


Fig. 4.13. SEM image of the surface of JE112 with fully (left) and partially (right) opened pores. Cluster like carbon structures are seen on the surface (left). The opened pores build isles on the surface, while the rest is closed (right).

literature. The sample JE116 was produced similar to JE112, when the p-side with alumina particles was turned on to the gas flow during the MOCVD. The pores on the p-side were not fully opened and their diameters were 3 times smaller than on the f-side. The CNT build the solid layer, which is not suitable for the FE (Fig. 4.14). The size of the pores  $< 20 \text{ nm}$  prohibit the growth of the CNT from them in the  $800^\circ\text{C}$  temperature range. In this case, if the p-side is turned to the gas flow the large amount of carbon detain on the surface, thus build the layer of CNT and amorphous carbon. No growth of CNT squared by pores was observed on the sample surface. As expected from the morphology of CNT seen in the SEM images, only few emitters were observed over the sample surface up to  $3 \text{ V}/\mu\text{m}$ . The maximum total current was  $I \sim 10 \mu\text{A}$  from the  $13 \text{ mm}^2$  sample. The investigation of another pieces of the membrane reveals strong emission from the few emitters at the edges. As expected, the large number of CNT, which grow fast on the p-side without additional alumina particles results in poor homogeneity and low emission current.

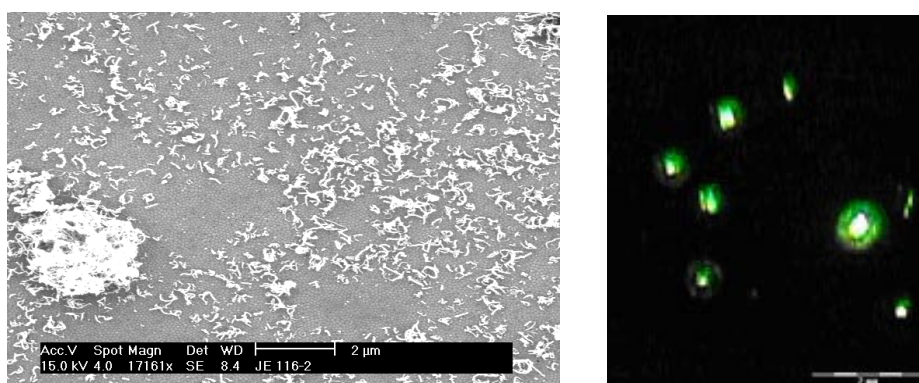


Fig. 4.14. SEM image of the JE116 surface and corresponding IMLS image at  $3 \text{ V}/\mu\text{m}$  with few edge emitters.

### 4.2.3 Influence of the sample curvature

In the MOCVD reactor the porous alumina substrates are heated up to 800<sup>0</sup>C. The mechanical stress which occurred due to shrinkage of the alumina at this temperature leads to the bending of the templates. Sometimes, they brake after the CVD process despite of the slow (some hours) cooling. Thus, porous alumina is always non-flat (see Chapter 2.1.2) and reveal randomly concave or convex geometry. In order to reduce the influence of the sample curvature to the FE the samples are usually broken into several 10 - 30 mm<sup>2</sup> pieces. However, even these small parts of the original template reveal the height difference up to  $\Delta Z_{\max} = 120$   $\mu\text{m}$  over the several mm length. This problem is usually occur for the EPAM, which have the thickness 100 - 200  $\mu\text{m}$ . It is not so brittle as 60  $\mu\text{m}$  thick Anodisc®, but does not allow bending. The curvature of the samples with thickness > 100  $\mu\text{m}$  can not be changed during installation in the apparatus and should be taken into account for calculations of the electric field. During the installation the distance from the sample holder to the luminescent screen is measured with the micrometer. This value include electrode spacing, sample thickness and glue button with known thickness of 250  $\mu\text{m}$ . In case of relatively flexible Anodisc® samples the precision of electrode spacing definition is about 10  $\mu\text{m}$  and includes only the micrometer error. This allows simple calculation of the applied electric field  $E = U/d$ , where  $d$  is electrode spacing measured with micrometer. In case of non-flat samples  $U(z)$  measurements should be provided for the effective electric field estimation (see Chapter 3.1.2) which have the form  $E_{\text{eff}} = U/\Delta z$ , where  $\Delta z$  is the effective electrode spacing estimated from the  $U(z)$  plot (Fig. 4.15).

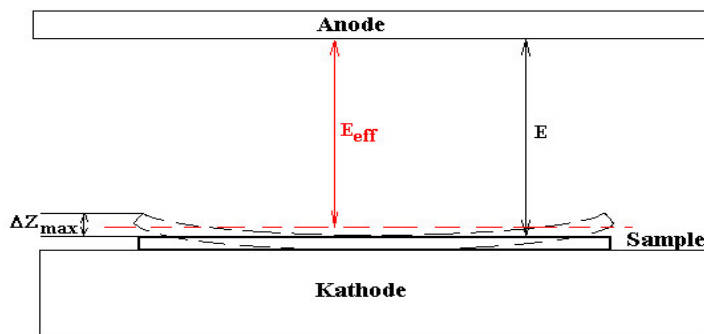


Fig. 4.15. Scheme for calculation of the electric field in case of the flat ( $E$ ) and convex curved ( $E_{\text{eff}}$ ) sample with the height difference  $\Delta Z_{\max}$ .

The precise calculation of the electric field is possible, however, only for known morphology of the investigated surface. The measurements of the sample curvature were made with the FRT Profilometer (see Chapter 3.3.2). The membrane curvatures were calculated in 3D illustration by means of the software Mark III [144] for different sample configurations. The examples of the curvature measurements are presented in Fig. 4.16 and 4.17.

The 190  $\mu\text{m}$  thick sample JE123 reveal the convex geometry, thus enhanced emission at the edges (Fig. 4.16). The maximum height difference between the edges and the central part was  $\Delta Z_{\max} = 100$   $\mu\text{m}$  over 4.7 mm length. Such a difference disturbs not only IMLS measurements, but the FESM scans too, though in a lesser degree.

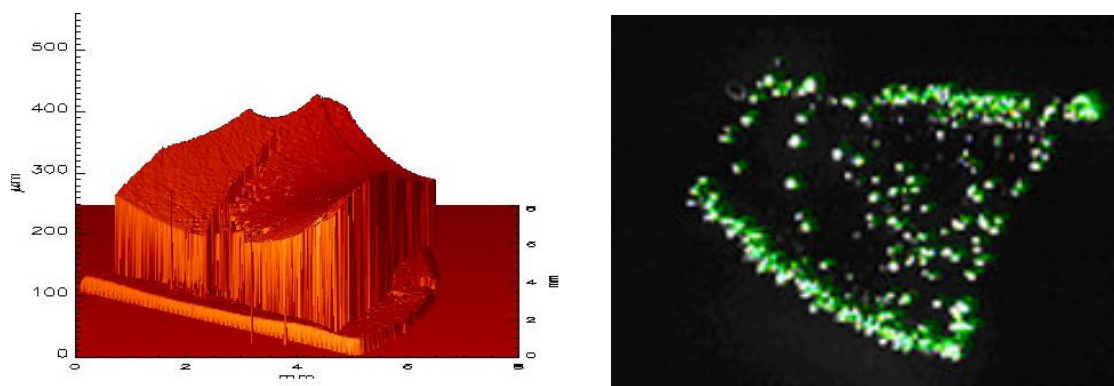


Fig. 4.16. Profile of the 22.4 mm<sup>2</sup> concave curved CNT sample on the EPAM JE123 (left) in 3D illustration and (right) corresponding IMLS image, which was taken in dc mode at  $I = 30 \mu\text{A}$  and  $U = 600 \text{ V}$  ( $E_{\text{eff}} = 3 \text{ V}/\mu\text{m}$ ).

By the usual electrode spacings of 300 - 400  $\mu\text{m}$  the applied electric field at the edges in this case is 25-30 % higher, than in the central part simply due to the geometry. The sample curvature at the voltage  $U = 600 \text{ V}$  results in the electric field difference at the edges and in the central part of  $\Delta E = 1.6 \text{ V}/\mu\text{m}$  and increases by the maximum reached voltage of  $U = 1090 \text{ V}$  to  $\Delta E = 2.9 \text{ V}/\mu\text{m}$ . This enormous values, if taken into account explain the high brightness of the edge regions of the sample in Fig. 4.16 (right). The emitter number density in the central part of the sample at  $U = 600 \text{ V}$  was  $\sim 1000/\text{cm}^2$  and increases to the edges up to  $\sim 5000/\text{cm}^2$ . Typically at high electric fields extremely high brightness is observed in the IMLS images, resulting in visual fusion of emitters at the edges. In such cases the emitter number density can not be precisely calculated.

Opposite side of the same sample reveal concave geometry with  $\Delta Z_{\text{max}} = 115 \mu\text{m}$  over 5.5 mm length respectively, resulting in at  $U = 1000 \text{ V}$  electric field difference of  $\Delta E = 2.3 \text{ V}/\mu\text{m}$  (Fig. 4.17). One should notice, that it is not possible to remove the samples without damaging from the glue. Thus, the different samples are the different pieces of the original template.

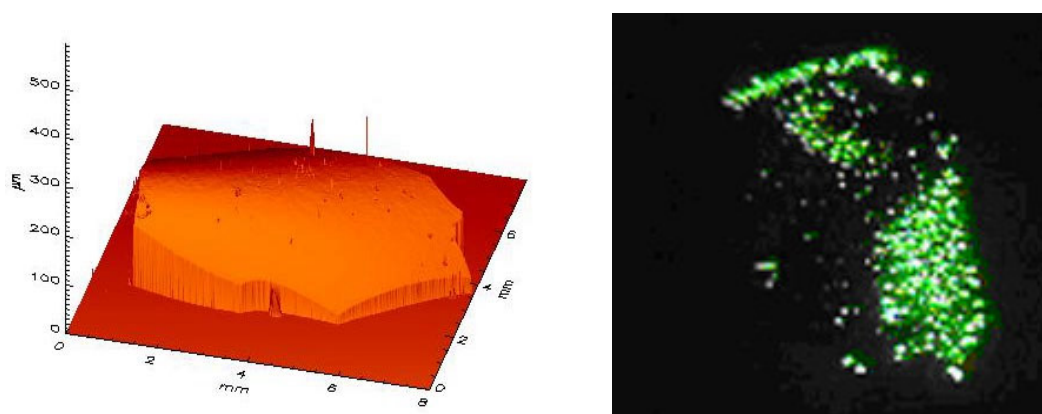


Fig. 4.17. Profile of the of 24 mm<sup>2</sup> convex curved CNT sample on the EPAM JE123 (left) in 3D illustration and (right) corresponding IMLS image, taken in dc mode at  $I = 40 \mu\text{A}$  and  $U = 750 \text{ V}$  ( $E_{\text{eff}} = 3.8 \text{ V}/\mu\text{m}$ ).



The distribution of emitters over the surface (Fig. 4.17(right)) is the reverse to that have seen for the sample in Fig. 4.16(right). The highest number of emitters is seen in the central part of the sample and decreases to the edges due to reduced electric field.

If the distance between CNT is much less than their height the shielding effect occurs. Despite of the comparatively low  $\Delta Z_{\max} = 22 \mu\text{m}$  (Fig. 4.18(left)) by the sample JE122 the emission is shown mostly at the edges up to  $E_{\text{eff}} = 5.3 \text{ V}/\mu\text{m}$  (Fig. 4.18(right)).

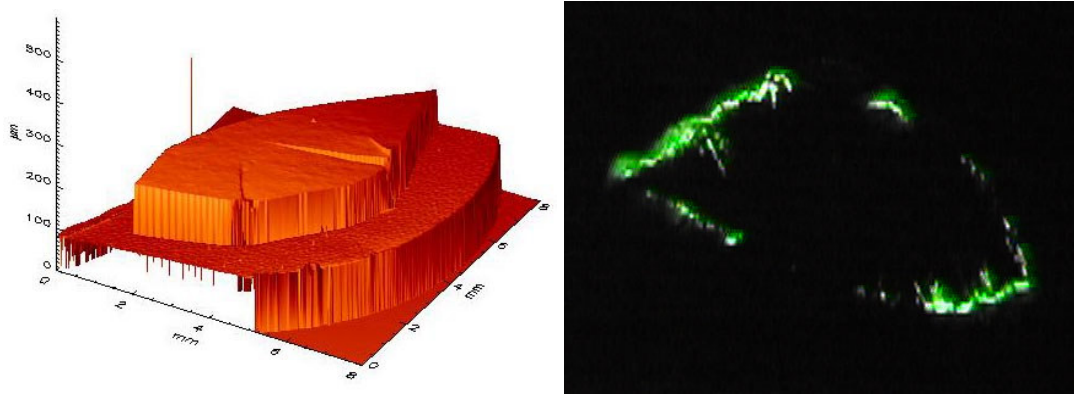


Fig. 4.18. Profile of the of  $27.7 \text{ mm}^2$  convex curved CNT sample from the EPAM membrane JE122 (left) in 3D illustration and (right) corresponding IMLS image, taken in dc mode at  $I = 20 \mu\text{A}$  and  $U = 1270\text{V}$ .

The long CNT at the edges are not shielded, which can be seen in the SEM. Moreover, the geometrical field enhancement there is higher that of single CNT due to additional enhancement at the edges. The emission from the central part is suppressed, resulting low overall emission current. The investigation of the emission from the central part of such a samples in the IMLS can be provided after the destruction of the strong edge emitters either by means of current conditioning or manually.

The integral FN curves of the CNT samples on porous alumina show non-linear dependencies (Fig. 4.19), which can be also influenced by the sample curvature. For the initial curve the integral field enhancement (calculated for  $\Phi = 4.9 \text{ eV}$ ) show two consecutive changes (see slope) from about 1900 to 1000. For the decrease and second increase curves the reproducible  $\beta = 1100, 2100, 1200$  and  $800$  were observed. This values corresponds at maximum to closed MWNT with  $20 \text{ nm}$  diameter and  $21 \mu\text{m}$  length. Similar enormous values were obtained by Bonard et al [32]. In the plane diode configurations the emission current is mainly influenced by rare very long nanotubes with aspect ratio at least 8 times higher than on the CNT generally seen in the SEM images. The activation (adsorbate effects, alignment in electric field, etching of emitter tips etc.) of emitters results in increase of the field enhancement. The partial degradation and destruction of emitters were also observed in the IMLS images, which results in reduction of the integral  $\beta$  (see Chapter 1.6).

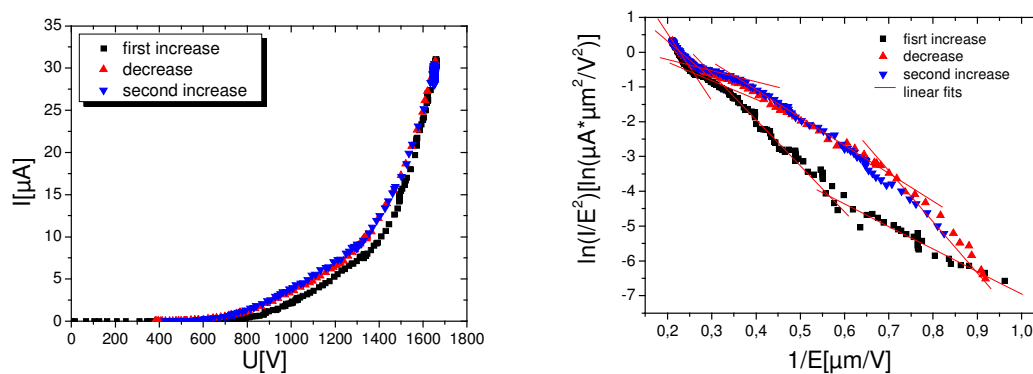


Fig. 4.19.  $I(U)$  curve of the sample JE109 in linear and in FN illustration (current increase – black, decrease-red, second increase - blue).

The onset of the emission from the emitters on porous alumina is usually observed at  $E_{on} \sim 0.5 - 0.8 \text{ V}/\mu\text{m}$ . The responsible emitters should have the field enhancement more than thousand. Such long CNT with most probably opened ends are usually can be found at the edges of the samples. This explain high initial  $\beta$  for the first ascending curve. At higher fields the onset of weak emitters with lower  $\beta$  leads to the reduction of the integral field enhancement. Further increase of the field enhancement can be triggered by the onset of strong emitters in e.g. in the center of the concave curved surface etc. These effects are common for the conditioning and explain the changes of the integral field enhancement at different field levels and the non-reproducibility for the initial ascending and descending curves. Usually, after the conditioning the CNT samples show reproducible I-V curves as shown for decrease and second increase curves in Fig. 4.19. Both enormous field enhancement factors and non-linearity of FN plots are enabled by the curved surface of the samples e.g. additional field enhancement at the edges and non-uniform distribution of the electric field over the sample surface.

The non-linearity of the FN curves was attributed in literature e.g. by Chen et al. to the effects of space charge, resulting from collision and ionisation of residual gas molecules by the emitted electrons [151,152]. The positive ions created are likely to approach the emitting surface and to exert additional electric fields. In order to directly prove the above explanation, two experiments were carried out: the effect of bake-out of the vacuum system and the heating of anode and the effect of varying gas pressures. Baking the system and heating the anode in vacuum improved the linearity of the F-N plot, which prove the nature of FN non-linearity due to conditioning effects. On the other hand, increasing helium pressure made the non-linearity more obvious. Nevertheless, since too many processes are involved, the results from these experiments cannot be considered as direct evidence to support the above view.

#### 4.2.4 FESM studies of CNT on Anodisc®

In order to understand the processes which occurred with single emitters, to investigate their FE parameters and their influence to the total emission current the FESM studies of CNT samples on Anodisc® were provided. The sample JE78-3 was installed into the UHV chamber and scanned with the W anode of  $\varnothing = 20 \mu\text{m}$  at an electrode spacing of  $20 \mu\text{m}$ . The in-situ SEM image of the scanned area (the brightest area in the IMLS images) is presented in Fig. 4.20.

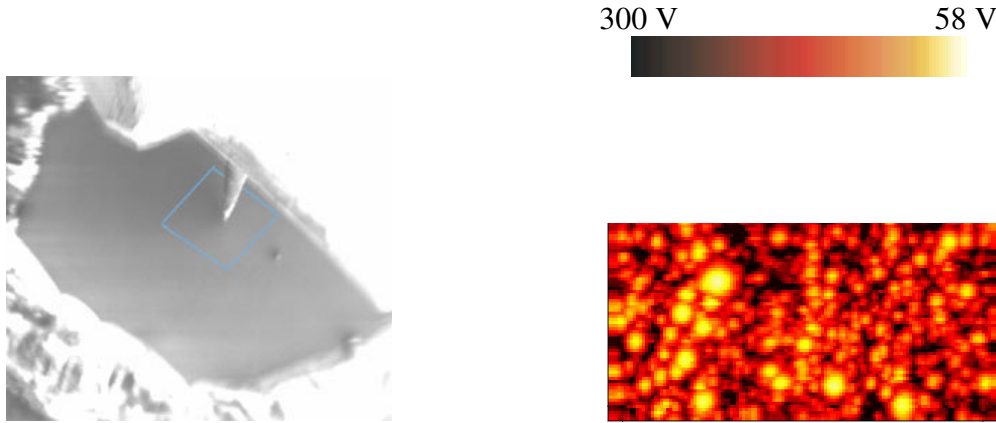


Fig. 4.20. In-situ SEM image of the JE78-3 sample surface with  $20 \mu\text{m}$  W anode above. Marked square is the scanned area of  $1 \times 1 \text{mm}^2$ .

Fig. 4.21. U-map (scan area  $1 \times 0.5 \text{mm}^2$ ) of the sample JE78-3 made by  $20 \mu\text{m}$  W anode at  $20 \mu\text{m}$  electrode spacing for the current of  $I = 10 \text{nA}$  at  $E < 8.8 \text{V}/\mu\text{m}$ .

The sample surface look flat, no scratches or external particles were observed in the scanned region. The corresponding U-map of the marked area of the sample (Fig. 4.20) show the maximum number of emitters at defined field level and is presented in Fig. 4.21. From the scanned area of  $1 \times 0.5 \text{mm}^2$  the emitter density of  $60000/\text{cm}^2$  was calculated for the emission current of  $10 \text{nA}$  at  $E < 8.8 \text{V}/\mu\text{m}$ . This emitter number density leads on average to only 1 emitter per square area of  $41 \times 41 \mu\text{m}^2$ , despite of much higher overall number of CNT  $\sim 10^6/\text{mm}^2$  (Fig. 4.6). Thus, the precise identification of emitters in the SEM images by such unstructured samples is not possible. Following the FN theory, the field enhancement of emitters  $\beta$  should be about 490. By the thickness of the emitting CNT  $\sim 20 \text{nm}$ , using conducting cylinder model their length should be in order of  $4.9 \mu\text{m}$ . Such a long CNT were not found on the SEM images probably due to two main reasons: (i) the sub  $100\text{-nm}$  SEM imaging does not allow the identification of  $\mu\text{m}$  long CNT, (ii) the layer of mixed CNT and alumina particles prevent their identification. Moreover, such an emitters should be perpendicular to the sample surface to reveal high  $\beta$ , which is also complicate their identification. For the opened CNT the estimated length reduced to more reasonable value of about  $3.3 \mu\text{m}$ , which were, however, not detected in the SEM images too.

The corresponding I-maps of the sample JE78-3 reveal the strongest emitters from that area and additionally show the variations of the onset fields of emitters. The emitter number

densities were 7500, 45000 and 55000/cm<sup>2</sup> at 3.5, 5.9 and 7.7 V/μm respectively, which also corresponds to the IMLS results (Fig. 4.22).

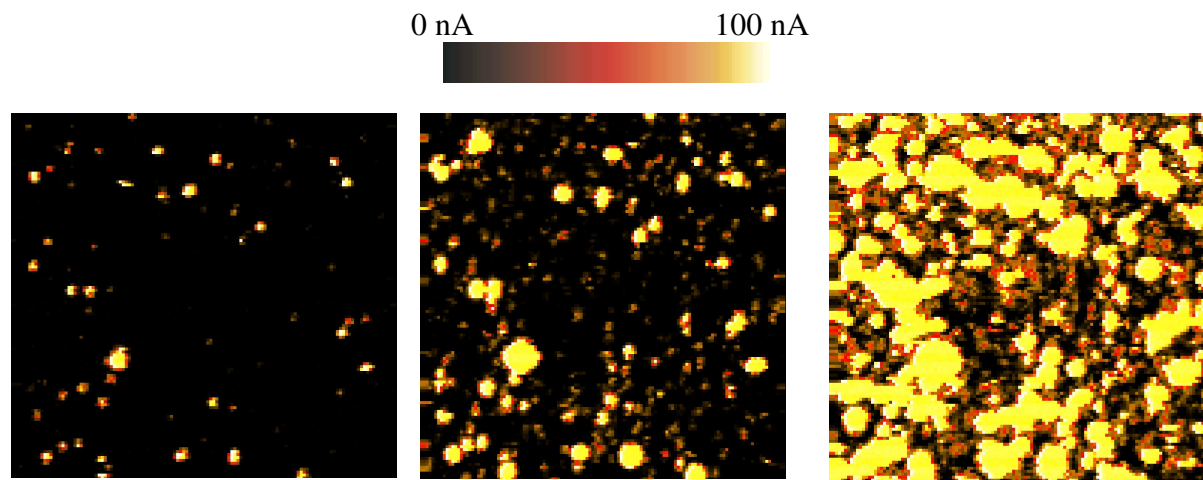


Fig. 4.22. I-maps of the 1 x 1 mm<sup>2</sup> scanned area of the sample JE78-3 made with  $\varnothing = 20 \mu\text{m}$  W anode at 20 μm electrode spacing for the current up to 100 nA at the voltages (a)  $U = 120 \text{ V}$  (b)  $U = 200 \text{ V}$  (c)  $U = 260 \text{ V}$ .

During the I-scans the emitters are often conditioned due to influence of the higher currents in comparison to U-scans. Such an effects are common for cold cathode materials [38,109] and can be used for improvement of the emission stability and/or homogeneity (see Chapter 4.2.8).

In order to measure the FE parameters of single emitters, local measurements for CNT on Anodisc® JE78-3 were made. In summary 30 random emitters were investigated. The Fig. 4.23. show the overview of the exemplary I-V curves of the investigated emitters in FN illustration. The graphs shows the changes of the emission current during ascending and descending voltage cycles. The emitters were tested up to  $I_{\text{max}} = 8.6 \mu\text{A}$ . Most of them, however, show strong instabilities at  $I < 1 \mu\text{A}$  and were not measured for higher currents. Most of the emitters (93%) reveal instabilities, which lead to the activation or degradation/destruction effects, which also corresponds to the IMLS investigations where flickering of emitters and their permanent activation/degradation were observed. The emitters #1-5 in Fig. 4.23 show the improvement of the emission by currents of 0.6 - 1.6 μA, however the form of the activation is different. While emitters #1 and #2 after the first increase reveal reproducibly improved curves, emitters #3-5 reveal strong fluctuations in the same current region, when the jumps between current levels were observed. The improvement corresponds to the increase of the emission current which is caused rather by changing of the geometry and/or effective emission area  $S$ . While the first effect can be explained by alignment of the CNT in electric field, the other is caused by adsorbate effects. In most of the instability cases ~ 60%, however, the degradation or destruction of emitters occurred (Fig. 4.23 (emitters #6-10)), which represents their partial damage. In a few cases the destruction of the emitters was observed in the first current increase already at  $I \sim 100 \text{ nA}$ . One should notice, that after the activation or degradation most of the emitters are located on the stable level and thus show the

reproducible I-V curves with changed  $\beta$ . In order to reach higher stability of the emission the CNT on porous alumina should be conditioned at high currents. Only few (7%) emitters like #11 or #12 showed reproducibly stable emission.

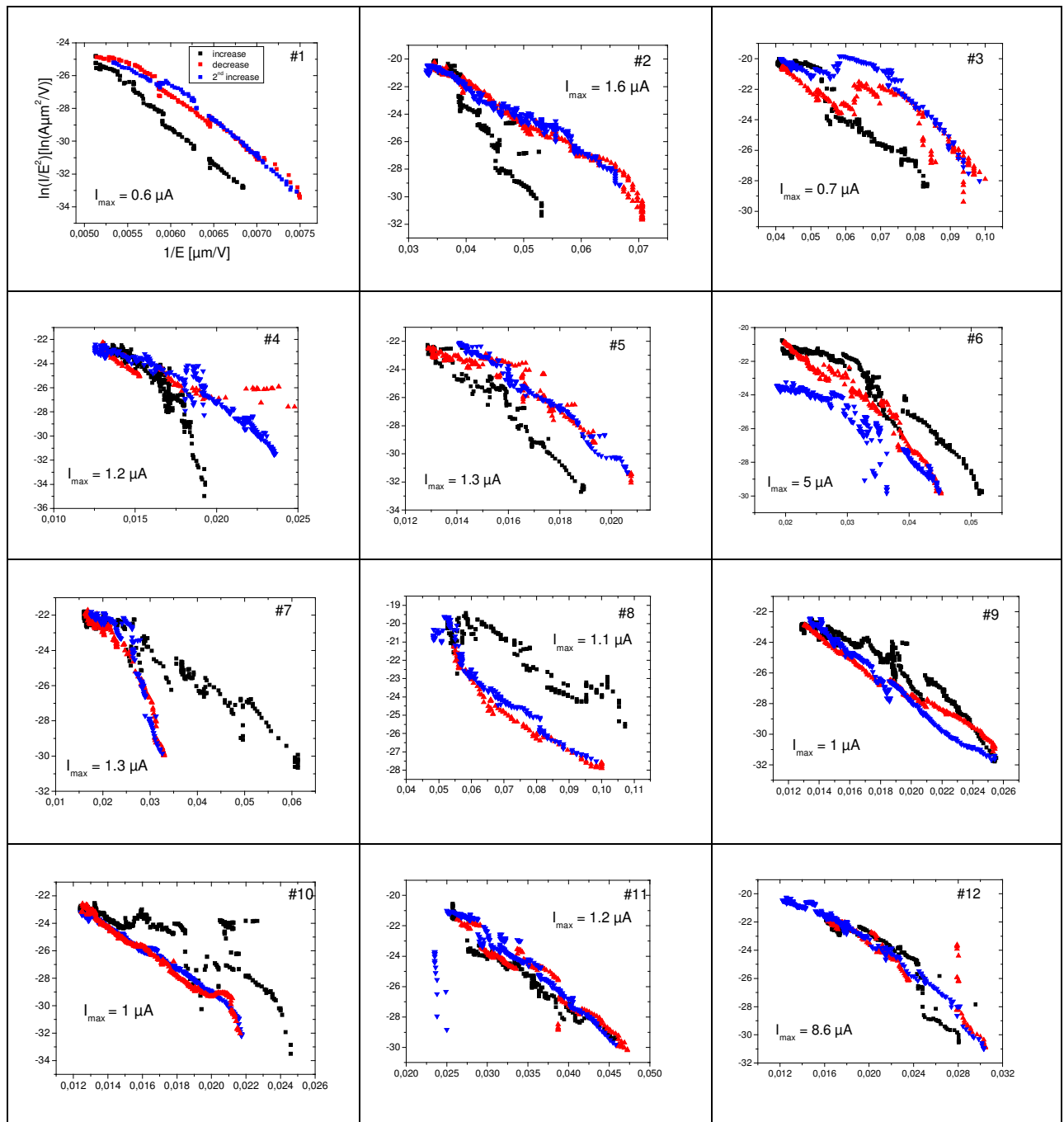


Fig. 4.23. I(U) curves of 12 random emitters of the sample JE78-3 in FN illustration (first current increase – black squares, decrease - red triangles ( $\Delta$ ) and second increase – blue triangles ( $\nabla$ )). All emitters were investigated with  $\sim 20 \mu\text{m W}$  anode at the distance of  $6 \mu\text{m}$  up to maximum current  $I_{\text{max}}$ .

Emitter #12 can survive the current of  $8.6 \mu\text{A}$ , while the emitter #11 shows degradation in the second current increase at  $1.2 \mu\text{A}$ . Investigations of the surface by means of in-situ SEM reveal no changes of the surface morphology in the  $\mu\text{m}$  range, which is common for e.g. the vacuum breakdowns. However, due to non structured surface, the evidence of the structural

damage of the emitters can not be directly proved for this material. One should notice, that the percentage statistic based on the investigation of 30 emitters have, unfortunately, high error. More realistic values can be obtained by the investigation of the processing effects of emitters in the IMLS images by means of AnalySIS® software (see Chapter 4.2.8).

From the slope of the FN curves the field enhancement factors for the work function  $\Phi = 4.9$  eV were calculated. The Fig. 4.24. shows the initial (first increase) and final (second increase)  $\beta$  values as a function of the extraction field for the current of 1 nA in linear and inversely. The onset field vary from 8 to 32.5 V/ $\mu\text{m}$ , thus both strong and weak emitters are presented in the graphs. The  $\beta$  values are between 15 and 870 and reveal the inverse dependence on the onset field (Fig. 4.24(left)).

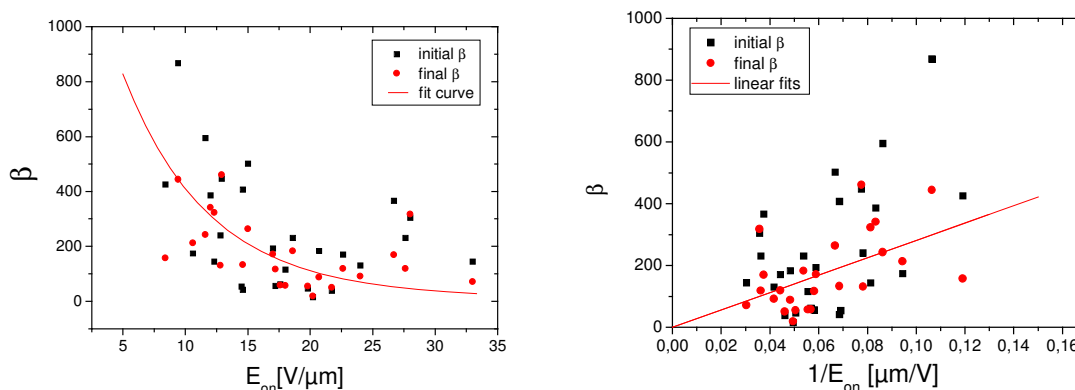


Fig. 4.24. Field enhancement factors  $\beta$  calculated for the ascending voltage of the single emitters of the sample JE78-3 as a function of extraction field for the current of 1 nA in linear (left) and inversely (right). The  $E_{\text{on}}$  was calculated for the 20  $\mu\text{m}$  W anode and the electrode spacing of 6  $\mu\text{m}$ .

More than 50% of emitters reveal  $\beta$  values below 200, moreover, 30% below 50, which correspond to the large number of the short (or shielded) CNT on Anodisc®. The illustration of  $\beta$  as a function of  $1/E$  (1nA) (Fig. 4.24(right)) reflect a scattering of emission strength by S-effects. The initial (final)  $\beta$  shows the deviation up to factor 3 (2) from the linear fit curves, which are in this case coincide for initial and final voltage cycles. For the ideal closed MWNT of  $\varnothing = 20$  nm the effective S should be in the order of the tip area  $\sim \pi \times 10^{-12}$   $\text{cm}^2$ . Calculation of the S factors for emitters on the linear fit curve show the values in the range of  $1 \div 3 \times 10^{-12}$   $\text{cm}^2$ . For the strongest emitter with  $\beta = 870$  the effective emission area was  $S = 6 \times 10^{-14}$   $\text{cm}^2$ , which reflect the CNT with opened tip. Due to unstructured surface the identification of these emitters in the ex-situ SEM is not possible. For the emitters with  $\beta \sim 50$  and onset field  $E = 14\text{-}15$  V/ $\mu\text{m}$  the calculated effective emission area was in order of  $10^{-10}$   $\text{cm}^2$ , which shows that  $\varnothing = 20$   $\mu\text{m}$  W anode extract the current from several emitters. The same effect was observed for densely packed MWCVD grown CNT.

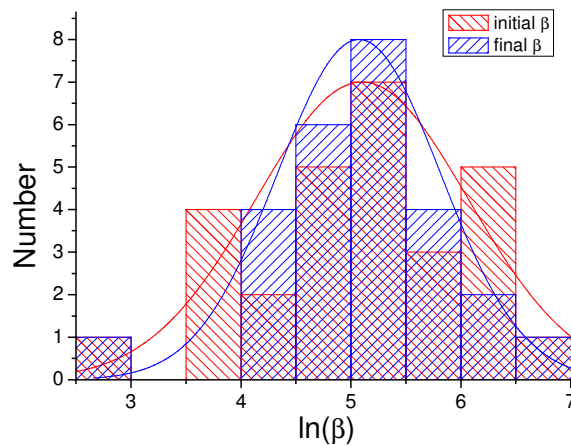


Fig. 4.25. Histogram and fitted Gaussian distributions (red line: initial, blue line: final) of  $\beta$  values obtained for 30 emission sites from FN curves. The mean values of  $\beta$  are about 200.

The corresponding histogram in Fig. 4.25 shows the changes of field enhancement during initial and final voltage cycles. The Gaussian fit for final field enhancement is narrower, which corresponds to the degradation of the strongest emitters ( $\beta > 400$ ) and activation of the weakest ( $\beta < 50$ ). This results in improved homogeneity of the emission by the samples conditioned at high currents. Both fits for initial and final voltage cycles show the mean values of  $\beta \sim 200$ . Comparison of the obtained field enhancement factors from the local measurements and the emitter distribution from the U-scan shows that only 2 from 30 found emitters are able to produce 1 nA current at  $E < 10$  V/ $\mu\text{m}$ . Thus, the number of emitters can be up to two orders of magnitude lower than the number of CNT on the surface (Fig. 4.6).

The comparison of the field enhancements of the emitters on Anodisc® with the dense MWCVD grown CNT (Fig. 4.4) shows similar values of  $E_{\text{on}}$  between 12 - 21 V/ $\mu\text{m}$ . The emitters on Anodisc® samples can be divided by strength into four different groups:

- (a) Emitters with  $\beta < 50$  and onset field  $15 < E_{\text{on}} < 20$  V/ $\mu\text{m}$ . These are the short shielded CNT which grow from the pores and have comparable lengths of  $\sim 200$  nm.
- (b) Emitters with  $50 < \beta < 200$  and onset field  $10 < E_{\text{on}} < 25$  V/ $\mu\text{m}$ . Such a field enhancements corresponds to the densely packed (shielded) CNT.
- (c) Emitters with  $200 < \beta < 500$  and onset field  $10 < E_{\text{on}} < 15$  V/ $\mu\text{m}$ . Such a field enhancement corresponds to up to some  $\mu\text{m}$  long free standing CNT.
- (d) Emitters with  $\beta > 500$  and onset field  $E_{\text{on}} < 10$  V/ $\mu\text{m}$ . Such rare, most probably opened CNT, are the main electron emitters on the porous alumina based FE cathodes. In particular they are registered by the luminescent screen of the IMLS as a strongest emitters.

Decreasing of the pore diameters of the porous alumina and their partial opening possibly reduce the density of emitters of the (a) and (b) groups, which results in the increase of the mean field enhancement factor and decrease the onset field.

#### 4.2.5 Influence of the pore diameter on the current density

As it was already mentioned in Chapter 4.2.2 for the EPAM the surface morphology is different on their opposite sides. One side have the fully opened pores (f-side) and another – partially (p-side) often with smaller spread pores. The main advantage of these substrates is the possibility of variation of their thickness and pore diameter. In all experiments the side with fully opened pores was exposed towards the gas flow. For the measurements the templates were broken into pieces 8 - 35 mm<sup>2</sup> and their both sides were tested in the IMLS. The EPAM are also generally thicker than Anodisc®, thus not so flexible. Most of the samples showed convex or concave geometries which can not be changed during the preparation, thus the sample curvature has been taken into account for the calculation of the electric field. For all samples the identical deposition of alumina particles was provided. The real pore diameter is not equal to the theoretically predicted. The deviations up to 50 % were observed due to not full control of the etching process during the membrane fabrication. The main FE properties of the investigated CNT samples on EPAM are presented in the Tab. 4.5. Similar to the Anodisc® samples the main limitation factor at high fields is the discharge

Sample name	Sample area [mm <sup>2</sup> ]	Config. of pores	Pore diameter [nm]		E <sub>on</sub> [V/μm] (1nA)	N/cm <sup>2</sup> at E=3V/μm	j [μA/cm <sup>2</sup> ] at E=3V/μm	N <sub>max</sub> /cm <sup>2</sup>	j <sub>max</sub> [μA/cm <sup>2</sup> ]	E <sub>maxeff</sub> [V/μm]
			Nom.	Real						
JE98	10	f,I	200	n.m.	1.4	n.m.	300	5000	2900	5.5
JE102	8	f,I	40	55-65	0.7	700	210	6000	800	4
JE103	31	f,I	100	33-50	2.2	n.m.	17	10000	32000	7.2
	11	p,O	-	n.m.	1.1	n.m.	110	750	200	3.6
JE120	13	f,I	52	60-70	1.8	200	110	1500	750	4.1
	7.5	p,O	-	38-55	1.5	215	310	420	360	3.1
JE122	14.7	f,I	65	22-35	1.3	390	62	2000	4000	4
	27.7	p,O	-	n.m.	0.8	250	10	500	70	5.3
JE123	22.4	f,I	65	22-35	0.6	400	313	>7000	12000	5.5
	24	p,O	-	19-25	0.7	180	250	>7000	83000	7
JE124	34.6	f,I	105	57-65	0.9	410	165	600	300	3.6
	12.5	p,O	-	23-39	0.7	150	72*	200	120	4

Tab. 4.5. Integral FE properties of the CNT samples on EPAM. The 3<sup>rd</sup> column shows that the sample have fully (f) or partially (p) opened pores and was the side gas-inlet (I) or –outlet (O) in the MOCVD. The nominal (estimated by the etching voltage) and the real (measured with the SEM) pore diameters are presented in the 4<sup>th</sup> column (n.m. means not measured). For each sample the initial emitter number (N) and dc current densities (j) at E = 3V/μm are compared to the final values at the maximum achieved field (E<sub>maxeff</sub>) after processing. (\*) For the sample JE124 only strong edge emission was observed.



occurrence. However, CNT samples on EPAM reveal higher current carrying capability, thus allow to achieve higher current densities.

The sample JE98, is the reproduction of the JE78-3 Anodisc® serie, but on basis of the EPAM with the same pore diameter and thickness. The sample showed comparable homogeneity of the emission, but lower emitter number density of about 5000/cm<sup>2</sup> at 5.5 V/μm. The onset of the emission for I = 1 nA was at E = 1.4 V/μm, which is higher than for Anodisc® too. For the next samples the pore diameters were drastically decreased. The idea is that the large 200 nm pores are mainly responsible for the growth of the large number of short nanotubes building up the shielded layer, which is not suitable for the enhanced FE. By the EPAM samples which have the smaller than 200 nm pores up to several μm long CNT were seen apart the sample surface mainly attached to the alumina clusters (Fig. 4.26). The influence of the mutual shielding of emitters, which is one of the main parameters reducing the FE current, is smaller for the configurations, where the CNT on the surface are spread. The mean distance between CNT bundles for JE103(f) is about 5 μm resulting in 4 × 10<sup>4</sup> potential emitters per mm<sup>2</sup> (Fig. 4.26), which is two orders of magnitude lower than for Anodisc®. However, this sample showed in the IMLS more than 10000 emitters/cm<sup>2</sup> in the brightest region of the emitting area at E = 7.2 V/μm, which is record resolved in the IMLS emitter number density for porous alumina samples (Fig. 4.27).

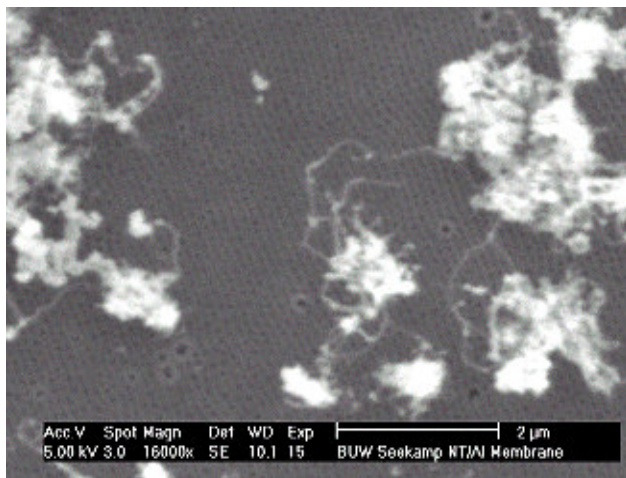


Fig. 4.26. SEM image of the f-side of JE103. The pore on the have  $\varnothing = 33\text{-}50$  nm. The CNT are attached to the alumina clusters and have up to 2 μm length.

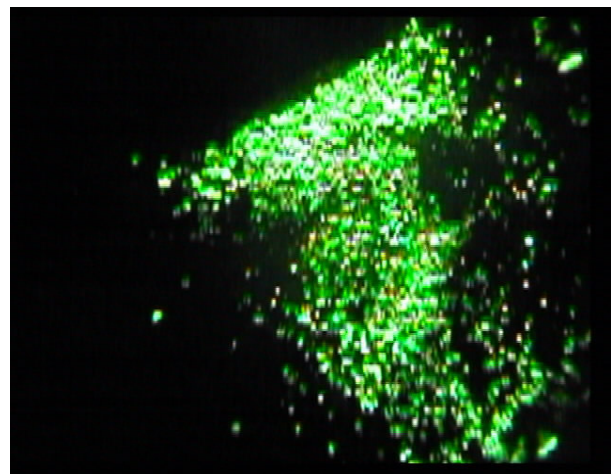


Fig. 4.27. IMLS image of the emission from the sample JE103(F,I) at E = 7.2 V/μm. The maximum emitter number density is ~ 10000/cm<sup>2</sup> in the brightest region.

Opposite side of the sample with partially opened pores, however, showed much lower emitter number density due to strong edge emission at the corresponding concave geometry with  $\Delta Z_{\text{max}} = 175$  μm. At such a values of height difference the IMLS can resolve only the edge emission.

In comparison to Anodisc® the sample JE98 reveal the lower current density of 0.5 mA/cm<sup>2</sup> at E = 3 V/μm. However, the maximum current density of 2.9 mA/cm<sup>2</sup> at E = 5.5 V/μm was higher, than obtained for the commercial membranes. The sample JE103 reveals

even higher current carrying capability. The current density of  $32 \text{ mA/cm}^2$  was reproducibly achieved from the  $28 \text{ mm}^2$  sample at  $E = 7.2 \text{ V}/\mu\text{m}$  (Fig. 4.28(left)).

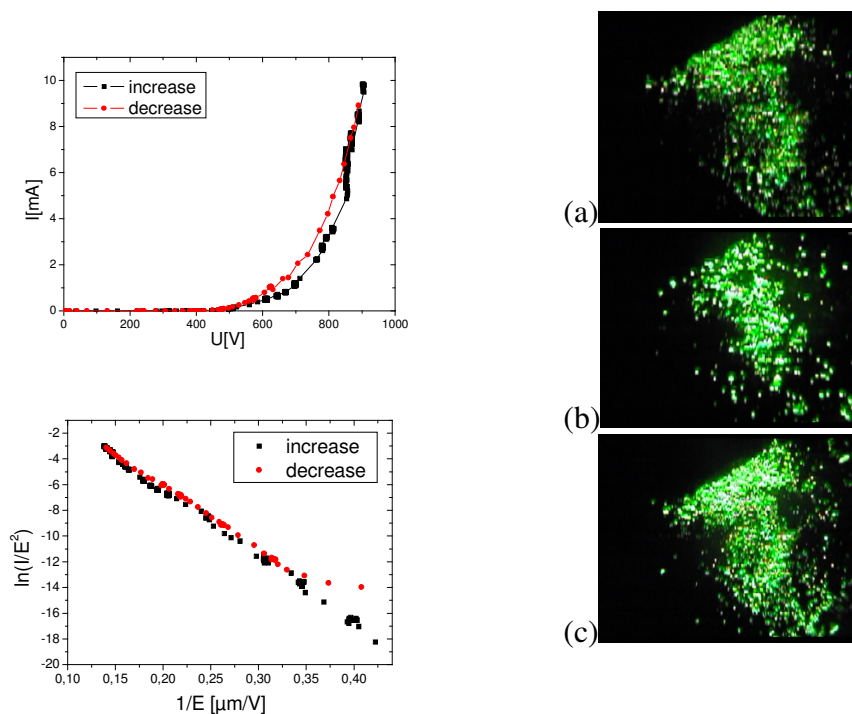


Fig. 4.28. Integrally measured  $I(U)$  curve of the sample JE103 in linear (top left) and FN (bottom left) illustrations (increase – black squares, decrease – red circles) with corresponding IMLS images taken at (a)  $I = 3 \text{ mA}$  ( $U = 280 \text{ V}$ ), (b)  $I = 7 \text{ mA}$  ( $U = 860 \text{ V}$ ) and (c)  $I = 10 \text{ mA}$  ( $U = 900 \text{ V}$ ). The electrode spacing  $\Delta z = 125 \mu\text{m}$ .

Due to convex geometry of the sample the electric field is lower at the edges, thus reduced number of emitters was observed there (Fig. 4.28(right)). The corresponding FN plot shows reproducible linearity by current increase and decrease, which show good current stability of the CNT on EPAM. High current densities were obtained also from the sample JE123. The side with average pore diameter of  $\sim 28 \text{ nm}$  (JE123(f, I) in Tab. 4.5) reveal the integral current density up to  $12 \text{ mA/cm}^2$  at  $E_{\text{eff}} = 5.5 \text{ V}/\mu\text{m}$  (Fig. 4.29). The emission was non-uniform due to the convex curvature of the sample. Converted IMLS images show, that the brightest emission area of  $1 \text{ mm}^2$  (Fig. 4.29(top right)) provides up to 8% of the total current.

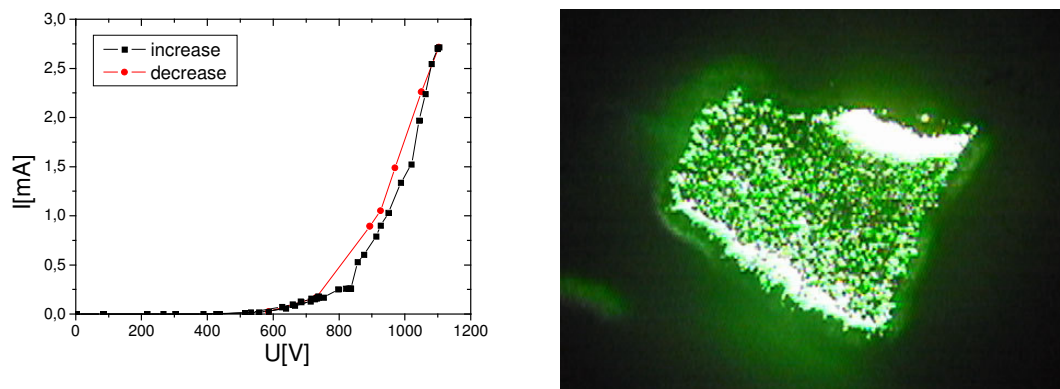


Fig. 4.29.  $I(U)$  curve of the sample JE123(f, I) and corresponding IMLS image taken at maximum voltage of  $U = 1090 \text{ V}$  and  $I = 2.7 \text{ mA}$  ( $\Delta z = 200 \mu\text{m}$ ).

At such a values the sensitive luminescent screen damages quickly, thus the emission current together with the emission homogeneity (imaging) can be measured only over several seconds. At  $E = 3 \text{ V}/\mu\text{m}$  the sample JE123 (f,I) showed slightly higher current density than the opposite side. However, at  $E = 5.5 \text{ V}/\mu\text{m}$  the sample JE123(p,O) provide  $37 \text{ mA}/\text{cm}^2$  and at  $E_{\text{eff}} = 7 \text{ V}/\mu\text{m}$  the highest current density of about  $83 \text{ mA}/\text{cm}^2$  (Fig. 4.30), which was achieved for the CNT samples on porous alumina in dc mode. Thus, the maximum current carrying capability of the p-side of the sample was factor 7 higher than for the f-side. Comparing the IMLS results of the best CNT samples on EPAM, the highest current density was achieved for the sample with the smallest pore diameter.

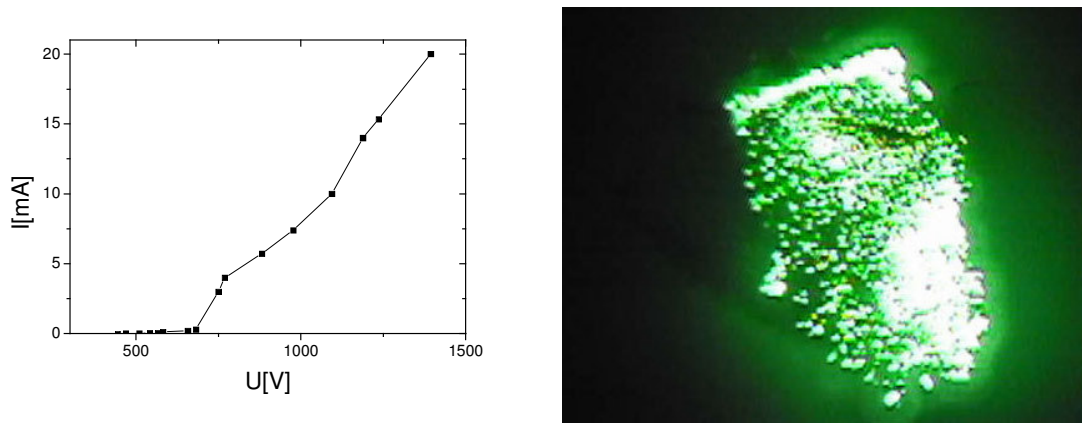


Fig. 4.30. I(U) curve of the sample JE123(p,O) and the corresponding IMLS image taken at maximum voltage of  $U = 1400 \text{ V}$  and  $I = 20 \text{ mA}$  ( $\Delta z = 200 \mu\text{m}$ ).

The CNT grow from the pores which are in the vicinity of the alumina clusters. Obviously, from a  $\sim 20 \text{ nm}$  pore only one CNT with the same diameter can grow. The pore diameters on the porous alumina are not precisely constant and show the deviation from the average value up to  $7 \text{ nm}$ . In order to investigate the influence of the pore diameter on the FE the current densities from CNT on all EPAM and one Anodisc® JE109 were compared at  $E = 4 \text{ V}/\mu\text{m}$ , since not all samples reached higher fields (Fig. 4.31). In order to decrease the current fluctuations and the influence of the strong emitters, the samples were conditioned over several hours to reach good current stability. Strong correlation of the current densities and pore diameters was observed (Fig. 4.31). The resulting maximum current density was extracted from the samples with the average pore diameter of  $\sim 22 \text{ nm}$  (JE122,123). The achievable current density decreases with the pore diameter and at about  $60 \text{ nm}$  reaches its minimum. Further increase of the pore diameter up to  $200 \text{ nm}$  does not significantly influence the current density. At this field level the samples showed the current density of about  $0.5 \text{ mA}/\text{cm}^2$  (JE98 and JE109).

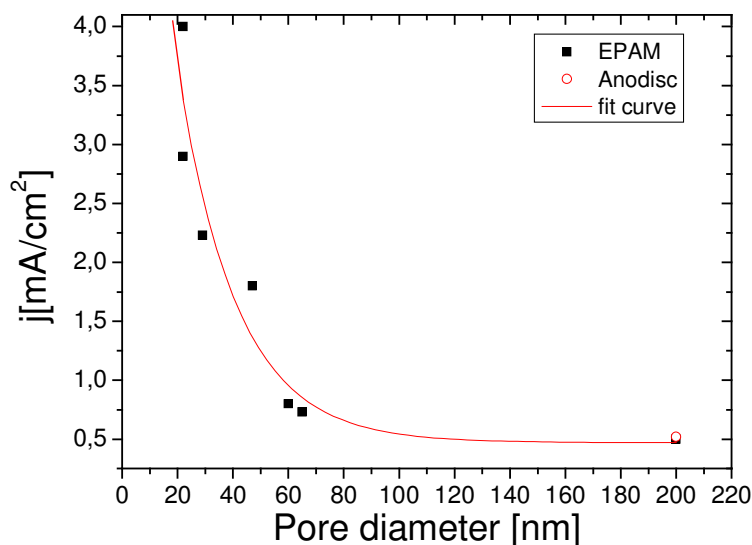


Fig. 4.31. Influence of the pore diameter on the current density from CNT samples on EPAM (black squares) and one Anodisc® (red ring). The results were compared for  $E = 4 \text{ V}/\mu\text{m}$ .

Estimation of the current carrying capabilities for other Anodisc® samples showed, that their current densities are higher than for JE109 at  $E = 4 \text{ V}/\mu\text{m}$ . Nevertheless, the virgin Anodisc® samples show after several hours up to by 60% decreased current values. One can expect that current densities for conditioned Anodisc® samples are far below  $1 \text{ mA}/\text{cm}^2$ . For the samples with pore  $\varnothing < 20 \text{ nm}$  the obtained current density should be poor similar to JE116 (p,I) due to the shielding effect (see Chapter 4.2.2). Thus, the optimum pore diameters for the extraction of high current densities are in a range of 20 - 40 nm.

Thus, the beneficial for FE pore configuration of the EPAM JE123(p,O) is shown in Fig. 4.32, where the partial opening of the pores leads to the decreased density of the CNT on the surface, thus reduction of the shielding effect.

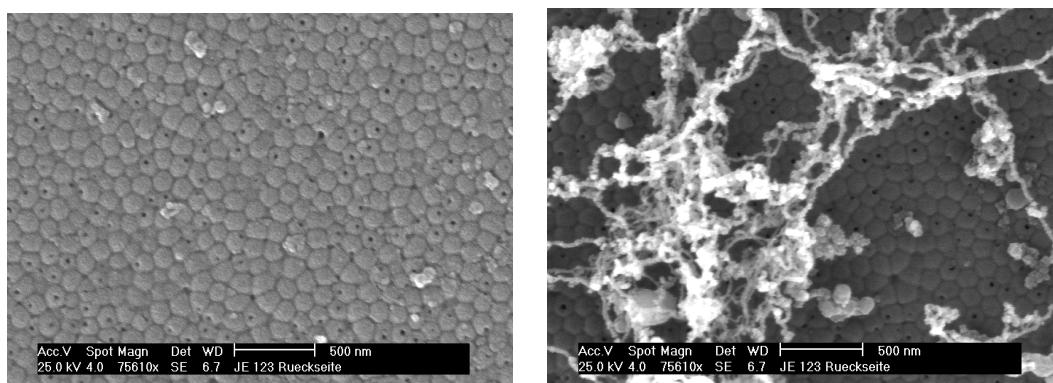


Fig. 4.32. SEM images of the sample JE123 (p,O) with  $\varnothing \sim 22 \text{ nm}$  spread pores before (left) and after (right) the MOCVD process. The mean distance between the pores is about 250 nm.

It is well known that the bundles of nanotubes show higher stability and current carrying capability than the single CNT [153]. The interweaving network of the CNT, found on the sample surface, additionally increase the stability of the emitters, which consist of several nanotubes (see Chapter 4.2.9).

#### 4.2.6 FESM studies of CNT on EPAM

In order to clarify the role in FE of full or partial opening of the pores and the influence of the exposure towards gas inlet flow in the MOCVD process the FESM studies were provided on the EPAM JE123 and JE103 respectively. At first, the side of the JE103, which was covered with alumina particles was used as inlet side for the gas flow in the MOCVD process (Tab. 4.5). Both inlet (I) and outlet (O) sides of the JE103 were scanned in

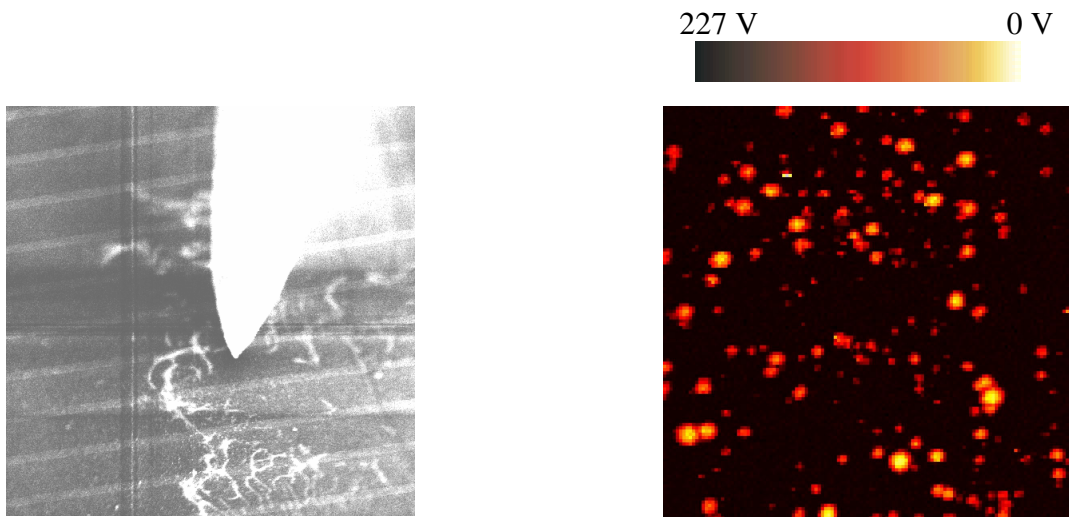


Fig. 4.33. SEM image of the JE103(I) sample surface covered with some alumina particles with  $\varnothing = 12 \mu\text{m}$  W anode above.

Fig. 4.34. U-map (scan area  $1 \times 1 \text{ mm}^2$ ) of the sample JE103(I) made with  $12 \mu\text{m}$  W anode at  $14 \mu\text{m}$  electrode spacing for the current of 1 nA. The resulting emitter number density is  $\sim 24000/\text{cm}^2$  at  $E < 12 \text{ V}/\mu\text{m}$ .

FESM with  $\varnothing = 12 \mu\text{m}$  W anode. The in-situ SEM image show that the JE103(I) sample surface is covered with the large alumina particles (Fig. 4.33). The calculated emitter number density from the U-maps of the area  $1 \times 1 \text{ mm}^2$  of JE103 (I) for the current  $I = 1 \text{ nA}$  was  $24000/\text{cm}^2$  at  $E < 12 \text{ V}/\mu\text{m}$  (Fig. 4.34). This value is higher than is obtained from the IMLS images due to higher electric field. In comparison, the O-part (Fig. 4.35) reveal higher number of emitters  $\sim 39000/\text{cm}^2$  than I-part (Fig. 4.36) at about the same electric field of  $11.5 \text{ V}/\mu\text{m}$ . Due to the concavity the scan was made only for  $300 \times 300 \mu\text{m}^2$  area.

Since there is a significant difference in FE properties between the I- and O-sides of the EPAM, the local measurements on the JE103 were made separately for both sides. In summary, 40 emitters were investigated on the I- and O-sides of the JE103, by means of the W anode of the  $\varnothing = 10 \mu\text{m}$  at electrode spacings of 6 -  $10 \mu\text{m}$ . The voltage in each of these measurements was increased until the strong instabilities were observed.

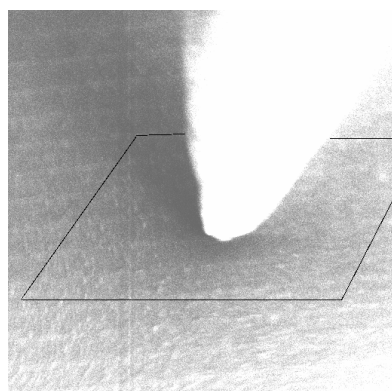


Fig. 4.35. SEM image of the JE103(O) sample surface with the 12  $\mu\text{m}$  W anode above.

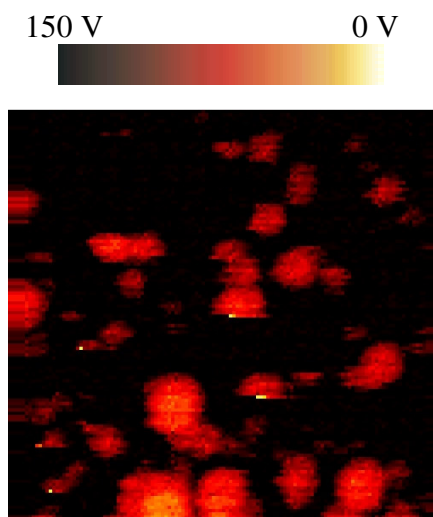


Fig. 4.36. U-map (scan area  $0.3 \times 0.3 \text{ mm}^2$ ) of the sample JE103 (O) made by 20  $\mu\text{m}$  W anode at 10  $\mu\text{m}$  electrode spacing at the 1 nA current. The resulting emitter number density is  $\sim 39000/\text{cm}^2$  at  $E < 11.5 \text{ V}/\mu\text{m}$ .

About 85% of the random CNT emitters on JE103 I-side showed instabilities, including 50% which are degraded and 35% destroyed during current increases. No activation of the emitters was observed. Emitters #1-4 in Fig. 4.37 show the degradation of the emission at  $I = 5 \mu\text{A}$  and further reproducible currents up to  $I_{\text{max}} = 6.8 \mu\text{A}$ . Part of the emitters was degraded (e.g. emitter 4) at the currents  $< 1 \mu\text{A}$ . However, in all cases, as it was already mentioned for Anodisc® samples, the reproducibly stable curves were obtained after the initial processing. About 15% of emitters reveal the stability in the current range of 1  $\mu\text{A}$ .

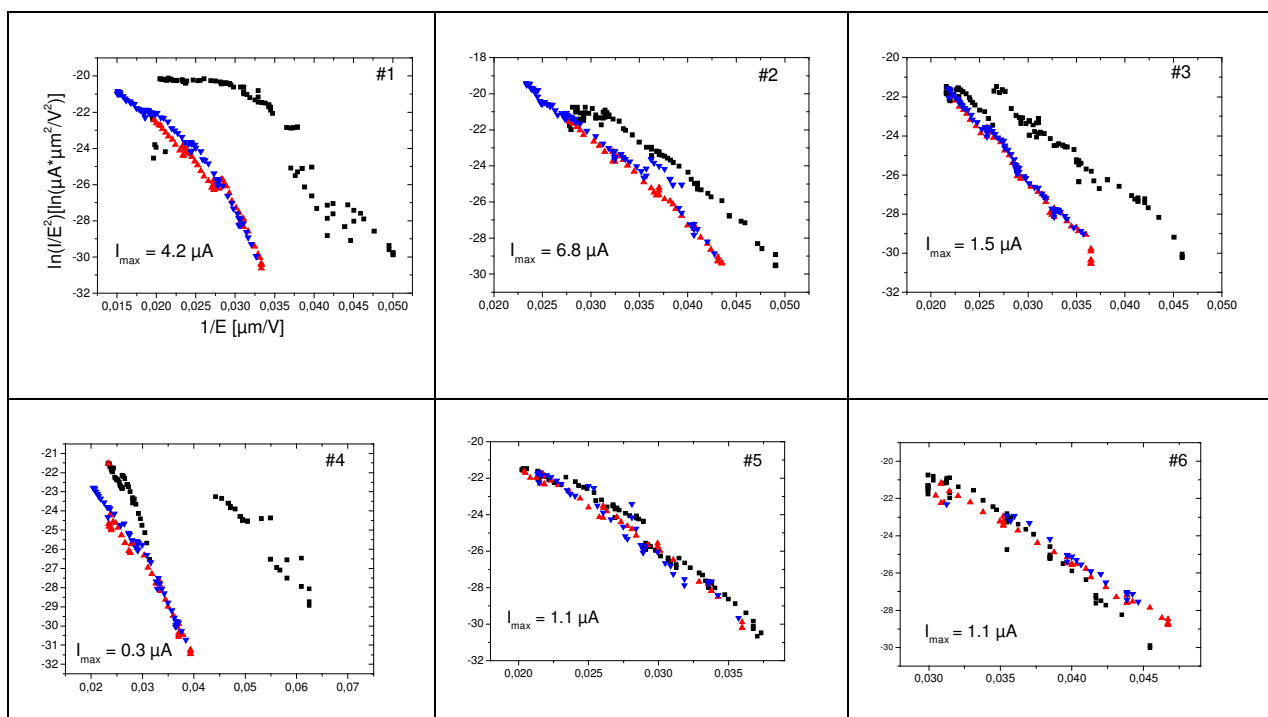


Fig. 4.37. I(U) curves of 6 random emitters of the sample JE103(I) in FN illustration. The first current increase – black squares, decrease - red triangles ( $\Delta$ ) and second increase – blue triangles ( $\nabla$ ). All emitters were investigated with  $\varnothing = 10 \mu\text{m}$  W anode at the distance of 6  $\mu\text{m}$  up to maximum current  $I_{\text{max}}$ .

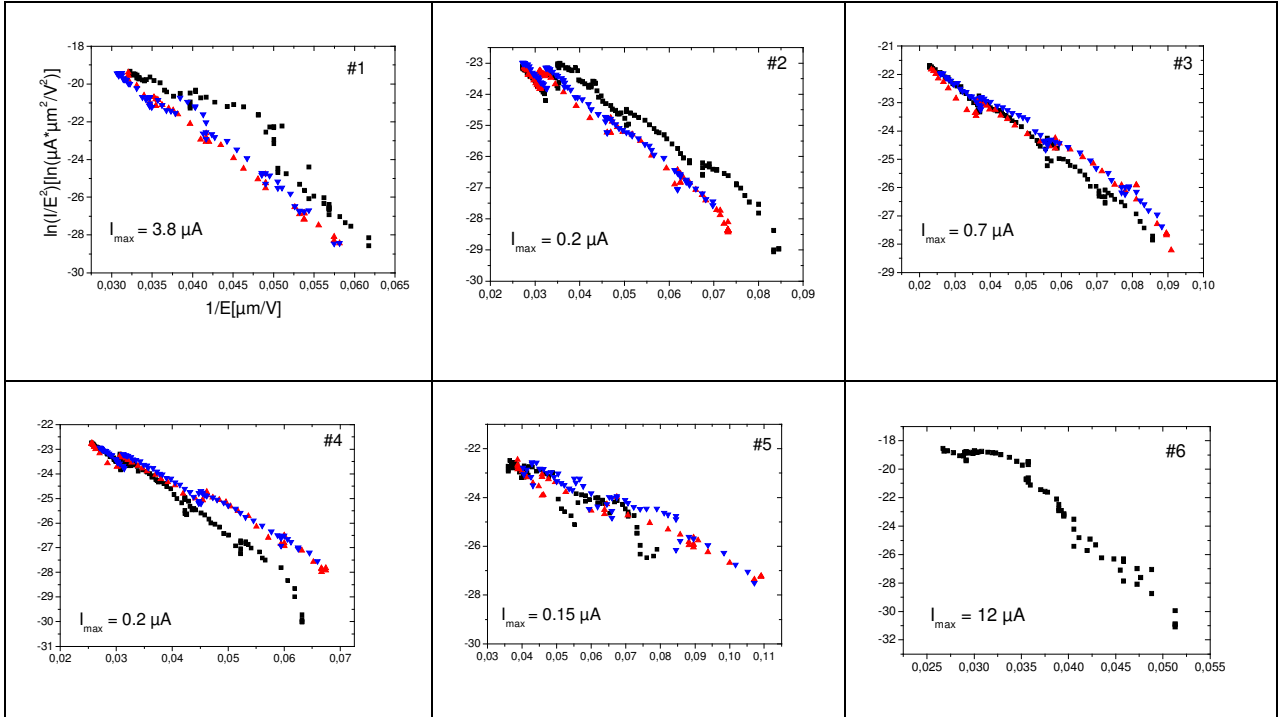


Fig. 4.38.  $I(U)$  curves of 6 random emitters of the sample JE103(O) in FN illustration. The first current increase – black squares, decrease - red triangles ( $\Delta$ ) and second increase – blue triangles ( $\nabla$ ). All emitters were investigated with  $\varnothing = 10 \mu\text{m}$  W anode at the distance of  $6 \mu\text{m}$ .

Similarly about 80% of the 20 investigated random emitters on the O-side of the sample JE103 showed instabilities. However, not only destruction of emitters (50%) or their degradation (10%) at the current range  $< 1 \mu\text{A}$  were observed (e.g. emitters #1 and #2 in Fig. 4.38). About 20% of emitters reveal activation (emitters #3 and #4) at different maximum currents  $0.2 - 4.5 \mu\text{A}$ . The stability was observed at the emission currents of  $1 \mu\text{A}$  for about 20% of emitters. The maximum emission current per emitter was  $12 \mu\text{A}$ , which, however, lead to its destruction (e.g. emitter #6).

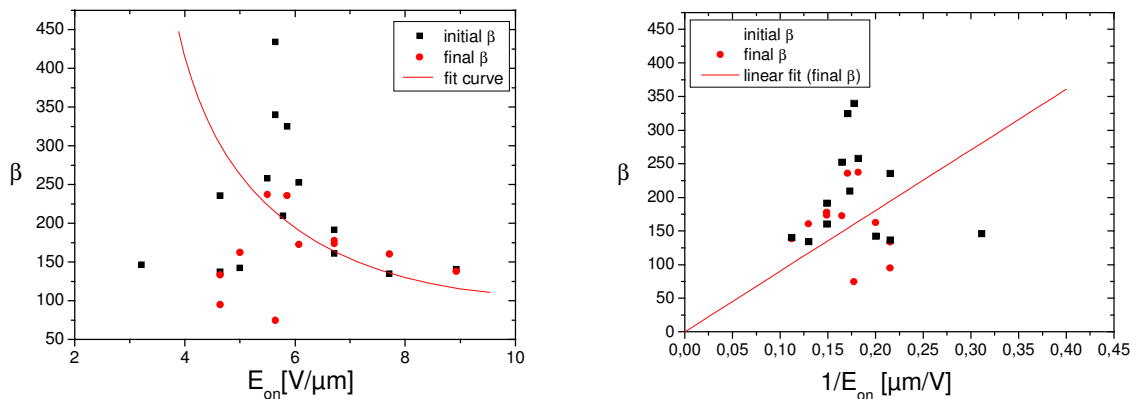


Fig. 4.39. Field enhancement factors  $\beta$  calculated for the initial (black) and final (red) voltage increases of the single CNT emitters on JE103(I) as a function of extraction field for the current of  $1 \text{ nA}$  in linear (left) and inverse dependence (right).

The  $\beta$  of the emitters of the sample JE103(I), calculated for  $\Phi = 4.9$  eV, lay below 500 with the onset fields  $E_{\text{on}} < 10$  V/ $\mu\text{m}$  (Fig. 4.39). The  $\beta$  distribution show the peak value of 450 at lower, than for the strongest CNT emitters on the Anodisc®, onset field of  $E_{\text{on}} = 6$  V/ $\mu\text{m}$ . The difference between the initial and conditioned (final)  $\beta$ , show the influence of the processing effects on the field enhancement, thus the evolution of the emitters. The  $\beta$  shows strong deviation from the inverse dependence on the onset field due to clear S-effects (see Chapter 4.2.4), which explain e.g. low onset field for the emitters with low field enhancement.

As for the emitters on the O-side the strongest emitters were observed at the  $E_{\text{on}} < 10$  V/ $\mu\text{m}$ . The  $\beta$  values show the hyperbola like dependence on the onset field, however, absolute values lay between 250 and 2850 (Fig. 4.40), which are at maximum higher than on the f-side.

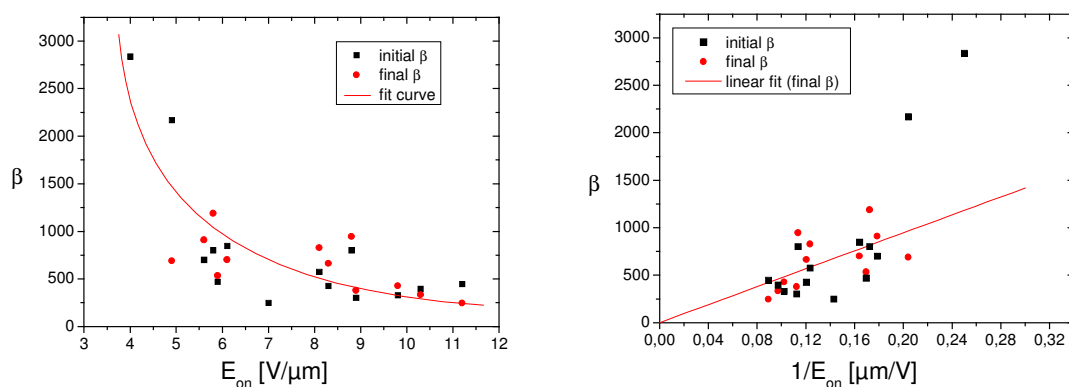


Fig. 4.40. Field enhancement factors  $\beta$  calculated for the initial (black) and final (red) voltage increases of the single CNT emitters on JE103 (O) as a function of extraction field for the current of 1 nA in linear (left) and inverse dependence (right).

Despite of the two strong CNT emitters with opened tips, the emitters are in general show lesser strong deviation from the fit curves as for I-side. Moreover, the most of the field enhancement factors are in the range between 400 and 1000. Thus, the emission current was extracted with  $\varnothing = 12$   $\mu\text{m}$  anode from sparse grown long CNT emitters. The CNT emitters on EPAM are on average longer than on the Anodisc®, which is also expected from the morphology of the CNT on their surfaces (s. SEM images in Fig. 4.5, 4.26). The absence of the short emitters grown from the pores, typical for Anodisc® (with  $\beta \sim 50$ ), which is proved also by the SEM images, is advantageous for the FE.

The histogram (Fig. 4.41) for the first and second V increases in the I-V curves shows, that the most of emitters on the I-side of the JE103 have the field enhancement factors in a range 150 - 200. The maximum of the  $\beta$  at the second increase voltage cycles for JE103(I) is shifted to the lower value due to conditioning effects. The large number of destroyed emitters after the first current increase, however, prevents the calculation of final  $\beta$  for the most of emitters. The histogram in Fig. 4.41(right) shows, that  $\beta$  of the CNT emitters on JE103 (O) are in the range between 400 and 650, which is factor 2-3 higher than on the I-side. As usual



the Gaussian fit for final field enhancement factors is narrower than for initial values due to conditioning effects.

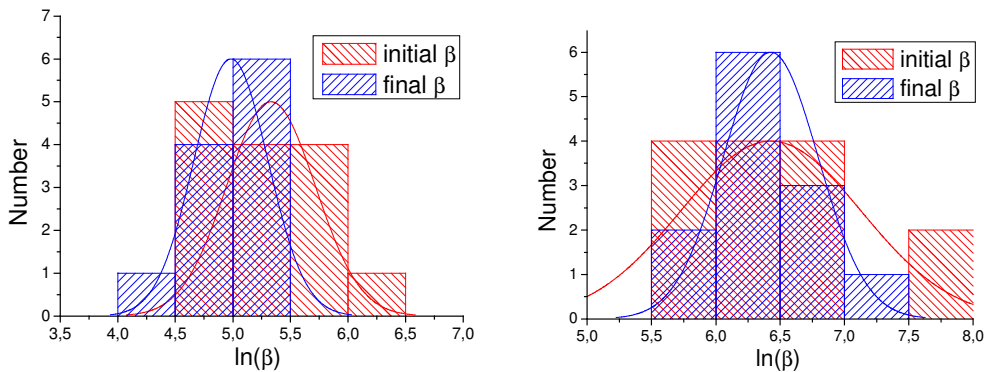


Fig. 4.41. Calculated histograms of the  $\ln(\beta)$  and fitted Gaussian distributions for initial (red) and final (blue) voltages increases show the changing of the  $\beta$  for the JE103(I) (left) and JE103(O) (right). The final mean values of  $\beta$  were 200 and 600 respectively.

The CNT on the inlet grow faster than on outlet side of the porous alumina and build in this way more dense emitter layer. Despite of the low onset field of emitters on both sides of JE103, the O-side show higher number of emitters and much higher field enhancement, thus more suitable for the FE.

The investigation of the role of partial(p) and full(f) opening of the pores of the EPAM on FE was provided for the sample JE123. The f-side have fully opened pores with  $\varnothing = 22\text{-}35$  nm, which is less than for JE103. The opposite side have the partially opened pores of  $\varnothing = 19\text{-}25$  nm with mean distance of about 250 nm between them (Fig. 4.32). The U scan of the JE123(p) (Tab. 4.5) surface reveal the emitter number density of  $56000/\text{cm}^2$  (Fig. 4.42(left)) at  $E < 18.9$  V/ $\mu\text{m}$ , which was estimated from the area of  $255 \times 275 \mu\text{m}^2$ . Convex geometry, unfortunately, prevents the scans of the larger area. The f-side reveal lower number of emitters  $\sim 48000/\text{cm}^2$  at  $E < 6.2$  V/ $\mu\text{m}$  (Fig. 4.42(right)). The black colour, which represents the highest onset field of the emission in Fig. 4.42(left) shows, that emitters grow there more sparse, than on the f-side. Moreover strong variation of the emitter strength also seen in the same image. The estimation of the emitter number density for p-side at  $E \sim 6$  V/ $\mu\text{m}$  results in the value  $\sim 12000/\text{cm}^2$ , which is factor 4 lower than for the f-side at the same field level.

The SEM images (Fig. 4.32) show that the sample surface is covered with long interweaved nanotubes with length required to provide 1 nA current. Calculation of the density of non-shielded nanotubes leads to a value of  $4 \times 10^5/\text{cm}^2$ . The amount of the CNT on the surface is about factor 7 higher than number of emitters calculated from the U – maps. Thus, the amount of CNT, which participate in the emission is  $\sim 15\%$  and is much higher than on the Anodisc®.

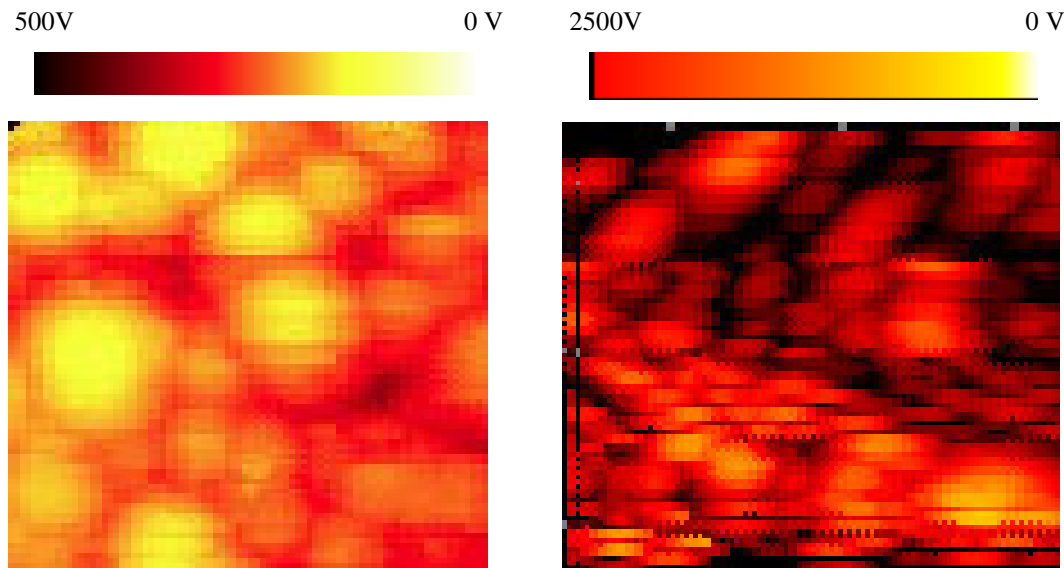


Fig. 4.42. U-maps (scan area  $275 \times 255 \mu\text{m}^2$ ) of the sample (left) JE123(f) and (right) JE123(p) made with  $10 \mu\text{m}$  W anode at  $\sim 30(40) \mu\text{m}$  electrode spacing at the  $1 \text{ nA}$  current for  $E < 6.2 \text{ V}/\mu\text{m}$  ( $E < 19.5 \text{ V}/\mu\text{m}$ ), respectively. The resulting emitter densities are  $\sim 48000/\text{cm}^2$  (left) and  $\sim 56000/\text{cm}^2$  (right).

For the JE123 sample 24 emitters were measured on the f- and p-sides of the membrane with the W anode of the  $\varnothing = 10 \mu\text{m}$  and at  $6 - 12 \mu\text{m}$  electrode spacings. For the sample JE123 (f) about 25% of emitters reveal the stability at currents up to  $15.4 \mu\text{A}$ . From the rest more than 60% of emitters were activated and only about 15% degraded. The emitters of this sample reveal on average higher current carrying capability. Moreover, no destruction

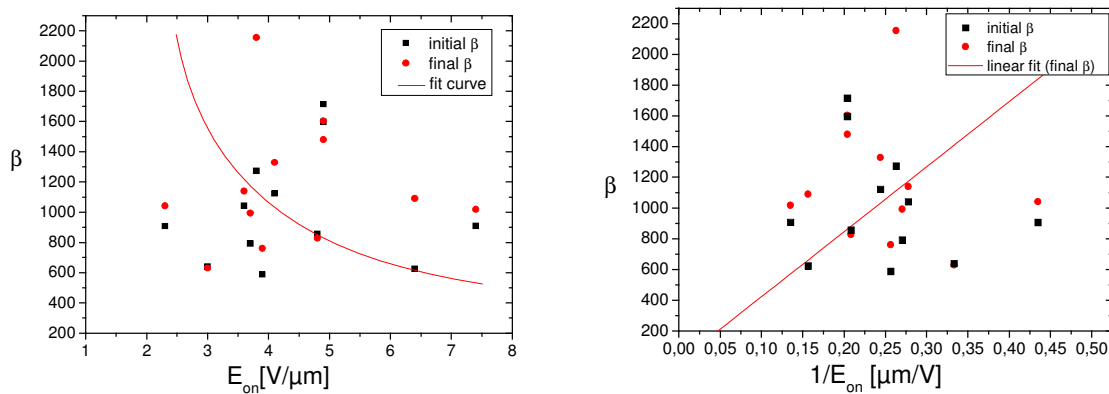


Fig. 4.43. Field enhancement factors  $\beta$  extracted from the initial (black) and final (red) voltage increases of the single CNT emitters on JE123(f) as a function of extraction field for the current of  $1 \text{ nA}$  (left) in linear and (right) inverse dependence.

of emitters was observed. For the sample JE123(p) more than 30% reveal the stability of the emission at maximum up to  $11.2 \mu\text{A}$ , about 50% the activation and 20% degradation. The maximum obtained current from the single emitter was  $18,7 \mu\text{A}$  at  $E = 37,6 \text{ V}/\mu\text{m}$ . This value is mostly at the limit of the single MWNT current carrying capability [154].

The emitters on the JE123(f) (Fig. 4.43) show the field enhancement factors up to 2200 at the fields  $< 8 \text{ V}/\mu\text{m}$ . Strong S-effects can be explained by the densely grown long emitters. In contrast, the emitters on the p-side (Fig. 4.44) show the field enhancement factors between 100 and 600 at onset fields 11-19  $\text{V}/\mu\text{m}$ , which is 2 times higher than on the f-side. The  $\beta$  values show the hyperbola like dependence on the onset field (Fig. 4.44). The emitters

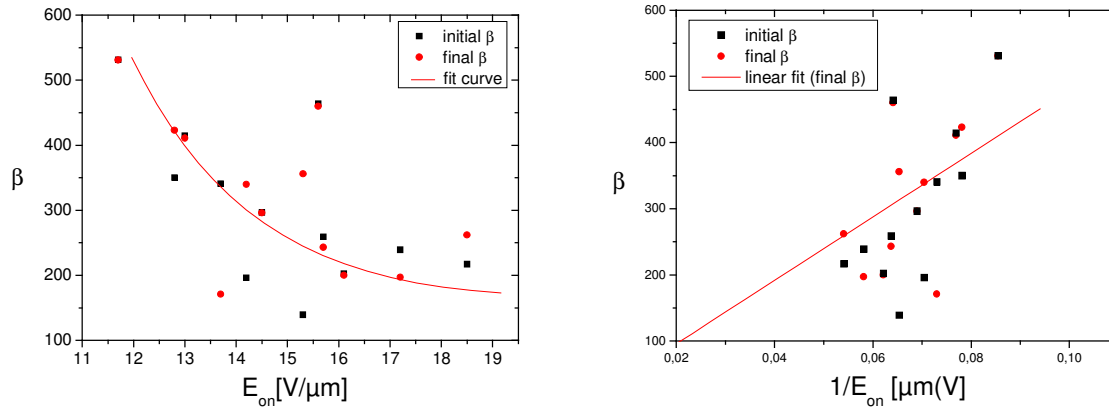


Fig. 4.44. Field enhancement factors  $\beta$  extracted from the initial (black) and final (red) voltage increases of the single CNT emitters on JE123(p) as a function of extraction field for the current of 1 nA (left) in linear and (right) inverse dependence.

seems to grow more sparsely and show lesser, as compared to the f-side, deviation of the  $\beta$  from the linear fit curve in Fig. 4.44(right). Indeed, the SEM images in Fig. 4.45 prove, that the surface on the f-side is covered with dense grown long CNT, which build the inhomogeneous layer. Alternatively, the surface of the p-side is covered with sparse grown CNT with up to  $8 \mu\text{m}$  length.

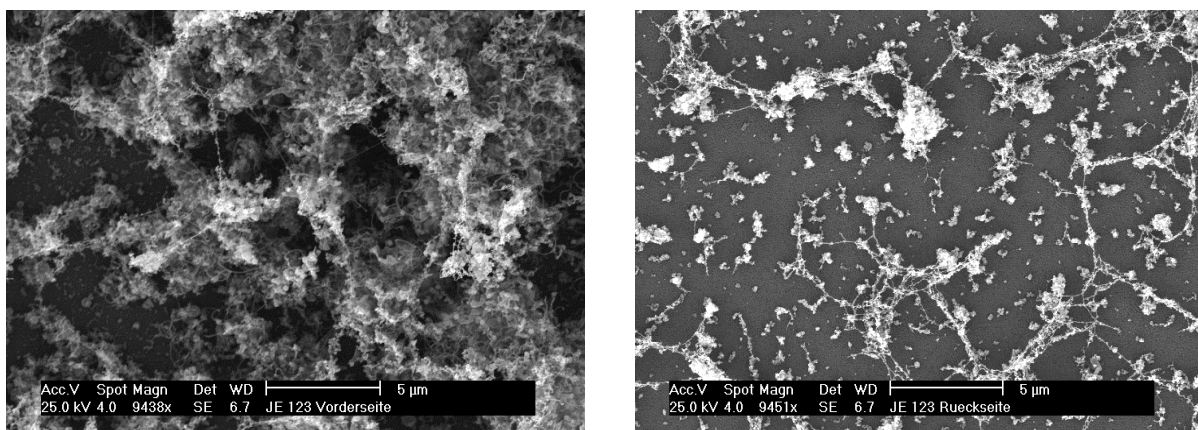


Fig. 4.45. SEM images of the f- (left) and p-sides (right) of the sample JE123.

The histogram in Fig. 4.46 shows, that final mean  $\beta$  are about 1100 for the sample JE123 (f) and about 320 for JE123 (p) respectively. Most of the emitters of JE123(f) have the  $\beta$  between 600 and 1600, which is much higher than maximum values on the p-side. In both cases the fits are shifted to the higher values due to activation of emitters.

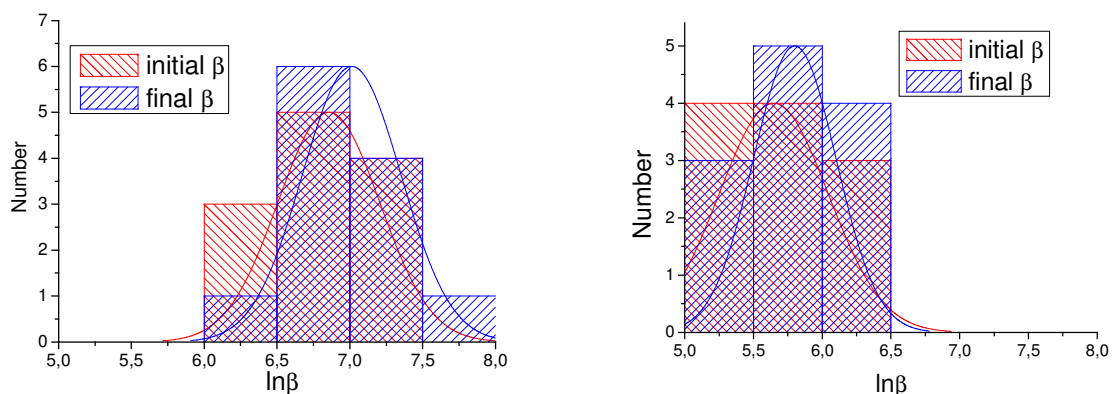


Fig. 4.46. Histograms of the  $\ln(\beta)$  values and fitted gaussian distributions for initial (red) and final (blue) voltages increases show the changing of the  $\beta$  for the JE123(f) (left) and JE123(p) (right). The final mean values of  $\beta$  were 1100 and 320 respectively.

The clear illustration of such a processing effects can be provided by the comparison of the emitter distribution on two measured U maps of CNT on EPAM JE102 (Fig. 4.47). The maps were obtained before and after the I-scans up to 100 nA in the same area. Obviously a local emitter current of 100 nA decreases the number density but increases the strength of the remaining emitters. The potential number of CNT emitters at high electric fields was determined by voltage scans was decreased from 62000/cm<sup>2</sup> to 45000/cm<sup>2</sup> at 23 V/ $\mu$ m.

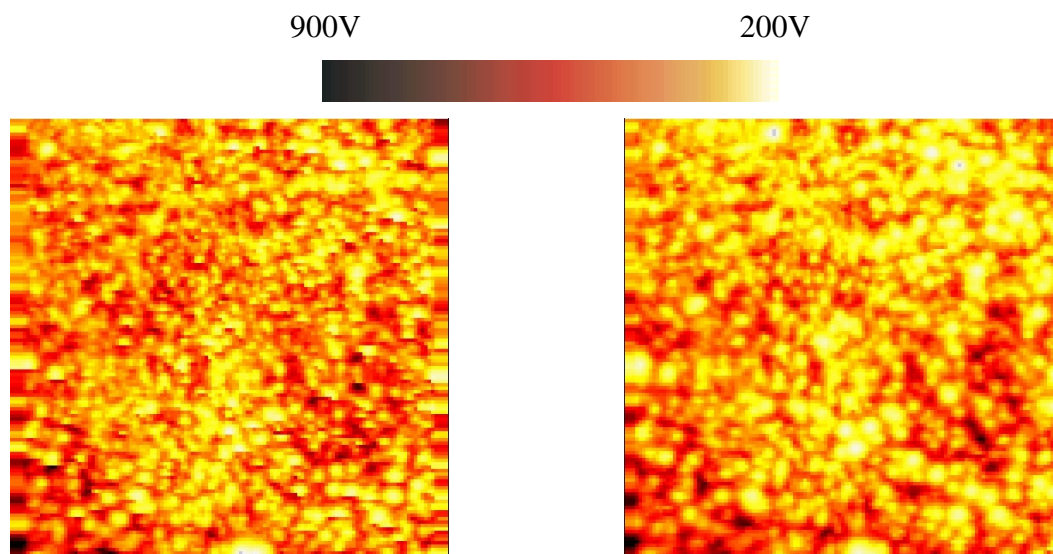


Fig. 4.47. FESM voltage maps between 200 V (bright) and 900 V (dark spots) corr. to fields between 5 and 23 V/ $\mu$ m required for 10 nA local ( $\varnothing$  5  $\mu$ m) current of the same 1 mm<sup>2</sup> area of a CNT sample on EPAM (JE102) during the (a) first and (b) second scan. While the resulting emitter number density has been reduced from 62000/cm<sup>2</sup> to 45000/cm<sup>2</sup>, most emitters have become stronger.

Two effects were observed in the FESM studies of the EPAM samples. The CNT on the I-side grow faster, thus build a shielded layer of emitters. The CNT on the O-side grow more sparsely, thus reveal higher field enhancement and larger emitter number densities in the U-maps for a given field. Reduction of the pore diameter with partial opening of the pores

results in even more sparse growth of CNT, while on the f-side the CNT number density increases. Moreover, fast grown CNT on the f-side reveal highest field enhancement factors, thus lowest onset fields and a portion of CNT as field emitters of about  $\sim 15\%$ , which is enormous value compared to Anodisc®. Thus, the field enhancement factors and the number density of CNT emitters depend more on the CVD growth conditions, than on pore diameter.

#### 4.2.7 Current stability of single CNT emitters

The IMLS tests can not give the information about the stability of the single emitters, because the integral emission current is influenced by all of them. Thus, the fluctuations of local emission sites are compensated and not visible in the integral I-V curves. In order to measure the long-term stability of the single emitters the tests in FESM were made with 20  $\mu\text{m}$  W anode at a distance of 10  $\mu\text{m}$  (Fig. 4.48). The current drift with the period of about 8

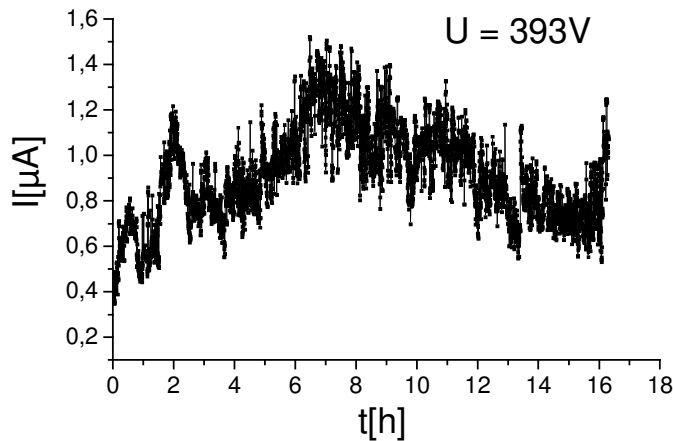


Fig. 4.48. Long-term stability test of the single emission site on the sample JE78-3.

hours was observed at constant  $E = 32.7 \text{ V}/\mu\text{m}$  for the emitter on Anodisc®. The emitter reveal the activation by factor 4 over 8 hours and than degradation to the previous level. The strong fluctuations in minute scale were observed in parallel. The long-term test of the emitter on the EPAM sample JE102 at  $E = 35.7 \text{ V}/\mu\text{m}$  reveal the current drift with the period of about 2.5 hours and a fluctuation of a current in an hour scale (Fig. 4.49). The current fluctuations were  $\sim 50\%$ , which is lower than for Anodisc®. Such instabilities seems to be natural for CNT emitters on porous alumina. Obviously, such an effect does not depends on the scale, while were observed both for nA and  $\mu\text{A}$  currents.

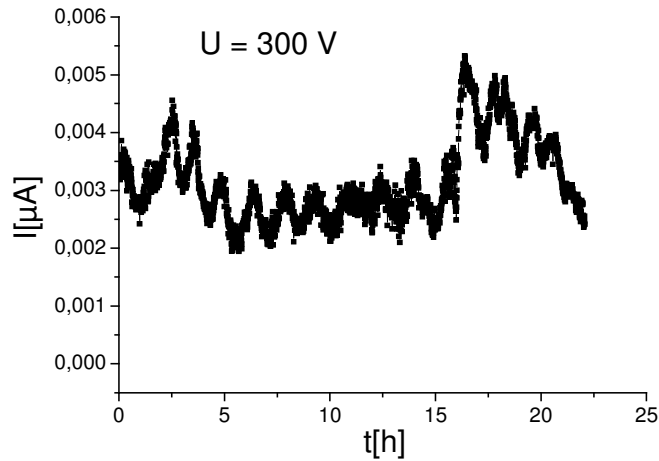


Fig. 4.49. Long-term stability test of the single emission site on the sample JE102.

The exponential form of the FN law shows that a small change of the  $\beta$  and/or  $\Phi$  can significantly alter the emission current [85,155]. The short-term measurements were made with the signal analyser which allow to measure the current fluctuations with ms speed. Fast ( $< \text{ms}$ ) reversible switching between current levels was detected (Fig 4.50), which reflect emission from different electronic states. The current is seen to fluctuate between at least 2 main levels. Moreover, it spends a variable length of time in each state from ms to some s. The histogram in Fig.4.50(right) was created from the entire sequence of the emission current pulses of about 1000 s and show at least 4 main peaks which represents the main electronic

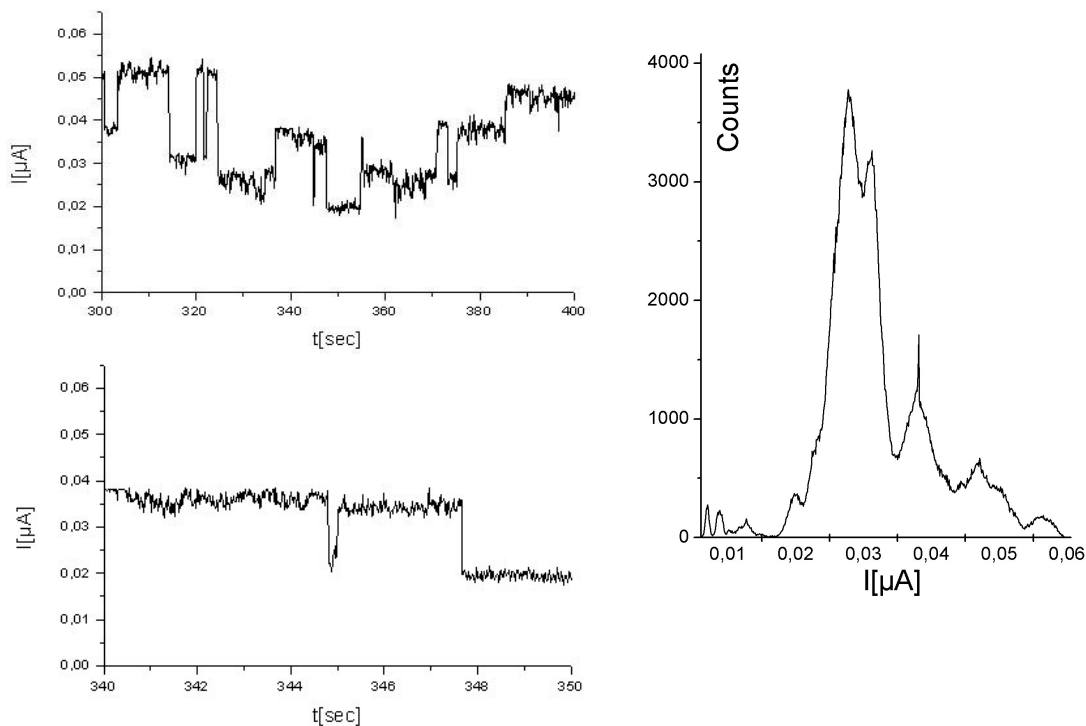


Fig. 4.50. Switching of the emitter between several electronic states (top left), the timely resolved bistable switching over 2 states (bottom left) and corresponding histogram of the multistable current (right) at  $U = 245 \text{ V}$ .

states (Fig. 4.50). The current drift, however, provide their widening. Another emitters reveal the switching between up to 7 electronic states, which produce sharp peak in histogram (Fig. 4.51).

Such instabilities can be successfully described by a flip flop process [156] whereby an adsorbate switches between two different states corresponding to different effective work functions. Moreover, the emitter in general rarely consists of only one CNT. Each nanotube influence the switching and possibly add several electronic states to the resulting histogram. In order to determine the physical processes leading to the switching the adsorbate species should be identified probably by the imaging atom probe approach [157].

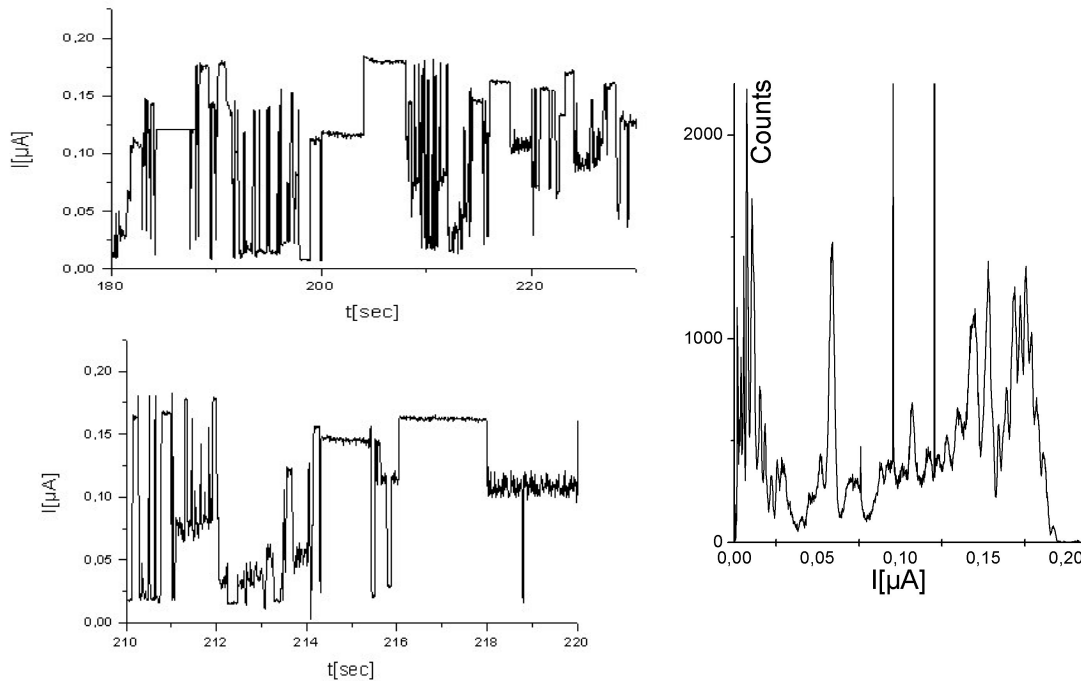


Fig. 4.51. Multistable switching of the emitter between several electronic states (left) and corresponding histogram of the current (right) at  $U = 158$  V resulting at least 7 electronic states.

#### 4.2.8 Current conditioning and pressure dependence of CNT cathodes

The local instabilities are averaged in the integrally measured emission current, but can be observed in the IMLS images. Usually after the first tests of the emission strength and uniformity of the CNT cathodes in the IMLS and some initial conditioning of enhanced edge emission [158], reproducible images with plenty of emitters distributed over the whole sample surface were obtained. During the first increase of the voltage, processing of some emitters has often been observed which leads to small permanent current jumps in the integrally measured I-V curve. Beside the repeated on and off switching of light spots within about seconds, a permanent activation or deactivation of emitters has also been seen in the IMLS videos. The current processing effects on that sample have been revealed by means of software image analysis as shown in Fig. 4.52, where short-term fluctuations have been suppressed by image averaging over 5 s. After a processing time of 10 min, 54(15)% of the

emitters have remained stable, while 29(19)% have been activated and 17(65)% deactivated for EPAM (Anodisc®) samples respectively. The IMLS images revealed more permanent changes of the emitter distribution. Often emitters are strongly activated (Fig. 4.52(left)), which suppress the emission from the rest of the sample surface.

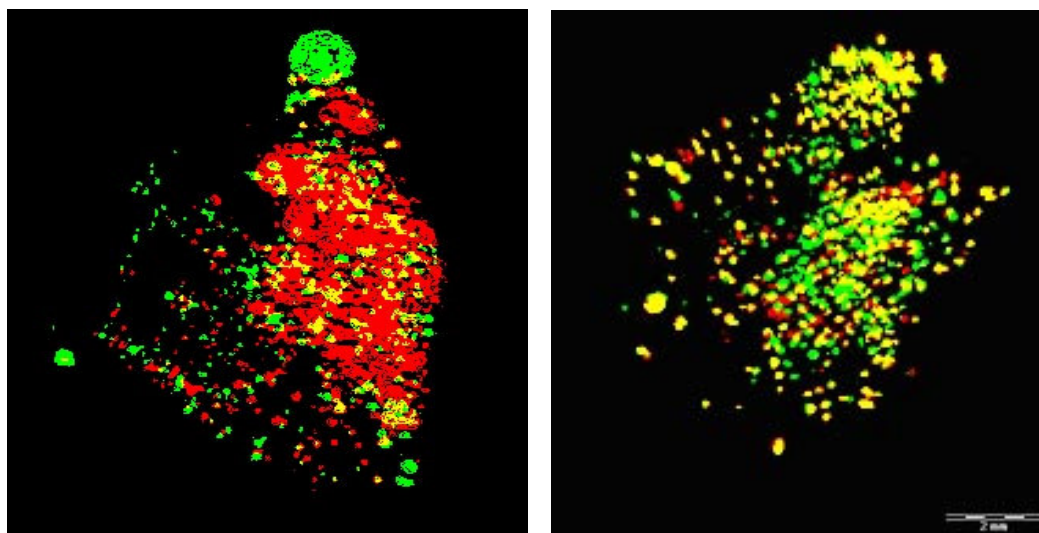


Fig. 4.52. Analysis of current processing effects on the samples JE78-2 and JE103. Compared are 5 s time-averaged IMLS images before and after a 10 min time interval, resulting in stable (yellow), activated (green) and deactivated emitters (red).

In some cases the strong activated emitters cause the discharges (Fig. 4.53). Usual discharge destroy both the sample and the luminescent screen in that area. Afterwards the increased emission from the discharge border is often observed (Fig. 4.53(left)), while the discharge area of some mm in diameter reveal mostly no emission.

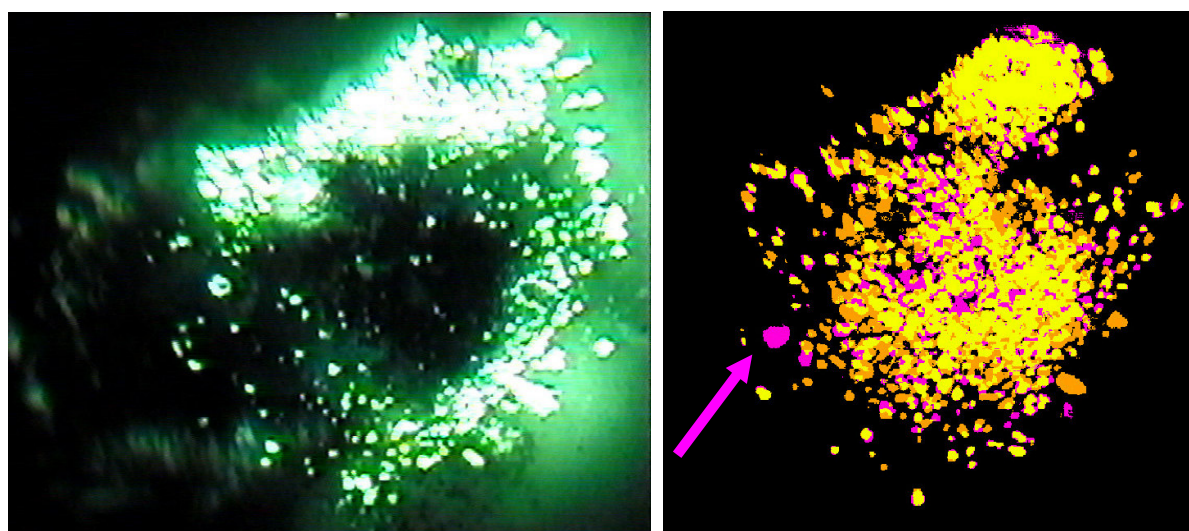


Fig. 4.53. IMLS image of the emission 100 ms after the discharge and the analysis of the discharge, resulting in partial destruction of CNT emitters. The comparison of the image taken 0.1 s before the discharge (orange) and the averaged image (20 over 2 s) (violet) shows the precursor of the discharge (marked emitter).



The analysis shows, that marked emitter in Fig. 4.53(right) is situated in the center of the destroyed area and was activated 0.1 s before the discharge occurs. The main reason of the discharges is the evaporation of the luminescent layer of the screen [146] e.g. due to high local emission currents.

The emitters on Anodisc® are less stable at high currents. After 2 hours of current processing at 250  $\mu\text{A}$  the total number of emitters at a given field increased about a factor of three (Fig. 4.54), which was provided by image analysis. The emitters on EPAM are more

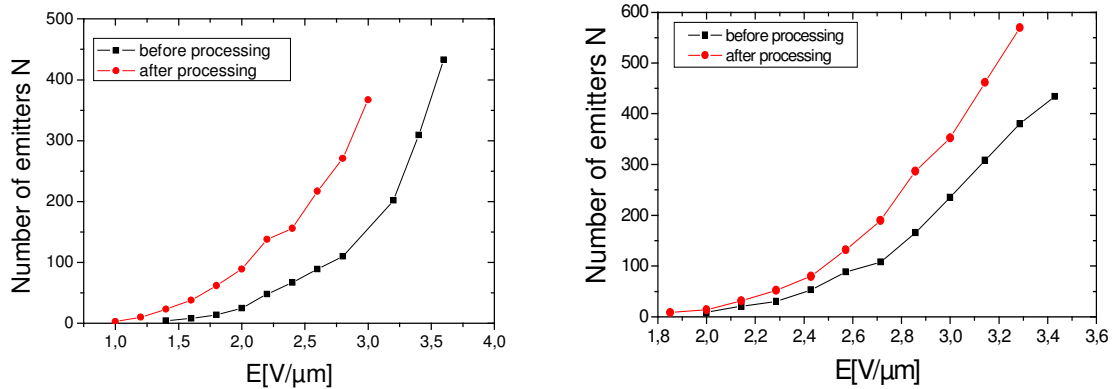


Fig. 4.54. Number of emitters versus electric field for CNT on Anodisc® (size 18 mm<sup>2</sup>) (left) and EPAM (size 20 mm<sup>2</sup>) (right) samples before and after 2 hours average current processing ( $\sim 250\mu\text{A}$ ) (made by image analysis).

stable (Fig. 4.54(right)), however, also reveal activation up to 30%, which is natural for the CNT. Such an effects were shown in the local measurements and correlate with the data obtained from the image analysis. Permanent alignment and desorption of gases are most often discussed as origin of CNT emitter activation, while shortening and disruption of CNT and adsorption of gases might cause deactivation. In order to distinguish these effects, the CNT sample on EPAM before and after a 30 min exposure to a pressure of  $2 \times 10^{-3}$  mbar was tested. The change of the emitter numbers as function of the applied field resulting from

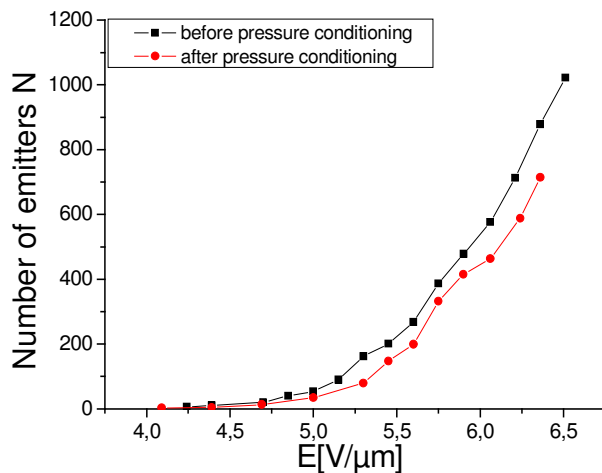


Fig. 4.55. Number of emitters found in IMLS images versus electric field for CNT on EPAM (size 20 mm<sup>2</sup>) at  $10^{-6}$  mbar before (black) and after (red) pressure conditioning (made by image analysis).

IMLS image analysis is given in Fig. 4.55. Obviously, there is some reduction of about 25%, which suggests a significant influence of the adsorbates on the integral FE strength of CNT emitters.

The stability improvement of the CNT cathodes on EPAM as compared to Anodisc® has been confirmed by long-term current processing in the pressure range between  $10^{-6}$  and  $5 \cdot 10^{-4}$  mbar (Fig. 4.56). The measurements were made with Cu anode, due to high sensitivity

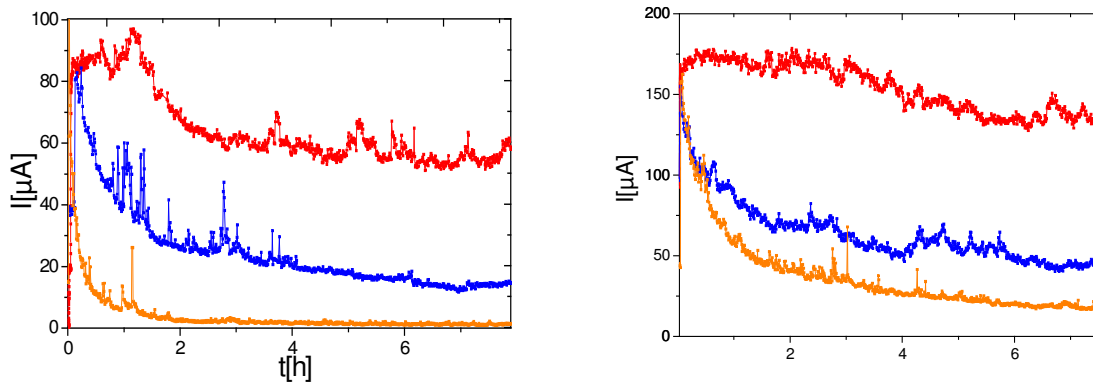


Fig. 4.56. Long-term current stabilities of a  $18 \text{ mm}^2$  CNT sample on Anodisc® ( $I_0 = 90 \text{ } \mu\text{A}$ ) at various pressures/fields:  $2 \cdot 10^{-6}$  mbar/ $5.1 \text{ V}/\mu\text{m}$  (upper);  $5 \cdot 10^{-5}$  mbar/ $5.8 \text{ V}/\mu\text{m}$  (middle);  $5 \cdot 10^{-4}$  mbar/ $7 \text{ V}/\mu\text{m}$  (lower curve) and of a  $28 \text{ mm}^2$  CNT sample on EPAM ( $I_0 = 150 \text{ } \mu\text{A}$ ) at pressures/fields:  $2 \cdot 10^{-6}$  mbar/ $4.6 \text{ V}/\mu\text{m}$  (upper);  $5 \cdot 10^{-5}$  mbar/ $5.3 \text{ V}/\mu\text{m}$  (middle);  $5 \cdot 10^{-4}$  mbar/ $6.5 \text{ V}/\mu\text{m}$  (lower curve) respectively.

of the luminescent screen. For CNT on Anodisc® the initial current of  $90 \pm 10 \text{ } \mu\text{A}$  ( $50 \text{ nA/emitter}$ ) degraded continuously over 8 hours to values between 66% for  $10^{-6}$  mbar, 14% for  $5 \times 10^{-5}$  mbar and 1% for  $5 \times 10^{-4}$  mbar (Fig. 4.56(left)). For the EPAM sample JE103 the initial current was  $I_0 = 150 \text{ } \mu\text{A}$ . The calculated current per emitter was  $\sim 50 \text{ nA}$  and was the same as for Anodisc® sample. On the EPAM the emission current remain at 90% level of the initial for  $2 \times 10^{-6}$  mbar, 30% for  $5 \times 10^{-5}$  mbar and 13% for  $5 \times 10^{-4}$  mbar (Fig. 4.56 (right)).

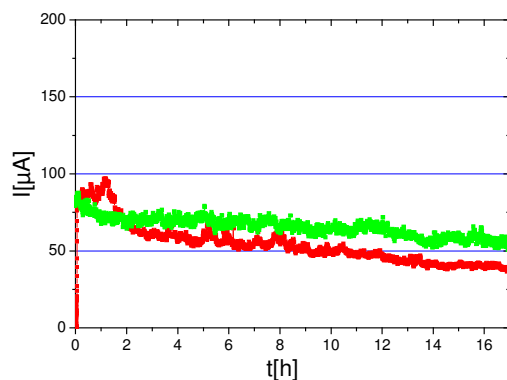


Fig. 4.57. Comparison of the FE current of the same CNT cathode as in Fig. 4.9 (JE78-3) at  $10^{-6}$  mbar initial current  $I \sim 70 \text{ } \mu\text{A}$  before (red curve) and after processing (green curve) (during which the current was raised to  $460 \text{ } \mu\text{A}$  at  $9.2 \text{ V}/\mu\text{m}$ ).

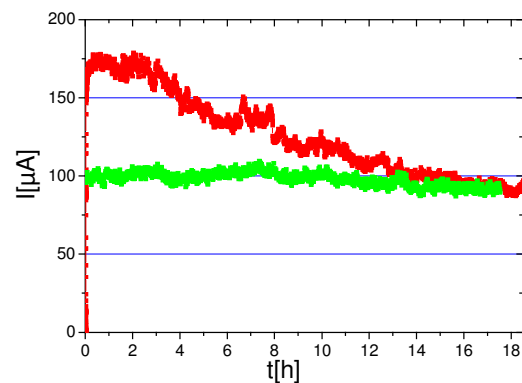


Fig. 4.58. Comparison of the FE current of the same CNT cathode as in Fig. 4.28 (JE103) at  $10^{-6}$  mbar and initial current of  $I \sim 100 \text{ } \mu\text{A}$   $4.6 \text{ V}/\mu\text{m}$  before (red curve) and after processing (green curve), during which the current was raised to  $700 \text{ } \mu\text{A}$  at  $6.5 \text{ V}/\mu\text{m}$ .

Accordingly, much better long-term stability was achieved for the EPAM samples after current processing up to 700  $\mu\text{A}$  for some hours. The overall emission current for CNT on the Anodisc® decreased by 60% over 17 hours (Fig. 4.57(red curve)). Consequently the voltage was increased to obtain the same initial current (green curve). As result of the processing, in Fig. 4.57 a good improved current stability for Anodisc sample was obtained. The stability was improved and the degradation rate decreases. However, despite of the processing the emission current decreased by 40% (Fig. 4.57(green curve)), which is not suitable for the applications. For the EPAM excellent current stability of  $100 \pm 10 \mu\text{A}$  is demonstrated (Fig. 4.58). After the initial activation and degradation to a level of 100  $\mu\text{A}$  the current remain stable over 18 hours. Thus, the conditioning of the samples at higher current greatly increase the emission current stability.

#### 4.2.9 Maximum current densities in dc and pulsed modes

The distribution of the emission current over the surface is due to curvature inhomogeneity. By means of the conversion of the IMLS images with the profilometer maps the influence of the sample curvature to the FE can be precisely determined. The calculation of the emission current in the brightest areas of the IMLS images (with highest electric field), reveal the differences of the emission distributed over the sample surface up to factor 4. At  $E_{\text{eff}} = 4 \text{ V}/\mu\text{m}$  the sample JE123(F,I) reveal in the brightest emitting area the highest current density of  $83 \mu\text{A}/\text{mm}^2$  at the concave geometry and thus additional field enhancement at the edges. At higher fields  $E_{\text{eff}} = 5.5 \text{ V}/\mu\text{m}$  (real electric field  $E_{\text{real}} = 8.4 \text{ V}/\mu\text{m}$ ) this sample showed the maximum current density of  $0.6 \text{ mA}/\text{mm}^2$ , resulting in  $60 \text{ mA}/\text{cm}^2$ . The absolute values of the current were higher for the sample JE123(p,O), which reveal the maximum current density of  $1.08 \text{ mA}/\text{mm}^2$  at  $E_{\text{real}} = 9.3 \text{ V}/\mu\text{m}$  (Fig. 4.59), results in  $108 \text{ mA}/\text{cm}^2$  in dc mode. This value is the highest integral current density obtained in the dc mode for the CNT on alumina membranes. The maximum current densities were up to a factor 5 higher than average values obtained for  $E_{\text{eff}}$  (Tab. 4.6).

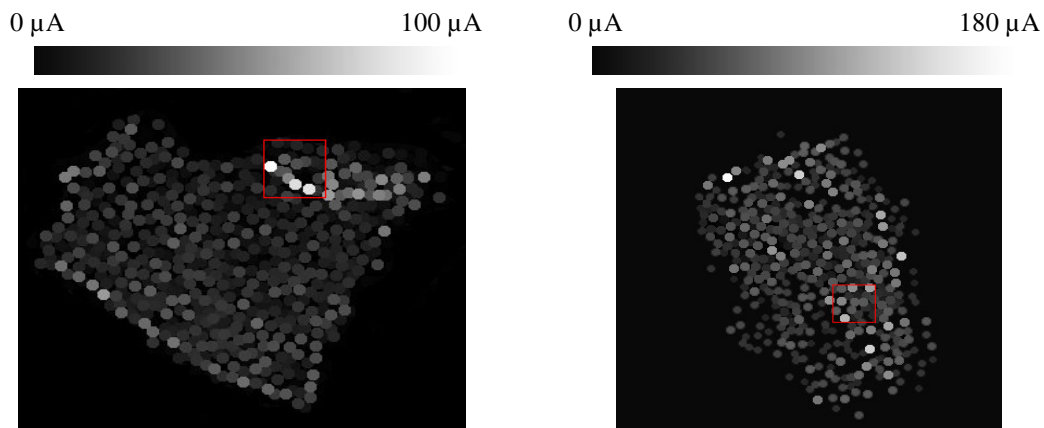


Fig. 4.59. Converted IMLS images of the samples JE123(f,I)(left) and JE123(p,O)(right) taken at  $E_{\text{eff}} = 5.5(7) \text{ V}/\mu\text{m}$ . The brightest areas (marked  $1 \times 1 \text{ mm}^2$ ) provide 0.6 (1.08) mA currents, respectively. It is remarkable, that the best emitter provides the current of 180  $\mu\text{A}$  (right).

Sample	Conf.of pores	Pore $\varnothing$ [nm]	$J(4V/\mu m)$ [mA/cm <sup>2</sup> ]	$J_{max}$ [mA/cm <sup>2</sup> ]	$E_{maxeff}$ [V/ $\mu m$ ]
N1	I	200	0.2	0.5	7.5
JE120	I	65	1.3	13	4.1
JE102	I	60	8	10	4
JE103	I	47	2.9	52	7.2
JE123	I	29	8.3	60	5.5
JE123	O	22	3.7	108	7

Tab. 4.6. Maximum obtained dc current densities at  $E_{eff} = 4 \text{ V}/\mu\text{m}$  and maximum effective field  $E_{maxeff}$ .

The pulsed operation have two main advantages as compared to dc: at first, the samples can be processed more effectively due to the higher achievable peak currents and secondly decreased heat loads on the luminescent screen reduce the discharge risk due to the duty cycle ratio (see Chapter 3.1.3).

After initial dc conditioning two samples N1 (Anodisc®, the reproduction of the JE78 serie) and JE120 (EPAM) were measured in pulsed mode in order to achieve better homogeneity of the emission. Temporary switching (in a s range), as well as permanent activation and degradation of emitters were observed at different duty cycles. Finally, the current processing effects were revealed from series of IMLS images taken in dc mode by means of image analysis as shown in Fig. 4.60, where the short-term fluctuations are suppressed by image averaging over 1 s.

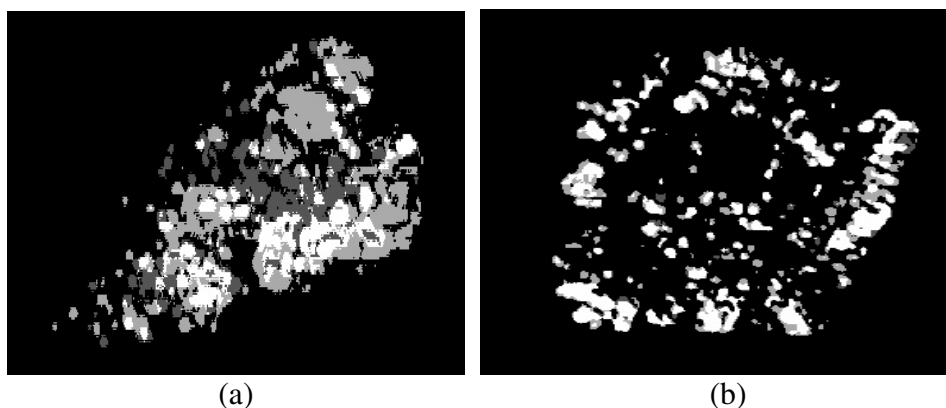


Fig. 4.60. Software analysis of IMLS images showing current processing effects. The emitter distribution has partially changed after 8 hours pulsed processing of CNT on Anodisc® (a) and EPAM (b) resulting in stable (white), activated (gray) and deactivated emitters (dark gray) [146].

The CNT sample on Anodisc® (size  $5 \text{ mm}^2$ ) shows after a processing time of 8 hours only 25% stable emitters, while 49% were activated and 26% deactivated (Fig. 4.60(a)), i.e. the emission uniformity was improved. At a constant electric field of  $8.4 \text{ V}/\mu\text{m}$  the peak current increased from  $6 \mu\text{A}$  to  $22 \mu\text{A}$ . At a voltage of 3150 V and duty cycle 1:24, a stable peak current density  $j_p$  of  $1.9 \text{ mA}/\text{cm}^2$  at  $E = 11.7 \text{ V}/\mu\text{m}$  was achieved. At fields up to  $19.2 \text{ V}/\mu\text{m}$  partial degradation of the emitters was observed resulting in the maximum current density of  $5.6 \text{ mA}/\text{cm}^2$ . In comparison, the CNT sample on EPAM (size  $7.5 \text{ mm}^2$ ) shows

lower uniformity of the emission (Fig. 4.60(b)) due to the concave geometry resulting in slightly enhanced edge emission. The EPAM provides higher stability of the CNT emitters, i.e. 54% of them remain stable, while about 40% were activated and only ~ 6% deactivated. Accordingly, a higher current carrying capability is obtained. For the IMLS measurements  $j_p$  values up to  $29 \text{ mA/cm}^2$  at  $E = 5.3 \text{ V}/\mu\text{m}$  ( $U = 1190 \text{ V}$ , duty cycle 1:24) were achieved for  $16.4 \text{ mm}^2$  sample, limited by the evidence of “phosphor” evaporation. Increasing the duty cycle to a 1:48 a peak current density of  $60 \text{ mA/cm}^2$  was achieved for CNT on EPAM at a field of  $7.6 \text{ V}/\mu\text{m}$ . This clearly shows, that the pulsed operation is very effective for the current processing and shift the critical field of the discharge to higher values. Moreover the electric field levels up to  $19.2 \text{ V}/\mu\text{m}$  were reached without the destruction of the sample, which is hardly achievable in dc operation.

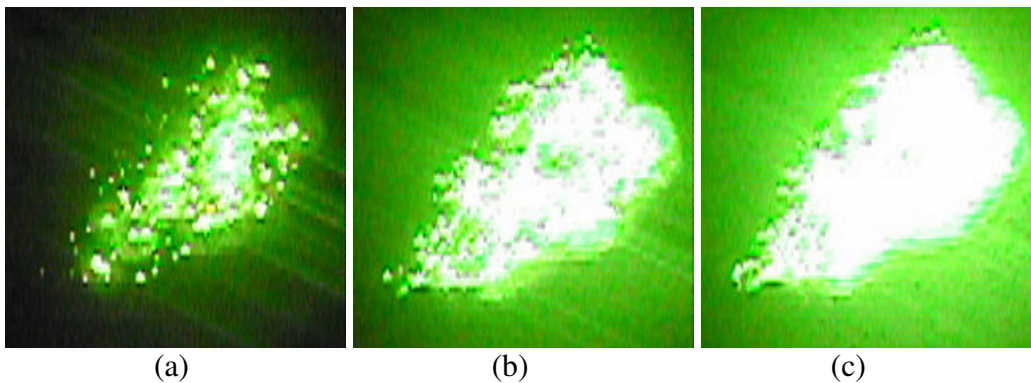


Fig. 4.61. Comparison of the IMLS images of CNT on Anodisc® (N1, size  $5 \text{ mm}^2$ ) at the same average current of  $3.9 \mu\text{A}$ : (a) in dc mode at  $U = 2100 \text{ V}$ , (b) for  $0.5 \text{ ms}$  long current pulses (duty cycle 1:12) at  $U = 2450 \text{ V}$ , (c) duty cycle 1:24,  $U = 3150 \text{ V}$ .

The comparison of the emission in dc and pulsed modes at the same average current shows great increase of the brightness of the luminescent screen at the duty cycle 1:24 (Fig. 4.61). The light spots fuse at repetition rates above  $80 \text{ Hz}$ . The increased number of emitters

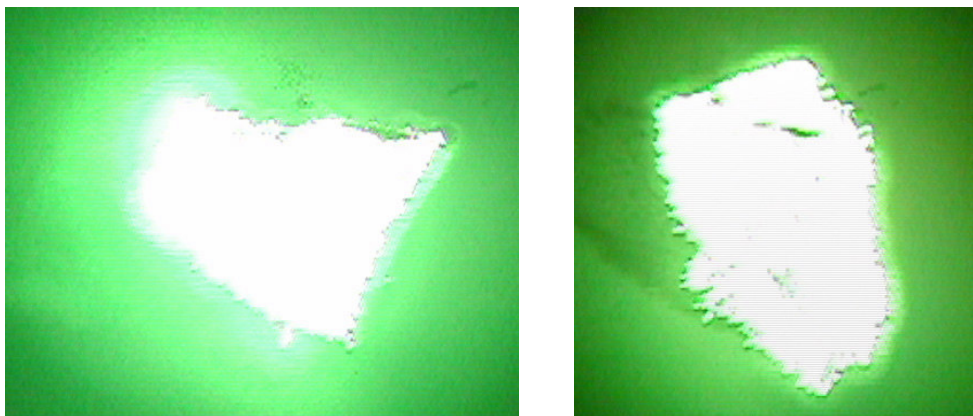


Fig. 4.62. IMLS images of the sample JE123 (f-side, size  $22.4 \text{ mm}^2$ ) taken in pulsed mode by duty cycle 1:10,  $t_{\text{pulse}} = 0.5 \text{ ms}$ , the average current  $\bar{I} = 1 \text{ mA}$  ( $U = 1500 \text{ V}$ ), resulting current density was  $j_p = 45 \text{ mA/cm}^2$  (left) and the sample JE123 (p-side,  $24 \text{ mm}^2$ ) taken by duty cycle 1:10,  $t_{\text{pulse}} = 0.5 \text{ ms}$ , the average current  $\bar{I} = 5 \text{ mA}$  ( $U = 2300 \text{ V}$ ), resulting current density was  $\sim 0.2 \text{ A/cm}^2$  (right). The 20% optic filter was used for the protection of the CCD camera for the sample JE123(p).

and enlarged halos leads to much improved luminescence and homogeneity of the emission. In Chapter 3 was shown, that in a pulsed operation the brightness of the screen at the duty cycle 1:12 decreases only by factor 4 in comparison to dc for the same peak currents. This afterglow effect is well known for the luminescent layers and favours the operation of CNT based light sources in pulsed regimes. The highest values of the current densities and best homogeneity of the emission were obtained by the EPAM sample JE123 (Fig. 4.62). The f-side of the sample JE123 showed the peak current density of  $45 \text{ mA/cm}^2$  at  $E = 7.5 \text{ V/}\mu\text{m}$  (Fig. 4.62(left)). The p-side of the same sample revealed much higher current density of about  $0.2 \text{ A/cm}^2$ . Moreover, the limit of the pulsed power supply (FUG HCN 250-5000) of 50 mA was reached for this sample at  $U = 2300 \text{ V}$ , which disabled the further increase of the electric field. The brightness of the luminescent screen was so high that for the protection of the CCD sensor the optical filter with 20% reduction was used (Fig. 4.62(right)). Thus, the real limit of the sample current carrying capability was not reached. This new record value from CNT samples on porous alumina clearly demonstrates the advantage of pulsed operation for power applications like x-ray tubes. The maximal currents obtained in pulsed mode for CNT on porous alumina are summarized in the Tab. 4.7.

Sample	Conf. of pores	Duty cycle	$J_{\text{peak}}[\text{mA/cm}^2]$	At $E_{\text{maxeff}}[\text{V/}\mu\text{m}]$
N1	I	1 :48	5.6	12.3
JE120	O	1 :12	58	7.6
JE123	I	1 :10	45	7.5
JE123	O	1 :10	>200	11.5

Tab. 4.7. Comparison of the maximal current carrying capabilities of the CNT on porous alumina membranes in pulsed mode. The applied duty cycle results in the maximum peak currents ( $J_{\text{peak}}$ ) obtained at the maximum effective field ( $E_{\text{maxeff}}$ ).

The maximum obtained current density for the Anodisc® sample N1 was about  $5.6 \text{ mA/cm}^2$  at the effective field level  $E = 12.3 \text{ V/}\mu\text{m}$ . In comparison the JE123 (O) showed  $> 200 \text{ mA/cm}^2$  at lower field of  $E = 11.5 \text{ V/}\mu\text{m}$ . While in pulsed mode the EPAM is more advantageous for power applications, both EPAM and Anodisc® can be used in a light sources.

### 4.3 Metallic nanowires

Four metallic nanowire samples, produced as described in the Chapter 2.2 were tested in the IMLS, and two in FESM (Tab. 4.8). Different configurations of the investigated nanowires were observed. While nanowires on the sample FM1 form the tower like structures, on the FM3 and FM4 they build densely packed and on the FM7 rare emitters distributed over the surface (Fig. 4.63). The production parameters of the Cu nanowire

samples are listed in the Tab. 4.8. The samples were on average  $\sim 20 \mu\text{m}$  thick and allow to fix them flat on the sample holders.

Sample name	Pore diameter [nm]	Fluency [ $\text{cm}^{-2}$ ]	L [ $\mu\text{m}$ ]	Sample area [ $\text{mm}^2$ ]	$N_{\text{max}}/\text{cm}^2$	$I_{\text{max}}$ [ $\mu\text{A}$ ]	$E_{\text{max}}$ [ $\text{V}/\mu\text{m}$ ]
FM1	$213 \pm 9$	$(1.06 \pm 0.09) \times 10^8$	18	29.7	37	3.1	6
FM3	$331 \pm 28$	$(1.97 \pm 0.09) \times 10^7$	15	27.9	10	0.26	8.3
FM4	$155 \pm 20$	$(1.69 \pm 0.14) \times 10^7$	10	6.2	10	0.27	7.5
FM7	$323 \pm 6$	$(0,76 \pm 0,2) \times 10^6$	13	15	1	2	7.8

Tab 4.8. Overview of the production parameters and FE properties of the Cu nanowire samples. For each sample the pore diameter in the Cu layer, thus the thickness of nanowires, the fluency of U atoms during the bombardment, the measured length of nanowires in the SEM and the sample area are shown. The last 3 columns show the integral results obtained in the IMLS.

In the diode configuration, the FE current from the Cu nanowire samples were provided by a few emitters at the sample edges yielding integral currents up to some  $\mu\text{A}$  at electric fields of  $E < 10 \text{ V}/\mu\text{m}$ . A rather unstable maximum current of about  $3 \mu\text{A}$  at the field  $6 \text{ V}/\mu\text{m}$  was obtained from about 11 emitters on the sample FM 1 (Fig. 4.64).

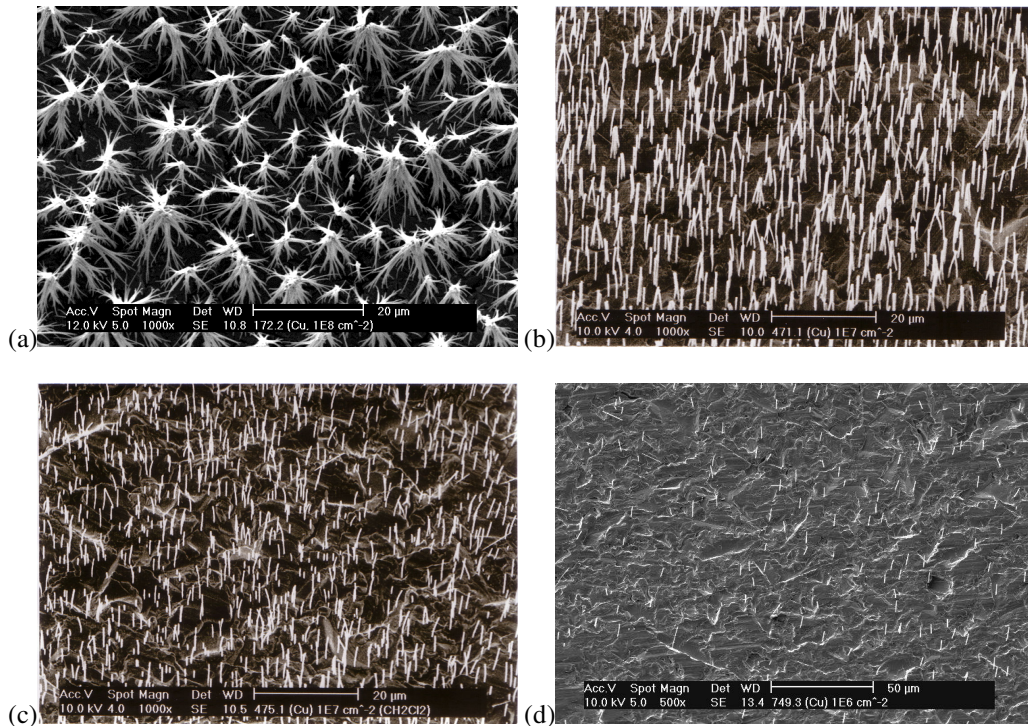


Fig. 4.63. SEM images of free-standing copper nanowires on Au/Cu backing layers (a) FM1, (b) FM3, (c) FM4, (d) FM7.

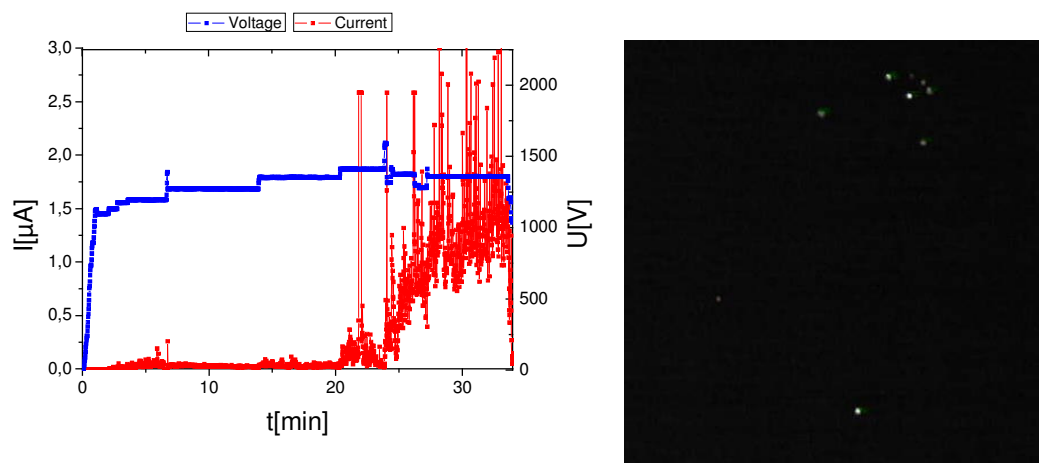


Fig. 4.64.  $U, I(t)$  curves of the sample FM1 and corresponding IMLS image taken at maximum current of  $3 \mu\text{A}$  at  $E = 6 \text{ V}/\mu\text{m}$ .

In order to determine the intrinsic FE properties of the Cu nanowires both voltage and current scans on two nanowire samples by means of FESM were performed (Fig. 4.65). The voltage scans for  $1 \text{ nA}$  reveal  $1732 \text{ emitters}/\text{mm}^2$  up to  $8.5 \text{ V}/\mu\text{m}$  on sample FM1, and  $76 \text{ emitters}/\text{mm}^2$  up to  $15 \text{ V}/\mu\text{m}$  on sample FM7, respectively. The current maps in Fig. 4.65 confirm the higher number of emitters  $N_e = 1.4 \times 10^5 \text{ cm}^{-2}$  on sample (d) as compared to  $N_e = 4.4 \times 10^4 \text{ cm}^{-2}$  for sample (a), both at fields around  $6 \text{ V}/\mu\text{m}$ . Only about  $0.13 \%$  (sample (a)) and  $6 \%$  (sample (d)) of all wires contribute to the FE.

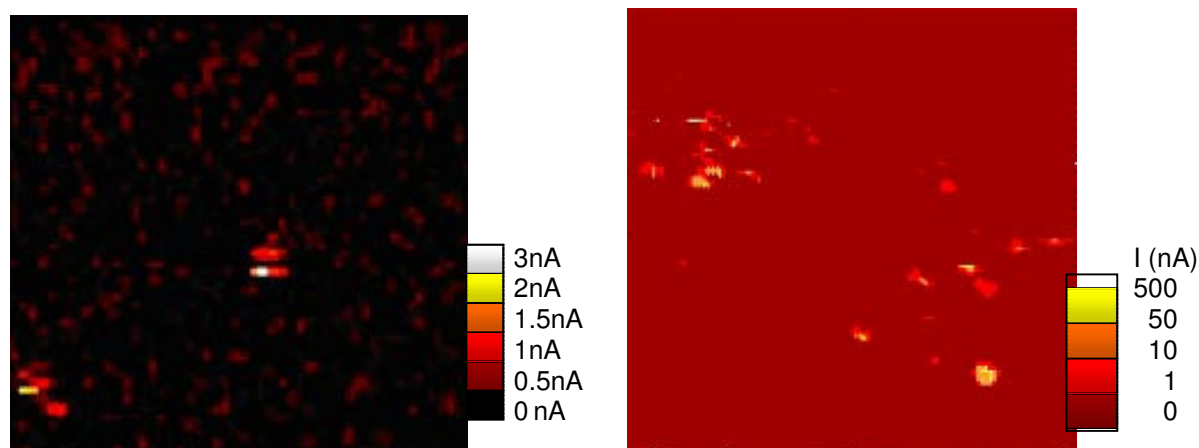


Fig. 4.65. Current distribution maps of Cu nanowire samples (scanned area  $0.5 \times 0.5 \text{ mm}^2$ ) obtained with FESM for (left) sample in Fig. 4.60 (a) with  $\sim 1.4 \times 10^5 \text{ emitters}/\text{cm}^2$  at  $6.4 \text{ V}/\mu\text{m}$  and (right) sample in Fig. 4.60 (d) with  $\sim 4.4 \times 10^4 \text{ emitters}/\text{cm}^2$  at  $5.7 \text{ V}/\mu\text{m}$ .

Obviously, the percentage for sample (a) must be corrected due to the agglomeration of several wires into a bundle which also seem to act as emitter. Unfortunately, the emission of both types of samples is still not very uniform despite of similar length and diameter of the nanowires.



Therefore, the local FESM measurements on 20 randomly chosen emitters of sample (a) by a cycle of ascending ( $\uparrow$ ) and descending ( $\downarrow$ ) voltages were performed. Most of the I-V curves show activation (enhanced  $\beta$  values at the descending cycle) or deactivation (lowered  $\beta$  values at the descending cycle) effects, but rarely stable FN behaviour.

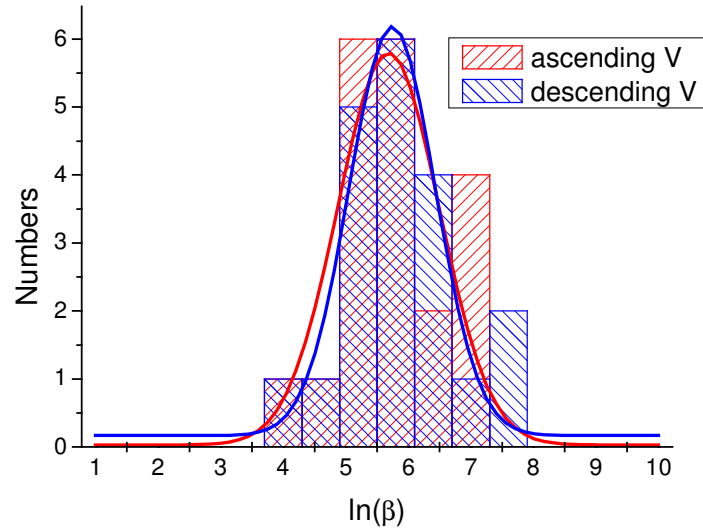


Fig. 4.66. Histogram and fitted Gaussian distributions (red line: ascending voltage, blue line: descending voltage) of  $\beta$  values obtained for 20 emission sites from FN curves which are slightly different for increasing and decreasing voltages. The  $\beta$  mean value is about 245 [73].

The  $\beta$  values extracted from all of these I-V curves can be fitted by a Gaussian distribution as shown in Fig. 4.66, resulting in a mean value of 245 which is about a factor of three higher than expected from the aspect ratio. The real tip shape of the nanowires is sharper than a half sphere, which is proved by the SEM investigations (see Chapter 1.2.2), thus the real values of field enhancement are higher.

In comparison to the CNT the obtained FE parameters of Cu nanowires should be optimised. Thus, the aspect ratio for the field emission should be decreased by means of e.g. thicker foil for the U atoms or additional etching. To reduce the influence of the shielding effect, which was observed in the measurements, when only a few nanowires corresponds to the Fe, the fluency of the atoms should be decreased. Resulting material should reveal higher stability and emitter number density. Additional structuring with e.g. glass mask by the ion bombardment can probably decrease the nanowire site density, thus increase the achievable uniformity and emission current.

#### 4.4 Status of FE from nanostructure cathodes

Carbon nanotubes of various structures have been received much attention over the past few years because of their unique characteristics, which are favourable for field emission. In the Tab. 4.9 are shown the overview of the typical and the best FE properties of the CNT reported in the literature and their comparison to the best results achieved in this work from the MOCVD grown CNT on porous alumina.

Key parameter	Wuppertal	Typical [28]	Best/Reference
Turn-on field [V/ $\mu\text{m}$ ] for 10 $\mu\text{A}/\text{cm}^2$	0.9	1	0.6 / [159,160]
Current density of a single CNT [ $\text{A}/\text{cm}^2$ ]	* $6 \times 10^6$	$10^5$	$10^7$ / [161]
Current density of CNT films [ $\text{A}/\text{cm}^2$ ]	0.2	0.1-1	6 / [153]
Threshold field [V/ $\mu\text{m}$ ] for 10 $\text{mA}/\text{cm}^2$	5	6	5 / [159,160]
Emission site density [ $\text{cm}^{-2}$ ]	$\sim 10^5$	$\sim 10^5$	$10^8$ / [162]

Tab. 4.9. Overview of the typical FE properties, achieved in this work from the CNT on porous alumina and the maximum values reported by so far. (\*) From single CNT emitter.

In particular, some works [159,160] have shown, that CNT have outstanding electrical FE properties with high emission currents with low onset field of the emission up to 0.6 V/ $\mu\text{m}$  and current as high as 0.1 mA from a single nanotube. However, it is also well known that the high emission capability of a single nanotube does not necessarily translate directly into high emission magnitudes from a large area sample containing many such nanotubes because of the shielding effect. The highest current densities from the CNT based cold cathode materials were measured nowadays from the lithographically patterned arrays 100- $\mu\text{m}$ -diameter area of MWNT bundles  $\sim 6 \text{ A}/\text{cm}^2$  at 20 V/ $\mu\text{m}$  [153]. Some works presents the current densities of 100 - 500  $\text{mA}/\text{cm}^2$  over the same areas [159,163,164]. Nillson et al. have shown through simulations that the optimum nanotube packing distance with the best field penetration occurs when the intertube distance is at least twice of their height, Suh et al. have shown through measurements that it is when the intertube spacing is equal to the nanotube height (s. Chapter 1.3). More recently, there are fundamental works on FE optimization of CNT using different emitter configurations [162], when the emitter number density up to  $10^8/\text{cm}^2$  was obtained. But achieving theoretically predicted high current densities (hundreds of amperes per square centimeter) over large nanotube areas with repeatability and emission longevity still remains a problem. Nevertheless, the MWNT nowadays are the most promising candidates for the cold FE cathode applications due to their simple fabrication, robustness and current carrying capability [165-167]. The FE properties of SWNT are often used for fundamental studies and simulations [30,167,168].

Field emission characterization of the quasi one-dimension nanomaterials has been mostly concentrated on the recording of I-V performance and emission site distribution [28,71,72,134,169,170,171]. In Tab. 4.10 the comparison of the current densities achieved by different cold cathode materials is shown.

As already mentioned in Chapter 1.2.2, if one is to ensure the uniformity of emission it is important to look for methods for synthesis of nanowire arrays having unique electronic property. Mo and W are important refractory metals and have very high melting points, relatively low work function, high electrical conductivity and robustness [71,72,169]. Therefore, they are considered to be important cold cathode materials.

Type	Materials	Maximum current density [mA/cm <sup>2</sup> ]	Threshold field	Reference
Metallic	Graphite nanofiber	50	2.5 V/μm (1 mA/cm <sup>2</sup> )	[169]
	Mo nanowire	30	2.2 V/μm (10 mA/cm <sup>2</sup> )	[71]
	MoO <sub>2</sub> nanowire	35	2.4 V/μm (10 mA/cm <sup>2</sup> )	
	W nanowire	0.2	5 V/μm (0.1 mA/cm <sup>2</sup> )	[72]
Wide-band gap	MoO <sub>3</sub> nanowire	13	3.5 V/μm (10 μA/cm <sup>2</sup> )	[170]
	SiC nanowire	19	2.5 V/μm (10 mA/cm <sup>2</sup> )	[134]
Narrow-band gap	Cu <sub>2</sub> S nanowire	0.6	6.5 V/μm (1 μA/cm <sup>2</sup> )	[28]
	CuO nanobelt	1.2	10.5 V/μm (1 μA/cm <sup>2</sup> )	[171]

Tab. 4.10. Various nanomaterials and their FE properties [28].

It is seen that most of the high-performing emitters are from wide band-gap semiconducting nanomaterials. Typically, linearity of FN plots obtained from wide band-gap semiconductor nanowires is much better than those obtained from CNT. The threshold field for 10 mA/cm<sup>2</sup> from SiC nanowires [134] is even lower than the best values obtained from CNT. Also, the uniformity of emission from aligned nanowire films seem to be better than those from CNT films.

Among other semiconducting nanomaterials the most interesting are those prepared at room temperature. These include Cu<sub>2</sub>S nanowire [28] and CuO nanobelt films [171]. Measurement of field emission characteristics showed that the typical threshold field for obtaining a current density of 1 μA/cm<sup>2</sup> was high (6.5 V/μm), but that a current density of 0.6 mA/cm<sup>2</sup> may be obtained regularly from the Cu<sub>2</sub>S nanowire films. Moreover, due to the narrow energy band-gap of the above nanomaterials, they are more likely to respond to heating or illumination by visible light. Finally, it is noticeable, that one cannot find obvious differences in the field emission properties of nanowires, nanotubes and nanobelts [28].

## 5. Field emission applications of nanostructures

For as long as nanostructures have been known to exist, the optimization of them for cold FE cathode applications has been an intensively developing field. Actually, most of advanced applications are based on the CNT. Various approaches, however, demand from the cathodes different requirements, which should be clearly understood. The range of cold FE cathode applications is wide. They should replace existing light and x-ray and make possible the construction of bright electron sources, field emission displays and multiple electron beams. While some of them are in the prototype stage, others still require optimization of the cathode material. Finally, the outlook for the presented key applications with respect to the tested materials will be discussed.

### 5.1 Requirements for cold FE cathodes

The main advantages of cold FE cathodes, as compared to existing thermionic, are low power consumption, instant turn-on, compactness, long lifetime and high electron beam quality. The utilisation of them in devices require a clear understanding of the cathode parameters, which are important for different applications. The requirements for the most promising cold cathode applications are summarised in the Tab. 5.1.

Application	Config.	Frequency range	Size[cm <sup>2</sup> ]	Uan/Ugate [kV]	J[A/cm <sup>2</sup> ]	N/cm <sup>2</sup>	$\Delta I/I_0$	t [years]
Light source	Diode	50 Hz	~ 1	2-5	0.5-0.2	~10 <sup>5</sup>	<50	>1
X-ray	Diode/ Triode	dc-100 kHz	<10	10-30	< 10 <sup>-2</sup>	~10 <sup>3</sup>	<10	>3
FED	Triode	100 Hz	10 - 10 <sup>3</sup>	0.01-0.1	<5x10 <sup>-5</sup>	~10 <sup>6</sup>	<10	>6
Multiple e-beam	Pentode	GHz	0.1	0.1	<10 <sup>-8</sup> /tip	~10 <sup>5</sup>	<5	>1

Tab. 5.1. Requirements for FE cathodes in different applications.

For light sources [34,172,173], which in general have diode configurations (cylindrical or planar) the high number of emitters is most important. At 2-5 kV anode voltage the current density should be in the order of 0.2 - 0.5 A/cm<sup>2</sup> to activate the phosphor, while the stability of the emitters is relatively unimportant. Currently such applications have, in general, suffered from phosphor ineffectiveness. Of course, the cathodes should have comparable lifetime with existing incandescent or fluorescent lamps. Diagnostic x-ray applications [32,34] require emission currents of 10 - 100 mA at an acceleration voltage of about 30 kV. The emitters should operate at high current density; thus, CNT must be spaced apart by at least their height, otherwise the field enhancement is reduced by screening effect. For the FED, which do not require high currents, but should have equally bright pixels [33,35,36,174], the most important parameters are the low onset fields, uniformity, and stability of emitters. This is

more easily achievable in triode configurations with an extraction electrode, which allows the use of a low voltage driver. The lifetime of the cathodes should be  $> 50.000$  hours, despite of the HV pressure ( $10^{-6}$  mbar) in the device. Multiple e-beam lithography [37] demands the highest requirements for the stability of emitters. The high brilliance of the beam should be achieved for sub-100 nm resolution. The market for this technology is so large, that even with a lifetime for the e-beams of some month it would still be commercially viable. However, the development is very complex and suffers from disalignment of the electrodes and imperfect addressing technique. Other applications for nanostructure based field emitters include the microwave amplifiers [175], electron guns for SEM [176], mass spectrometers, high precision space thrusters and charge neutralisers in space applications [28], which are not so commercially viable as FED.

## 5.2 Light source demonstrators

Common light sources are light bulbs and fluorescent tubes, which on average have efficiencies of 15 and 40 lm/W respectively. Light sources based on cold cathodes are preferred due to the absence of mercury, instant turn-on possibility, high intensity, and a large working temperature range. For this purpose the electrons are accelerated in cylindrical or flat diode configurations and excite the luminescent anode.

The field enhancement in cylindrical configuration can be found similar to planar case by the replacement of macroscopic field at the cathode surface  $U/d$ , where  $U$  is applied voltage and  $d$  is the interelectrode spacing, by the field  $U/(r_1 \ln(r_2/r_1))$  (Fig. 5.1). The principle is nearly the same as used in FEM [177]. Thus, the resulting  $\beta$  is much higher than in the planar case. Experimental prototypes on basis of MWNT are already present [172]. The experimental cylindrical configuration with  $r_1 = 0.5$  mm and  $r_2 = 21$  mm shows for an applied voltage of  $U = 5.4$  kV the emission current of  $0.06$  mA/cm<sup>2</sup> on the anode resulting in the luminance of  $10^4$  cd/m<sup>2</sup>. In the cylindrical geometry, the cathode has to emit far higher current densities, than in a planar arrangement for a given current density on the anode (e.g. to reach a given brightness with a phosphor layer). The efficiency of the device was about 10 lm/W, which is mainly affected by the inefficient phosphors.

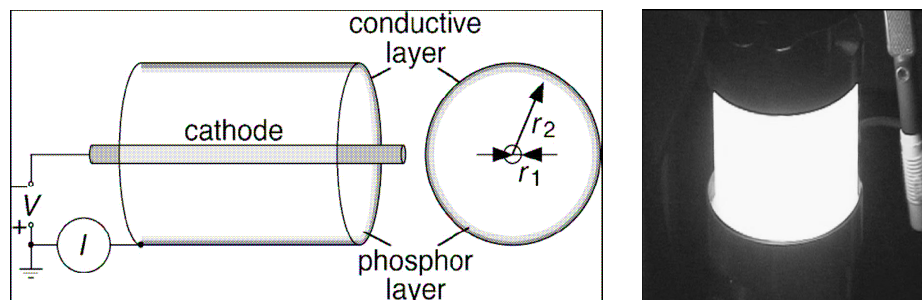


Fig. 5.1 Luminescent FE light source in cylindrical configuration (left) and the realised luminescent tube with a MWNT cathode (right) [172]. The cathode of radius  $r_1$  is placed in the symmetry axis of the cylindrical anode with radius  $r_2$ . The cylinder has the phosphor layer on the inner side.

The principle of the flat light source is the same. The electrons accelerated between two planar electrodes and excite the luminescent layer (Fig. 5.2). At Lightlab/Sweden [173] a light source based on CNT with 90% effectiveness as compared to the present Hg lamps has been developed (Fig. 5.2). The first commercial flat light source on the basis of CNT grown on glass substrate was constructed at XINTEK/USA [34].

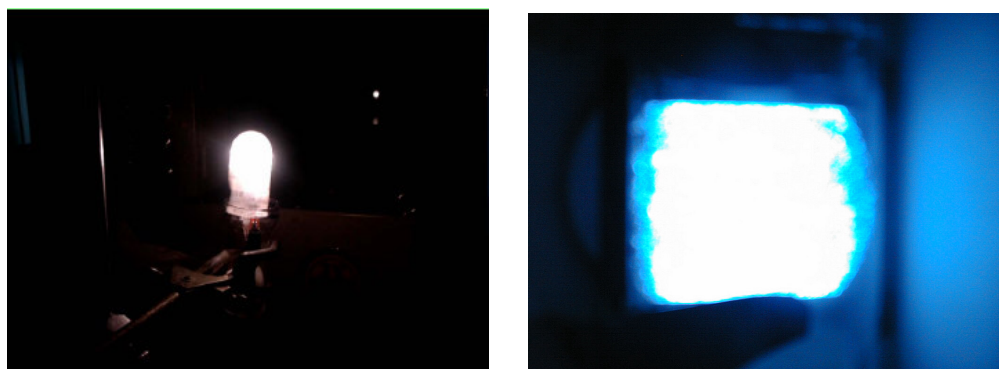


Fig. 5.2. Cold cathode based light sources developed at the Lightlab/Sweden (left)[173] and XINTEK (right)[34].

At the University of Wuppertal a mobile light source demonstrator based on CNT on porous alumina was developed. Fig. 5.3 shows a general view of the demonstrator and the example of the luminescent screen brightness produced by a 13 mm<sup>2</sup> EPAM cathode at

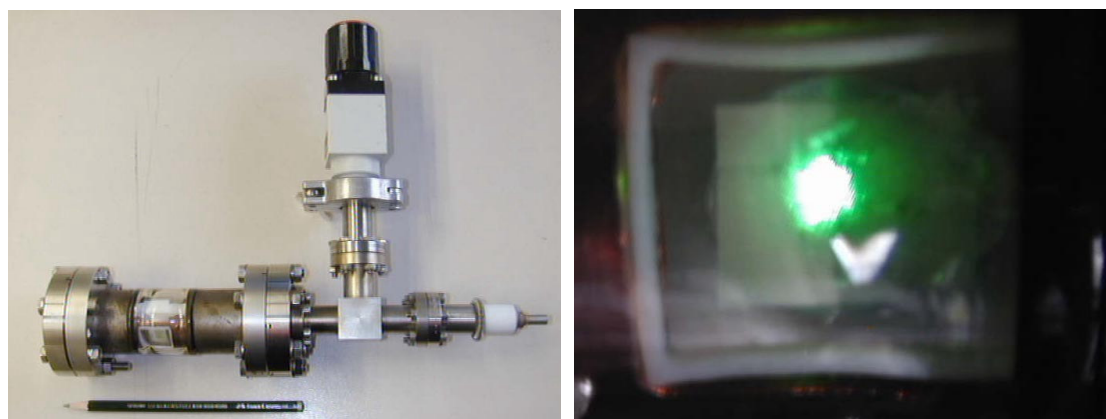


Fig. 5.3. General view of the demonstrator (left) and the image of its luminescent screen taken in pulsed mode at  $U = 1$  kV (duty cycle 1:20) (right). The FE cathode used was 13 mm<sup>2</sup> size EPAM.

$U = 1$  kV. Below the luminescent screen of 19 x 19 mm<sup>2</sup> is positioned a CNT cathode, which is glued to the aluminium sample holder. The same construction as for the IMLS allows spacer free electrode positioning. The parallelness of the sample and the luminescent screen can be set manually with the micrometer and controlled visually from one side, which has a special cut. The distance calibration is, however, limited by the cylindrical configuration of the load-bearing elements. This allows the precise tilting only in the direction parallel to the symmetry axis of the tube. The right part of the demonstrator in Fig. 5.3 is the t-tube. From one side it is connected to the gate, which can be connected to the pump stand. After about an hour a pressure of about  $5 \times 10^{-6}$  mbar is achievable. From the other side the high voltage

feedthrough is made for the connection to the power supply. The demonstrator showed at 1 kV and in pulsed operation (duty cycle 1:10) a high brightness, which was visually comparable to the above presented prototypes (Fig. 5.2), though from a smaller area.

ISE/Japan has succeeded to use CNT electron emitters for the high brightness light source (Fig. 5.4).

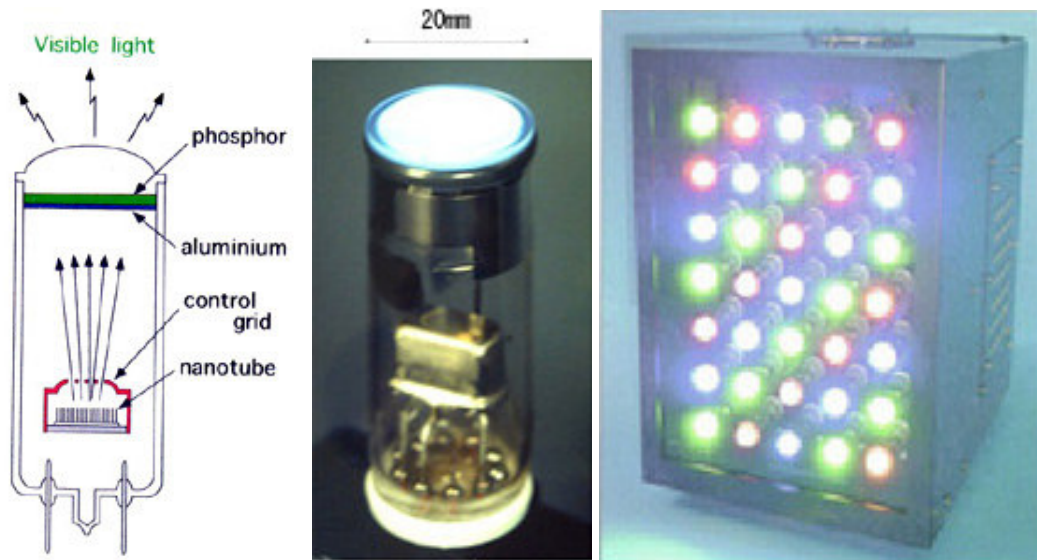


Fig. 5.4. Electronic scheme of the triode light source (left), the single light element (center) and the prototype of the display based on these light sources with different phosphors produced by ISE/Japan [33].

As in a CRT device, the electrons pass through a control grip and strike a phosphor screen that produces visible light. The luminance exceeds  $50.000 \text{ cd/m}^2$ , which provides high legibility even during day-time and can be used in advertising panels, signs etc. The brightness is about two times higher than existing competing light sources which use thermionic emission. The absence of the heating element provides a low power consumption which is comparable to that for an LED. The proven lifetime of 8000 hours is commercially viable.

### 5.3 RF-gun with high brightness

In the accelerator physic there is a permanent interest in the electron sources with high beam quality. First studies of electron guns based on the RF-cavity (RF-guns) started in 1984 [178]. Two major concepts of them with thermionic or photocathodes has been studied intensively [179]. The FE based electron sources provide excellent e-beam quality without complicated laser triggering and at room temperatures. Experience with these cathodes is, however, still limited. An RF-gun has been constructed in the group of Prof. Dr. T. Weis at the Dortmund Electron Test Accelerator (DELTA) which gives and opportunity to investigate FE cathodes with the diameter up to 8 mm and height of up to 2 mm in the environment of an S-band test field [180]. The sample (cathode) is exposed during  $4 \mu\text{s}$  pulses with 3 GHz

oscillated field. The geometry of the chamber produces a homogeneous electric field over the whole sample surface (Fig. 5.5) [181].

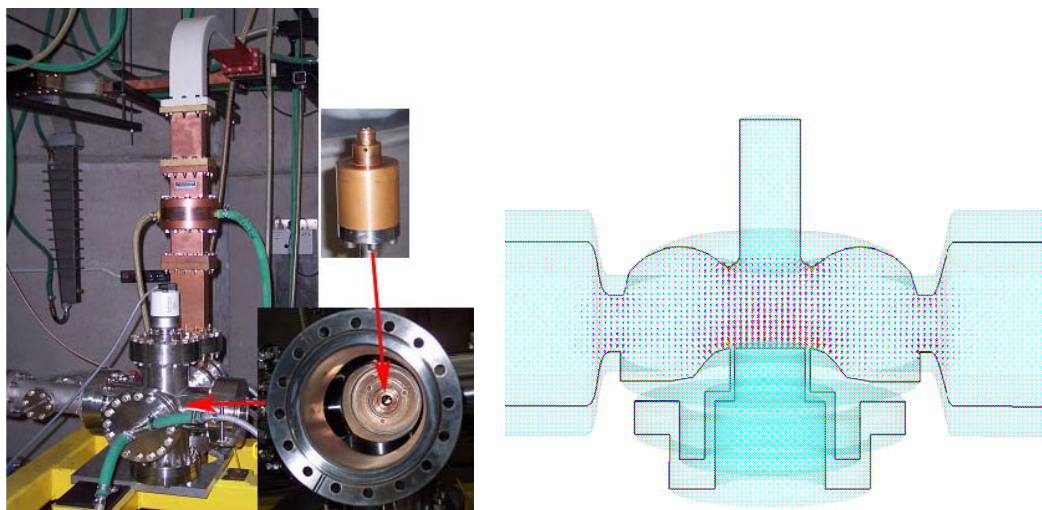


Fig. 5.5. Side view of the RF-gun with a schematic of the cathode installation into the chamber (red arrows) (left) and a section of the resonator chamber with calculated homogeneous field distribution (right) [181].

The peak electric field on the sample surface can be set up to  $20 \text{ V}/\mu\text{m}$ . The maximum repetition rate of the high frequency pulses is  $10 \text{ Hz}$ , thus yielding a duty cycle of  $4 \times 10^{-5}$ . The measurement of the emission current is provided by the Faraday cup. It can be changed by the YAG (Yttrium Aluminium Granat) screen with focusing solenoid, which allows the observation of the emission area. Both Anodisc® and EPAM were installed into the system. The CNT sample on Anodisc® reproducibly showed a  $I_{\text{max}} = 0.68 \text{ A}$  at  $E = 15 \text{ V}/\mu\text{m}$  from a  $25 \text{ mm}^2$  area, which results in the peak current density of  $j_p = 2.2 \text{ A}/\text{cm}^2$  (Fig. 5.6).

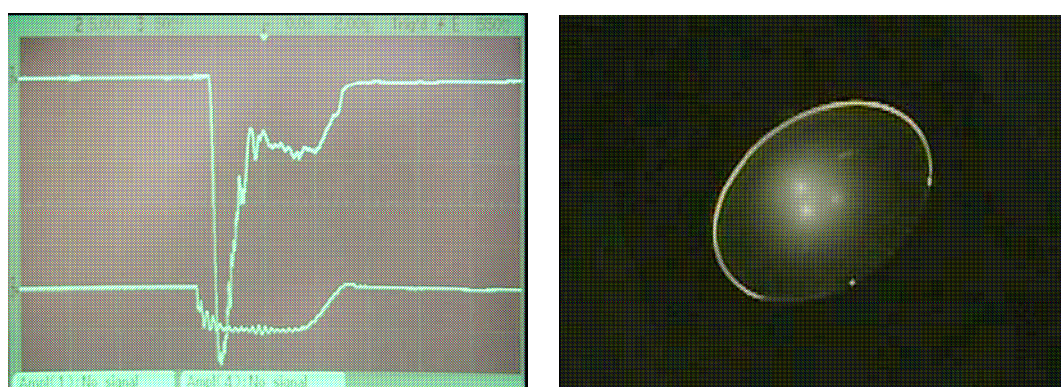


Fig. 5.6. Measurement of the voltage on the Faraday cup with the 40 dB absorber from the Anodisc® (left) and the image of the emission with the YAG screen (right).

The current remain constant over 1 hour. The corresponding image of the sample area show the 3 major emitting clusters, which should have a current carrying capability  $> 100 \text{ mA}$ . The  $12 \text{ mm}^2$  size EPAM sample JE103 at the same electric field showed  $I = 0.8 \text{ A}$  which results in high value of the current density of  $j_p = 6.7 \text{ A}/\text{cm}^2$ . The reproducibility was measured over 1.5



hours. The results show that by measurements at 250 kHz rate the intrinsic current limit of the CNT is much higher than in the ms range. Moreover, the high current densities obtained show that the CNT cathodes are a viable choice for high brightness FE based RF electron guns.

#### 5.4 Compact x-ray tubes

A conventional x-ray tube is composed of a metal cathode (filament) which emits electrons, when resistively heated to about 1000°C, at which point the electrons have sufficient energy to overcome the work function. They strike a metal anode (target), which emits the x-rays (bremsstrahlung). The design of existing cathodes have several limitations. In general thermionic cathodes have slow response times and high power consumption. The FE is more attractive mechanism for electron extraction, due to the room temperature working range, lack of previous heating, and instant switching. The first prototype x-ray tube based on cold cathode was developed by G. Z. Yue et al in a year 2002 [32]. The cathode was SWNT coated on a metal substrate (Fig. 5.7). The gate (metal mesh) was about 200 μm from the cathode. Electron emission was triggered by a voltage applied between the gate and the cathode. The output current is voltage controllable, as compared to the conventional tubes.

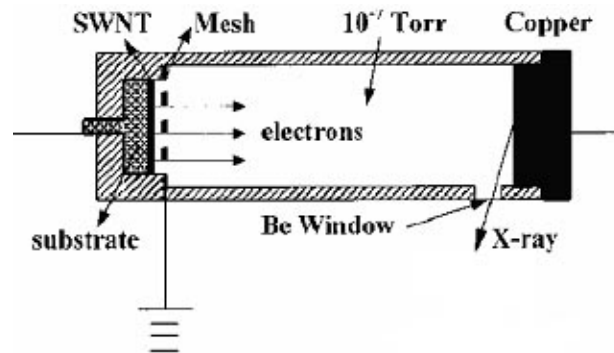


Fig. 5.7. Schematic of the triode-type FE x-ray tube [32].

The first commercial product was developed at XINTEK/USA (Fig. 5.8) [34]. The device can readily produce both continuous and pulsed x-ray (>100KHz) with a programmable wave form and repetition rate. Moreover, it can produce sufficient intensity to image the human anatomy. The new technology also outperforms the lifetime of existing cathodes, which in general work less than a year. Since the size of the device is greatly decreased one can imagine portable x-ray devices for use in medicine. Another feature of CNT based x-ray tubes is the high resolution imaging of objects, due to their rapid pulsation capability and ultra-fine focal spot, resulting in the 3D images and x-ray films.



Fig. 5.8. Image of x-ray tubes based on CNT cold cathodes [34] and an x-ray image taken with this tubes.

## 5.5 Field emission displays (FED)

The principle of operation of a FED is very similar to a CRT, with the same mechanism of light generation of cathodoluminescence. An electric field is applied between the phosphor screen and the emitter arrays. Electrons generated by field emission are accelerated in high vacuum to impact a phosphor dot deposited on the screen (Fig. 5.9).

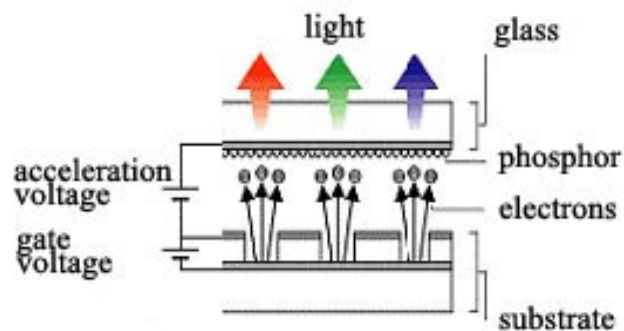


Fig. 5.9. Architecture of the CNT based FED.

In comparison to CRT every pixel has its own electron source, which is independently addressed. Some hundreds of emitters define a single pixel. Redundancies are built in so that if a small percent of the emitters do not work, the pixel does not fail. A phosphor coating is applied to the lower surface of the anode plate and sub-pixels are designed to generate the primary colours. The important parameter for the FED is the low onset voltage, which allows for matrix addressed displays using low-voltage CMOS drivers, as in LCDs. CNT-FEDs are characterized by low power consumption, high brightness, wide viewing angle, fast response rate and a wide operating temperature range.

The FED was first presented by Samsung, which has developed several prototypes in the past years [35,36]. The last 5 inch display was operated at 100 V and an anode biases of 1.5 kV. The image was observed with a duty ratio of 1/120 and a frequency of 100 Hz (Fig. 5.10 (left)). The 40'' FED was presented also by ISE/Japan in year 2002 [33] (Fig. 5.10

(right)). The main problem of both was the homogeneity, where even with a high emitter number density of  $10^6/\text{cm}^2$  some pixels drop out.

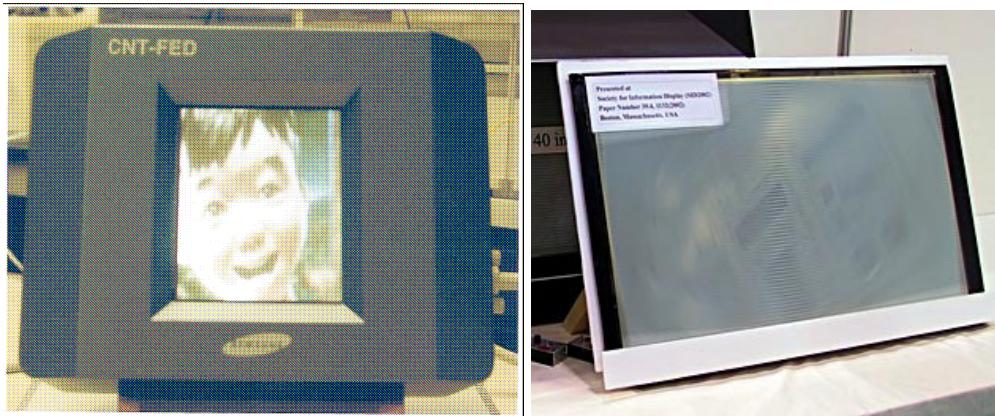


Fig. 5.10. Colour 5'' FED presented by Samsung/Korea (left) and the 40'' prototype presented by ISE /Japan (right) in the year 2002.

The commercial advantage of the Samsung technology, in comparison to another, is that all CNT-based materials are printable inks, which can be deposited on a substrate like the conventional screen-printing of thick films [174]. After a heat treatment the organic binder is removed and the CNT are embedded in the metal electrodes. The inhomogeneity problem for this material, however, was not resolved over the last 5 years. More promising approach for the pixel formation was presented by Dean et al. [182]. They developed self-assembled CNT growth on Ni patches of size  $5 \times 10 \mu\text{m}^2$  with low temperature CVD. This approach enables one to produce high number densities  $\sim 10^7/\text{cm}^2$  of CNT emitters with  $\beta > 1000$  and good redundancy. Moreover, this technology is easy to scale up for mass production. This material was employed for the construction of a brilliant FED by Dijon et al. in 2005 [183]. The device of  $320 \times 240$  resolution and pixel size  $350 \mu\text{m}$ , showed the luminance of  $\sim 800 \text{ cd}/\text{m}^2$  and good uniformity in a range of 5%. Unfortunately, there are still problems in pixel drop-out.

## 5.6 Multiple e-beam lithography

The semiconductor lithography and mask production required now the sub-100 nm techniques. Electron beam direct writing which is now chosen as a potential candidate for this application, has a very low speed due to the employment of only a single e-beam. To solve this problem the straight forward concept of writing with multiple e-beams was developed. The feasibility of this approach was demonstrated using an array of miniature electron beam columns by Muray [184]. Binh et al. [185] developed a microgun concept which uses a nanotip with micron-sized electrostatic extraction, while focus and deflection lenses were fabricated on the single silicon substrate. The resulting e-beam have the nm spot size. The EC funded IST project, which investigates the feasibility of parallel e-beam lithography, showed

the initial concept based of 32 microguns [37]. Of course, the required objective is to achieve high throughput maskless direct writing capability with an array of 1 million microguns.

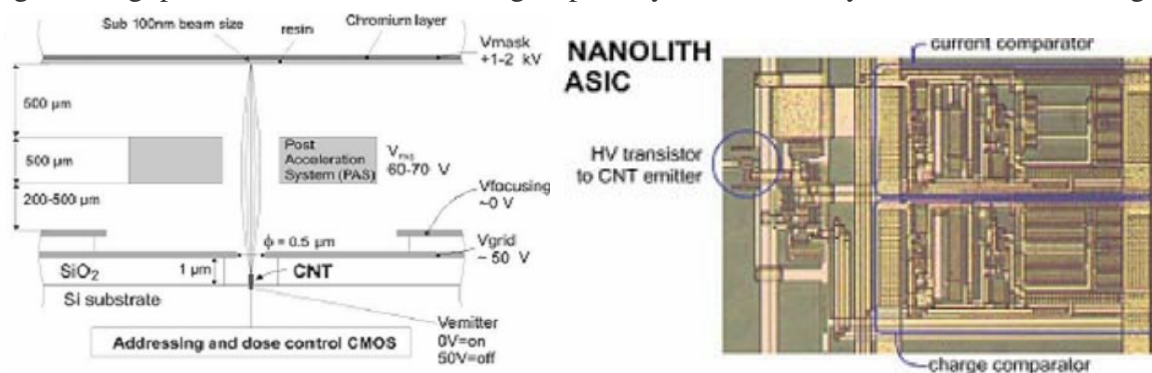


Fig. 5.11. Design of one element/microgun of the ‘Nanolith’ writing head (left) and optical micrograph of the dose control ASIC (right) [37].

In Fig. 5.11 is schematically shown a single element of the writing head which includes the microgun, active matrix dose control CMOS circuitry and a post acceleration system (PAS) [37]. The PAS electrically screens the low voltage microgun from the high acceleration voltage (1–2 keV), and also physically shields the microgun from back ion bombardment due to the outgassing of the resist during exposure. The CMOS circuits (ASIC in Fig. 5.11(right)) precisely control the dose produced by each microgun, since each emitter will have variations in emitted current. The addressing of large number of microguns is still a problem. The expected spot size for this system will be nearly equal to the diameter of CNT. In such a complicated pentode configuration the most critical parameter for obtaining sub-100 nm resolution is the alignment between the emitter and the extraction gate hole, thus a technique with mutual self alignment is required.

## 5.7 Outlook

The utilisation of the advantages of cold FE cathodes in electronic is a very competitive task. On the one hand, the concepts of different FE applications have existed more than 10 years, while on the other hand there are still difficulties in developing commercial products. Thus, the problem of inefficient phosphors keep the diode FE light sources in the prototype stage, despite of various cathode materials, which fulfill the requirements (Tab. 5.1). It is quite feasible, however, to use triode CNT based lighting elements to assemble a full-colour display with video frame speed for large pixel screens for stadiums, signs etc.

X-ray tubes are now fully commercialised and will have to compete against existing x-ray sources and three-dimensional tomographic imaging techniques. Utilisation of the main advantage of CNT based x-ray tubes – compactness, will lead to portable and miniature x-ray sources for industrial and medical applications.

The FED application has been a huge attraction because the total display market is \$50 billion per year. It is, however, currently dominated by liquid crystal displays (LCD), where the image is formed by varying light transmission through a series of many liquid crystal pixels. The advantages of FED over LCD are a higher video rate, higher power efficiency, and operating temperature range. A previous disadvantage of LCD of small viewing angle was corrected some years ago and is no longer an issue. J. Robertson [186] summarised the

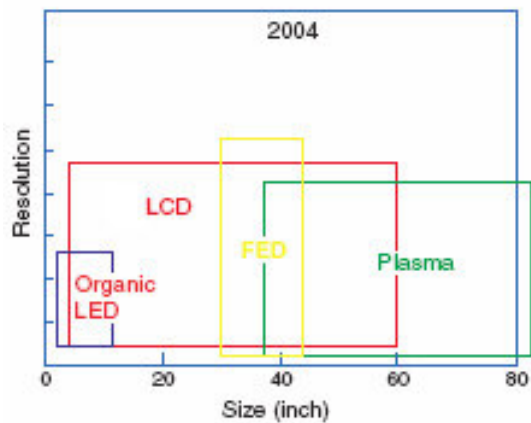


Fig. 5.12. Schematic showing the dominant areas of display technologies as a function of display size and resolution. In 2004, LCD span small and large area applications, plasma has taken over at larger areas, while organic light emitting diodes (OLED) are entering the small area display market. This leaves FED as a large area display market around 34" [186].

information in the year 2004 about the existing technologies showing the dominant areas of display technologies as a function of size and resolution (Fig. 5.12). After the first success of CNT implementation for FED in 1995 was predicted that they should be first used, as an example, as 5" units in car navigation displays and as seat-back TVs in airplanes. However, the development difficulties of FED pushed the LCD technology into the first place, having captured the small display market (e.g. cell phones). In addition, organic light-emitting diodes (OLED) are a promising future technology for sub-5" displays. The Fig. 5.12 shows that the whole region 5-80 inch is occupied now by LCD and PDP. The FED, however, have a lower cost base and better power efficiency than PDP. If the FED

technology is to succeed in the near future, it will most probably occupy the large area display market over 30".

The CNT emitters are ideal for the multi e-beam application, however, more work should be invested to reach required stability and brilliance of the every of multiple e-beam. Most probably, due to easily controlled geometry the metallic nanowires will be one of the potential candidates for this application. More investigations, however, should be provided for the implementation of such materials. Since currently a set of photomasks for CMOS costs ~ 2 million euros the advantage of these technique, even if not fulfill the requirements for the mass IC production, will be observable in the near future. The FE applications are also likely to succeed where cost is not a key issue, such as RF-guns, electron guns for SEM, etc.

---

## Summary

The main objectives of this work consisted in the improvement of the integral measurement system (IMLS) and in the optimization of FE properties of CNT and metallic nanowire based cold cathodes.

The IMLS hardware was extended by a power supply with a PID regulated 5 kV voltage output, which provides safe conditioning of the cathodes at a constant currents of up to 50 mA. The pulsed regime was also enabled for this power supply, which provides an increase of the output voltage from 0 to 5 kV within 2 ms. Thereby, the heat loads on the luminescent screen are much reduced, and discharges have been prevented up to 20 V/ $\mu\text{m}$ . Moreover, high peak currents in pulsed mode provide faster conditioning of the cathodes.

The image data acquisition of the IMLS has been facilitated by means of the AnalySIS® software package. It automatizes the time consuming operations e.g. emitter number calculation and classification, size calibration etc. Imaging with a 10 Hz frequency allows detailed investigation of the fluctuations of single emitters and long-term stabilities of the cathodes. An algorithm for the conversion of the IMLS images into current maps was developed for the fast analysis of the current distribution over the sample surface without FESM. The calibration of the light intensity of the luminescent screen as a function of current, voltage, and power was performed on typical IMLS images. Resulting I-maps attribute the local emission current to the light clusters and allow to determine the current carrying capability and stability of different emission areas. Moreover, it give additional opportunities for emitter counting and classification.

The first part of the results is dedicated to the investigation of the shielding effect. Therefore, the tests of MWCVD grown CNT on Si, which build a densely packed layer of emitters on the surface, were performed. In the IMLS, an insufficient emission current of 300 nA was observed only from a few spots at 6 V/ $\mu\text{m}$ . The FESM U-scans show the emitter number density of 9600/cm<sup>2</sup> at  $E < 17.5$  V/ $\mu\text{m}$ . The local measurements show, that the emitters can be splitted into two groups, shielded CNT in the central area of the dense layer and free standing CNT at the edges. The emitters reveal high onset fields of 12-21 V/ $\mu\text{m}$  and field enhancement values of 140-370. The emitter number and current densities lay far below the requirements of the relevant applications.

The main part of the results is dedicated to the investigation of the CNT samples on porous alumina, which allows to control the number density of emitters. The porous alumina for the CNT growth are divided into two groups – commercial Anodisc® with fixed morphology and self-made EPAM, with variable pore diameter and thickness.

The influence of the catalyst type and morphology to the FE was investigated on the basis of CNT samples on Anodisc®. Five metalorganic precursors: nickelocene, chromocene, cobaltocene, Fe-Co-S complex and ferrocene were tested for CNT growth in order to find the preferred catalyst. The ferrocene grown CNT reveal the best homogeneity of the emission, highest emitter ( $\sim 7000/\text{cm}^2$ ) and current density of 1.1 mA/cm<sup>2</sup> at 3.5 V/ $\mu\text{m}$ . This precursor

was chosen as the best candidate for the FE cathodes on porous alumina. It was also found, that the amount of the precursor influence the quantity of the CNT on the surface, thus FE parameters. Comparison of the CNT samples grown with 70 and 100 mg ferrocene show, that higher amount of catalyst leads to a pronounced shielding effect, thus higher operation fields. The samples produced with 70 mg ferrocene reveal on average factor 5 higher current densities at 5 V/ $\mu\text{m}$ , than the samples produced with 100 mg. Thus, the amount of ferrocene allows to vary the output parameters of the CNT samples towards high currents or low operation fields.

The alumina particles on the porous template surface partially close the pores reducing the CNT growth and serve as an anchor for them, increasing the mechanical stability of emitters. In contrast, large amount of alumina particles isolate the sample surface resulting in insufficient field emission. The resulting CNT samples reveal, consequently, mostly no emission. In order to simplify the fabrication process and grow porous alumina controlled CNT, the etching technique without alumina particles was tested. The resulting sample show isles of grouped pores with only a few CNT on the surface. Decreasing of the pore diameter on the inlet side in the MOCVD process yielded a solid layer of CNT. In both cases emission currents, useless for FE applications were obtained.

The mechanical stress due to shrinking of the porous alumina, which occurred during the heating in the MOCVD, resulted in randomly bent sample pieces of some  $\text{mm}^2$  size revealing height differences up to 200  $\mu\text{m}$ , which results in severe electric field variations. The curvature of these samples could not be avoided and has been taken into account for the calculation of the electric field in the IMLS. It was regularly estimated from the  $U(z)$  calibration plots and results in the effective electric field. Alternatively, it was precisely determined by means of a new profilometer and revealed the real changes of the electric field over the surface as measured for few samples. The curvature of the samples also triggers the non-linearity of the integral FN plots through the enormous field enhancement of emitters at the edges and inhomogeneous distribution of the electric field.

In order to understand the properties of single emitters, investigate their FE parameters and their contribution to the total emission current, the FESM studies were performed for CNT samples on Anodisc®. Emitter number densities up to 60000/ $\text{cm}^2$  were observed in U-maps at  $E < 9 \text{ V}/\mu\text{m}$ . This value leads, on average, to about 1 emitter per square area of  $40 \times 40 \mu\text{m}^2$ , despite of a much higher overall number of CNT  $\sim 10^6/\text{mm}^2$ . The local measurements of 30 single CNT emitters show instabilities – activation, degradation and destruction effects at currents of 1–10  $\mu\text{A}$ . Only a few of them provide stable FN behavior. The field enhancement factors 15-870 were correlated to the onset fields. The smallest  $\beta$  values can be explained by a large number of short shielded CNT grown from the pores. Only 2 of 30 random emitters were able to produce 1 nA current at  $E < 10 \text{ V}/\mu\text{m}$ . Thus, only a very small portion of CNT participate in the emission of such cathodes, resulting in limited current densities.

The best results show the CNT samples on EPAM, which provide the highest  $\beta$  values, higher stability and current carrying capability. Moreover, it was found that the current densities are strongly influenced by the pore diameter. As expected, a strong increase of the dc current density at 4 V/ $\mu\text{m}$  has been found for pore diameters below 60 nm. The maximum current density of 83 mA/cm<sup>2</sup> was extracted at  $E = 7$  V/ $\mu\text{m}$  from the EPAM with an average pore diameter of  $\sim 22$  nm. Thus, the highest current densities can be achieved only for EPAM. Since from a  $\sim 20$  nm pore only one CNT with the same diameter can grow, further decrease of the pore diameter should drastically worsen the FE parameters.

FESM scans of the CNT samples on EPAM show, that the number of emitters on the side, which was exposed to the gas inlet flow in the MOCVD process  $\sim 48000/\text{cm}^2$  at 6.2 V/ $\mu\text{m}$  is a factor of 4 higher than for opposite at the same field. SEM studies have revealed MWNT, which are longer and more densely on the inlet side. Accordingly, quite different field enhancement factors  $\beta$  of single emitters have been found on both sides  $\sim 200$ -500 (outlet) and  $\sim 600$ -2100 (inlet). Thus, the field enhancement factors and the emitter number densities depend more on the CVD growth conditions, than on pore diameters. It is remarkable that the sparsely grown CNT on the outlet side are favorable for high current densities. Less shielding and a better anchoring of the CNT for matched pore diameters might cause the improved current carrying capability of the samples on porous alumina.

Single CNT emitters on both Anodisc® and EPAM have shown fluctuations, long-term instabilities, and strong ( $\sim 50\%$ ) current drift over some hours. Resolved in the ms time scale the emission current shows a switching between several electronic states, which is caused by the adsorbates. Usually, during the first increase of the voltage, processing of some emitters has been observed which leads to small permanent current jumps in the integrally measured I-V curve. Besides the repeated on and off switching of light spots within seconds, a permanent activation or deactivation of emitters has also been seen in the IMLS videos, which result in lower stability of the Anodisc® cathodes. The instabilities of the strong emitters on the surface often lead to discharges due to high local currents. The long-term stability of CNT cathodes was tested at different pressures over several hours, resulting in strong degradation of the emission current at  $5 \times 10^{-4}$  mbar for all samples. At  $10^{-6}$  mbar the emission current of Anodisc® degraded continuously by  $\sim 35\%$  over 8 hours, for the EPAM only by 10%. Accordingly much better current stability was achieved for the EPAM samples by means of current processing. The excellent current stability of  $\pm 10\%$  over 18 hours was demonstrated.

It was established by means of the converted IMLS images that the distribution of the current density over the sample surface is inhomogeneous, mainly due to curvature. In some areas the current density is up to a factor of 5 higher, than the average integral value. In this way dc current densities of up to 108 mA/cm<sup>2</sup> were observed for the CNT samples on EPAM. The current carrying capability and emission homogeneity of CNT on both Anodisc® and EPAM substrates were improved due to processing in the pulsed operation. The optimised



CNT samples on Anodisc® show a current density of  $5.6 \text{ mA/cm}^2$  in pulsed operation at  $E = 12.3 \text{ V/}\mu\text{m}$ . The CNT on EPAM yielded much higher peak current densities of up to  $0.2 \text{ A/cm}^2$  at  $E = 11.5 \text{ V/}\mu\text{m}$ , which is close to the maximum values reported in the literature.

The first experiments on the metallic nanowires with different geometrical properties resulted in an emission site density of up to  $1.4 \times 10^5 \text{ cm}^{-2}$  at  $6 \text{ V/}\mu\text{m}$ . Only 6% of the free-standing and vertically aligned nanowires were strong emitters. Nearly all wires showed unstable FN behaviour with a mean  $\beta$  value of  $\sim 250$ , which is a factor three higher than expected from the emitter shape due to influence of the tip geometry. For nanowires of  $18 \mu\text{m}$  length and submicron spacing, several hundred nanowires agglomerated into bundles, which show good FE properties. The application potential of these nanostructures, however, require more optimization towards low onset fields, current densities, and emission uniformity.

Finally, the investigated CNT based porous alumina cathodes reveal low onset fields, high emitter number and current densities and good current stability. They, however, still suffer from emission inhomogeneity, extreme brittleness and curvature of the substrates, which is not suitable for the most applications like FED, x-ray tubes, etc. Nevertheless, the increased number of emitters and enlarged halos in the pulsed regimes leads to a much improved luminescence and homogeneity of the emission, which was used for the construction of a light source demonstrator.

---

## Acknowledgements

First and foremost, I would like to thank my adviser, Prof. Dr. Günter Müller, for the outstanding leadership and support that he provided over the past several years. He encouraged me to develop independent thinking and research skills. He continually stimulated my analytical thinking and greatly assisted me with scientific writing.

I would like to thank Jahan Pouryamout for always being available to help me in the minor and major problems and for his excellent knowledge in vacuum technique.

I thank my colleague M. Tech. Arti Dangwal for the local FESM measurements and for the constructive discussions about field emission. She was always ready to help and support me.

Without the cooperation partners this work would have not been possible. I would like to thank Prof. Dr. J. J. Schneider and Dr. J. Engstler at the Technical University of Darmstadt for providing the CNT samples and constructive discussions. I want also to thank Dipl.- Phys. Florian Maurer for providing the interesting possibility of the investigation of metallic nanowires.

I thank Dipl.-Phys. Andreas Gasper at the University of Dortmund, with whom the investigations of the CNT cathodes in the RF-gun were performed at DELTA.

Special thanks to Dr. Ralf Heiderhoff for providing the SEM facility in the electrical engineering department.

I thank Prof. Dr. Ronald Frahm for his willingness to review this work.

I would like to thank my wife, Alena for the great support and understanding during the writing. She always motivates me to work harder and do my best.

I thank the VolkswagenStiftung(Germany) for the financial support.

---

## References

- [1] R.W. Wood, *Rhys. Rev.* 5(1), 1 (1897).
- [2] R. H. Fowler, L. W. Nordheim, *Proc. Royal Soc.(London)* A119, 173 (1928).
- [3] D. Alpert, D. A. Lee, E. M. Lyman, H. E. Tomaschke, *J. Vac. Sci. Technol.* 1, 35 (1964).
- [4] D. K. Davies, M. A. Biondi, *J. Appl. Phys.* 39, 2979 (1968).
- [5] C. J. Bennette, L. W. Swanson, F. M. Charbonnier, *J. Appl. Phys.* 38, 634 (1967).
- [6] Ph. Niedermann, These No 2197, University of Genf/Switzerland (1986).
- [7] E. Mahner, Dissertation, WUB-DIS 95-7, University of Wuppertal (1995).
- [8] N. Pupeter, Dissertation, WUB-DIS 96-16, University of Wuppertal (1996).
- [9] I. Brodie, *J. Appl. Phys.* 35, 2324 (1967).
- [10] J. P. Barbour, W. W. Dolan, J. K. Trolan, E. E. Martin, W. P. Dyke, *Phys. Rev.* 92, 45 (1953).
- [11] F. M. Charbonnier, C. J. Bennette, L. W. Swanson, *J. Appl. Phys.* 38, 627 (1967).
- [12] S. Iijima, *Nature* 354, 56 (1991).
- [13] M. S. Dresselhaus, G. Dresselhaus, R. Saito, *Phys. Rev. B* 45, 6234 (1992).
- [14] J. W. Mintmire, B. I. Dunlap, C. T. White, *Phys. Rev. Lett.* 68, 631 (1992).
- [15] J. M. Planeix, N. Coustel, B. Coq, V. Brotons, P. S. Kumbahr, R. Dutartre, P. Geneste, P. Bernier, P. M. Ajayan, *J. Am. Chem. Soc.* 116, 7934 (1995).
- [16] A. G. Rinzler, J. H. Hafner, P. Nickolaev, L. Lou, S. G. Kim, D. Tomanek, D. Colbert, R. E. Smalley, *Science* 269, 1550 (1995).
- [17] P. J. Britto, K. S. V. Santhanam, P. M. Ajayan, *Bioelectrochem. Bioenergetics* 41, 121 (1996).
- [18] A. Thess, R. Lee, P. Nickolaev, H. Dai, P. Petit, J. Robert, C. Xu, Y. H. Lee, S. G. Kim, A. G. Rinzler, D. T. Colbert, G. E. Scuseria, D. Tomanek, J. E. Fischer, R. E. Smalley, *Science* 273, 483 (1996).
- [19] J. W. G. Wildöer, L. C. Venema, A. G. Rinzler, R. E. Smalley, C. Dekker, *Nature* 391, 59 (1998).
- [20] T. W. Odom, J. L. Huang, P. Kim, C. M. Lieber, *Nature* 391, 62 (1998).
- [21] H. D. Wagner, O. Lourie, Y. Feldman, T. Tenne, *Appl. Phys. Lett.* 72, 188, (1998).
- [22] Q. H. Wang, T. D. Corrigan, J. Y. Dai, R. P. H. Chang, A. R. Krauss, *Appl. Phys. Lett.* 70, 3308 (1997).
- [23] W. de Heer, A. Chatelain, D. Ugarte, *Science* 270, 1179 (1995).
- [24] J. Liu, A. G. Rinzler, H. Dai, J. H. Hafner, R. K. Bradley, P. J. Boul, A. Lu, T. Iverson, K. Shelimov, C. B. Huffman, F. Rodriguex-Macia, D. T. Colbert, R. E. Smalley, *Science* 280, 1253 (1998).
- [25] W.Z. Li, S.S. Xie, L.X. Qian, B.H. Chang, B.S. Zou, W.Y. Zhou, R.A. Zhao, G. Wang, *Science*, 274, 1701 (1996).
- [26] M. Meyyappan, L. Delzeit, A. Cassell, D. Hash, *Plasma Sources Sci. Technol.* 12, 205 (2003).
- [27] J. J. Schneider, J. Engstler, S. Franzka, K. Hofmann, B. Albert, J. Ensling, P. Gütlich, P. Hildebrandt, S. Döpner, W. Pflöging, B. Günther, G. Müller, *Chem. Eur. J.* 7, 2888 (2001).
- [28] N.S. Xu, S.E. Huq, *Mater. Sci. Eng. R* 48, 47 (2005).
- [29] Y.B. Li, Y. Bando, D. Golberg, K. Kurashima, *Appl. Phys. Lett.* 81, 5048 (2003).

- 
- [30] G. Müller, Technical digest of the 18<sup>th</sup> Vacuum Nanoelectronics Conf., Oxford, IEEE Cat. No.05TH8837, 66 (2005).
- [31] Y. Saito, S. Uemura, Carbon 38, 169, (2000).
- [32] G. Z. Yue, Q. Qiu, B. Gao, Y. Cheng, J. Zhang, H. Shimoda, S. Chang, J.P. Lu, O. Zhou, Appl. Phys. Lett. 81, 355 (2002).
- [33] <http://www.noritake-elec.com/itron/>
- [34] [www.xintek.com](http://www.xintek.com)
- [35] W.B. Choi, D.S. Chung, J.H. Kang, H.Y. Kim, Y.W. Jin, I.T. Han, Y.H. Lee, J.E. Jung, N.S. Lee, G.S. Park, J.M. Kim, Appl. Phys. Lett. 75, 3129 (1999).
- [36] D.-S. Chung, S.H. Park, H.W. Lee, J.H. Choi, S.N. Cha, J.W. Kim, J.E. Jang, K.W. Min, S.H. Cho, M.J. Yoon, J.S. Lee, C.K. Lee, J.H. Yoo, J.-M. Kim, J.E. Jung, Y.W. Jin, Y.J. Park, J.B. You, Appl. Phys. Lett. 80, 4045 (2002).
- [37] K. B. K. Teo, M. Chhowalla, G. A. J. Amaratunga, W. I. Milne, P. Legagneux, G. Pirio, E. Balossier, D. Pribat, V. Semet, V. Thien Binh, W. H. Bruenger, J. Eichholz, H. Hanssen, D. Friedrich, S. B. Lee, D. G. Hasko, H. Ahmed, J. Vac. Sci. Technol., B 21, 693 (2003).
- [38] B. Günther, Dissertation, WUB-DIS 02-8, University of Wuppertal (2002).
- [39] W. Schottky, Z. Physik 14, 63 (1923).
- [40] B. S. Gossling, Phil. Mag. 1, 609 (1926).
- [41] R. A. Millikan, C. F. Eyring, Phys. Rev. 27, 51 (1926).
- [42] R. J. Piersol, Phys. Rev. 31, 441 (1928).
- [43] R. A. Millikan, C. C. Lauritsen, Phys. Rev. 33(4), 598 (1926).
- [44] J. R. Christman, Fundamentals of solid state physics, John Wiley & Sons, New York (1988).
- [45] R. E. Burgess, H. Kroemer, J. M. Houston, Phys. Rev. 90, 515 (1953).
- [46] W. P. Dyke, J.K. Trolan, Phys. Rev. 89(4), 799 (1953).
- [47] C. D. Ehrlich, E. W. Plummer, Phys. Rev. B 18, 3767 (1978).
- [48] G. Lea, R. Gomer, Phys. Rev. Lett. 26, 92 (1971).
- [49] P. H. Cutler, J. He, M. N. Miskovsky, J. Vac. Sci. Technol. B11(2), 387 (1993).
- [50] T. Utsumi, IEEE Transactions on Electron Devices 38, 2276 (1991).
- [51] H. Dai, Acc. Chem. Res. 35, 1035 (2002).
- [52] M. S. Dresselhaus, G. Dresselhaus, P. Avouris, „Carbon Nanotubes Synthesis, Structure, Properties and applications“, Springer: Berlin (2001).
- [53] Y. Cui, Q. Q. Wei, H. K. Park, C. M. Lieber, Science 293, 1289 (2001).
- [54] P. M. Ajayan, O. Stephan, C. Colliex, D. Trauth, Science 265, (1994).
- [55] Z. Yu, C. Rutherglen, S. Li, P.J. Burke, Nanotech. 3, 123 (2005).
- [56] C. J. Lee, S. C. Lyu, H. W. Kim, C. Y. Park, C. W. Yang, Chem. Phys. Lett. 359, 109 (2002).
- [57] C. Dekker, Phys. Today 52, 22 (1999).
- [58] P.L. McEuen, Phys. World 13 (6), 43 (2000).
- [59] W. Liang, M. Bockrath, C. Bozovic, J. Hafner, M. Tinkham, H. Park, Nature 411, 665 (2001).
- [60] J. Kong, E. Yenilmez, T. W. Tombler, W. Kim, H. Dai, R. B. Laughlin, L. Liu, C. S. Jayanthi, S. Y. Wu, Phys. Rev. Lett. 87, 106801 (2001)
- [61] W. Zhu, G. P. Kochanski, S. Jin, L. Siebels, J. Vac. Sci. Technol. B 14, 2011 (1996).
- [62] W. Zhu, C. Bower, O. Zhou, G. P. Kochanski, S. Jin, Appl. Phys. Lett. 75, 873 (1999).
- [63] O. Gröning, O. M. Küttel, C. Emmengger, P. Gröning, L. Schlapbach, Appl. Phys. Lett. 73, 2113 (1998).

- 
- [64] L. Nilsson, O. Groening, P. Groening, O. Kuettel, L. Schlappbach, *J. Appl. Phys.* 90, 768 (2001).
- [65] O. Gröning, O. M. Küttel, C. Emmenger, P. Gröning, L. Schlappbach, *J. Vac. Sci. Techn. B* 18, 665 (2000).
- [66] Y. Saito, K. Hamaguchi, K. Hata, K. Tohji, A. Kasuya, Y. Nishina, K. Uchida, Y. Tasaka, F. Ikazaki, M. Yumura, *Ultramicroscopy* 73, 1 (1998).
- [67] S. Han, J. Ihm, *Phys. Rev. B*, 61, 9986 (2000).
- [68] J. Engstler, Dissertation, FB Chemie, University of Duisburg-Essen (2003).
- [69] J. Cumings, A. Zettl, M. R. McCartney, J.C. H. Spence, *Phys. Rev. Lett.* 88, 056804 (2002).
- [70] X. Zheng, G. H. Chen, Z. Li, S. Deng, N. Xu, *Phys. Rev. Lett.* 92, 106803 (2004).
- [71] J. Zhou, S. Z. Deng, N. S. Xu, J. Chen, J. C. She, Technical Digest of 15th IVMC and 48th IFES, Lyon, France, PM15 (2002).
- [72] Y. H. Lee, C. H. Choi, Y. T. Jang, E. K. Kim, B. K. Ju, N. K. Min, J. H. Ahn, *Appl. Phys. Lett.* 81, 745 (2002).
- [73] F. Maurer, A. Dangwal, D. Lysenkov, G. Müller, M. E. Toimil-Molares, C. Trautmann, J. Brötz, H. Fuess, *Nucl. Instr. and Meth. in Phys. Res. B* 245, 337 (2006).
- [74] Z. Zhang, X. Sun, M. S. Dresselhaus, J. Y. Ying, J. Heremans, *Phys. Rev. B* 61, 4850 (2000).
- [75] P. A. Smith, C. D. Nordquist, T. N. Jackson, T. S. Mayer, B. R. Martin, J. Mbindyo, T. E. Mallouk, *Appl. Phys. Lett.* 77, 1399 (2000).
- [76] L. Nilsson, O. Groening, C. Emmenegger, O. Kuettel, E. Schaller, L. Schlappbach, H. Kind, J. M. Bonard, K. Kern, *Appl. Phys. Lett.* 76, 2071 (2000).
- [77] J. M. Bonard, N. Weiss, H. Kind, T. Stockli, L. Forro, K. Kern, A. Chatelain, *Adv. Mater.* 13, 184 (2001).
- [78] K.B.K. Teo, M. Chhowalla, G. A. J. Amaratunga, W. I. Milne, G. Pirio, P. Legagneux, D. Pribat, D. G. Hasko, *Appl. Phys. Lett.* 80, 2011 (2002).
- [79] J. S. Suh, K. S. Jeong, J. S. Lee, "Study of field screening effect of highly ordered carbon nanotube arrays", *Appl. Phys. Lett.* 80, 2392-239 (2002).
- [80] A. Zeitoun-Fakiris, B. Jüttner, *J. Phys. D: Appl. Phys.* 24, 750 (1991).
- [81] A. Zeitoun-Fakiris, B. Jüttner, *J. Phys. D: Appl. Phys.* 21, 960 (1988).
- [82] L.W. Swanson, R.W. Crouser, *Phys. Rev.* 13, 622 (1967).
- [83] R.H. Good, E. W. Müller "Handbuch der Physik", Springer-Verlag, Berlin (1956).
- [84] G. Ehrlich, F.G. Hudda, *J.Chem. Phys.* 35, 1421 (1961).
- [85] T. Habermann, Dissertation, WUB-DIS 98-18, University of Wuppertal (1998).
- [86] C. B. Duke, M. E. Alferieff, *J. Chem. Phys.* 46, 923 (1967).
- [87] J. W. Gadzuk, *Phys. Rev. B* 1, 2110 (1970).
- [88] K. M. Ho, S. G. Louie, J.R. Chelikovsky, M.L. Cohen, *Phys. Rev. B* 15, 1755 (1977).
- [89] K. A. Dean, B. R. Chalamala, *Appl. Phys. Lett.* 76, 375 (2000).
- [90] K. A. Dean, P. von Allmen, B. R. Chalamala, *J. Vac. Sci. Technol. B* 17, 1959 (1999).
- [91] P. G. Collins, K. Bradley, M. Ishigami, A. Zettl, *Science*, 287, 1801 (2000).
- [92] C. Li, D. Zhang, X. Liu, S. Han, T. Tang, J. Han, C. Zhou, *Appl. Phys. Lett.* 82, 1613 (2003).
- [93] G. Stan, M. J. Bojan, S. Curtarolo, S. M. Gatica, M. W. Cole, *Phys. Rev. B*, 62, 2173 (2000).
- [94] D. A. Wharam, T. J. Thornton, R. Newbury, M. Pepper, H. Ahmed, J. E. F. Frost, D. G. Hasko, D. C. Peacock, D. A. Ritchie, G. A. C. Jones, *J. Phys. C: Solid State Phys.* 21, 209 (1988).
- [95] S. Sanvito, Y.K. Kwon, D. Tomanek, C.J. Lambert, *Phys. Rev. Lett.* 84, 1974 (2000).
- [96] H. J. Li, W.G. Lu, J.J. Li, X.D. Bai, C.Z. Gu, *Phys. Rev. Lett.* 95, 086601 (2005)

- 
- [97] W. Yi, L. Lu, D. L. Zhang, Z. W. Pan, S. S. Xie, *Phys. Rev. B*, 59, R9015 (1999).
- [98] Z. Yao, C.L. Kane, C. Dekker, *Phys. Rev. Lett.* 84, 2941 (2000).
- [99] B. Bhushan, „Springer handbook of nanotechnology“, Springer-Verlag Berlin Heidelberg (2004).
- [100] M. E. Toimil-Molares, E. M. Höhberger, Ch. Schaefflein, R. H. Blick, R. Neumann, C. Trautmann, *Appl. Phys. Lett.*, 82, 2139 (2003).
- [101] M. P. Zach, K. H. Ng, R. M. Penner, *Science*, 290, 2120 (2000).
- [102] R. V. Latham, K. H. Bayliss, B. M. Cox, *J. Phys. D: Appl. Phys.* 19, 219 (1986).
- [103] R. V. Latham, “High voltage vacuum insulation: basic concepts and technological practice”, Academic Press (1995).
- [104] J. M. Bonard, C. Klinke, K. A. Dean, B. F. Coll, *Phys. Rev. B* 67, 115406 (2003).
- [105] S. M. Lee, Y. H. Lee, Y. G. Hwang, J. R. Hahn, H. Kang, *Phys. Rev. Lett.* 82, 217 (1999).
- [106] K. A. Dean, T. P. Burgin, B. R. Chalamala, *Appl. Phys. Lett.* 79, 1873 (2001).
- [107] S. T. Purcell, P. Vincent, C. Journet, V. T. Binh, *Phys. Rev. Lett.* 88, 105502 (2002).
- [108] P. Vincent, S. T. Purcell, C. Journet, V.T. Binh, *Phys. Rev. B* 66, 075406 (2002).
- [109] Y. Wei, C. Xie, K. A. Dean, B. F. Coll, „Stability of carbon nanotubes under electric field studied by scanning electron microscopy“, *Appl. Phys. Lett.* 79, 4527 (2001).
- [110] Z. L. Wang, P. Poncharal, W.A. de Heer, *Appl. Phys. Lett.* 80, 856 (2002).
- [111] C. Journet, W. K. Maser, P. Bernier, A. Loiseau, M. Lamy de la Chapelle, S. Lefrant, P. Deniard, R. Lee, J. E. Fischer, *Nature (London)*, 388, 756 (1997).
- [112] L. Alvarez, T. Guillard, J.L. Sauvajol, G. Flamant, D. Laplaze, *Appl. Phys. A* 70, 169 (2000).
- [113] J.-F. Colomber, J.-M. Benoit, C. Stephan, S. Lefrant, G. Van Tendeloo, J. B. Nagy, *Chem Phys. Lett.*, 345, 11 (2001).
- [114] V. Ivanov, A. Fonseca, J. B. Nagy, A.A. Lucas, D. Bernaerts, X.B. Zhang, *Carbon*, 33, 1727 (1995).
- [115] P. Piedigrosso, Z. Konya, J. F. Colomber, A. Fonseca, J. B. Nagy, *Phys. Chem. Chem. Phys.* 2, 163 (2000).
- [116] Y. Saito, *Carbon* 33, 979 (1995).
- [117] H. N. Lin, Y.H. Chang, J.H. Yen, J.H. Hsu, I.C. Leu, M.H. Hon, *Chem. Phys. Lett.*, 399, 422 (2004).
- [118] H. Dai, *Surf. Sci.* 500, 218 (2002).
- [119] T. Nozaki, Y. Kimura, K. Okazaki, *J. Phys. D*, 35, 2779 (2002).
- [120] G. Y. Zhang, X.C. Ma, D. Y. Zhong, E. G. Wang, *J. Appl. Phys.*, 91, 9324 (2002).
- [121] Y. J. Lee, E. K. Lee, S. Kim, *Phys. Rev. Lett.* 86, 999 (2001).
- [122] F. Ding, K. Bolton, A. Rosen, *J. Vac. Sci. Technol. A* 22, 1471 (2004).
- [123] K. F. Peters, J. B. Cohen, Y. W. Chung, *Phys. Rev. B* 57, 13430 (1998).
- [124] S. L. Lai, J. Y. Guo, V. Petrova, G. Ramanath, L. H. Allen, *Phys. Rev. Lett.* 77, 99, (1996).
- [125] A. N. Goldstein, C. M. Echer, A. P. Alivisatos, *Science* 256, 1425 (1992).
- [126] F. Ding, A. Rosen, K. Bolton, *Chem. Phys. Lett.* 393, 309 (2004).
- [127] S. Maruyama, Y. Miyauchi, T. Edamura, Y. Igarashi, S. Chiashi, Y. Murakami, *Chem. Phys. Lett.* 375, 553 (2003).
- [128] C. Klinke, J.-M. Bonard, K. Kern, *Phys. Rev. B* 71, 035403 (2005).
- [129] C. J. Lee, J. Park, Y. Huh, J. Lee, *Chem. Phys. Lett.* 343, 33 (2001).
- [130] [www.whatman.com](http://www.whatman.com)
- [131] J. Khachan, B. W. James, A. Marfoure, *Appl. Phys. Lett.* 77, 2973 (2000).
- [132] L. de Poucques, J. Bougdira, R. Hugon, G. Henrion, P. Alnot, *J. Phys. D* 34, 896 (2001).

- 
- [133] V. V. Dvorkin, N. N. Dzbanovski, P. V. Minakov, N. V. Suetin, A. Yu. Yur'ev, *Plasma Physics Reports*, 29, 9 (2003).
- [134] H.C. Lo, D. Das, J.S. Hwang, K.H. Chen, C.H. Hsu, C.F. Chen, L.C. Chen, *Appl. Phys. Lett.* 83, 1420 (2003).
- [135] S.Z. Deng, Z.S. Wu, J. Zhou, N.S. Xu, J. Chen, J. Chen, *Chem. Phys. Lett.* 356, 511 (2002).
- [136] I. U. Schuchert, M.E. Toimil-Molares, D. Dobrev, J. Vetter, R. Neumann, M. Martin, *J. Electrochem. Soc.* 150, 189 (2003).
- [137] M.E. Toimil-Molares, V. Buschmann, D. Dobrev, R. Neumann, R. Scholz, I. U. Schuchert, J. Vetter, *Adv. Mater.* 13, 62 (2001).
- [138] D. Lysenkov, G. Müller, *Int. J. Nanotechnology* 2, 239 (2005).
- [139] N. V. Suetin, priv. comm. Moscow State University/Russia.
- [140] [www.keithley.com](http://www.keithley.com)
- [141] [www.soft-imaging.net](http://www.soft-imaging.net)
- [142] [www.microsoft.com](http://www.microsoft.com)
- [143] R. Heiderhoff, priv. comm. University of Wuppertal.
- [144] [www.frt-gmbh.com](http://www.frt-gmbh.com)
- [145] K. B. K. Teo, M. Chhowalla, G. Amaratunga, W. Milne et al., *APL* 80, 2011 (2002).
- [146] D. Lysenkov, G. Müller, *J. Vac. Sci. Technol. B* 24 (2006).
- [147] H. Dai, A. G. Rinzler, P. Nikolaev, A. Thess, D. T. Colbert, R. E. Smalley, *Chem. Phys. Lett.* 260, 471 (1996).
- [148] J. Kong, A. M. Cassell, H. Dai, *Chem. Phys. Lett.* 292, 567 (1996).
- [149] J. H. Hafner, M. J. Bronikowski, B. R. Azamian, P. Nikolaev, A. G. Rinzler, D. T. Colbert, K. A. Smith, R. E. Smalley, *Chem. Phys. Lett.* 296, 195 (1998).
- [150] E. Flahaut, A. Govindaraj, A. Peigney, Ch. Laurent, A. Rousset, C. N. R. Rao, *Chem. Phys. Lett.* 300, 236 (1999).
- [151] N. S. Xu, Y. Chen, S. Z. Deng, J. Chen, X. C. Ma, E. G. Wang, *Chin. Phys. Lett.* 18, 1278, (2001).
- [152] N. S. Xu, Y. Chen, S.Z. Deng, J. Chen, X.C. Ma, E.G. Wang, *J. Phys. D: Appl. Phys.* 34, 1597 (2001).
- [153] H. M. Manohara, M.J. Bronikowski, M. Hoenk, B. D. Hunt, P. H. Siegel, *J. Vac. Sci. Technol. B*23(1), 157 (2005).
- [154] V. Semet, V. T. Binh, P. Vincent, D. Guillot, K. B. K. Teo, M. Chhowalla, G. A. J. Amaratunga, W. I. Milne P. Legagneux and D. Pribat, *Appl. Phys. Lett.*, 81, 343, (2002).
- [155] R. Gomer, *Surf. Sci.* 299/300, 129, (1994).
- [156] J. R. Chen, R. Gomer, *Surf. Sci.* 79, 413 (1979).
- [157] J. A. Panitz, *Prog. Surf. Sci.* 8, 219, (1978).
- [158] D. Lysenkov, H. Abbas, G. Müller, J. Engstler, K.P. Budna, J.J. Schneider, *J. Vac. Sci. Technol. B* 23, 809 (2005).
- [159] A.M. Rao, D. Jacques, R.C. Haddon, W. Zhu, C. Bower, S. Jin, *Appl. Phys. Lett.* 76, 3813 (2000).
- [160] H. Murakami, M. Hirakawa, C. Tanaka, H. Yamakawa, *Appl. Phys. Lett.* 76, 1776 (2000).
- [161] J. C. She, N. S. Xu, S. Z. Deng, J. Chen, *Appl. Phys. Lett.* 83, 2671 (2003).
- [162] J. M. Bonard, H. Kind, T. Stockli, L.O. Nilsson, *Solid-State Electron.* 45, 893 (2001).
- [163] J. T. L. Thong, C. H. Oon, W. K. Eng, W. D. Zhang, L. M. Gan, *Appl. Phys. Lett.* 79, 2811 (2001).

- 
- [164] J. I. Sohn, S. Lee, Y. H. Song, S. Y. Choi, K. I. Cho, K. S. Nam, *Appl. Phys. Lett.* 78, 901 (2001).
- [165] K. Kawakita, K. Hata, H. Sato, Y. Saito, Technical digest of the 18<sup>th</sup> Vacuum Nanoelectronics Conf., Oxford, IEEE Cat. No. 05TH8837, 192 (2005).
- [166] D. Lysenkov, G. Müller, Technical digest of the 18<sup>th</sup> Vacuum Nanoelectronics Conf., Oxford, IEEE Cat. No. 05TH8837, 155 (2005).
- [167] N. Xu, Technical digest of the 18<sup>th</sup> Vacuum Nanoelectronics Conf., Oxford, IEEE Cat. No. 05TH8837, 31 (2005).
- [168] S. D. Liang et al, Technical digest of the 18<sup>th</sup> Vacuum Nanoelectronics Conf., Oxford, IEEE Cat. No. 05TH8837, 64 (2005).
- [169] W.J. Zhang, Y. Wu, W.K. Wong, X.M. Meng, C.Y. Chan, I. Bello, Y. Lifshitz, S.T. Lee, *Appl. Phys. Lett.* 83, 3365 (2003)
- [170] J. Zhou, S.Z. Deng, N. S. Xu, J. Chen, J.C. She, *Appl. Phys. Lett.* 83, 2653 (2003).
- [171] J. Chen, S.Z. Deng, N. S. Xu, W.X. Zhang, X.G. Wen, S.H. Yang, *Appl. Phys. Lett.* 83, 746 (2003).
- [172] J. M. Bonard, T. Stöckli, O. Noury, A. Chatelain, *Appl. Phys. Lett.* 78, 2775 (2001).
- [173] [www.lightlab.se](http://www.lightlab.se)
- [174] S.Z. Deng, Z.S. Wu, N.S. Xu, J. Chen, *Ultramicroscopy* 89, 105 (2001).
- [175] W. I. Milne, K. B. K. Teo, G. A. J. Amaratunga, P. Legagneux, L. Gangloff, J. P. Schnell, V. Semet, V. T. Binh, O. Groening, *J. Mater. Chem.* 14, 933 (2004).
- [176] N. de Jonge, Y. Lamy, K. Schoots, T. H. Oosterkamp, *Nature*, 420, 393 (2002).
- [177] E. W. Müller, *Z. Physik* 106, 541 (1937).
- [178] G. A. Westenskow, J. M. J. Madey, *Microwave Electron Gun and Particle Beams* 2, 223 (1984).
- [179] C. Travier, *Part. Acc.* 36, 33 (1991).
- [180] A. Gasper, Diplomarbeit, Dortmund (1998).
- [181] A. Gasper, C. Piel, T. Weis, A. Göhl, T. Habermann, G. Müller, *Proc. 6th European Particle Accelerator Conf.*, Stockholm, IOP Publishing, 1471 (1998).
- [182] K. A. Dean, B. F. Coll, E. Howard, S. V. Johnson, M. R. Johnson, H. Li, D. C. Jordan, L. Hilt Tisinger, M. Hupp, S. G. Thomas, E. Weisbrod, S. M. Smith, S. R. Young, J. Baker, D. Weston, W. J. Dauksher, Y. Wei, and J. E. Jaskie, *SID Symposium Digest of Technical Papers*, 36 (1), 1936 (2005).
- [183] J. Dijon, CEA LETI (2005).
- [184] L. P. Muray, J. P. Spallas, C. Stebler, K. Lee, M. Mankos, Y. Hsu, M. Gmur, T. H. P. Chang, *J. Vac. Sci. Technol., B*, 18, 3099 (2000).
- [185] V. T. Binh, V. Semet, D. Guillot, P. Legagneux, D. Pribat, *Appl. Phys. Lett.*, 73, 2048 (1998).
- [186] J. Robertson, *Mater. Today*, October, 46 (2004).